A *Drosophila* Model of Generalised Epilepsy and Paroxysmal Dyskinesia: Generation, Characterisation, and Functional Analysis

A thesis for the degree of

Doctor of Philosophy

at

UCL

by

Patrick Kratschmer

Declaration

I, Patrick Kratschmer, confirm that the work presented in this thesis is my own. Where information has been derived from other sources, I confirm that this has been indicated in the thesis.

To Health -

the most precious of things.

Abstract

Generalised epilepsy and paroxysmal dyskinesia (GEPD) patients present with epilepsy (absence- and generalised tonic-clonic seizures), paroxysmal dyskinesia (non-kinesigenic), or a combination thereof. GEPD is linked to a missense mutation (D434G) in *KCNMA1*, which encodes the α-subunit of the BK channel, a Ca^{2+}- and voltage-activated K^+ channel. Previous studies have demonstrated that this mutation causes a gain of BK channel function by potentiating the allosteric coupling between Ca^{2+} binding and channel opening. Due to the role of BK channels in action potential repolarisation, it has been hypothesised that the D434G mutation narrows action potential width and increases neuronal firing frequencies, leading to seizures and dyskinetic attacks.

However, BK channels are expressed broadly throughout the human body, including various extra-neuronal tissues, and, on a subcellular level, localise not only to the plasma membrane but also to various intracellular organelles. Due to this pleiotropy, the organismal effects of the D434G mutation remain unclear. In this thesis, I present the generation, characterisation, and functional analysis of a novel knock-in fly model carrying the D434G-equivalent E366G mutation in *slowpoke* (*slo*), the *Drosophila* orthologue of *KCNMA1* – this novel *slo* allele is termed *slo^{E366G}*.

Evidence is provided that the E366G mutation increases the Ca^{2+}-sensitivity of Slo channels *ex vivo*. Moreover, *slo^{E366G}/+* animals exhibit a severe decrease in locomotion and altered action selection, phenotypes that correlate with aberrant motoneuron activity, as shown via electrophysiology and live optical imaging. Using a genetic approach, I demonstrate that cholinergic neurons mediate this locomotor defect. Further, via RNA-sequencing I provide evidence that *slo^{E366G}/+* flies exhibit altered metabolic-, redox-, and immune function, and that the stress-responsive transcription factor *foxo* genetically interacts with *slo^{E366G}*. Together, these data suggest a pathogenic locus for GEPD and define molecular pathways involved in GEPD pathogenesis.

4

Impact Statement

The work presented in this thesis has direct academic impact within the fields of epilepsy and dyskinesia research, while also laying a foundation from which to potentially derive clinical benefit in the future. Importantly, the academic impact of this work reaches across scientific disciplines, as it provides a novel genetic tool with which to address a variety of questions within the biomedical sciences.

Prior to the work presented in this thesis, GEPD – a combined epilepsy-paroxysmal dyskinesia syndrome (Du et al., 2005) – had not been studied in a living organism due to the lack of an *in vivo* model. As a result, the pathogenesis of GEPD remained incompletely understood. This thesis presents the generation of the first *in vivo* model of GEPD, which I generated by introducing the mutation linked to GEPD – a D434G missense mutation in *KCNMA1* (Du et al., 2005) – into the *Drosophila* orthologue *slo*, establishing the novel allele *slo^{E366G}*.

By studying this allele *in vivo*, two fundamental discoveries have been made: (1) the GEPD-linked mutation exerts its effects in cholinergic neurons – a finding of great academic and clinical interest because the neuroanatomical origins of dyskinesia are unclear (Kaji et al., 2018). Hence, localising GEPD pathology might inform translational dyskinesia research and facilitate the discovery of targeted therapeutics with minimal side effects. (2) GEPD pathogenesis is linked to perturbed metabolism. This unexpected finding is intriguing because it expands the scope of potential molecular mechanisms underlying both dyskinesia and epilepsy (Erro et al., 2017). Further research into these mechanisms might lead to novel therapeutic approaches for GEPD patients as well as for dyskinesia and epilepsy patients more generally.

Although *slo* was cloned in 1991 (Atkinson et al., 1991), the *slo^{E366G}* allele presented in this thesis is the first gain-of-function allele of this gene in *Drosophila*. As such, it will greatly facilitate the study of the behavioural, cellular, and molecular functions of *slo*. The results of such investigations might have far-reaching academic and clinical implications, because *KCNMA1* is widely expressed throughout the human body and involved in a variety of physiological mechanisms. Consequently, novel insight into *Drosophila slo* function might

translate into an increased understanding of a wide range of human diseases and disorders.

Altogether, the novel *Drosophila* knock-in model of GEPD presented in this thesis is predicted to contribute to both clinical and academic research into the pathophysiology underlying dyskinesia and epilepsy, while also impacting other areas within medicine and the biomedical sciences – with the ultimate aim to improve the treatment and lives of patients.

Table of Contents

List of Figures

List of Tables

Abbreviations

$[Ca^{2+}]$	Ca^{2+} concentration
ACh	acetylcholine
AED	anti-epileptic drug
AMP	anti-microbial peptide
AP	action potential
ATP	adenosine triphosphate
AZ	active zone
BBB	blood-brain barrier
BDGP	Berkley *Drosophila* Genome Project
BDSC	Bloomington *Drosophila* Stock Center
BH	Benjamini-Hochberg
BP	biological process
Ca_v channel	voltage-gated Ca^{2+} channel
CBGT	cortico-basal ganglia-thalamocortical
CC	cellular component
CCD	cortical collecting duct
cDNA	complementary DNA
CNS	central nervous system
CPG	central pattern generator
CRE	*cis*-regulatory element
CRISPR	clustered regularly interspaced short palindromic repeats
CTD	cytoplasmic tail domain
DAM	*Drosophila* Activity Monitor
DART	*Drosophila* ARousal Tracker
DBS	deep brain stimulation
DEG	differentially expressed gene
DEL	deletion
DGE	differential gene expression
DGRC	*Drosophila* Genomics Resource Center
DLM	dorsal longitudinal flight muscle
DN1p	posterior dorsal neuron 1 cluster
DPGP	*Drosophila* Population Genomics Project
DS	Dravet syndrome
dscDNA	double-stranded cDNA
dUTP	deoxyuridine triphosphate
EB	ellipsoid body
EEG	electroencephalogram
EJC	excitatory junctional current
EJP	excitatory junction potential
ELISA	enzyme-linked immunosorbent assay
EMS	ethyl methanesulfonate

fAHP	fast after-hyperpolarisation
FDR	false discovery rate
FISH	fluorescence *in situ* hybridization
FTP	File Transfer Protocol
GABA	γ-aminobutyric acid
gDNA	genomic DNA
GECI	genetically-encoded Ca^{2+} indicator
GEFS+	genetic epilepsy with febrile seizures plus
GEPD	generalised epilepsy and paroxysmal dyskinesia
GLM	generalised linear model
GLUT1	glucose transporter type 1
GLUT1-DS	GLUT1 deficiency syndrome
GO	gene ontology
GP(i/e)	globus pallidus (internus/externus)
GRN	gene regulatory network
HFS	high-frequency stimulation
HR	homologous recombination
hs	heat shock
HSV	hue, saturation, value
I_A	voltage-gated fast K^+ current
ICCA	infantile convulsions and choreoathetosis
I_{CF}	Ca^{2+}-gated fast K^+ current
I_{CS}	Ca^{2+}-gated delayed K^+ current
IGV	Integrative Genomics Viewer
I_K	voltage-gated delayed K^+ current
IMM	inner mitochondrial membrane
I_{Nap}	persistent sodium current
INM	inner nuclear membrane
INS	insertion
IPC	insulin-producing cell
iPSC	induced pluripotent stem cell
IQR	inter-quartile range
KEGG	Kyoto Encyclopaedia of Genes and Genomes
K_v channel	voltage-gated K^+ channel
L3	third instar
LFC	$\log_2$(fold-change)
LFS	low-frequency stimulation
LID	levodopa-induced dyskinesia
LN	local neuron
LSD	lysosomal storage disease
LTD	long-term depression
LTP	long-term potentiation
megaRNP	large ribonucleoprotein

mEJP	miniature EJP
MF	molecular function
miRNA	microRNA
MN	motoneuron
mPTP	mitochondrial protein transition pore
MRI	magnetic resonance imaging
mRNA	messenger RNA
MSN	medium spiny neuron
mtBK channel	mitochondrial BK channel
Na_v channel	voltage-gated Na^+ channel
nBK channel	nuclear BK channel
ncRNA	non-coding RNA
NE	nuclear envelope
NES	normalised enrichment score
NMJ	neuromuscular junction
NPC1/2	Niemann-Pick disease type C1/2
OMM	outer mitochondrial membrane
ONM	outer nuclear membrane
PCA	principle component analysis
PCR	polymerase chain reaction
PD	Parkinson's disease
PED	paroxysmal exercise-induced dyskinesia
PGD	pore-gate domain
PI	pars intercerebralis
PKD	paroxysmal kinesigenic dyskinesia
PNKD	paroxysmal non-kinesigenic dyskinesia
PxD	paroxysmal dyskinesia
qPCR	quantitative PCR
RCK1/2	regulator of K^+ conductance 1/2
redox	reduction–oxidation
RIN	RNA Integrity Number
rlog	regularised logarithm
RNA-seq	RNA-sequencing
RNAi	RNA interference
ROI	region of interest
ROS	reactive oxygen species
rRNA	ribosomal RNA
RT	room temperature
SD	synaptic depotentiation
SNARE	soluble NSF attachment protein receptor
SNc	substantia nigra pars compacta
SNP	single-nucleotide polymorphism
SNr	substantia nigra pars reticulata

STN	subthalamic nucleus
SWD	spike-wave discharge
TCA	tricarboxylic acid
TEM	transmission electron microscopy
TF	transcription factor
TM	transmembrane
TOPO	pCR-Blunt II-TOPO
UAS	upstream activating sequence
UCSC	University of California, Santa Cruz
$V_{1/2}$	voltage at half-maximum conductance
VDRC	Vienna *Drosophila* Resource Center
VNC	ventral nerve cord
VSD	voltage-sensing domain

1 Introduction

1.1 Paroxysmal Dyskinesia

Paroxysmal dyskinesia (PxD) describes a group of hyperkinetic movement disorders characterised by episodically occurring involuntary movements, the latter presenting mainly as dystonic, choreiform, ballistic, or a combination thereof (Bhatia, 2011; Blakeley and Jankovic, 2002). Dystonia is characterised by twisting movements that result in abnormal postures; chorea by brief, irregular movements of individual body parts; and ballismus by large-amplitude movements of the proximal parts of the limbs (Kandel et al., 2013). Three clinically distinct PxDs have been described, based on how dyskinetic attacks are triggered: paroxysmal kinesigenic dyskinesia (PKD), paroxysmal non-kinesigenic dyskinesia (PNKD), and paroxysmal exercise-induced dyskinesia (PED) (Bhatia, 2011). Their distinct characteristics, including triggers, are listed in Table 1.

Table 1 Paroxysmal Dyskinesias

	PKD	PNKD	PED
Trigger of attacks	sudden movement[1,5]	mainly caffeine[1,5] and alcohol[1,2,5]	mainly exertion[1,5] and exhaustion[1,5]
Clinical manifestation	dystonia[1,2], chorea[1,2], ballismus[1]	dystonia[1], chorea[1], ballismus[2]	dystonia[1,2], chorea[2]
Attack duration	seconds[1,2]	minutes to hours[1,2,5]	minutes[1,2,5]
Attack frequency	mostly daily[1,2]	mostly weekly[1,2]	mostly weekly[1,2,5]
Age of onset	mainly childhood[1,2,5]	mainly childhood[1,2]	mainly childhood[1,2]
Genetic cause	*PRRT2*[2,3,5]	*PNKD*[1,2,3,5]	*SLC2A1*[1,2,3,5]
Inheritance pattern	autosomal dominant[3]	autosomal dominant[1]	autosomal dominant[4]
Common treatment	carbamazepine[1,5] and phenytoin[1]	clonazepam[2] and diazepam[2]	ketogenic diet[1,2,4]

[1](Bhatia, 2011), [2](Erro et al., 2014), [3](Erro et al., 2017), [4](De Giorgis and Veggiotti, 2013), [5](Gardiner et al., 2015)

Of note, the information in Table 1 lists the most common characteristics, including the most common genetic causes, of the three PxDs and is not exhaustive. PxD is considered to be relatively rare, with one study describing its occurrence in 0.76% of 12063 movement disorder patients (Blakeley and Jankovic, 2002) – however, its exact prevalence in the general population is unknown (Bhatia, 2011). PxD can either be genetic (primary) or acquired (secondary), the latter of which can be elicited by stroke, trauma, infection, autoimmune disease, migraine, and hypo- as well as hyperglycaemia (Bhatia, 2011; Blakeley and Jankovic, 2002). While common genetic mutations underlying each of the PxDs have been identified (Table 1), it should be noted that there is clinical overlap between these genotype-phenotype relationships. For example, patients with *PRRT2* and *PNKD* mutations can also present with PED, while patients with mutations in *SLC2A1* can also present with PKD and PNKD (Erro et al., 2014; Gardiner et al., 2015). Moreover, mutations in these genes can be associated with additional clinical phenotypes, either in isolation or in combination with PxD – most notably with seizures and migraine (Gardiner et al., 2015). The severity of paroxysmal attacks tends to decrease with age in PKD and PNKD, but not in PED (Erro et al., 2017).

1.2 Pathophysiology of Paroxysmal Dyskinesia

1.2.1 Genetic and Molecular Mechanisms

Defining the physiological functions of the genes associated with PxD is an important pre-requisite for understanding their pathogenicity when mutated. An increased molecular understanding of PxD might allow for the development of targeted treatment approaches, aimed at improving the lives of patients with minimal side effects.

1.2.1.1 *PRRT2*

The PRRT2 protein is 340 amino acids long and carries two transmembrane (TM) domains (Erro et al., 2017). While three PRRT2 splice isoforms have been described, the majority of pathogenic mutations in *PRRT2* occur in a conserved region included in each splice variant (Erro et al., 2017). Most *PRRT2* mutations

associated with PKD lead to loss-of-function alleles (Gardiner et al., 2015; Tan et al., 2018). *PRRT2* is expressed in the mammalian spinal cord and brain, particularly in the cerebral cortex, basal ganglia, hippocampus, and cerebellum (Chen et al., 2011; Heron et al., 2012; Lee et al., 2012a). Importantly, *PRRT2* localises to pre-synaptic termini and physically interacts with components of the SNARE complex, as shown via co-immunoprecipitation (Coleman et al., 2018; Lee et al., 2012a; Tan et al., 2018; Valente et al., 2016). Since the SNARE protein complex is responsible for membrane fusion between pre-synaptic neurotransmitter-containing vesicles and the plasma membrane (Ungar and Hughson, 2003), these data suggest a role for PRRT2 in pre-synaptic neurotransmitter release.

Indeed, knock-down of *PRRT2* in primary rat hippocampal cultures caused a decrease in synaptic density and synaptic release probability, as identified via immuno-staining and autaptic electrophysiological recordings, respectively (Valente et al., 2016). While these data suggest that PRRT2 facilitates neurotransmitter release, more recent studies have provided strong evidence for PRRT2 to inhibit exocytosis. Using a mouse model recapitulating the c.649dupC loss-of-function *PRRT2* mutation, which is linked to PKD, it could be shown that wild-type PRRT2 inhibits SNARE complex formation (Tan et al., 2018). Consequently, dis-inhibition of SNARE complex formation in response to a loss of PRRT2 function was demonstrated to facilitate synaptic transmission at the cerebellar parallel fibre-Purkinje cell synapse (Tan et al., 2018). Intriguingly, conditional Cre-mediated knock-out of *PRRT2* in granule cells of the cerebellum recapitulated the electrophysiological and behavioural phenotypes exhibited by germline mutant mice, suggesting a pathogenic locus for PKD (Tan et al., 2018). Moreover, reconstituted *in vitro* fusion assays showed that PRRT2 negatively regulates SNARE-mediated vesicle fusion by affecting the vesicle docking/priming process (Coleman et al., 2018). Interestingly, the dis-inhibitory effect of two human PKD mutations on SNARE-mediated vesicle fusion correlated with the severity of their associated clinical symptoms, suggesting a molecular mechanism underlying PKD pathogenesis (Coleman et al., 2018).

In addition to these pre-synaptic functions, *PRRT2* has also been shown to negatively regulate the voltage-gated Na$^+$ channels (Na$_v$ channels) Na$_v$1.2 and

Na$_v$1.6 at the axon initial segment via direct protein-protein interactions, as determined by co-immunoprecipitation (Fruscione et al., 2018). Indeed, iPSC-derived neurons carrying the c.649dupC mutation in *PRRT2* exhibited increases in Na$_v$ channel currents and intrinsic excitability, as determined via single-cell patch clamp recordings (Fruscione et al., 2018). Altogether, these studies suggest that PRRT2 negatively regulates both neurotransmitter release at pre-synaptic termini and Na$_v$ channel currents at the axon initial segment. Hence, PKD-linked loss-of-function mutations of *PRRT2* are predicted to potentiate both of these processes.

1.2.1.2 *PNKD*

PNKD expresses at least three splice isoforms, the largest one of which, PNKD-L, is 385 amino acids long (Erro et al., 2017). Immunohistochemistry experiments in mice revealed a brain-specific expression pattern of PNKD-L, including the basal ganglia, cerebellum, and spinal cord (Lee et al., 2012b; Shen et al., 2011). Expression of GFP-tagged PNKD-L as well as immuno-staining against wild-type PNKD-L *in vitro* provided strong evidence for PNKD-L to be a membrane-associated protein (Shen et al., 2011). While PNKD-linked mutations in *PNKD* have been suggested to lead to loss-of-function alleles via protein truncation or degradation (Gardiner et al., 2015; Shen et al., 2011), recent evidence indicates that they might, in fact, be neo- or hypermorphic (Shen et al., 2015). While *PNKD* knock-out mice exhibited lower levels of glutathione in the cerebral cortex, indicating a role for PNKD in regulating cellular redox state (Shen et al., 2011), more recent studies have linked PNKD function to the regulation of pre-synaptic neurotransmitter release.

Carbon fibre amperometry identified dysregulated dopamine signalling in striatal slices from a mouse model recapitulating human *PNKD* mutations, implicating PNKD in nigrostriatal neurotransmission, disturbance of which might be involved in PNKD pathogenesis (Lee et al., 2012b). Using c-Fos staining after dyskinetic attacks in this PNKD mouse model, increased activation of the basal ganglia was observed, providing additional evidence for it to contain the pathogenic locus for PNKD (Lee et al., 2012b). Importantly, a recent study showed a direct interaction between PNKD and Rab3-interacting molecule 1

(RIM1) and RIM2 at active zones (AZs) via co-immunoprecipitation and immunogold electron microscopy (Shen et al., 2015). RIMs are large scaffold proteins that associate with vesicle-, AZ-, and plasma membrane proteins, and are involved in regulating neurotransmitter release (Wang and Südhof, 2003), supporting a role for PNKD in neurotransmission. Indeed, using the pH-sensitive GFP indicator VGluT1-pHluorin in primary rat hippocampal cultures, it was demonstrated that PNKD inhibits exocytosis (Shen et al., 2015). Importantly, PNKD carrying human *PNKD* mutations failed to inhibit exocytosis, suggesting dis-inhibition of neurotransmitter release as a pathogenic mechanism underlying PNKD (Shen et al., 2015). Altogether, these data indicate an important role for PNKD in the regulation of pre-synaptic neurotransmitter release, which is suggested to be dysregulated in PNKD.

1.2.1.3 *SLC2A1*

SLC2A1 encodes the glucose transporter type 1 (GLUT1), an integral membrane protein with 12 TM domains and a length of 492 amino acids (Mueckler et al., 1985; Wang et al., 2000). GLUT1 is expressed on the plasma membrane of most cells, and catalyses the facilitated diffusion of glucose across the lipid bilayer, acting as a uniporter (Brockmann, 2009; Deng et al., 2014). Importantly, GLUT1 is the principal glucose transporter in erythrocytes, astrocytes, and endothelial cells of the brain microvasculature, where it facilitates the transport of glucose across the blood-brain barrier (BBB) (De Giorgis and Veggiotti, 2013). Impaired glucose transport into the brain leads to unmet neuronal energy demands and hypoglycorrhachia – low glucose concentrations in the cerebrospinal fluid (CSF) – eliciting the clinical symptoms of PED (Brockmann, 2009; De Giorgis and Veggiotti, 2013). Indeed, the effectiveness of the ketogenic diet in treating PED illustrates the malfunction of GLUT1: the ketogenic diet is a dietary intervention classically consisting of a fat:(carbohydrate + protein) ratio of 4:1, designed to mimic the metabolic state of fasting (De Giorgis and Veggiotti, 2013). In the absence of sufficient glucose transport into the brain, this fasting-like state induces the production of ketone bodies via fatty acid degradation in the liver (De Giorgis and Veggiotti, 2013). Since ketone bodies use a GLUT1-independent mechanism of transport into the central nervous system (CNS) – facilitated

diffusion via the monocarboxylate transporter 1 (MCT1) – they provide an alternative energy source to glucose, restoring brain energy metabolism and relieving PED symptoms (De Giorgis and Veggiotti, 2013). Of note, the crystal structure of the human GLUT1 protein has recently been reported in an inward-open conformation at 3.2 Å resolution – this resource may allow for the effects of PED-causing mutations on protein function to be appraised on a structural level (Deng et al., 2014).

1.2.1.4 A Pathological Framework Based on Protein Function

Since *PRRT2* and *PNKD* regulate pre-synaptic neurotransmitter release, a dysregulation of this process is proposed to underlie PKD and PNKD, respectively. Due to this association of PKD and PNKD with synaptic defects, these disorders have been classified as "synaptopathies" (Erro et al., 2017). Similarly, due to the role of GLUT1 as a glucose transporter, *SLC2A1*-linked PED has been classified as a "transportopathy" (Erro et al., 2017). This pathological framework is completed by "channelopathies", describing diseases caused by intrinsic changes to ion channel function (Erro et al., 2017; Shen et al., 2015).

1.2.2 Neuroanatomy

While movement disorders can theoretically originate in the cortex, the cerebellum, or the basal ganglia (Lee et al., 2012b), the cortico-basal ganglia-thalamocortical (CBGT) circuit has been shown to be frequently affected (Kandel et al., 2013). Figure 1.1 illustrates a simplified version of the CBGT circuit based on the "three-pathway model" of the basal ganglia, comprising (1) the movement-inducing *direct* striatopallidal pathway, (2) the movement-inhibiting *indirect* striatopallidal pathway, and (3) the modulatory activity of the *striosomal* striatonigral pathway (Graybiel et al., 2000). Notably, four similar circuits of this architecture exist, differentiated by their topographical cortico-striatal projections, which serve motor-, oculomotor-, executive/associative-, and emotion/motivation processing (Kandel et al., 2013; Poewe et al., 2017). However, only the motor circuit will be discussed due to its importance in PxD.
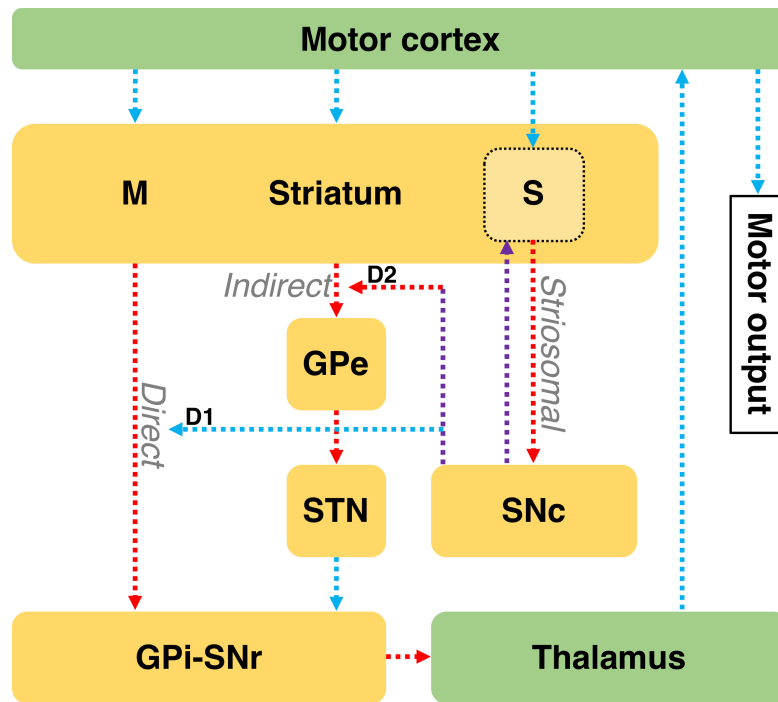
Figure 1.1 The Cortico-Basal Ganglia-Thalamocortical Circuit

This simplified diagram of the CBGT motor circuit illustrates the three-pathway model of the basal ganglia. The motor cortex forms excitatory connections (cyan arrows) with the striatal matrix component (M) and the striosomal component (S) of the striatum. The direct pathway sends inhibitory connections (red arrows) from M to the globus pallidus internus (GPi) and the substantia nigra pars reticulata (SNr), while the indirect pathway first sends inhibitory connections from M to the globus pallidus externus (GPe). The GPe inhibits the subthalamic nucleus (STN), which in turn excites the GPi and SNr. The GPi and SNr are the main output structures of the basal ganglia and inhibit the thalamus. Via their differences in connectivities, direct pathway activation causes increased-, and indirect pathway activation decreased thalamic activity. The thalamus sends excitatory connections back to the motor cortex, activating descending motor circuits and inducing motor output. Via the striosomal pathway from S to the substantia nigra pars compacta (SNc), the striatum can regulate dopaminergic modulatory input from the SNc (violet arrows), which acts on excitatory dopamine receptors (D1) of the direct-, and on inhibitory dopamine receptors (D2) of the indirect pathway. This figure was adapted from the following publications: (Goto et al., 2005; Graybiel et al., 2000; Kaji et al., 2018).

A complex interaction between the direct-, indirect-, striosomal-, and other pathways within the basal ganglia, thalamus, and cortex implicate the CBGT circuit in motor behaviours such as action selection, movement preparation, and movement execution (Kandel et al., 2013). Disturbances in any of its components can cause aberrant network activity, manifesting as movement disorders that can be hypo- or hyperkinetic (Kandel et al., 2013). Evidence for a dysregulation of the

CBGT circuit in PxD is derived from animal models as well as from functional and structural brain imaging in humans.

Evidence for basal ganglia dysregulation in PNKD is provided by studies of a mouse model recapitulating human *PNKD* disease mutations, as introduced in Paragraph 1.2.1.2 (Lee et al., 2012b). These mice showed stress-, caffeine-, and alcohol-induced dyskinesia reminiscent of the human phenotype, which correlated with a specific increase in activity of the GP, STN, and SNr, as determined via immuno-staining for c-Fos (Lee et al., 2012b). Two lines of evidence strongly suggest dysregulated striatal dopamine signalling in this model of PNKD: (1) the PNKD mice showed altered striatal expression of proteins involved in dopamine signalling, and (2) exhibited decreased dopaminergic neurotransmitter release in the striatum (Lee et al., 2012b). Since injection of quinpirole, a specific D2 dopamine receptor agonist, was sufficient to induce dyskinesia in this PNKD mouse model, strong evidence points towards the indirect striatopallidal pathway as a pathogenic locus in PNKD (Figure 1.1) (Lee et al., 2012b).

Evidence for an involvement of the striatum in PED is provided by a study reporting a five-generation family with inherited PED and epilepsy linked to a heterozygous missense mutation in *SLC2A1* (Suls et al., 2008). Using interictal fludeoxyglucose-positron emission tomography (FDG-PET), which measures the uptake of the glucose analogue fludeoxyglucose (FDG) into tissue, PED patients were shown to exhibit an increased metabolic demand in the putamen and midtemporal cortex bilaterally and in the right lingual cortex, while a decreased metabolic demand was detected in the thalamus, anterior cingulate cortex, and midfrontal and superior frontal cortex bilaterally (Suls et al., 2008). Interestingly, a positive correlation was found between the frequency of PED attacks and hypermetabolism in the left putamen as well as hypometabolism in the left superior frontal- and bilateral anterior cingulate cortex (Suls et al., 2008). Moreover, ictal single-photon emission computed tomography (SPECT) revealed hyperperfusion of the left putamen during a dyskinetic episode (Suls et al., 2008). These findings establish a link between altered glucose metabolism, activity in cortico-striatal areas, and PED (Erro et al., 2017; Suls et al., 2008).

Structural brain imaging has provided evidence for morphological abnormalities of the thalamus in PKD patients (Kim et al., 2015). Structural magnetic resonance imaging (MRI) volumetric analyses revealed a reduced bilateral thalamic volume in PKD patients compared to controls, while no difference could be detected in the caudate nucleus, putamen, GP, amygdala, and hippocampus (Kim et al., 2015). These data also showed significant alterations in thalamic morphology in PKD patients, and diffusion tensor imaging (DTI) demonstrated changes in thalamic fractional anisotropy (FA) in PKD patients, associating macro- as well as microstructural thalamic changes with this disorder (Kim et al., 2015).

The CBGT circuit is involved in a variety of other disorders affecting movement, including Parkinson's disease (PD), levodopa-induced dyskinesia (LID), and dystonia. Neuronal loss in areas of the SNc and intracellular accumulation of α-synuclein ("Lewy bodies") are characteristic features of PD (Poewe et al., 2017). The resulting decrease in dopaminergic nigrostriatal signalling differentially affects the direct and indirect striatopallidal pathways, leading to increased GPi activity and a concomitant decreased activity of thalamocortical projections, manifesting as bradykinesia, rigidity and/or rest tremor (Figure 1.1) (Poewe et al., 2017). While L-DOPA is the standard treatment for PD, its long-term use can precipitate hyperkinetic motor problems classified as LID, which can manifest as choreic or dystonic (Poewe et al., 2017). The alterations in CBGT network activity in LID are incompletely understood, but might involve plasticity changes in CBGT connections due to discontinuous L-DOPA delivery (Graybiel et al., 2000; Poewe et al., 2017). In order to treat both PD and LID, deep-brain stimulation (DBS) of the STN or GPi has the strongest evidence-base: DBS applies high-frequency stimulation (HFS; 100-200 Hz) to the target brain area, mimicking the effect of a lesion without the need to remove brain tissue (Poewe et al., 2017). How the same manipulation of the CBGT circuit can be an effective treatment for both hypo- (PD) and hyperkinesia (LID) is not understood, but might be linked to differential plasticity changes in the matrix- and striosomal components of the striatum (Figure 1.1) (Graybiel et al., 2000).

Dystonia causes sustained muscle contractions that can result in abnormal postures and twisting movements (Kaji et al., 2018). Autopsy studies on patients with X-linked dystonia-parkinsonism (XDP) identified striosomal-specific lesions in the striatum during the dystonic phase of the disease, specifically implicating the degeneration of striosomal medium spiny neurons (MSNs) in dystonia (Figure 1.1) (Kaji et al., 2018). A loss of striosomal MSNs is predicted to disrupt striato-nigro-striatal signalling, reminiscent of the endophenotype suggested to underlie LID, and might lead to dystonia by dis-inhibiting dopamine release from the SNc (Figure 1.1) (Kaji et al., 2018).

Despite the evidence linking the basal ganglia to the pathogenesis of movement disorders, including PxD, it must be stressed that up- and downstream structures might also be involved – particularly the cerebellum, which sends projections to the basal ganglia via the intralaminar thalamic nuclei and has been associated with dystonia (Kaji et al., 2018; Kandel et al., 2013). Neuroimaging studies have linked cervical dystonia to cerebellar abnormalities (Batla et al., 2015), while dystonic symptoms in a dystonia rat model were relieved by cerebellectomy (LeDoux et al., 1993). Moreover, acute *in vivo* knock-down of *TOR1A*, mutations in which are linked to DYT1 dystonia, in the cerebellum was sufficient to induce dystonia in mice (Fremont et al., 2017). The cerebellum has also been linked to PxD: as discussed in Paragraph 1.2.1.1, studies on a PKD mouse model recapitulating the human c.649dupC mutation in *PRRT2* provided strong evidence for the cerebellum to be the pathogenic locus of PKD (Tan et al., 2018). Hence, while the basal ganglia are clearly important for the pathogenesis of movement disorders, afferent cerebellar inputs might also be involved (Kaji et al., 2018).

1.3 Association of Paroxysmal Dyskinesia with Epilepsy

1.3.1 Epilepsy

Epilepsy is a neurological disorder that chronically predisposes patients to the development of seizures and affects ~65 million people worldwide (Devinsky et al., 2018). A seizure is defined as a transient change in behaviour, internal or external, caused by pathologically increased activation or synchronisation of

neural circuits in the brain (Devinsky et al., 2018). According to the International League Against Epilepsy (ILAE) classification scheme (Scheffer et al., 2017), seizures are grouped into three categories, based on the location of seizure onset: (1) *focal seizures* originate in isolated areas in one hemisphere, (2) *generalised seizures* have a more widespread origin in both hemispheres, while the origin of (3) *unknown seizures* is undetermined (Devinsky et al., 2018). Each of these three seizure categories can be sub-divided into motor- and non-motor seizures (Devinsky et al., 2018). Epilepsy can be caused by trauma, immunological challenges, metabolic disturbances, or genetic mutations (Devinsky et al., 2018).

Research into the pathogenesis of epilepsy can be divided into the study of epileptogenesis and the study of ictogenesis – the former describing the pathological changes in neuronal structure and function that predispose a brain to epilepsy, the latter describing the mechanisms underlying the development of seizures (Devinsky et al., 2018). Several cellular and molecular changes have been associated with epileptogenesis, such as aberrantly high levels of mossy fibre sprouting in the hippocampus and altered adenosinergic signalling (Boison, 2016; Buckmaster, 2012; Devinsky et al., 2018). Studies on ictogenesis have demonstrated mechanistic differences between generalised and focal seizures. Absence seizures, a type of generalised seizure, often show bilaterally synchronous spike-wave discharges (SWDs) – symmetrical neuronal activity patterns that can be detected via electroencephalogram (EEG) – emanating from thalamo-cortical networks (Figure 1.1) (Devinsky et al., 2018; Snead III, 1995). Focal epilepsy is associated with two main interictal network events: (1) interictal epileptiform spikes (IESs), characterised by transiently synchronised activity of cortical principal neurons, and (2) fast high frequency oscillations (HFOs), generated by fast synchronised activity of pathologically interconnected cortical principal neurons (Devinsky et al., 2018; Staley et al., 2011; Zijlmans et al., 2012). Anti-epileptic drugs (AEDs) are the primary treatment for epilepsy (Devinsky et al., 2018). However, while they can reduce seizure frequency and severity, they do not treat the underlying cause (Devinsky et al., 2018). Drug-resistant epilepsy (~36% of cases) can be treated via surgery, the implantation of a

neurostimulatory device, or dietary intervention, such as the ketogenic diet (Devinsky et al., 2018).

1.3.2 Combined Paroxysmal Dyskinesia-Epilepsy Syndromes

The co-occurrence of PxD and epilepsy in the same family or individual has been increasingly recognised (Erro et al., 2017). Three PxD-epilepsy syndromes have been described, each combining different types of PxD and epilepsy: infantile convulsions and choreoathetosis (ICCA), GEPD, and GLUT1 deficiency syndrome (GLUT1-DS). An overview of these syndromes, including the types of PxD and seizures they combine, is presented in Table 2.

Table 2 Combined Paroxysmal Dyskinesia-Epilepsy Syndromes

	ICCA		GEPD	GLUT1-DS
Type of PxD	PKD[1]		PNKD[1,3]	PED[1,2]
Type of seizures	mainly focal[5]	afebrile focal[1,4] and generalised tonic-clonic[1,4]	mainly absence[1,3], rare generalised tonic-clonic[1,3]	mainly absence[1,2]
Epilepsy age of onset	Infancy[1,5]	early childhood[4]	childhood[3]	infancy or early childhood[2]
Genetic cause	*PRRT2*[1]	*SCN8A*[1,4]	*KCNMA1*[1,3]	*SLC2A1*[1,2]
Inheritance pattern	autosomal dominant[1,5]	autosomal dominant[4]	autosomal dominant[1,3]	autosomal dominant[2]
Treatment	variable	variable	valproate[3] and lamotrigine[3] for seizures, clonazepam[3] for PNKD	primarily ketogenic diet[2]

[1](Erro et al., 2017), [2](De Giorgis and Veggiotti, 2013), [3](Du et al., 2005), [4](Gardella et al., 2016), [5](Szepetowski et al., 1997)

Of note, the information in Table 2 lists the most common characteristics of the three combined PxD-epilepsy syndromes and is not exhaustive. Indeed, variability in the types of seizures for ICCA and GLUT1-DS has been described

(Erro et al., 2017; De Giorgis and Veggiotti, 2013). Moreover, GLUT1-DS has a broad spectrum of clinical presentations, including epilepsy, intellectual disability, acquired microcephaly, as well as paroxysmal and non-paroxysmal movement disorders (De Giorgis and Veggiotti, 2013). Hence, GLUT1-DS is not necessarily a combined PxD-epilepsy syndrome, but can present as such. While GLUT1-DS and ICCA have been observed in multiple families (Erro et al., 2017), there is only one reported family presenting with GEPD (Du et al., 2005).

It is interesting to note that *PRRT2* and *SLC2A1* are linked to both PxD and combined PxD-epilepsy syndromes (Table 1 and Table 2). This might be explained by varying effects of different genetic mutations on protein function. It has been suggested, for example, that a 25-35% decrease in GLUT1 function might result in milder-, a 40-75% decrease in more severe phenotypes, manifesting as PED and GLUT1-DS, respectively (Erro et al., 2017; De Giorgis and Veggiotti, 2013). On the other hand, the same *PRRT2* mutation (c.649dupC) has been shown to result in varying clinical presentations inter- and intrafamilially – a pleitropic effect that is not yet understood, but likely attributable to environmental factors and the presence of modifier genes (Erro et al., 2017; Nobile and Striano, 2014). While mutations in *PNKD*, the main genetic cause for PNKD (Table 1), are not linked to epilepsy, GEPD patients present with a combined PNKD-epilepsy phenotype (Du et al., 2005).

1.3.3 Generalised Epilepsy and Paroxysmal Dyskinesia

GEPD has been reported in a single family of European descent, in which 4 individuals presented with epilepsy, 7 with PxD, and 5 with a combination of both (Du et al., 2005). PxD was classified as PNKD, with an age of onset between infancy and childhood and clinical presentations of dystonic or choreiform movements affecting the mouth, tongue, and extremities (Du et al., 2005). These attacks were triggered by caffeine, alcohol, and stress, occurring weekly during the time of onset but gradually decreasing in frequency with age (Du et al., 2005). PNKD attacks lasted seconds to minutes, and were partially responsive to clonazepam in some family members (Du et al., 2005). Epileptic seizures were found to be generalised in all cases, mainly presenting as absence seizures – generalised SWDs were detected via EEG (Paragraph 1.3.1) – as well as

generalised tonic-clonic seizures in two individuals (Du et al., 2005). Epileptic seizures started between infancy and early childhood, occurring daily at first but decreasing in frequency to monthly in adolescence with valproate and lamotrigine treatment (Du et al., 2005). Pedigree analysis suggested an autosomal dominant inheritance pattern of GEPD, while microsatellite marker analysis restricted the mutational location to the chromosomal 10q22 region (Du et al., 2005). Sanger sequencing detected a heterozygous D434G missense mutation in exon 10 of *KCNMA1*, which was only present in affected individuals and not in unaffected family members and 500 independent healthy controls (Du et al., 2005). Moreover, the D434G missense mutation creates a Tsp45I restriction site, which was used to confirm the Sanger sequencing data via restriction fragment length polymorphism (RFLP) analysis (Du et al., 2005). Since *KCNMA1* encodes the α-subunit of the BK channel, which is discussed in detail in Paragraph 1.4, GEPD has been classified as a channelopathy (Erro et al., 2017), as part of a classification scheme introduced in Paragraph 1.2.1.4.

1.3.4 *KCNMA1* Beyond GEPD

Four additional mutations in *KCNMA1* have recently been linked to PxD and epilepsy. Two unrelated Chinese boys were reported to carry distinct heterozygous *de novo* missense mutations in *KCNMA1*, E884K or N1053S, as identified via Next Generation Sequencing of candidate genes, and confirmed by Sanger sequencing (Zhang et al., 2015). These patients presented with PNKD in infancy, which was successfully treated in one patient with clonazepam (Zhang et al., 2015). Developmental delay was present in both patients, but not epilepsy (Zhang et al., 2015). A second *de novo* case of the heterozygous N1053S mutation was independently reported in another Chinese boy using the same experimental pipeline as described above (Wang et al., 2017a). This patient presented with PNKD in infancy, the frequency of which could be reduced with clonazepam (Wang et al., 2017a). Developmental delay was present in this patient, but not epilepsy (Wang et al., 2017a) .

In a third study, two sisters from a consanguineous Saudi family were reported as homozygous for an autosomal recessive frameshift duplication in *KCNMA1* (Y676Lfs*7), as identified via autozygosity mapping and exome

sequencing, and confirmed by Sanger sequencing (Tabarki et al., 2016). Both patients presented with myoclonic seizures in infancy, which were well controlled with valproate in one patient, while evolving into tonic- and generalised tonic-clonic seizures in the other (Tabarki et al., 2016). Both patients showed developmental delay, hypotonia, and severe non-progressive cerebellar atrophy, as revealed via MRI, but did not exhibit PxD (Tabarki et al., 2016).

A fourth study reported the discovery of a *de novo* heterozygous N995S missense mutation in *KCNMA1* in two individuals from two independent families of European descent, as identified via whole-exome sequencing, and confirmed by Sanger sequencing (Li et al., 2018). One patient presented with generalised myoclonic absence seizures in early childhood, the other with absence seizures in infancy and additional myoclonic seizures in early childhood (Li et al., 2018). Both patients were effectively treated with levetiracetam and were not diagnosed with PxD (Li et al., 2018).

Interestingly, only the D434G mutation is linked to a combined PxD-epilepsy syndrome (GEPD), while the other four *KCNMA1* mutations correlate with isolated PxD or isolated epilepsy. Altogether, these mutations provide strong evidence for an important role of BK channels in PxD and epilepsy.

1.4 BK Channels

In order to understand how the GEPD-linked D434G mutation in *KCNMA1* might elicit PNKD and epilepsy, the structure and function of BK channels under physiological conditions need to be defined. Hence, this paragraph describes (1) their protein structure and function, (2) their expression pattern, and (3) their physiological functions. Further, it discusses how these attributes might be affected by the D434G mutation.

1.4.1 Protein Structure and Function

1.4.1.1 Physiological Structure and Function

BK channels are Ca^{2+}- and voltage-sensitive K^+ channels that assemble as homotetramers of α-subunits, encoded by *KCNMA1* (Latorre et al., 2017). They belong to the 6 TM voltage-gated K^+ channel (K_v channel) superfamily, yet

contain a seventh TM segment (S0), which results in an extracellular N-terminus (Miller, 2000). BK channels comprise three structural domains: a voltage-sensing domain (VSD), a pore-gate domain (PGD), and an intracellular cytoplasmic tail domain (CTD), which can be thought of as functionally independent units that dynamically interact (Yang et al., 2015). The VSD is made up of 4 TM segments (S1-S4) and the PGD of 2 TM segments (S5-S6) separated by an intramembrane pore-loop, while the CTD is devoid of hydrophobic entry sites into the lipid bilayer but comprises two-thirds of the entire protein (Miller, 2000; Yuan et al., 2010). A schematic of one *KCNMA1*-encoded α-subunit is depicted in Figure 1.2.
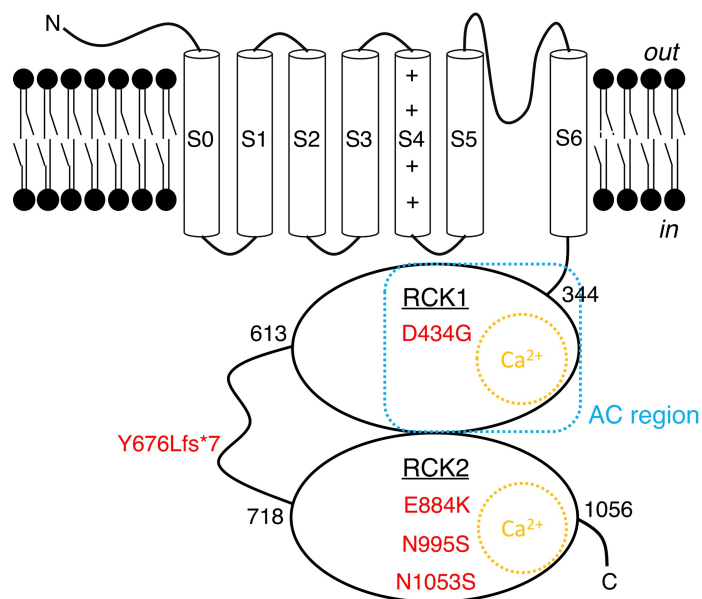
Figure 1.2 The α-subunit of the BK Channel

This schematic illustrates the structure of one α-subunit of the BK channel, encoded by *KCNMA1*, as well as the locations of mutations linked to PxD, epilepsy, and combined PxD-epilepsy, shown in red (Paragraphs 1.3.3 and 1.3.4). The α-subunit comprises three major domains: (1) the VSD (S1-S4), (2) the PGD (S5-S6 and a linker), and (3) the intracellular CTD. The CTD has two regulator of K^+ conductance (RCK) domains, RCK1 and RCK2, which both contain a Ca^{2+} binding site (orange). The AC region, a 76-bp region including the secondary structures βA-αC (cyan), comprises the N-terminus of RCK1. Amino acid positions are shown as numbers next to the RCK domains. This figure was adapted from the following publications: (Wang et al., 2017a; Yang et al., 2010; Yuan et al., 2012)

In order to form a BK channel, four α-subunits arrange symmetrically around an aqueous pore in the lipid bilayer, which contains a selectivity filter for K^+ ions,

rejecting other ions (Miller, 2000). BK (Big Kalium) channels derive their name from their high unitary conductance for K^+ (100-300 pS), which is, in fact, the highest amongst K^+ channels (Yang et al., 2015). This high conductance is achieved by clusters of acidic residues at the intra- and extracellular sides of the pore, which attract local clusters of K^+ ions, as well as a large inner vestibule and cytosolic entry site (Yang et al., 2015). However, BK channels are not constitutively open, but gated by physiological signals, transitioning between open- and closed conformations (Miller, 2000). The open-closed transition of the PGD is regulated by two processes: voltage-sensing by the VSD and ligand-binding to the CTD (Yang et al., 2015). Indeed, the VSD and the CTD are covalently attached to the N- and C-terminus of the PGD, respectively, and transduce physical- and chemical- into mechanical energy, respectively, leading to conformational changes of the PGD that open and close the pore (Yang et al., 2015). Voltage alone is sufficient to open BK channels, but BK channels show lower voltage-sensitivity than K_v channels (Yang et al., 2015). Indeed, the voltage-sensing amino acid residues of BK channels are not concentrated in the S4 segment, as for K_v channels, but distributed over several TM segments between S1 and S4, leading to complex conformational rearrangements upon voltage-sensing that result in pore opening (Yang et al., 2015).

The large CTD is a unique feature of BK channels, containing binding sites for Ca^{2+}, Mg^{2+}, H^+, carbon monoxide, ethanol, and lipids (Yang et al., 2015). Ca^{2+} binds with high affinity to the CTD, and is sufficient to open BK channels independent of voltage (Yang et al., 2010). The main structural components of the CTD are two RCK domains, RCK1 and RCK2 (Figure 1.2) (Yang et al., 2015). In the tetrameric BK channel structure, 8 RCK domains from 4 CTDs assemble into a large gating ring that is covalently bound to the C-terminus of the PGD, with the RCK1 domains facing the lipid bilayer (Wu et al., 2010; Yang et al., 2015). X-ray crystallography of human CTDs has confirmed that each RCK domain can be further divided into three functional subdomains: (1) an N-terminal Rossmann-folded subdomain forms the core of the gating ring, (2) an intermediate helix-crossover domain connects the RCK1 and RCK2 domains within α-subunits, and (3) a C-terminal subdomain connects RCK domains between α-subunits to form

the gating ring (Wu et al., 2010). The gating ring has a diameter of ~81 Å and a central hole of ~20 Å that facilitates K^+ ion transfer even in the absence of Ca^{2+} (Wu et al., 2010; Yuan et al., 2012).

Ca^{2+} binds to RCK domains within a concentration range of 100 nM – 300 μM and induces a conformational change of the gating ring that pulls on the PGD and opens the channel, leading to the transfer of K^+ ions (Yang et al., 2015). The major conformational change upon Ca^{2+} binding occurs at the N-terminal RCK1 domain, which rotates relative to the RCK2 domain and increases in diameter from ~81Å to ~93 Å via a process that has been likened to the movement of "petals opening on a flower" (Yuan et al., 2012). There are two main Ca^{2+} binding sites in the CTD, one in RCK1 and another in RCK2 – the latter is known as the "Ca^{2+} bowl" (Latorre et al., 2017). X-ray crystallography of human CTDs has revealed that the Ca^{2+} bowl forms a helix-loop-helix motif similar to the EF-hand structure of calmodulin, and is located close to the "assembly interface" between RCK1 and RCK2, a strategic position to modulate protein structure upon Ca^{2+} binding (Wu et al., 2010; Yuan et al., 2010). Within the Ca^{2+} bowl, Ca^{2+} is coordinated via carboxylate groups at amino acid residues D895 and D897 as well as carbonyl groups at amino acid residues Q889 and D892 (Yuan et al., 2010). X-ray crystallography data further suggest that the Ca^{2+} binding site within the RCK1 domain coordinates Ca^{2+} via carboxylate groups at amino acid residues D367 and E535 as well as a carbonyl group at amino acid residue R514 (Wu et al., 2010). These residue numbers are based on the human BK channel. The two Ca^{2+} binding sites are located ~25 Å apart, and have been shown to contribute roughly equally and independently to the Ca^{2+} sensitivity of the CTD (Yang et al., 2015). Importantly, biochemical and electrophysiological analyses of the GEPD-linked D434G mutation in *KCNMA1* have revealed that the RCK1 and RCK2 domains mediate BK channel opening via independent allosteric mechanisms, and that the D434G mutation affects a specific allosteric pathway that couples Ca^{2+} binding to channel opening (Yang et al., 2010).

1.4.1.2 Structure and Function in GEPD

The D434G mutation is located within the N-terminus of the RCK1 domain of the CTD, in a structure called the "AC region" (Figure 1.2) (Yang et al., 2010). The

AC region contains the RCK1 Ca^{2+} binding site and is positioned close to the S6 segment of the PGD (Yang et al., 2010). Although the D434G mutation does not lie within the Ca^{2+} binding site, but rather very close to it, electrophysiological analyses showed that it increases the Ca^{2+} sensitivity of BK channels (Yang et al., 2010). Expressing the D434G-equivalent murine D369G mutation in *Xenopus laevis* oocytes, inside-out patch clamp recordings at varying Ca^{2+} concentrations ($[Ca^{2+}]$) found a shift of the voltage at half-maximum conductance ($V_{1/2}$) towards more negative voltages, as compared to wild-type BK channels (Yang et al., 2010). To dissociate Ca^{2+}- from voltage-sensitivity, the authors repeated these recordings at a holding voltage of -140 mV, showing that step-wise increases of $[Ca^{2+}]$ resulted in higher channel open probabilities in the presence of D369G (Yang et al., 2010). Together, these data provide strong evidence for the D369G mutation to increase the Ca^{2+} sensitivity of BK channels, resulting in a gain-of-function.

By selectively mutating the two Ca^{2+} binding sites within the CTD, it could be shown that D369G mediates its effects specifically via the RCK1 Ca^{2+} binding site, independent of the Ca^{2+} bowl (Yang et al., 2010). While an increased viscosity of the recording solution normally potentiates the Ca^{2+} sensitivity of BK channels, this effect was lost in the presence of the D369G mutation (Yang et al., 2010). These data suggest that the D369G mutation enhances the allosteric coupling between Ca^{2+} binding to the RCK1 domain and channel opening by increasing the rigidity of the CTD (Yang et al., 2010). Indeed, molecular dynamics simulations strengthen this hypothesis, illustrating the importance of the AC region in transducing chemical energy released upon Ca^{2+} binding into mechanical energy that can pull on the PGD to open the BK channel pore (Yang et al., 2010). Altogether, these *in vitro* studies have provided great insight into the biophysical effects of the GEPD-linked mutation on BK channel function. However, in order to understand how these effects might contribute to GEPD pathology, further aspects of BK channels need to be understood, including their expression pattern and contribution to physiological functions.

1.4.2 Expression Pattern

BK channels are broadly expressed throughout the human body, including nervous-, digestive-, and endocrine tissue (Bailey et al., 2019). Within the CNS, the BK channel expression pattern is equally broad, including the basal ganglia, thalamus, and cerebellum (Bailey et al., 2019). On a cellular level, BK channel expression in the CNS covers various neuronal subtypes, including glutamatergic-, GABAergic-, and cholinergic neurons, as well as non-neuronal cells, such as astrocytes (Girouard et al., 2010; Griguoli et al., 2016). On the neuronal plasma membrane, BK channels have been detected at the pre- and post-synaptic termini, along the axon, and at the soma (Griguoli et al., 2016; Latorre et al., 2017). Furthermore, BK channels are expressed on a variety of intracellular organelles, including the nucleus, mitochondria, and lysosomes (Balderas et al., 2015; Li et al., 2014; Zhu, 2017). Altogether, this broad expression profile of BK channels makes it difficult to predict how the D434G gain-of-function *KCNMA1* allele would affect an entire organism, since a vast array of physiological functions might be perturbed.

1.4.3 Physiological Functions

In addition to the broad nature of BK channel expression (Bailey et al., 2019) (Paragraph 1.4.2), functional diversity is amplified via three mechanisms: (1) BK channels associate with 8 different subunits, 4 β- (β_1-β_4) and 4 γ-subunits (γ_1-γ_4), which modulate Ca^{2+}-sensitivity, voltage dependence, gating properties, and the sensitivity to pharmacological agents to varying degrees (Griguoli et al., 2016). Indeed, the selective association between the BK channel α-, β- and γ-subunits in different tissues, and in different subcellular compartments, fine-tunes BK channel function for specific environmental- and cellular requirements (Latorre et al., 2017). β-subunits consist of 2 TM segments, an extracellular loop, and intracellular N- and C-termini, and associate with the VSDs of α-subunits (Latorre et al., 2017). γ-subunits consist of a single TM segment and a large extracellular N-terminal leucine-rich repeat domain (Latorre et al., 2017). (2) The mRNA of *KCNMA1* and of genes encoding the β-subunits (*KCNMB1-4*) exhibit extensive alternative splicing, which can affect both BK channel function and localisation

(Griguoli et al., 2016; Latorre et al., 2017; Li and Gao, 2016). (3) Post-translational modifications of BK channels, including phosphorylation and lipidation, further modify BK channel function, especially via the CTD (Griguoli et al., 2016; Latorre et al., 2017). Altogether, these modulatory mechanisms result in functional adaptation of BK channels to different subcellular compartments.

1.4.3.1 BK Channels on the Plasma Membrane

BK channels have been detected on the plasma membrane of a variety of cell types. For example, they are prominently expressed on the plasma membrane of vascular smooth muscle cells, where they have been implicated in the negative regulation of vascular tone and blood pressure (Latorre et al., 2017). Interestingly, the β_1-subunit is selectively expressed in smooth muscle cells, and has been shown to render BK channels Ca^{2+}-insensitive at $[Ca^{2+}]$ below 300 nM, while increasing BK channel Ca^{2+} sensitivity at higher $[Ca^{2+}]$ (Latorre et al., 2017). BK channels are also expressed in urinary- and airway smooth muscle cells, negatively regulating urinary bladder contraction and airway inflammatory responses, respectively (Latorre et al., 2017).

In the kidney, BK channels are expressed on the apical side of principal- and intercalated cells in the cortical collecting duct (CCD), contributing to K^+ homeostasis by K^+ secretion into the CCD (Latorre et al., 2017). In these cells, BK channels might be directly coupled to TRPV4 Ca^{2+} channels, which are activated by luminal fluid flow-induced shear stress, facilitating BK channel activation via Ca^{2+} entry and binding to the intracellular CTD (Latorre et al., 2017). Interestingly, BK channels in principal- and intercalated cells associate with β_1- and β_4-subunits, respectively, implicating functional diversity in these neighbouring cells (Latorre et al., 2017).

BK channels are also expressed on the plasma membrane of inner- and outer cochlear hair cells, together with β_1- and β_4-subunits (Latorre et al., 2017). While the role of BK channels in the cochlea remains incompletely understood, their expression on murine inner hair cells has been implicated in affecting central auditory processing and the ability to discriminate auditory stimuli (Kurt et al., 2012).

In neurons, BK channels can be expressed at different locations along the plasma membrane, including the pre- and post-synaptic termini, the soma, and along axons (Griguoli et al., 2016; Latorre et al., 2017). At all these locations, BK channels are gated by a combination of membrane potential depolarisation and increases in [Ca^{2+}] (Griguoli et al., 2016). K^+ release by somatodendritic BK channels narrows the action potential (AP) width and mediates the fast after-hyperpolarisation (fAHP) phase of the AP, thereby contributing to membrane potential repolarisation (Griguoli et al., 2016). In some neurons, this repolarising effect of BK channels is required for the initiation of APs, and therefore excitatory. For example, *KCNMA1*$^{-/-}$ knockout mice exhibit ataxia that correlates with an inhibition of cerebellar Purkinje Cells due to depolarisation block and a concomitant dis-inhibition of deep cerebellar nuclei (Sausbier et al., 2004). Hence, in Purkinje Cells, BK channel-mediated repolarisation is required to de-inactivate Na_v channels, a necessary process for AP initiation. In other neurons, BK channels dampen neural activity and prevent hyperexcitability. For example, hippocampal dentate gyrus granule cells of $\beta_4^{-/-}$ knockout mice exhibit faster gating kinetics that lead to AP narrowing, higher firing frequencies, and temporal lobe seizures (Brenner et al., 2005). The β_4-subunit is most prominently expressed in the CNS, increasing BK channel Ca^{2+} sensitivity, while, importantly, slowing its gating kinetics, leading to a broadening of AP width (Latorre et al., 2017). Hence, in the dentate gyrus of $\beta_4^{-/-}$ knockout mice, slow-activating BK channels were effectively transformed into fast-activating BK channels, exhibiting a narrowed AP width and increased firing frequencies (Brenner et al., 2005). Consequently, in these neurons, BK channels inhibit neuronal activity. These opposing roles of BK channels are a prominent feature in the CNS, differentially affecting neuronal subpopulations.

At the pre-synaptic terminus, BK channels associate with voltage-gated Ca^{2+} channels (Ca_v channels) within nanodomains and couple Ca^{2+} influx to K^+ efflux (Griguoli et al., 2016). Indeed, a co-localisation between BK channels and L-, P/Q-, and N-type Ca_v channels has been demonstrated to be necessary for BK channel opening within a physiological range of membrane potentials (Berkefeld et al., 2006). BK channels negatively regulate neurotransmission by

limiting Ca^{2+} entry through Ca_v channels, thereby lowering the cytosolic $[Ca^{2+}]$ below the threshold for membrane fusion (Griguoli et al., 2016; Latorre et al., 2017). However, in some neurons, such as hippocampal CA3 pyramidal cells, electrophysiological recordings have shown that pre-synaptic BK channels are not involved in neurotransmitter release under basal conditions (Griguoli et al., 2016; Hu et al., 2001). In these neurons, it has been proposed, BK channels act as "emergency breaks", becoming activated only in response to physiologically stressful states that cause substantial increases in intracellular $[Ca^{2+}]$, such as epilepsy (Griguoli et al., 2016). Of note, due to a suggested preferential expression in excitatory neurons, BK channels might also modulate the excitatory-inhibitory balance within neuronal circuits, which has been implicated in a variety of neuropsychiatric disorders (Griguoli et al., 2016).

1.4.3.2 BK Channels on the Mitochondrial Membrane

Mitochondria are double membrane-bound organelles responsible for cellular ATP production via oxidative phosphorylation (Nunnari and Suomalainen, 2012). They are composed of an outer mitochondrial membrane (OMM) and an inner mitochondrial membrane (IMM), creating an intermembrane space between these two lipid barriers as well as an inner matrix that is enclosed by the IMM (Li and Gao, 2016). The TCA cycle occurs within the mitochondrial matrix, generating the reducing agents NADH and $FADH_2$, which donate electrons to the electron transport chain (ETC) located on the IMM, producing ATP via the establishment and release of a H^+ gradient across the IMM (Nunnari and Suomalainen, 2012). Apart from ATP production, mitochondria are involved in a variety of cellular processes, including biosynthetic pathways, such as fatty acid β-oxidation, apoptosis, and Ca^{2+} homeostasis (Nunnari and Suomalainen, 2012).

Mitochondria express a variety of ion channels on the OMM and IMM (Li and Gao, 2016). Amongst them, BK channels have been detected electrophysiologically and via immuno-staining on the IMM in excitable and non-excitable cells of various species, including humans, being termed mtBK channels (Li and Gao, 2016). Patch clamp recordings from mitoplasts – mitochondria stripped off the OMM – determined that the mtBK channel N-terminus faces the intermembrane space (Li and Gao, 2016). Notably, all four β-

subunits have been identified to assemble with mtBK channels in a cell type-specific manner, presumably fine-tuning mtBK channel function for different environments (Li and Gao, 2016). Interestingly, Western blots and immuno-staining revealed that the β_1- and β_3-subunits were not-, and the β_2-subunit only weakly expressed in the adult rat brain, while the β_4-subunit was broadly expressed, with particularly high expression levels in thalamus and brainstem (Piwonska et al., 2008).

Most studies on the physiological role of mtBK channels have been performed on cardiomyocytes, because these cells lack BK channels on the plasma membrane, while expressing high levels of mtBK channels (Li and Gao, 2016). These studies revealed that mtBK channel activity mediates a cardioprotective effect upon myocardial ischaemia, as pre-ischaemic exposure of hearts to the BK channel agonist NS1619 significantly reduced myocardial infarct size (Singh et al., 2013; Xu et al., 2002). A recent study demonstrated that the levels of reactive oxygen species (ROS), by-products of oxidative phosphorylation, were elevated in murine $KCNMA1^{-/-}$ cardiomyocytes in post-anoxic conditions when compared to controls, providing a possible explanation for the cardioprotective role of mtBK channels (Soltysinska et al., 2014). Moreover, oxidative phosphorylation capacities were reduced in $KCNMA1^{-/-}$ cardiomyocytes both during normoxia and upon re-oxygenation after anoxia (Soltysinska et al., 2014). These data suggest that mtBK channels are required for appropriate energy supply to the myocardium during normoxic conditions and upon re-oxygenation after anoxia, while also regulating the oxidative state of cardiomyocytes during post-anoxic conditions (Soltysinska et al., 2014).

Moreover, mtBK channels have been shown to directly regulate the Ca^{2+} retention capacity of mitochondria by inhibiting mitochondrial protein transition pores (mPTPs) (Cheng et al., 2008, 2011). Since mPTPs are linked to the indirect activation of the intrinsic apoptotic pathway, it has been suggested that mtBK channel activity has an anti-apoptotic effect (Cheng et al., 2008, 2011). Indeed, a direct inhibition of mtBK channels by the pro-apoptotic protein Bax was demonstrated to activate mPTPs and induce the release of cytochrome c, a pro-apoptotic factor (Cheng et al., 2011; Li and Gao, 2016). Altogether, these data

implicate mtBK channels with fundamental mitochondrial physiology, suggesting that changes in mtBK channel activity might affect a variety of cell types.

1.4.3.3 BK Channels on the Nuclear Envelope

The nucleus is a double membrane-bound organelle separating the genome from the cytoplasm and regulating gene expression (Li and Gao, 2016). The nuclear envelope (NE) surrounds the nucleus and is composed of an inner nuclear membrane (INM) and an outer nuclear membrane (ONM), generating the perinuclear space between these membranes and the nucleoplasm enclosed by the INM (Li and Gao, 2016). Molecular and ionic transport between the cyto- and nucleoplasm is mediated by nuclear pore complexes, large protein complexes spanning both the INM and ONM (Li and Gao, 2016).

In addition to a variety of ion channels expressed on both the INM and the ONM, nuclear patch clamp recordings, immuno-staining, and immunoelectron microscopy have confirmed the presence of BK channels on the ONM, termed nBK channels (Li et al., 2014). Of note, the β_4-subunit was found to co-assemble with nBK channels on the ONM (Li et al., 2014). Voltage imaging of murine hippocampal neurons revealed that nBK channels regulate the membrane potential across the ONM, as inhibition of nBK channels rendered the perinuclear lumen more negative (Li et al., 2014). Importantly, the perinuclear space is an independent Ca^{2+} store with the ability to raise the nuclear $[Ca^{2+}]$ by releasing Ca^{2+} into the nucleus, which regulates activity-dependent gene expression (Li and Gao, 2016). Indeed, Ca^{2+} imaging in murine hippocampal neurons demonstrated that specific inhibition of nBK channels increased nuclear $[Ca^{2+}]$ – a process mediated by perinuclear Ca^{2+} release through ryanodine receptors located on the INM (Li et al., 2014). Via Western blots and immuno-staining, the authors could demonstrate that the inhibition of nBK channels, and the concomitant increase in nuclear $[Ca^{2+}]$, induced the phosphorylation of the transcription factor (TF) CREB, which resulted in transcriptional changes leading to increased dendritic arborisation (Li et al., 2014). These data provide strong evidence for a direct regulatory role of nBK channels in gene expression, rendering conceivable the notion that aberrant nBK channel activity may be involved in various pathophysiological processes.

1.4.3.4 BK Channels on the Lysosomal Membrane

Lysosomes are membrane-enclosed intracellular organelles important for the catabolism and recycling of intra- and extracellular macromolecules, including proteins, carbohydrates, lipids, and nucleic acids (Platt et al., 2018). Lysosomes are dynamic and undergo complex cellular trafficking, being involved in a variety of signalling processes, including nutrient sensing, ion homeostasis, and the exchange of metabolites and Ca^{2+} with other intracellular organelles (Platt et al., 2018). In order to fulfil these tasks, lysosomes express a variety of proteins, including membrane-bound ion channels, which are important regulators of lysosomal pH (~4.5-5), lysosomal membrane potential (which is negative with respect to the cytosol), and lysosomal signalling processes (Zhu, 2017).

Recent evidence confirmed the presence of BK channels on the lysosomal membrane via immuno-staining and whole-endolysosomal patch clamp recordings (Cao et al., 2015; Zhu, 2017). However, the function of BK channels on lysosomes remains unclear. One study reported that lysosomal BK channels generate a positive feedback loop between Ca^{2+} efflux from- and K^+ influx into the lysosomal lumen, the latter being mediated by BK channel activation upon Ca^{2+} binding to the cytosol-facing CTD (Cao et al., 2015). K^+ influx would increase the driving force of Ca^{2+} efflux, resulting in increased Ca^{2+} release from lysosomes (Cao et al., 2015). Interestingly, BK channels were found to co-localise with lysosomal Ca^{2+} channels (MCOLN1) on the lysosomal membrane, efficiently coupling Ca^{2+} efflux to K^+ influx – reminiscent of BK channel coupling to Ca_v channels on the neuronal plasma membrane (Cao et al., 2015).

A more recent study confirmed that lysosomal BK channels are activated by cytosolic Ca^{2+} (Wang et al., 2017b). However, rather than being required for lysosomal Ca^{2+} release, this study identified BK channels to be important for the replenishment of lysosomal Ca^{2+} (Wang et al., 2017b). Despite these differences, both studies demonstrated that the loss of BK channels caused lysosomal trafficking- and storage defects (Zhu, 2017). These findings associate BK channel function with a spectrum of metabolic disorders classified as lysosomal storage diseases (LSDs) – such as Niemann-Pick disease type C1/2 (NPC1/2), which is caused by mutations in *NPC1* and *NPC2* (Platt et al., 2018). Patients with NPC1/2

present with a variety of symptoms, including ataxia, dystonia, and seizures (Platt et al., 2018). Importantly, NPC patients exhibit decreased lysosomal Ca^{2+} release, leading to impaired lysosomal trafficking and fusion, increased lysosomal lipid accumulation, mitochondrial dysfunction, and inflammation (Platt et al., 2018). Interestingly, it has been shown that overexpressing BK channels in human fibroblasts from NPC1 patients decreased lysosomal lipid accumulation by increasing lysosomal Ca^{2+} release, implicating BK channels with lysosomal trafficking and LSD pathology (Cao et al., 2015).

1.4.4 Understanding GEPD

The above sections collectively illustrate the complexity of BK channel expression and function. Hence, while *in vitro* studies on the D434G missense mutation have provided important insights into its biophysical effects on BK channel gating (Yang et al., 2010), it is impossible to bridge these data and the neurological phenotype exhibited by GEPD patients. In particular, two fundamental questions remain: (1) *where* does the D434G mutation exert its pathogenic effects? (2) *What* are the pathogenic effects of GEPD on a molecular level?

In the original description of GEPD, the authors posited that an increased Ca^{2+} sensitivity and concomitant gain of BK channel function would likely result in a narrowing of APs and increased neuronal firing frequencies, hence causing PxD and epilepsy (Du et al., 2005). This hypothesis simultaneously suggests a pathogenic locus (the brain) and a molecular mechanism (increased neuronal firing frequencies) for GEPD.

While it is possible that the D434G mutation increases neuronal firing frequencies, this effect might only apply to some neurons, while others could be affected differently, as described in Paragraph 1.4.3.1 (Griguoli et al., 2016). Moreover, how does the D434G mutation affect non-neuronal cells? Although GEPD patients present with predominantly neurological symptoms, it does not necessarily follow that the mutation exerts its pathogenic effects exclusively in the brain. Indeed, GLUT1-DS and most forms of PED are caused by mutations in *SLC2A1*, which encodes the glucose transporter GLUT1, as described in Paragraph 1.2.1.3 (De Giorgis and Veggiotti, 2013). In these disorders, PxD and epilepsy are caused by a lack of glucose transport across the BBB, rather than

CNS-intrinsic defects (De Giorgis and Veggiotti, 2013). A dysregulation in energy metabolism could also occur due to aberrant insulin release from pancreatic β-cells, which have been shown to express BK channels (Düfer et al., 2011; Houamed et al., 2010) – might this contribute to GEPD? A variety of pathophysiological mechanisms in other cell types eliciting GEPD via different means are conceivable.

In addition to identifying the pathogenic locus of GEPD, it would be of interest to reveal the molecular mechanisms via which the D434G mutation exerts its pathophysiological effects. BK channels regulate various processes apart from shaping the AP, as described in Paragraph 1.4.3 (Latorre et al., 2017). Hence, in addition to changing neuronal firing frequencies, altered BK channel function might affect the regulation of oxidative stress, transcription, and metabolism, all of which could contribute to GEPD (Cao et al., 2015; Li and Gao, 2016). Consequently, in order to understand the pathogenesis of GEPD, the organismal effects of the D434G mutation need to be defined. This would require the study of an animal model replicating the GEPD genotype, which, to my knowledge, does not exist.

1.5 *Drosophila* Models in Neurology

Drosophila melanogaster has been used as a model organism for more than a century, and during this time elucidated a number of fundamental principles in biology, including the chromosomal theory of heredity, the physical mapping of genes, the mutational effects of ionising radiation, and embryological development (Rubin and Lewis, 2000). There are two main advantages to the use of *Drosophila* in disease research: (1) the vast array of genetic tools available, and (2) the conservation of genetic-, molecular-, and behavioural processes between flies and humans (Wangler et al., 2015, 2017; Wu and Lloyd, 2015). Indeed, *Drosophila* has been used to study a variety of neurological pathologies (Wu and Lloyd, 2015), lending itself to the study of GEPD.

1.5.1 Advantages of *Drosophila*

Drosophila melanogaster exhibits various intrinsic features that render it a versatile and efficient model organism, including a short generation time (~10

days), cheap and easy maintenance, high fecundity, a small and sequenced genome (4 sets of chromosomes), and a relatively low level of genetic redundancy (Cunliffe et al., 2015; St Johnston, 2002). Moreover, a variety of tools have been developed that aid genetic studies. For example, the coupling of balancer chromosomes, large chromosomal inversions that prevent meiotic recombination (St Johnston, 2002), to dominant markers allows for phenotype-to-genotype inferences to be made, frequently eliminating the need for molecular genotyping. Furthermore, a large collection of *Drosophila* stocks carrying transposable element insertions throughout the *Drosophila* genome is commercially available (Bellen et al., 2011). In addition to disrupting most of the genes in the *Drosophila* genome, these insertions can introduce useful sequences into the endogenous genome that allow for protein tagging, the visualisation of gene expression, or site-specific recombination (Bellen et al., 2011). Other mutagenic strategies, including EMS- and X-ray mutagenesis, have been employed to add to the list of available mutants (St Johnston, 2002). These mutant stocks can be used in forward- and reverse genetic screens aimed at identifying novel genes and genetic interactions (St Johnston, 2002; Venken et al., 2011). In order to manipulate gene expression in a spatially and temporally restricted manner, the Gal4/UAS system is available (Brand and Perrimon, 1993; Venken et al., 2011). This binary expression system is based on the binding of the Gal4 yeast TF to the Upstream Activating Sequence (UAS), resulting in transcriptional initiation of responder elements downstream of UAS (Venken et al., 2011). Spatially controlled transcription of responder elements is achieved via tissue-specific *Gal4* expression (Figure 1.3) (Venken et al., 2011).
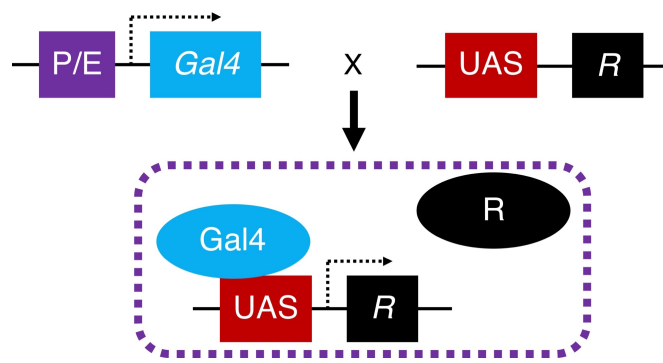
Figure 1.3 The Gal4/UAS Binary Expression System

Two separate transgenic *Drosophila* lines, carrying a *Gal4* driver- and a UAS-responder construct, are crossed together, resulting in the Gal4-mediated activation of UAS and the expression of a responder element (*R*) in the progeny. Spatial control of *R* expression is achieved by the conditional expression of *Gal4* (violet), which is under the control of tissue-specific promoters/enhancers (P/E).

Depending on the responder element downstream of UAS, over-expression or knock-down of specific genes can be achieved as well as the labelling of cellular subpopulations (Venken et al., 2011). As for transposable element insertions, a vast array of transgenic *Drosophila* lines carrying *Gal4-* and UAS constructs is commercially available, facilitating the transcriptional manipulation of most of the genes in the *Drosophila* genome (Perrimon et al., 2010). Of note, the core structure of the Gal4/UAS system illustrated in Figure 1.3 has been expanded extensively. Gal4 activity can be repressed by Gal80, while the split-Gal4 system expresses two *Gal4* heterodimers under separate regulatory control, only initiating transcription of the responder element when their expression patterns overlap (Venken et al., 2011). Moreover, two alternative binary expression systems exist, the LexA/LexOp- and the QF/QUAS system, which can be used alone or in combination with the Gal4/UAS system (Venken et al., 2011). To obtain temporal control over the expression of responder elements, heat- and drug-activatable versions of TFs and their repressors are available (Venken et al., 2011).

In *Drosophila* neurobiology research, the Gal4/UAS system is regularly used to selectively modulate neuronal activity via the conditional expression of pro-apoptotic genes (*hid*, *reaper*, *grim*), blockers of synaptic transmission (TNT, *Shibire^{ts1}*), inhibitory K^+ channels (*Kir2.1*, *EKO*, *dOrk*), excitatory cation channels (*TrpA1*, *NaChBac*), and photo-activatable ion channels and -pumps to activate or

inhibit neurons (*ChR2* and *Arch*, respectively) – an experimental strategy often employed to link neural activity to behaviour (Venken et al., 2011). In addition to manipulating neural activity, the latter can be passively recorded with conditionally expressed genetically-encoded Ca^{2+} indicators (GECIs), such as GCaMP, a fusion protein that undergoes a conformational change upon Ca^{2+} binding, resulting in increased fluorescence (Chen et al., 2013).

For the study of human disease-causing mutations, it might be desirable to precisely replicate disease-linked mutations in flies. While recessive diseases may be studied by using commercially available hypomorphic- or null alleles, some human disease-causing mutations are neo- or hypermorphic, as observed in GEPD (Du et al., 2005). Various gene editing technologies are available to generate fly models that precisely replicate such mutations, including ends-in- and ends-out homologous recombination (HR) and the CRISPR-Cas9 system (Bier et al., 2018; Wesolowska and Rong, 2010). Importantly, these methods modify genes at their endogenous loci, preserving endogenous regulation that might contribute to pathology (Venken et al., 2011).

A further advantage of *Drosophila* as a model organism in neurological disease research is the conservation of genetic-, molecular-, and behavioural processes between flies and humans. It has been estimated that ~64% of human genes linked to neuropathologies are conserved in flies (Fortini et al., 2000), despite the evolutionary divergence of these two species an estimated 782.7 million years ago (Hedges et al., 2006). The fly brain contains ~90000 neurons, about 1 million-fold fewer than the human brain, but it uses the same neurotransmitters (glutamate, ACh, GABA) and biogenic amines (dopamine, serotonin) to facilitate conserved mechanisms of neurotransmission (Venken et al., 2011). Moreover, ionic processes underlying the initiation and propagation of APs are conserved between flies and humans, including genes encoding various ion channels (Venken et al., 2011). However, there are important differences between the fly- and human brain: neuronal cell bodies in the *Drosophila* brain surround a brain neuropil, which is composed of axons, dendrites, and synapses, whereas the human brain contains both neurites and somata (Venken et al., 2011). Notably, the roles for glutamate and ACh are reversed in fly- and human brains, the former using ACh as the main excitatory neurotransmitter in the brain

and glutamate at the neuromuscular junction (NMJ), and vice versa for the latter (Venken et al., 2011). Nevertheless, the study of human genes linked to neurological diseases and disorders can provide important functional insight into conserved pathophysiological processes of translational value, as has been demonstrated for a variety of neuropathologies.

1.5.2 *Drosophila* Disease Models

Studies in *Drosophila* have made important contributions to neurological disease research, particularly in the investigation of polyglutamine repeat diseases, frontotemporal dementia, Alzheimer's disease, neurodegeneration, amyotrophic lateral sclerosis, sleep disorders, PD, and epilepsy (Cunliffe et al., 2015; Wu and Lloyd, 2015). While PxD has, to my knowledge, not yet been modelled in flies, studies on dystonia, a component of PxD, have led to an increased understanding of the molecular mechanisms underlying this movement disorder.

Autosomal dominant early-onset torsion dystonia (DYT1 dystonia) is linked to a 3-bp deletion in *TOR1A* ($TOR1A^{\Delta302/303}$), encoding the ATP-binding protein TorsinA, and considered the most common and severe form of hereditary dystonia (Ozelius et al., 1997). Early studies investigating the function of the fly *TOR1A* orthologue *torsin* applied conditional knock-down- and over-expression approaches to show that it prevents age-related retinal degeneration and might be involved in lysosomal function and the regulation of oxidative stress (Muraro and Moffat, 2006). The investigation of a *torsin* null allele – generated via ends-out HR – identified decreased GTP cyclohydrolase I (GTPCH) protein levels in *torsin* null heterozygotes, implicating altered dopamine metabolism in DYT1 dystonia (Wakabayashi-Ito et al., 2011). Indeed, a locomotor defect of *torsin* null L3 larvae could be rescued by dopamine supplementation (Wakabayashi-Ito et al., 2011). These results could be replicated via neuronal over-expression of human $TOR1A^{\Delta302/303}$, which acted in a dominant negative manner to reduce GTPCH protein levels in adult and larval brains, as shown via Western blots (Wakabayashi-Ito et al., 2015). Interestingly, transmission electron microscopy (TEM) revealed that loss of *torsin* results in the peri-nuclear retention of large ribonucleoproteins (megaRNPs) due to their abnormal attachment to the INM – suggesting a role for Torsin in NE budding, an important process for mRNA export

from the nucleus (Jokhi et al., 2013). Consequently, megaRNP-associated mRNAs were shown via FISH to be mostly absent from post-synaptic termini at the *torsin* null larval NMJ, leading to an abnormal development of synaptic boutons (Jokhi et al., 2013). Since NE budding mediates part of the Wnt signalling pathway via Frizzled2, disruption of which was also found to result in aberrant synaptic bouton development at the larval NMJ, these data implicate a role for Torsin in synaptic development and plasticity (Speese et al., 2012).

Autosomal dominant myoclonus-dystonia, a combined dystonia syndrome defined by non-epileptic myoclonic jerks and mild to moderate dystonia, has been linked to a missense mutation in *KCTD17*, encoding a Cullin-3 adaptor protein (Mencacci et al., 2015). Interestingly, two independent screens for *Drosophila* sleep mutants demonstrated that loss of *insomniac* (*inc*), the fly orthologue of *KCTD17*, causes severely reduced sleep duration and consolidation (Pfeiffenberger and Allada, 2012; Stavropoulos and Young, 2011). Weighted gene co-expression network analysis (WGCNA) based on human brain transcriptomic data identified *HPCA*, encoding a neuronal Ca^{2+} sensor protein, to be co-expressed with *KCTD17* in the putamen, suggesting a functional connection between these genes (Mencacci et al., 2015). Intriguingly, not only have missense and null mutations in *HPCA* been linked to DYT2 dystonia (Atasu et al., 2018; Charlesworth et al., 2015), a recent study has shown that its fly orthologue *Neurocalcin* (*Nca*) regulates night-time sleep in *Drosophila* (Chen et al., 2019). Since conserved endophenotypes can elicit profoundly different organismal behaviours across species (Lehner, 2013), the investigation of *Drosophila* sleep might, therefore, lead to a better understanding of the molecular mechanisms underlying dystonia in humans, illustrating the versatility of this model organism in neurological disease research.

The study of epilepsy in *Drosophila* focusses, in part, on the "bang-sensitive" class of *Drosophila* mutants, which exhibit seizure-like states both behaviourally and electrophysiologically, and are used as a model for human intractable epilepsy (Cunliffe et al., 2015; Parker et al., 2011). Larval motoneurons (MNs) of the bang-sensitive mutant *slamdance* (*sda*), for example, were shown to exhibit an increased persistent sodium current (I_{Nap}), which has also been associated with symptomatic and idiopathic epilepsy (Cunliffe et al.,

2015; Marley and Baines, 2011). Interestingly, this increase in I_{Nap} was shown to be mediated by activity-dependent alternative splicing of the *paralytic* (*para*) transcript, which encodes the α-subunit of the only fly Na_v channel (Cunliffe et al., 2015; Lin et al., 2009, 2012), illustrating how *Drosophila* can uncover novel molecular mechanisms underlying epileptogenesis, potentially contributing to improved AED design.

To directly study human epilepsy syndromes in flies, the point mutations in *SCN1A* linked to Dravet syndrome (DS) and genetic epilepsy with febrile seizures plus (GEFS+) were introduced into the fly orthologue *para* via ends-out HR (Schutte et al., 2014; Sun et al., 2012). Both knock-in flies exhibited temperature-induced seizures, and whole-cell recordings from local neurons (LNs) in the dorsolateral antenna lobe revealed that the GEFS+ mutation increased-, while the DS mutation decreased Na_v channel function (Schutte et al., 2014; Sun et al., 2012). However, both mutations resulted in decreased evoked and spontaneous firing frequencies of LNs, suggesting shared cellular mechanisms underlying the seizure phenotypes (Schutte et al., 2014; Sun et al., 2012). These studies illustrate how *Drosophila* knock-in models of known epilepsy mutations can lead to novel insights into the nature of human epilepsy syndromes.

1.5.3 *Drosophila slo*

1.5.3.1 Physiological Functions of *slo*

As introduced in Paragraph 1.3.3, GEPD is linked to a D434G missense mutation in *KCNMA1* (Du et al., 2005), whose *Drosophila* orthologue is called *slo*. Both genes encode the α-subunit of the voltage- and Ca^{2+}-activated BK channel, also known as Slo (Latorre et al., 2017) (Paragraph 1.4). In fact, *Drosophila slo* was the first Slo channel α-subunit to be cloned and sequenced (Atkinson et al., 1991). Subsequent inside-out patch clamp recordings form *Xenopous laevis* oocytes demonstrated that *Drosophila* Slo is functionally homologous to mammalian Slo, being both voltage- and Ca^{2+}-sensitive (Adelman et al., 1992), as described in Paragraph 1.4.3.1 (Griguoli et al., 2016; Latorre et al., 2017). Indeed, combinatorial expression of the murine and *Drosophila* N-terminal core-

and C-terminal tail domains of Slo in *Xenopus laevis* oocytes resulted in the assembly of chimeric Slo channels functionally similar to full-length Slo of either species, as shown via inside-out patch clamp recordings (Wei et al., 1994). Importantly, as described for *KCNMA1* (Latorre et al., 2017) (Paragraph 1.4.3), *Drosophila slo* exhibits extensive alternative splicing, giving rise to isoforms of varying biophysical properties, such as marked differences in Ca^{2+}-sensitivity (Lagrutta et al., 1994).

slo is broadly expressed in *Drosophila* larvae and adults, prominently in neurons and muscles, but also in the trachea and midgut (Becker et al., 1995). Within the adult brain, *slo* shows a broad expression pattern and strongly localises to the neuropil (Becker et al., 1995; Jepson et al., 2012). However, no regulatory β- and γ-subunits have been described in *Drosophila* (Griguoli et al., 2016). Instead, Slo function has been shown to be regulated by 4 direct- and indirect binding partners: (1) Slowpoke binding protein (Slob) was identified via a yeast two-hybrid screen to bind to the large CTD of Slo, a physical interaction that was confirmed via co-immunoprecipitation (Schopperle et al., 1998). The application of Slob to Slo-containing inside-out patches potentiated Slo currents, initially suggesting that Slob acts as a positive regulator of Slo activity (Schopperle et al., 1998). However, more recent studies have identified 6 Slob splice isoforms, four of which (Slob71, Slob65, Slob53, and Slob47) increase the voltage-sensitivity of Slo, while the other 2 (Slob57 and Slob51) decrease its voltage-sensitivity and increase its deactivation kinetics (Zeng et al., 2005). Hence, Slob can both activate and inhibit Slo function. (2) Using Slob as a bait in a follow-up yeast two-hybrid screen, the ζ isoform of 14-3-3 was identified as a physical interaction partner of Slob, as confirmed via co-immunoprecipitation (Zhou et al., 1999). While not directly binding to Slo, 14-3-3 negatively regulates Slo currents via Slob, significantly decreasing the voltage-sensitivity of Slo and Slo-mediated evoked current responses (Zhou et al., 1999). (3) *dyschronic* (*dysc*) was identified through a forward-genetic screen for arrhythmic locomotor behaviour in adult flies and its protein product Dysc shown to physically interact with Slo via co-immunoprecipitation (Jepson et al., 2012). Dysc was shown to be required for the expression of Slo in the *Drosophila* brain, as Slo

immunofluorescence was almost entirely lost in homozygous *dysc* null flies (Jepson et al., 2012). Whole-cell patch clamp recordings from *dilp2*-expressing neurons in the pars intercerebralis (PI) of the adult *Drosophila* brain demonstrated that Slo currents were significantly reduced in a *dysc* null background (Jepson et al., 2012). It was further shown that *slo* and *dysc* act in a common genetic pathway to regulate AZ structure and evoked synaptic transmission at the *Drosophila* larval NMJ (Jepson et al., 2014). (4) Perforated patch-clamp recordings from the posterior dorsal neuron 1 (DN1p) cluster have recently shown that *wide awake* (*wake*) positively regulates the fAHP, which is partly mediated by Slo (Tabuchi et al., 2018). Co-immunoprecipitation experiments demonstrated that Wake and Slob physically interact, suggesting that Wake affects Slo currents via Slob (Tabuchi et al., 2018). Indeed, immuno-staining for Slob suggested a model in which Wake facilitates the binding of Slob to Slo, thereby modulating Slo currents in a circadian manner (Tabuchi et al., 2018).

1.5.3.2 Phenotypes Associated with Loss of *slo*

While, to my knowledge, no *Drosophila* gain-of-function *slo* allele has been generated, the study of several loss-of-function alleles has greatly contributed to an increased understanding of *slo* function on a behavioural and cellular level.

The first *slo* null allele, *slo¹*, was recovered during a screen for homozygous EMS-induced mutations that caused adult fly paralysis upon exposure to 38°C (Elkins et al., 1986). *slo¹* homozygotes were not completely paralysed at 38°C, but displayed uncoordinated movements and remained motionless for several minutes when transferred to 22°C after a 4-min exposure to 38°C (Elkins et al., 1986). Moreover, *slo¹* homozygotes exhibited a general locomotor defect, leg-shaking under anaesthesia, and diminished flight ability (Elkins et al., 1986). The temperature-induced semi-paralytic phenotype was later termed "sticky-feet" because the legs of *slo* null homozygotes would remain anchored to the ground even if flies were physically pushed sideways (Atkinson et al., 2000). In addition to heat shock, this phenotype could be induced with "cool but very bright light" (Atkinson et al., 2000). Interestingly, the *ash2¹⁸* allele, a deletion that removes neuronal-, but not muscle-specific promoters of *slo*,

complemented the *slo* flight defect but not the sticky-feet phenotype, suggesting the former to be due to a loss of *slo* in muscle tissue, while the latter is due to loss of neuronal *slo* (Atkinson et al., 2000). Moreover, slo^1 homozygotes exhibited altered male courtship song patterns, most notably lower amplitude pulses and longer inter-pulse intervals (Peixoto and Hall, 1998). The expression of *slo* cycles in a circadian manner, and *slo* null homozygotes (slo^1 and slo^4, an X-ray-induced chromosomal inversion) showed arrhythmic locomotor activity under free-running conditions (constant darkness, DD), without a change in overall activity levels (Ceriani et al., 2002; Fernández et al., 2007). In particular, loss of *slo* expression resulted in a loss of morning anticipation, which, in slo^4 homozygotes, was linked to disrupted dorsal projections of *pdf*-expressing neurons, possibly desynchronising the circadian network (Ceriani et al., 2002; Fernández et al., 2007). Moreover, neuronal *slo* expression is necessary and sufficient for the development of rapid tolerance to the sedative effects of benzyl alcohol and ethanol, defined as a decrease in drug responsiveness as a result of prior drug exposure (Cowmeadow et al., 2005, 2006; Ghezzi et al., 2004). Interestingly, electrophysiological recordings from the dorsal longitudinal flight muscles (DLMs) showed that the increase in neuronal *slo* expression following benzyl alcohol exposure lowered the seizure threshold (Ghezzi et al., 2010). This result is congruent with earlier findings that *slo* null homozygotes exhibit increased seizure thresholds compared to controls (Kuebler et al., 2001). These data suggest that increased neuronal *slo* expression can have excitatory effects in the nervous system. Electrophysiological studies of *slo* null homozygotes have directly assessed this possibility in both muscles and neurons.

Intracellular recordings from the DLMs of slo^1 homozygotes demonstrated that these mutants exhibited broadened DLM spikes (Elkins et al., 1986). Under voltage-clamp, it could be shown that slo^1 homozygotes specifically lacked the Ca^{2+}-gated fast K^+ current (I_{CF}), while retaining the other three K^+ currents: I_{CS}, I_A, and I_K (Elkins et al., 1986). Hence, this study established an important role for *slo* in mediating the fast repolarisation of the muscle AP. In response to a constant depolarising current, DLMs usually exhibit a delay before spike initiation, a process called "delayed excitation" (Elkins and Ganetzky, 1988). In slo^1 homozygotes, delayed excitation in DLMs was entirely lost (Elkins and Ganetzky,

1988). Current clamp recordings from the DLMs further showed that slo^1 homozygotes exhibited abnormal AP train firing, initiating overshooting APs of longer duration for every AP except the first in a train, which can be mediated by I_A (Elkins and Ganetzky, 1988). A role for slo in mediating I_{CF} and contributing to AP repolarisation was confirmed via electrophysiological recordings from L3 larval body wall muscles as well as from cultured neuroblasts, both exhibiting broadened APs in a slo^1 background (Saito and Wu, 1991; Singh and Wu, 1990). Despite the excitatory effects associated with a loss of slo, early electrophysiological recordings from the larval NMJ of slo^1 homozygotes identified a decreased amplitude of excitatory junctional currents (EJCs) (Warbington et al., 1996). More recent larval NMJ studies have shown that loss of slo had either no effect (Lee et al., 2008, 2014), or caused an increase in EJC amplitude (Jepson et al., 2014). Morphological abnormalities of the larval NMJ have also been identified in response to a loss of slo: the area of synaptic boutons and pre-synaptic AZs was found to be increased (Jepson et al., 2014), while another study identified an increased number of synaptic boutons and the emergence of satellite boutons, small boutons budding off from larger ones (Lee and Wu, 2010). Via voltage-imaging using Archaerhodopsin3, it could be shown that slo^1 homozygotes exhibit an increased AP width at pre-synaptic termini of MNs at the larval NMJ, an effect that was particularly strong during trains of repetitive nerve stimulation (Ford and Davis, 2014). Moreover, the Ca^{2+}-dependent modulation of AP width was lost in slo^1 homozygotes, suggesting that slo mediates I_{CF} in MN pre-synaptic termini as well, where it would act as a break on neurotransmitter release (Ford and Davis, 2014). Whole-cell patch clamp recordings *in situ* confirmed that slo is required to mediate I_{CF} and the fAHP in larval MNs (Kadas et al., 2015). Consequently, the endogenous intraburst firing frequencies of MNs decreased in slo null homozygotes (slo^1 and slo^4), while the synaptic drive potential amplitudes increased (Kadas et al., 2015). Thus, Slo channel activation can also lead to increased firing frequencies in neurons, possibly by promoting Na_v channel de-inactivation (Kadas et al., 2015).

1.6 Project Aim

Three themes can be extracted from this chapter: (1) The pathogenic mechanisms underlying PxD and combined PxD-epilepsy syndromes are incompletely understood (Erro et al., 2017); (2) GEPD is linked to a D434G missense mutation in *KCNMA1*, but despite *in vitro* studies elucidating the biophysical effects of this mutation, it is unclear how it causes GEPD *in vivo* (Du et al., 2005; Yang et al., 2010); (3) *KCNMA1* has a *Drosophila* orthologue, *slo*, and flies have been successfully used in the past to study a range of neurological pathologies (Wu and Lloyd, 2015).

Hence, the project aim of this thesis is to generate a *Drosophila* knock-in model of GEPD, in order to investigate the pathophysiological mechanisms underlying this PxD-epilepsy syndrome in a living organism. Using this model, three main questions will be addressed: (1) what are the organismal effects of the D434G-equivalent mutation in flies? (2) Where is the mutation required to exert its pathogenic effects? (3) What are the molecular mechanisms underlying GEPD?

2 Generation of a GEPD Fly Model

2.1 Introduction

While the biophysical effects of the GEPD-linked D434G missense mutation on BK channels have been thoroughly described – demonstrating an increased efficiency of the allosteric coupling between Ca^{2+}-binding and channel opening (Yang et al., 2010) (Paragraph 1.4.1.2) – GEPD pathogenesis on an organismal level is not yet understood. To address this problem, I used ends-out HR to introduce the GEPD-linked point mutation into the *Drosophila* gene *slo*, the fly orthologue of *KCNMA1*. This mutation results in a codon change from GAG to GGG via an A1097G transition, replacing glutamic acid with glycine at amino acid position 366 in Slo, thereby generating a novel allele called *slo^E366G*. The E366G amino acid change is equivalent to human D434G (Du et al., 2005). Ends-out HR relies on *in vivo* HR between the endogenous *slo* locus and an artificially introduced DNA sequence, referred to as "donor template" (Figure 2.1). This donor template was designed to carry the A1097G point mutation, thus introducing the GEPD-linked missense mutation into the endogenous *Drosophila* genome.
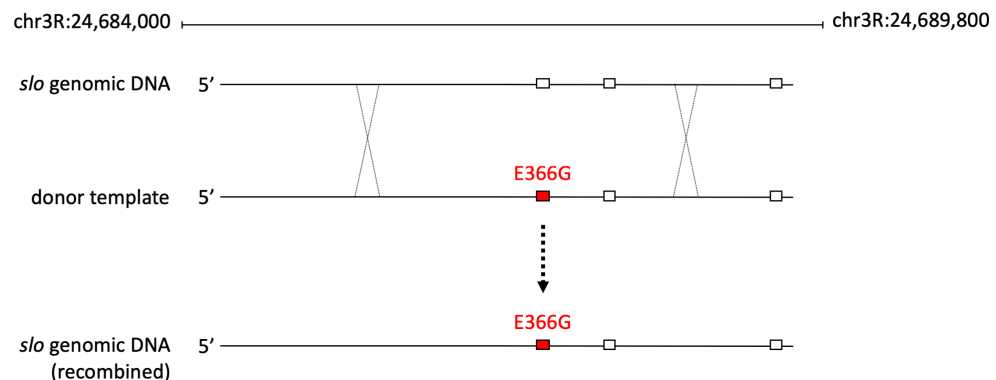
Figure 2.1 Ends-out Homologous Recombination

Ends-out HR relies on an experimentally introduced donor template to recombine with its homologous locus within endogenous *slo*. The donor template carries the A1097G point mutation, introducing the GEPD-linked amino acid change (E366G, red) into *slo*. Exons, represented as rectangles, are drawn to scale, with their genomic positions indicated at the top.

This chapter describes the generation and validation of *slo^E366G*. To this end, I followed a protocol that has successfully been used previously to generate *Drosophila* knock-in models of epilepsy syndromes via ends-out HR (Schutte et al., 2014; Staber et al., 2011; Sun et al., 2012). It starts with the design and construction of a plasmid construct that carries homology arms to the locus of interest within *slo*. This plasmid construct is injected into fly embryos, where it randomly integrates into the endogenous genome via P-element transposition. Subsequently, the integrated plasmid is experimentally excised and linearised *in vivo*, in order to act as a donor template for HR at the endogenous *slo* locus (Staber et al., 2011). Successful germline recombination events were verified via PCR and Sanger sequencing. The resulting recombinants were then outcrossed into isogenic background and sequence-validated, confirming the successful generation of the first *in vivo* model of GEPD.

2.2 Statement of Contribution

2.2.1 Direct Contributions

This project was initially conceptualised by Dr. James Jepson, who designed the homology arms and PCR primers for their amplification. Dr. James Jepson's contributions are acknowledged in the relevant figure legends (Figure 2.3, Figure 2.4, Figure 2.5). Dr. Ko-Fan Chen optimised the PCR parameters for the amplification of the homology arms, which I used as an entry point to this project – this is also acknowledged in the relevant figure legend (Figure 2.5).

2.2.2 Indirect Contributions

Dr. James Jepson has been a fantastic fly genetics teacher and guided me with his experience through the ends-out HR protocol. Dr. Ko-Fan Chen was an equally fantastic teacher in molecular biology and an endless resource of experience and ideas, which were invaluable during the cloning stages of the ends-out HR protocol.

2.3 Materials and Methods

2.3.1 Genetic Nomenclature

The genotypes of flies used in this chapter are listed in Paragraph 2.3.2. In the main text, only transgenes, mutant constructs, and mutations deviating from iso^{31} – an isogenised w^{1118} strain – are denoted. Semicolons in the main text are omitted, unless they are necessary to separate chromosomes. For example, $;;slo^{E336G}/TM6B,Tb$ is denoted as $slo^{E366G}/TM6B,Tb$. The fourth chromosome is disregarded in both notations. Flies carrying the slo^{E366G} and slo^{loxP} alleles might be referred to collectively as "post-Cre" flies.

2.3.2 Fly Stocks

Table 3 Fly Stocks of Chapter 2

Genotype	Source
iso^{31}	Kind gift from Dr. Kyunghee Koh
w^{1118}	BestGene Inc.
$y,w;hs\text{-}FLP,hs\text{-}I\text{-}SceI/CyO;$	BDSC: 6934
$w;P[w25.2]\text{-}Arm2^{E366G}\text{-}Arm1/CyO;$	This thesis
$y,w,ey\text{-}FLP;;$	BDSC: 5580
$w;Sco/CyO;$	Kind gift from Dr. Kyunghee Koh
$w;;TM2,Ubx^{130}/TM6B,Tb$	Kind gift from Dr. Kyunghee Koh
$w;;slo^{E366G[w+]}/TM6B,Tb$	This thesis
$w;;slo^{loxP[w+]}/TM6B,Tb$	This thesis
$y,w,Cre;;D^*/TM3,Sb$	BDSC: 851
$w;;slo^{E366G}/TM6B,Tb$	This thesis
$w;;slo^{loxP}/TM6B,Tb$	This thesis

2.3.3 Fly Husbandry

Unless otherwise indicated, fly stocks were maintained at room temperature (RT) on standard fly food, using the recipe shown in Table 4.

Table 4 Fly Food Recipe

Reagent	Concentration
Agar	10 g/L
Sucrose	15 g/L
Glucose	33 g/L
Yeast	35 g/L
Maize Meal	15 g/L
Wheatgerm	10 g/L
Treacle	30 g/L
Soya Flour	7.22 g/L
Nipagin	1g (in 10 mL ethanol)/L
Propionic acid	5 mL/L

2.3.4 Bioinformatics

The Human Genome Assembly GRCh38.p12 and the *Drosophila melanogaster* Genome Assembly BDGP6 were used throughout this chapter, as well as Ensembl v. 95 (Zerbino et al., 2018). For analyses using the UCSC Genome Browser (http://genome.ucsc.edu), the genome assembly release from August 2014 was used (Kent et al., 2002).

2.3.4.1 Amino Acid Sequence Alignments

For conservation analysis between human KCNMA1 and fly Slo, the amino acid sequences corresponding to their longest transcripts (human KCNMA1-210 and *Drosophila* Slo-RT, respectively) were retrieved from Ensembl and globally aligned to each other using the EMBOSS Needle pairwise sequence alignment tool (Needleman and Wunsch, 1970). For multiple sequence alignments of Sanger sequencing results, the Clustal Omega multiple sequence alignment tool was used (Sievers et al., 2011).

2.3.4.2 BoxShade Plots

The BOXSHADE software (v. 3.21), provided by ExPASy (Gasteiger et al., 2003), was used to generate BoxShade plots (https://embnet.vital-it.ch/software/BOX_doc.html).

2.3.4.3 Design of Homology Arms

To design homology arms around the E366 locus within *slo*, the UCSC genome browser was used. Sequence conservation between *Drosophila melanogaster* and related species was judged by manual inspection.

2.3.4.4 Sequence Analysis of *slo^{E366G}* and *slo^{loxP}*

To analyse the sequence variation present within endogenous *slo^{E366G}* and *slo^{loxP}* of post-Cre flies, I first downloaded genomic variation data for *Drosophila melanogaster* from the Ensembl File Transfer Protocol (FTP), provided in genome variation format (GVF) (Reese et al., 2010). Using the BLASTN tool on Ensembl, I extracted the absolute genomic positions for each of the variants identified in post-Cre flies, and, using basic Unix commands, queried the GVF file for any annotated variation at these genomic positions.

2.3.5 DNA Extraction

2.3.5.1 Standard Protocol

This protocol was adapted from BDGP Resources and is available at https://www.fruitfly.org/about/methods/inverse.pcr.html. It was used to extract genomic DNA (gDNA) for the following downstream applications: (1) cloning the homology arms, (2) confirmation of positive recombinants via PCR, (3) allele identification of positive recombinants, and (4) sequence-validation of post-Cre flies. 10-30 anaesthetised flies were frozen at -80°C for 30 min, before being homogenised in 400 μL Buffer A (100 mM Tris-HCl at pH = 7.5, 100 mM EDTA, 100 mM NaCl, 0.5% SDS), using a tissue grinder (Kimble, 749540-0000) and disposable pestles (Kimble, 749521-0500). The homogenates were incubated at 65°C for 30 min, before adding 800 μL LiCl/KAc solution (1 part 5 M KAc stock:2.5 parts 6 M LiCl stock) and incubating on ice for 10 min. The samples were then centrifuged at 14000 rpm for 15 min at RT, and 1 mL of the supernatant transferred into fresh 2 mL eppendorf tubes. 600 μL of isopropanol (Sigma-Aldrich, I9516-500ML) were added and mixed well with the samples, before centrifuging at 14000 rpm for 15 min at RT. The supernatant was discarded and 1 mL of 70% ethanol (Sigma-Aldrich, E7023-500ML) added to each sample, followed by centrifugation at 14000 rpm for 10 min at RT. The ethanol was

discarded and the samples dried at RT. 30 μL of warm nuclease-free water (50°C) were added to the dry pellets to resuspend the DNA. The samples were either used immediately for downstream applications or stored at -20°C.

2.3.5.2 Quick Protocol

This protocol was adapted from (Gloor et al., 1993). It was used to extract gDNA for the PCR-based outcrossing of post-Cre recombinants. Single flies were placed into individual 1.5 mL eppendorf tubes and frozen at -80°C for 30 min. Flies were then squashed in 50 μL "squishing buffer" (10 mM Tris-HCl at pH = 8, 1 mM EDTA, 25 mM NaCl, 200 g/mL Proteinase K), using a 200 μL pipette tip (Gloor et al., 1993). Proteinase K (NEB, P8107S) was added freshly to the squishing buffer stock solution prior to every gDNA extraction. The samples were incubated at 37°C for 30 min, before heat-inactivating Proteinase K at 95°C for 2 min and centrifuging the samples at 14000 rpm for 7 min at RT. Lastly, the supernatant (containing the DNA) was transferred to fresh eppendorf tubes and either used immediately for downstream applications or stored at 4°C.

2.3.6 PCR

2.3.6.1 PCR Primer Design

To design PCR primers, the online tool Primer3Plus was used (Untergasser et al., 2012). The standard parameters were changed as follows: Max Tm Difference was set to 5°C, Min GC % to 40.0, and Max GC % to 60.0. Product Size Range was adjusted as required. Primers were ordered from Sigma-Aldrich.

2.3.6.2 PCR Primers

The primers used to amplify the homology arms from *iso31* gDNA are shown in Table 5.

Table 5 PCR Primers to Amplify the Homology Arms

Target	Forward Primer	Reverse Primer
Arm1	CGTACGTCCCCAAGTACAGACAGCAA	GGCGCGCCGTTGTCAGTGTGTCGTGTGC
Arm2	GGTACCGCAGCTCAATGGAATGTGATT	GCGGCCGCACGCTTATTCTGGGACTTCG

In order to validate recombination events, PCR was performed using the primers shown in Table 6.

Table 6 PCR Primers to Validate Recombination Events

Primer Name	Primer Sequence
pW-Acc3_F (forward primer)	GCTCAGCTTGCTTCGCGATGTGTTCAC
pW-Acc1_R (reverse primer)	TTAGTTGAGTGCTTAAATTCAAAGGAT

The primers used for PCR-based outcrossing of post-Cre recombinants are shown in Table 7.

Table 7 PCR Primers for Post-Cre Outcrossing

Primer Name	Primer Sequence
OCF (forward primer)	AGACTAGTCTAGGGTACCGCA
OCR (reverse primer)	TAGTTCCTTGAATTGGCAGCG

To validate the PCR strategy before commencing PCR-based outcrossing, an alternative forward primer was used, shown in Table 8. The same reverse primer as shown in Table 7 was used for this PCR.

Table 8 PCR Validation Forward Primer

Primer Name	Primer Sequence
a2_F1 (forward primer)	GCAGCTCAATGGAATGTGATT

The primers used to amplify Arm1 and Arm2 from the gDNA of post-Cre flies are shown in Table 9 and Table 10, respectively.

Table 9 PCR Primers to Amplify Arm1 Post-Cre

Primer Name	Primer Sequence
GEPD_arm1_F1 (forward primer)	CGCCCATCGATTTGCGTTTT
GEPD_arm1_R1 (reverse primer)	CACATTCCATTGAGCTGCGG

Table 10 PCR Primers to Amplify Arm2 Post-Cre

Primer Name	Primer Sequence

Acc1_F (forward primer)	CATTATACGAAGTTATCTAGACTAGTCTAGGGTAC
Acc1_R (reverse primer)	TTAGTTGAGTGCTTAAATTCAAAGGAT

2.3.6.3 Pre-digestion

To facilitate PCR using the primers shown in Table 5, Table 6, Table 9, and Table 10, the gDNA was pre-digested with the restriction enzyme XhoI (NEB, R0146S) at 37ºC for 16 h. XhoI does not cut the loci of interest, but fragments the gDNA and increases primer accessibility. The reaction mixture used for pre-digestion is shown in Table 11. XhoI was heat-inactivated at 65ºC for 20 min.

Table 11 XhoI Pre-digestion of gDNA

Reagent	Volume / μL
Nuclease-free water	41
gDNA	3
NEB CutSmart Buffer	5
XhoI enzyme	1
Final volume	**50**

2.3.6.4 PCR Reaction

PCR using the primers shown in Table 5, Table 6, Table 9, and Table 10 was performed with the Q5 High-Fidelity 2X Master Mix (NEB, M0492S), using the reaction mixture shown in Table 12.

Table 12 Q5 PCR Reaction

Reagent	Volume / μL
Nuclease-free water	18
Forward primer	2.5
Reverse primer	2.5
gDNA	2
Q5 High-Fidelity 2X Master Mix	25

Final volume	**50**

PCR using the primers shown in Table 7 and Table 8 was performed with the GoTaq G2 Green Master Mix (Promega, M7822), using the reaction mixture shown in Table 13.

Table 13 GoTaq PCR Reaction

Reagent	Volume / μL
Nuclease-free water	8
Forward primer	1.25
Reverse primer	1.25
gDNA	2
GoTaq G2 Green Master Mix (2X)	12.5
Final volume	**25**

2.3.6.5 PCR Cycling Parameters

The underlined bases of the primer sequences in Table 5 denote restriction site overhangs added to genomic sequences and required for downstream applications: CGTACG = BsiWI (NEB, R0553S); GGCGCGCC = AscI (NEB, R0558S); GGTACC = Asc65I (NEB, R0599S); GCGGCCGC = NotI (NEB, R0189S). Due to their presence, a two-stage PCR was performed. The cycling parameters used to amplify Arm1 and Arm2 are shown in Table 14 and Table 15, respectively.

Table 14 PCR Cycling Parameters to Amplify Arm1

Repeats	Temperature / °C	Duration / s
1	98	30
15	98	10
	60.2	30
	72	120
25	98	10
	72	150

1	72	300

Table 15 PCR Cycling Parameters to Amplify Arm2

Repeats	Temperature / °C	Duration / s
1	98	30
15	98	10
	64.3	30
	72	120
25	98	10
	72	150
1	72	300

The PCR cycling parameters for the primers shown in Table 6 are listed in Table 16.

Table 16 PCR Cycling Parameters to Validate Recombination Events

Repeats	Temperature / °C	Duration / s
1	98	150
35	98	10
	61	30
	72	120
1	72	120

The PCR cycling parameters used for the primers shown in Table 7 and Table 8 are listed in Table 17.

Table 17 PCR Cycling Parameters to Outcross Post-Cre Recombinants

Repeats	Temperature / °C	Duration / s
1	95	300
15	95	30
	60	30
	72	120

1	72	300

The PCR cycling parameters used for the primers shown in Table 9 and Table 10 are listed in Table 18 and Table 19, respectively.

Table 18 PCR Cycling Parameters for Sequence-validation of Arm1

Repeats	Temperature / °C	Duration / s
1	98	150
35	98 69.7 72	10 30 120
1	72	120

Table 19 PCR Cycling Parameters for Sequence-validation of Arm2

Repeats	Temperature / °C	Duration / s
1	98	150
35	98 61 72	10 30 120
1	72	120

2.3.7 Gel Electrophoresis

Gel electrophoresis of PCR products was performed on 0.6-1% agarose gels (Sigma-Aldrich, A9539-25G), using GelRed as a nucleic acid dye (Biotium, 41002) and the Quick-Load Purple 2-Log DNA Ladder as a size reference (NEB, N0550S). Images were acquired using the GelDoc-It Imaging System (UVP). The runtime of gel electrophoresis varied between 30 min and 2.5 h, increasing with larger amplicons.

2.3.8 Molecular Cloning

2.3.8.1 DNA Gel Purification

PCR products were gel-purified using the Wizard SV Gel and PCR Clean-Up System (Promega, A9281), and DNA concentrations determined using a NanoDrop 2000 Spectrophotometer (Thermo Fisher Scientific, ND-2000).

2.3.8.2 TOPO Cloning

The two homology arms amplified using the primers shown in Table 5 were separately cloned into pCR-Blunt II-TOPO (Zero Blunt TOPO PCR Cloning Kit, Thermo Fisher Scientific, 450245), referred to as TOPO, using the reaction mixture shown in Table 20. This reaction was incubated for 30 min at RT.

Table 20 TOPO Cloning Reaction

Reagent	Volume / μL
Homology arm PCR product (gel-purified)	4 (~100 ng)
Salt solution	1
TOPO	1
Final volume	**6**

The TOPO plasmids were then transformed into XL1-Blue competent cells (Stratagene, 200130). Once the competent cells were thawed on ice, the whole TOPO reaction mixture (6 μL) was added and incubated on ice for 30 min. The competent cells were then heat-shocked at 42°C for 45 s, and immediately put back on ice for 2 min. 250 μL of pre-heated (42°C) S.O.C. medium (Invitrogen, 15544034) were then added to the competent cells, and the mixture shaken horizontally at 37°C and 225 rpm for 1 h. 100 μL of the mixture were spread onto a pre-warmed (37°C) kanamycin-containing agar plate (50 μg/mL kanamycin), which was prepared by adding a stock solution of kanamycin (50 mg/mL) to a 3.5 % solution of LB Broth with agar (Sigma Aldrich, L2897-1KG). The agar plates coated with the transformed XL1-Blue competent cells were incubated at 37°C for 16-18 h. Individual bacterial colonies were poked with a pipette tip and dropped into separate 14 mL round-bottom tubes containing 3 mL of 2.5 % LB

liquid medium (Sigma Aldrich, L3022-1KG) with 50 μg/mL kanamycin, followed by shaking at 225 rpm and 37°C for 16-18 h. To recover the TOPO plasmid DNA from the transformed bacteria, a miniprep was performed using the PureYield Plasmid Miniprep System (Promega, A1223).

2.3.8.3 P[w25.2] Cloning

One TOPO-Arm1- and one TOPO-Arm2 sample, prepared as described in Paragraph 2.3.8.2, were amplified via transformation into XL1-Blue cells, as described in Paragraph 2.3.8.2. Plasmid midipreps were performed using the Plasmid Midi Kit (Qiagen, 12143). TOPO-Arm2 and P[w25.2] were double-digested as described in Table 26, followed by Antarctic Phosphatase treatment of the P[w25.2] plasmid (NEB, M0289S), using the reaction mixture shown in Table 21. This reaction was performed at 37°C for 1 h, before heat-inactivating both Antarctic Phosphatase and the restriction enzymes at 70°C for 5 min.

Table 21 Antarctic Phosphatase Treatment of P[w25.2]

Reagent	Volume / μL
Nuclease-free water	15
P[w25.2]	2 (~100 ng)
Antarctic Phosphatase Reaction Buffer (10X)	2
Antarctic Phosphatase	1
Final volume	**20**

Arm2 and the cut P[w25.2] plasmid were then gel-purified, followed by the ligation of the former into the latter using T4 Ligase (NEB, M0202S) and the reaction mixture shown in Table 22. This reaction was performed at 16°C for 16 h, before heat-inactivating T4 Ligase at 65°C for 10 min.

Table 22 T4 Ligation of Arm2 into P[w25.2]

Reagent	Volume / μL
10X T4 DNA Ligase Buffer	2
Arm2 insert	9 (~64 ng)

P[w25.2]	8 (~64 ng)
T4 DNA Ligase	1
Final volume	**20**

The ligation products were amplified by transformation into XL1-Blue cells, as described in Paragraph 2.3.8.2. However, instead of 50 μg/μL kanamycin, as for TOPO cloning, P[w25.2] was grown in the presence of 100 μg/μL ampicillin. In order to insert Arm1 into P[w25.2]-Arm2, TOPO-Arm1 and P[w25.2]-Arm2 were restriction-digested as shown in Table 27, and column-purified using the Wizard SV Gel and PCR Clean-Up System (Promega, A9281). The purified digestion products were then subjected to another restriction digestion as shown in Table 28. P[w25.2]-Arm2 was treated with Antarctic Phosphatase as described for P[w25.2] in Table 21, before heat-inactivating AscI and Antarctic Phosphatase at 80°C for 20 min. The BsiWI- and AscI-cut P[w25.2]-Arm2 backbone was column-purified, as described above, while the BsiWI- and AscI-cut Arm1 of TOPO-Arm1 was gel-purified. Arm1 was then ligated into P[w25.2]-Arm2 at 16°C for 16 h using T4 Ligase and the reaction mixture shown in Table 23, before heat-inactivating T4 Ligase at 65°C for 10 min.

Table 23 T4 Ligation of Arm1 into P[w25.2]-Arm2

Reagent	Volume / μL
Nuclease-free water	6
10X T4 DNA Ligase Buffer	2
Arm1 insert	5 (~117 ng)
P[w25.2]-Arm2	6 (~75 ng)
T4 DNA Ligase	1
Final volume	**20**

The ligation products were amplified by transformation into XL1-Blue cells as described above.

2.3.8.4   Restriction Digestion

NEBcutter v. 2.0 was used for *in silico* digestion of all plasmids to predict the resulting amplicon sizes (Vincze et al., 2003). In order to confirm that the TOPO plasmids carried the correct inserts, restriction digestion with the restriction enzyme NotI-HF (NEB, R3189S) was performed, using the reaction mixture shown in Table 24. The reaction was run at 37°C for 18 h, before NotI-HF was heat-inactivated at 65°C for 20 min.

Table 24 NotI Restriction Digestion

Reagent	Volume / μL
Nuclease-free water	42
TOPO (carrying either Arm1 or Arm2)	2 (~1 μg)
NEB CutSmart Buffer	5
NotI-HF enzyme	1
Final volume	**50**

An alternative restriction digestion of TOPO was performed with the restriction enzyme EcoRI-HF (NEB, R3101T), using the reaction mixture shown in Table 25. The reaction was run at 37°C for 16 h, before EcoRI-HF was heat-inactivated at 65°C for 20 min. The same restriction digestion was performed with P[w25.2]-Arm2 after ligation of Arm2 into P[w25.2].

Table 25 EcoRI Restriction Digestion

Reagent	Volume / μL
Nuclease-free water	42
TOPO (carrying either Arm1 or Arm2) or P[w25.2]-Arm2	2 (~1 μg)
NEB CutSmart Buffer	5
EcoRI-HF enzyme	1
Final volume	**50**

Double-digestion of TOPO-Arm2 and P[w25.2] was performed with the restriction enzymes NotI (NEB, R0189) and Acc65I (NEB, R0599), using the reaction

mixture shown in Table 26. Double digestion was performed at 37°C for 3 h (TOPO-Arm2) and 2 h (P[w25.2]).

Table 26 NotI/Acc65I Double-Digestion

Reagent	Volume / μL
Nuclease-free water	39
TOPO-Arm2 or P[w25.2]	4 (~2 μg)
NEBuffer 3.1	5
NotI enzyme	1
Acc65I enzyme	1
Final volume	**50**

Restriction digestion of P[w25.2]-Arm2 and TOPO-Arm1 was performed with BsiWI (NEB, R0553S), using the reaction mixture shown in Table 27. This reaction was performed at 55°C for 4 h, followed by heat-inactivation of BsiWI at 65°C for 20 min.

Table 27 BsiWI Restriction Digestion

Reagent	Volume / μL
Nuclease-free water	38
P[w25.2]-Arm2 or TOPO-Arm1	5 (~3 μg)
NEBuffer 3.1	5
BsiWI enzyme	2
Final volume	**50**

The purified restriction products from Table 27 were used for restriction digestion with the restriction enzyme AscI (NEB, R0558S), using the reaction mixture shown in Table 28. Restriction digestion was performed at 37°C for 3 h (TOPO-Arm1) and 2h (P[w25.2]-Arm2).

Table 28 AscI Restriction Digestion

Reagent	Volume / μL
Nuclease-free water	33

NEB CutSmart Buffer	5
P[w25.2]-Arm2 or TOPO-Arm1 (digested with BsiWI)	10 (~1 μg)
AscI enzyme	2
Final volume	**50**

To confirm the identities of P[w25.2]-Arm2-Arm1 and P[w25.2]-Arm2^{E366G}-Arm1, restriction digestion with the meganuclease I-SceI (NEB, R0694S) was performed, using the reaction mixture shown in Table 29. This restriction digestion was run at 37°C for 4 h, before heat-inactivating I-SceI at 65°C for 20 min.

Table 29 I-SceI Restriction Digestion

Reagent	Volume / μL
Nuclease-free water	40
P[w25.2]-Arm2-Arm1 or P[w25.2]-Arm2^{E366G}-Arm1	3 (~1 μg)
NEB CutSmart Buffer	5
I-SceI meganuclease	2
Final volume	**50**

In order to introduce the A1097G point mutation into P[w25.2]-Arm2, P[w25.2]-Arm2 and pMA-T were double-digested with the restriction enzymes BglII (NEB, R0144S) and Acc65I (NEB, R0599S), using the reaction mixture shown in Table 30. Restriction digestion was performed at 37°C for 6 h (pMA-T) and 5 h (P[w25.2]-Arm2).

Table 30 BglII/Acc65I Double-Digestion

Reagent	Volume / μL
Nuclease-free water	38
P[w25.2]-Arm2 or pMA-T	4 (~1 μg)
NEBuffer 3.1	5
BglII enzyme	1.5

Acc65I enzyme	1.5
Final volume	**50**

2.3.8.5 Introducing the A1097G point mutation into P[w25.2]-Arm2-Arm1

In order to introduce the A1097G point mutation into Arm2 of P[w25.2]-Arm2-Arm1, a customised DNA fragment was ordered from GeneArt Gene Synthesis (Thermo Fisher Scientific), which is provided inside the pMA-T plasmid. This DNA fragment is sequence-analogous to the 5' 722 bp of Arm2, apart from the A1097G point mutation located at nucleotide position 402. It also carries a 5' Acc65I restriction site, resulting in a 728 bp fragment, and an endogenous 3' BglII restriction site, allowing for a cut-and-paste approach to exchange the endogenous 722 bp in Arm2 with this fragment. To do so, P[w25.2]-Arm2 and pMA-T were double-digested as shown in Table 30, before treating the cut P[w25.2]-Arm2 with Antarctic Phosphatase as described for P[w25.2] in Table 21. Antarctic Phosphatase and Acc65I were then heat-inactivated for 5 min at 70°C (BglII cannot be heat-inactivated). The cut P[w25.2]-Arm2 and the released 722 bp fragment (carrying the A1097G point mutation) were gel-purified, before ligating the latter into the former with T4 Ligase, using the reaction mixture shown in Table 31. The ligation was performed at 16°C for 16 h, before heat-inactivating T4 Ligase at 65°C for 10 min.

Table 31 T4 Ligation of A1097G into P[w25.2]-Arm2-Arm1

Reagent	Volume / μL
Nuclease-free water	13
10X T4 DNA Ligase Buffer	2
P[w25.2]-Arm2	1 (~75 ng)
722 bp fragment (harbouring the A1097G point mutation)	3 (~25 ng)
T4 DNA Ligase	1
Final volume	**20**

The ligation products were amplified by transformation into XL1-Blue cells as described in Paragraph 2.3.8.3, resulting in the successful retrieval of a P[w25.2]-Arm2 plasmid carrying the E336G-causing A1097G point mutation, termed P[w25.2]-Arm2[E366G]. In order to generate a P[w25.2] plasmid carrying both wild-type Arm1 and mutant Arm2[E366G], the latter was excised from P[w25.2]-Arm2[E366G] and cloned into P[w25.2]-Arm2-Arm1 in exchange for wild-type Arm2, following the same cloning procedure as described for the cloning of Arm2 from TOPO-Arm2 into empty P[w25.2] (Paragraph 2.3.8.3) – resulting in a plasmid termed P[w25.2]-Arm2[E366G]-Arm1.

2.3.9 Sanger Sequencing

DNA samples were sent to Source BioScience for Sanger sequencing (https://www.sourcebioscience.com/). Sanger sequencing primers were generated and ordered as described for PCR primers in Paragraph 2.3.6.1.

2.3.9.1 Sequence Validation of P[w25.2]-Arm2[E366G]-Arm1

To confirm the absence of unwanted mutations in P[w25.2]-Arm2[E366G]-Arm1, Sanger sequencing was performed using sequencing primers shown in Table 32.

Table 32 Sanger Sequencing Primers for P[w25.2]-Arm2[E366G]-Arm1

Primer Name	Primer Sequence
slo_arm1_F_1	TCCCCAAGTACAGACAGCAA
slo_arm1_F_3	GCTCGGCGATTTCATTTGAT
slo_arm1_F_4	GAGCAATCGATTTGGCGCAT
slo_arm1_F_5	TGAAGTTCTTCTTTCGTTTTAGCG
slo_arm1_F_6	ACTTGGTATGGGAAGAATGCCT
slo_arm1_R_1	TGTCAAAGCCAGTTCACAAGC
slo_arm1_R_2	GTTGTCAGTGTGTCGTGTGC
slo_arm2_F_1	GCAGCTCAATGGAATGTGATT
slo_arm2_F_3	AGCGACTAGACACAGTCAGT
slo_arm2_F_5	GTTTCCGGTTGCTGCTGATG
slo_arm2_F_6	TCCGTACAGTTTTTATACTCCCA
slo_arm2_R_1	TGTGTTGTTGAAGGTGGGGG

slo_arm2_R_2	ACGCTTATTCTGGGACTTCGG

2.3.9.2 Allele Identification of Successful Recombinants

In order to identify the $slo^{E366G[w+]}$ and $slo^{loxP[w+]}$ alleles in successful recombinants, Sanger sequencing was performed using the sequencing primers shown in Table 33.

Table 33 Sanger Sequencing Primers for Allele Identification

Primer Name	Primer Sequence
a2_alternative_R2-validation_F (R2F)	TCCGCTTTAATCGCACACTA
GEPD_seq_1	CCCCCACCTTCAACAACACA

2.3.9.3 Sequence-validation of slo^{E366G} and slo^{loxP}

In order to confirm the absence of additional mutations in endogenous slo^{E366G} and slo^{loxP} of post-Cre flies, the genomic Arm1 and Arm2 regions were Sanger-sequenced using the sequencing primers shown in Table 34 and Table 35, respectively.

Table 34 Sanger Sequencing Primers for Arm1

Primer Name	Primer Sequence
Asc2_F	CTCGTTTTGCATTTGTATTAGCCCTTG
Asc1_F	TCAGTGATTGGTGTTTATTATTGTGTT
Asc3_F	TATTCATCCTAGCCTCGTTTTGCATTT
slo_arm1_F_1	TCCCCAAGTACAGACAGCAA
slo_arm1_R_1	TGTCAAAGCCAGTTCACAAGC
slo_arm1_F_2	TCTCTCTTCAAACCTTCAATCAGT
slo_arm1_F_3	GCTCGGCGATTTCATTTGAT
slo_arm1_F_4	GAGCAATCGATTTGGCGCAT
slo_arm1_F_5	TGAAGTTCTTCTTTCGTTTTAGCG
slo_arm1_F_6	ACTTGGTATGGGAAGAATGCCT
slo_arm1_F_7	ACCTCATCGAAGAACATGCACT
slo_arm1_R_2	GTTGTCAGTGTGTCGTGTGC

Table 35 Sanger Sequencing Primers for Arm2

Primer Name	Primer Sequence
a2_alternative_R2-validate_F	TCCGCTTTAATCGCACACTA
slo_arm2_F_1	GCAGCTCAATGGAATGTGATT
slo_arm2_F_2	AGTGGTCTTTCTCCATCGGT
slo_arm2_F_3	AGCGACTAGACACAGTCAGT
slo_arm2_F_4	CCCCCGATTGTCAGGTGTC
slo_arm2_F_5	GTTTCCGGTTGCTGCTGATG
slo_arm2_F_6	TCCGTACAGTTTTTATACTCCCA
slo_arm2_F_7	TCGTTTGCTTTTGTTACGTTGT
slo_arm2_R_1	TGTGTTGTTGAAGGTGGGGG
slo_arm2_R_2	ACGCTTATTCTGGGACTTCGG
slo_a2_F_2_2	ATCGGGAGGATGTCGATGTC

2.3.10 Embryonic injection

Embryonic injections were performed by BestGene Inc., a *Drosophila* embryo injection service (http://www.thebestgene.com). I purchased "Plan C - P-element Premium Service". P[w25.2]-Arm2^{E366G}-Arm1 was injected into 200 individual w^{1118} embryos. Of these, 120 survived into the larval-, and 65 into the adult stage, which were then back-crossed into the w^{1118} genetic background. From these crosses, 10 w^+ F1 flies were recovered, representing successful germline integrations.

2.4 Results

2.4.1 Homology Between Human KCNMA1 and *Drosophila* Slo

In order to generate a *Drosophila* model of any mutation linked to a human disease, the protein affected by the mutation must be sufficiently conserved between the two species. An amino acid sequence comparison between the longest transcripts of KCNMA1 (Transcript ID: KCNMA1-210) and its fly orthologue Slo (Transcript ID: Slo-RT) revealed a sequence identity of 48.1% (Figure 2.2). Modelling GEPD in flies would be facilitated further if the pathogenic locus within the KCNMA1 protein was particularly well conserved, which would suggest functional significance. Indeed, the locus 10 amino acids up- and downstream of the D434G mutation is 81% conserved (Figure 2.2). However, it is important to note that the amino acid mutated in GEPD (D434) is only functionally conserved in the fly (E366): instead of aspartic acid, *Drosophila melanogaster* carries a glutamic acid residue at this position. However, there is strong electrophysiological evidence that aspartic- and glutamic acid at position 434 of KCNMA1 result in functionally equivalent BK channels (Yang et al., 2010), as discussed in Paragraph 2.5.1. Hence, I hypothesise that a change of either aspartic- or glutamic acid to glycine at this position will result in similar changes in protein function, and therefore conclude that *Drosophila melanogaster* is a valid model system to study GEPD.

```
KCNMA1-210    1  MANGGGGGGGGSGGGGGGGGGSSLRMSSNIHANHLSLDASSSSSSSSSSSSSSSSSSSSSSSSVHEPKMDALIIPVTMEVPCD
Slo-RT        1  -------------------------------------------------MSGCDQSTVESLADDPTDSPFDAD---D

KCNMA1-210   81  SRGQRMWWAFLASSMVTFFGGLFIILLWRTLKYLWTVCCH-------CGGKTKEAQKINNGSSQADGTLKPVDEKEEAVA
Slo-RT       26  CLKVRKYWCFLLSSIFTFLAGLLVVLLWRAFAF---VCCRKEPDLGPNDPKQKE-QKASRNKQEFEGT------------

KCNMA1-210  154  AEVGWMTSVKDWAGVMISAQTLTGRVLVVLVFALSIGALVIYFID-SSNPIESCQNFYKDFTLQIDMAFNVFFLLYFGLR
Slo-RT       90  ----FMTEAKDWAGELISGQTTTGRILVVLVFILSIASLIIYFVDASSEEVRCQKWSNNITQQIDLAFNIFFMVYFFIR

KCNMA1-210  233  FIAANDKLWFWLEVNSVVDFFTVPPVFVSVYLNRSWLGLRFLRALRLIQFSEILQFLNILKTSNSIKLVNLLSIFISTWL
Slo-RT      166  FIAASDKLWFMLEMYSFVDYFTIPPSFVSIYLDRTWIGLRFLRALRLMTVPDILQYLNVLKTSSSIRLAQLVSIFISVWL

KCNMA1-210  313  TAAGFIHLVENSGDPWENFQNNQALTYWECVYLLMVTMSTVGYGDVYAKTTLGRLFMVFFILGGLAMFASYVPEIIELIG
Slo-RT      246  TAAGIIHLLENSGDPLD-FNNAHRLSYWTCVYFLIVTMSTVGYGDVYCETVLGRTFLVFFLLVGLAVFASWIPEITELAA

KCNMA1-210  393  NRKKYGGSYSAVSGRKHIVVCGHITLESVSNFLKDFLHKDRDDVNVEIVFLHNISPNLELEALFKRHFTQVEFYQGSVLN
Slo-RT      325  QRSKYGGTYSKDPRKRHIVVCGHITYESVSHFLKDFLHEDREDVDVEVVFLHREKEPDLELEGLLKRHYTTVAFFQGTMMN

KCNMA1-210  473  PHDLARVKIESADACLILANKYCADPDAEDASNIMRVISIKNYHPKIRIITQMLQYHNKAHLLNIPSWNWKEGDDAICLA
Slo-RT      405  AVDLERVKVHEADACLVLANKYCQDPDAEDAANIMRVISIKNYSDDIRVIIQLMQYHNKAYLLNIPSWDWKQGDDVICLA

KCNMA1-210  553  ELKLGFIAQSCLAQGLSTMLANLFSMRSFIKIEEDT--WQKYYLEGVSNEMYTEYLSSAFVGLSFPTVCELCFVKLKLLM
Slo-RT      485  ELKLGFIAQSCLAPGFSTMMANLFAMRSF-KTSPDTQAWQNDYLQGTGCEMYTETLSPSFTGMTFPQASELCFSKLKLLL

KCNMA1-210  631  IAIEYKSANR--ESRILINPGNHLKIQEGTLGFFIASDAKEVKRAFFYCKACHDDITDPKRIKKCGCKR-----------
Slo-RT      564  LAIEIKGAEEGADSKISINP-RGAKIQANTQGFFIAQSADEVKRAWFYCKACHEDIKDETLIKKCKCKNYVGMIMMQTGM

KCNMA1-210  698  -----------------------PKMSIYKRMRRACCFDCGRSERDCSCMSGRVR---------------GNVDTLERA
Slo-RT      643  VNQGITSVMNTMEDEHHPAPTFTPPELPKRVHVRGSVSGDITRDREDTNLLNRNVRRPNGTGNGTGGMHHMNNTAAAAAA

KCNMA1-210  739  FPLSSVSVNDCSTSFRAFEDEQPSTLSPKKKQRNGGMRNSPNTSPKLMRHDPLLIP--------------------GN
Slo-RT      723  AAAAGKQVNKVKPTVNVSRQVEGQVISPSQYNRPPENDANPYAGYQLAYEVKKLMPTSRSSGTGTQNQNGGVSLPAGIAD

KCNMA1-210  797  DQIDNMD--SNVKYDSTGMFHWCAPKEIEKVILTRSEAAMTVLSGHVVVCIFGDVSSALIGLRNLVMPLRASNFHYHEL
Slo-RT      803  DQSKDFDFEKTEMKYDSTGMFHWSPAKSLEDCILDRNQAAMTVLNGHVVVCLFADPDSPLIGLRNLVMPLRASNFHYHEL

KCNMA1-210  875  KHIVFVGSIEYLKREWETLHNFPKVSILPGTPLSRADLRAVNINLCDMCVILSANQNNIDDTSLQDKECILASLNIKSMQ
Slo-RT      883  KHVVIVGSVDYIRREWKMLQNLPKISVLNGSPLSRADLRAVNVNLCDMCCILSAKVPSNDDPTLADKEAILASLNIKAMT

KCNMA1-210  955  FDDSIGVLQANSQGFTPPGMDRSSPDNSPVHGMLRQPSITTGVNIPIITELVNDTNVQFLDQDDDDDPDTELYLTQPFAC
Slo-RT      963  FDDTIGVLSQRGPEFD----NLSATAGSPI--VLQRRGSVYGANVPMITELVNDSNVQFLDQDDDDDPDTELYLTQPFAC

KCNMA1-210 1035  GTAFAVSVLDSLMSATYFNDNILTLIRTLVTGGATPELEALIAEENALRGGYSTPQTLANRDRCRVAQLALLDGPFADLG
Slo-RT     1037  GTAFAVSVLDSLMSTTYFNQNALTLIRSLITGGATPELELILAEGAGLRGGYSTVESLSNRDRCRVGQISLYDGPLAQFG

KCNMA1-210 1115  DGGCYGDLFCKALKTYNMLCFGIYRLRDAHLSTPSQC---TKRYVITNPPYEFELVPTDLIFCLMQFDHN----------
Slo-RT     1117  ECGKYGDLFVAALKSYGMLCIGLYRFRD----TSSSCDASSKRYVITNPPDDFSLLPTDQVFVLMQFDPGLEYKPPAVRA

KCNMA1-210 1182  -AGQSRASLSHSSHSSQSSSKSSSVHSIPSTANRQNRPKSRESRDKQNATRMNRMGQEKKWFTDEPDNAYPRNIQIKPM
Slo-RT     1193  PAGGRGTNTQGSGVGGGGSNKDDNS-----------------------------------------------------

KCNMA1-210 1261  STHMANQINQYKSTSSLIPPIREVEDEC
Slo-RT           --------------------------
```

```
KCNMA1-210  424   F L K D F L H K D R D D V N V E I V F L H
Slo-RT      356   F L K D F L H E D R E D V D V E V V F L H
```

Figure 2.2 Sequence Conservation Between KCNMA1 and Slo

Amino acid pairwise sequence alignment between the longest transcripts of KCNMA1 (KCNMA1-210) and Slo (Slo-RT) shows 48.1% overall amino acid sequence identity. Black shading indicates full-, grey shading functional-, and white shading no conservation. The protein sequence 10 amino acids up- and downstream of the D434 residue is shown enlarged at the bottom and exhibits 81% amino acid sequence identity. The location of human D434 and fly E366 is highlighted in violet, showing functional conservation.

84

2.4.2 Designing Homology Arms

Throughout this chapter, the following protocol has been used as an experimental guide: (Staber et al., 2011) – any major deviations from it are specified in the main text. The donor template used to introduce the A1097G point mutation into the endogenous *Drosophila* genome is generated *in vivo* via the excision and linearisation of a DNA sequence that will be introduced into the gDNA via transposition of a P-element donor construct. This donor construct is prepared by cloning homology arms designed *in silico* into a dedicated plasmid called P[w25.2]. Each of the homology arms must be at least 2.5 kb in length, to allow for efficient HR, and both arms need to be positioned so as to span the E366 residue within *slo*. Simultaneously, the homology arms must flank an intronic sequence that is poorly conserved across different *Drosophila* species and other insects, because this sequence will be replaced by a remnant vector sequence of 76 bp at the end of this protocol: the Cre-mediated removal of a floxed mini-*white* gene from the recombined *slo* locus (Figure 2.13). A lack of sequence conservation across species is used as an indicator that the sequence is unlikely to be functionally significant. The endogenous- and the remnant vector sequence should also approximately match in length in order to preserve genomic spacing. Using the UCSC genome browser to compare gDNA sequences around the E366 locus between *Drosophila melanogaster* and 27 other insect species, 23 of them other *Drosophilae*, an 18 bp region 5' of E366 was identified that shows almost no conservation: chr3R:24,686,816-24,686,833 (Figure 2.3).

85
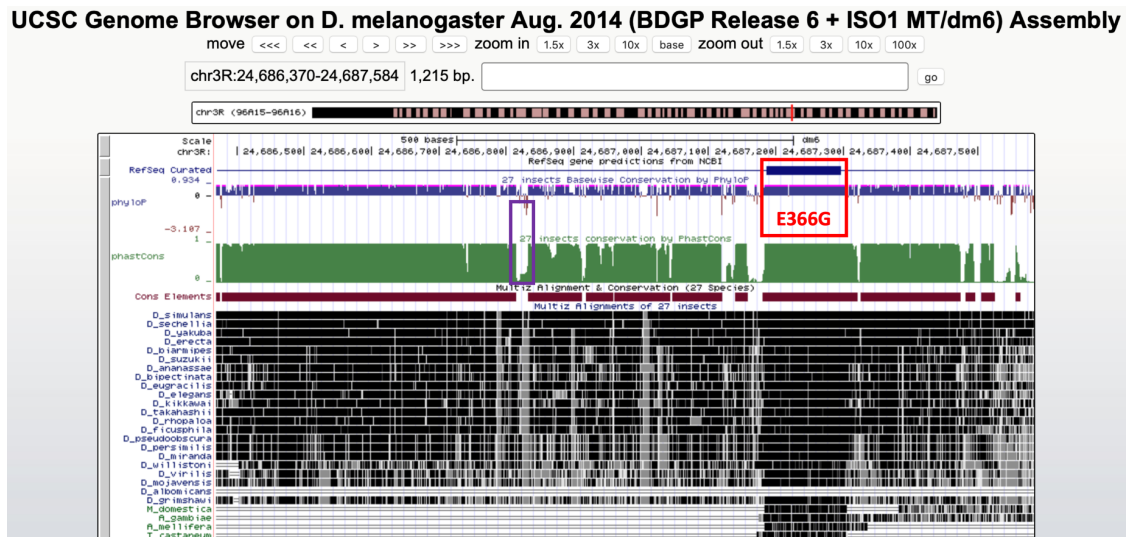
Figure 2.3 Positioning the Homology Arms

The UCSC genome browser was used to identify a non-conserved intronic region close to the E366 locus, around which the homology arms could be centred. A sequence of 18 bp (chr3R:24,686,816-24,686,833) was identified to be non-conserved across the 27 species listed on the left and is highlighted by a violet box. Exon 10 of *slo*, containing the E366 locus, is highlighted by a red box. This analysis was originally performed by Dr. James Jepson, and the screenshot for this figure taken from the UCSC Genome Browser (http://genome.ucsc.edu).

PCR primers were designed that could be used to amplify two homology arms within this region. The homology arm 5' of the flanked non-conserved sequence is referred to as Arm1, while the homology arm 3' of this sequence is referred to as Arm2. The identified primers amplify 2491 bp 5' of position chr3R:24,686,818 (Arm1) and 2731 bp 3' of position chr3R:24,686,862 (Arm2). This creates a 45 bp gap between the two homology arms that contains the 3' 16 bp of the 18-bp non-conserved sequence shown in Figure 2.3 and an additional 29 bp 3' of that sequence. As a result of this design, 45 bp of endogenous intronic sequence will be replaced by 76 bp of vector remnant sequence upon Cre-mediated excision of the floxed mini-*white* gene at the end of the ends-out HR protocol. This constitutes a compromise between leaving conserved endogenous sequences intact, preserving genomic spacing, and the availability of successful PCR primers to amplify the homology arms. To control for possible effects of this sequence replacement, a control allele will be generated that replicates this sequence replacement without carrying the A1097G point mutation. The final design of the homology arms is shown in Figure 2.4.
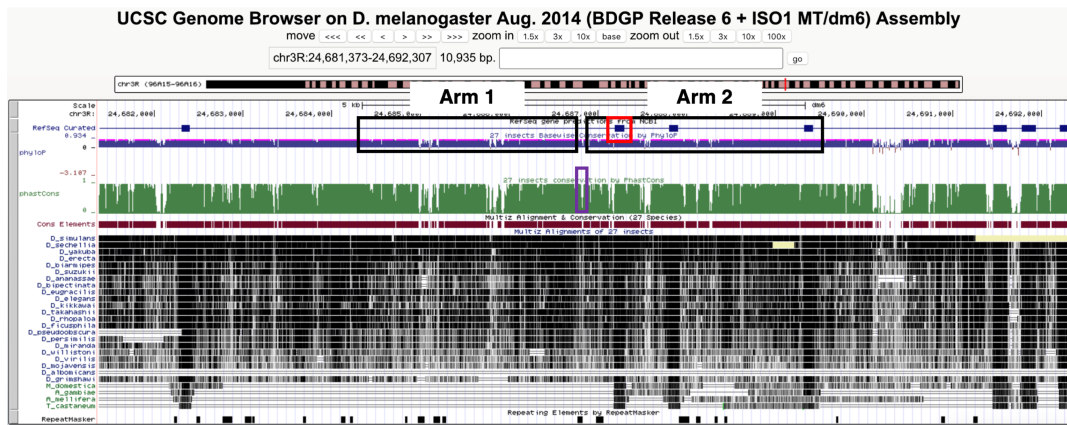
Figure 2.4 Anatomy of the Homology Arms

This figure shows a zoomed-out version of Figure 2.3. The non-conserved region around which both homology arms are centred is enclosed by a violet box. The two homology arms are shown as black boxes and are drawn to scale. Arm2 contains exon 10 (red rectangle), which carries the E366 amino acid residue that will be changed to glycine upon introduction of the A1097G point mutation, recapitulating the GEPD-linked D434G genotype. This analysis was originally performed by Dr. James Jepson, and the screenshot for this figure taken from the UCSC Genome Browser (http://genome.ucsc.edu).

2.4.3   Cloning of Homology Arms into P[w25.2]

With the homology arms designed *in silico*, I began the construction of a plasmid donor construct carrying these homology arms. This plasmid will later be injected into fly embryos, randomly integrating into the endogenous genome via P-element transposition. Subsequent excision and linearisation of this construct *in vivo* generate the donor template for HR. To this end, I extracted the gDNA from 20 isogenic flies (*iso[31]*), PCR-amplified and gel-purified the homology arms, and inserted them individually into TOPO plasmids, before sub-cloning them into a dedicated plasmid called P[w25.2], a P-element construct containing the floxed mini-*white* gene flanked by FRT- and I-SceI recognition sequences (Figure 2.5).
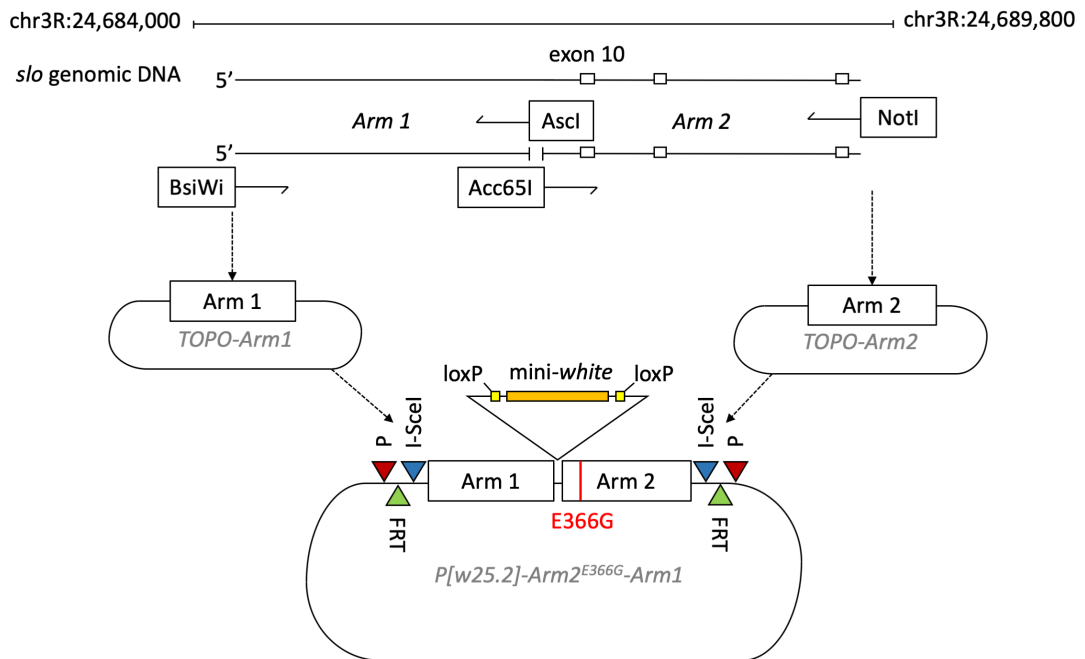
Figure 2.5 Cloning of Homology Arms into P[w25.2]

This schematic shows the steps involved in generating a P[w25.2] plasmid carrying both homology arms and the E366G mutation in Arm2 – denoted as P[w25.2]-Arm2^{E366G}-Arm1. On top, the absolute genomic location is shown, below which the genomic *slo* locus is indicated, with exons illustrated by rectangles and drawn to scale – exon 10 carries the E366 locus. The PCR strategy used to amplify the homology arms is shown by primers drawn as arrows and their tracing overhang restriction sites as rectangles. The homology arms are first separately cloned into TOPO plasmids, before being sub-cloned into P[w25.2]. A floxed mini-*white* gene separates the two homology arms. Short DNA sequences required for the random integration (P-element recognition sequences), excision (FRT inverted repeats), and linearisation (I-SceI recognition sites) of P[w25.2]-Arm2^{E366G}-Arm1 are shown as coloured triangles. The primers used to amplify the homology arms were designed by Dr. James Jepson and the PCR parameters optimised by Dr. Ko-Fan Chen.

Once both homology arms had been inserted separately into TOPO, I confirmed their identity via diagnostic restriction digestion with the restriction enzyme NotI. TOPO and Arm2 each carry one internal NotI restriction site, while Arm1 does not harbour this sequence. Hence, digesting TOPO-Arm1 with NotI causes a linearisation of the plasmid, with a length of 6024 bp. Depending on the orientation of Arm2 within TOPO, two possible combinations of fragments can be released from a restriction digestion with NotI: (1) 3487 bp + 2777 bp, or (2) 6224 bp + 40 bp. I performed this restriction digestion with two independent TOPO-Arm1- and two independent TOPO-Arm2 plasmid preparations, confirming by gel electrophoresis that all four plasmids carry the correct inserts (Figure 2.6).
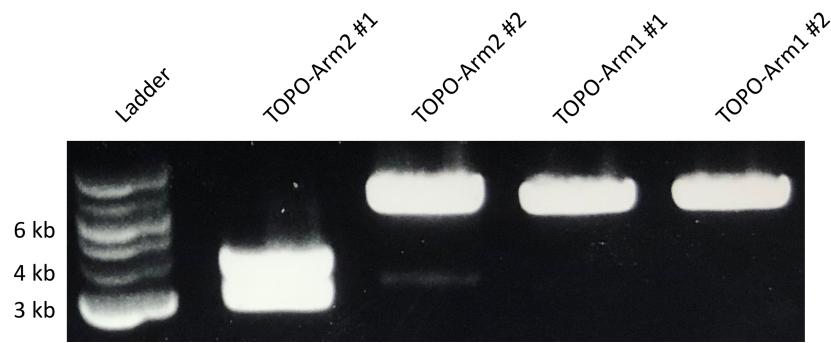
Figure 2.6 NotI Restriction Digestion of TOPO-Arm1/2

Two independent TOPO-Arm1- and two independent TOPO-Arm2 plasmid preparations were digested with the restriction enzyme NotI. The expected fragment size for digested TOPO-Arm1 is 6024 bp, which was observed for both TOPO-Arm1 plasmids. The TOPO-Arm2 plasmids show two different band arrangements because of different insert orientations, resulting in two fragments of 3487 bp and 2777 bp (TOPO-Arm2 #1), and two fragments of 6224 bp and 40 bp (TOPO-Arm2 #2). The 40 bp fragment lies outside the range of this gel.

I then chose one TOPO-Arm1- and one TOPO-Arm2 plasmid for downstream applications. Upon amplification of these plasmids, I performed a second diagnostic restriction digestion to ensure that the correct plasmids had been amplified. This time, I digested TOPO-Arm1 and TOPO-Arm2 with the restriction enzyme EcoRI, because the resulting digestion pattern is more distinct than the one resulting from NotI digestion: EcoRI cuts TOPO-Arm1 twice, resulting in two bands of 3501 bp and 2523 bp in length. TOPO-Arm2 is cut four times by EcoRI, yielding the following fragments: 3501 bp, 1440 bp, 814 bp, and 509 bp. Indeed, digesting both plasmids with EcoRI, I observed this exact pattern via gel electrophoresis, confirming the identity of TOPO-Arm1 and TOPO-Arm2 (Figure 2.7).
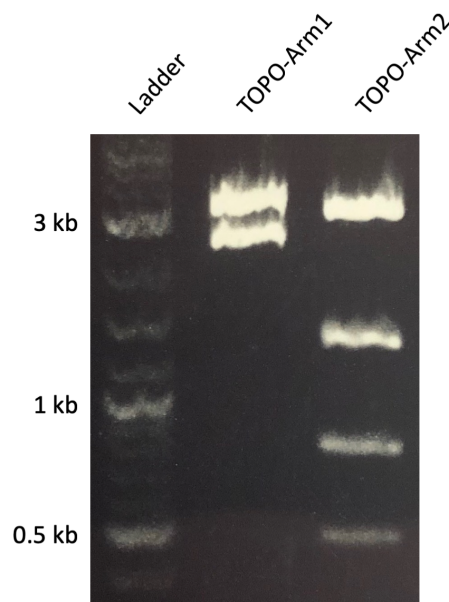
Figure 2.7 EcoRI Restriction Digestion of TOPO-Arm1/2

TOPO-Arm1 and TOPO-Arm2 were digested with EcoRI. The expected restriction fragments for TOPO-Arm1 are 3501 bp and 2523 bp in length, the ones for TOPO-Arm2 3501 bp, 1440 bp, 814 bp, and 509 bp. All six fragments are present, confirming the identities of TOPO-Arm1 and TOPO-Arm2.

With both homology arms successfully cloned into TOPO, I began the process of sub-cloning them sequentially into the P[w25.2] plasmid (Figure 2.5). Upon ligation of Arm2 into P[w25.2], I confirmed via diagnostic restriction digestion using EcoRI that P[w25.2]-Arm2 had successfully been generated. P[w25.2]-Arm2 carries 4 EcoRI restriction sites, resulting in the following expected fragments upon EcoRI digestion: 6248 bp, 4641 bp, 509 bp, and 295 bp. Indeed, this is the band arrangement I observed upon digesting three independent P[w25.2]-Arm2 plasmid preparations with EcoRI (Figure 2.8).
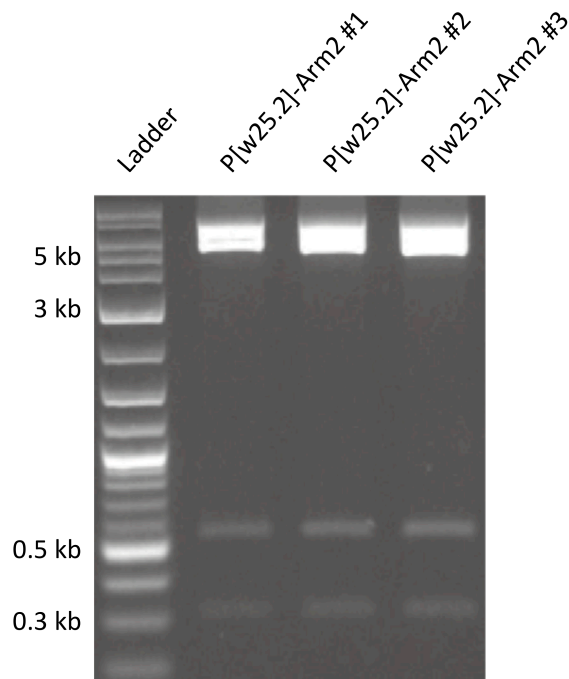
Figure 2.8 EcoRI Restriction Digestion of P[w25.2]-Arm2

Upon ligation of Arm2 into P[w25.2], the P[w[25.2]-Arm2 construct was digested with the restriction enzyme EcoRI. This gel shows the presence of the 4 expected restriction fragments: 6248 bp, 4641 bp, 509 bp, and 295 bp. Note that the ladder ran slightly faster than the samples. Nevertheless, the correct relative fragment sizes were observed, confirming the plasmid identities.

Following the successful generation of P[w25.2]-Arm2, the other homology arm (Arm1, carried within TOPO-Arm1, Figure 2.7) was ligated into one of the P[w25.2]-Arm2 preparations. To confirm that I had successfully generated a P[w25.2] plasmid carrying both homology arms, denoted as P[w25.2]-Arm2-Arm1, I performed a diagnostic restriction digestion with the meganuclease I-SceI. This enzyme will cut the I-SceI recognition sequences that flank the two homology arms and the mini-*white* gene (Figure 2.5). If both arms are present within P[w25.2], the expected products of this restriction digestion are 10027 bp (Arm1 + mini-*white* + Arm2) and 4121 bp (P[w25.2] plasmid backbone). Indeed, digesting 6 independent P[w25.2]-Arm2-Arm1 plasmid preparations, I was able to confirm the presence of these two bands in each of the samples (Figure 2.9).
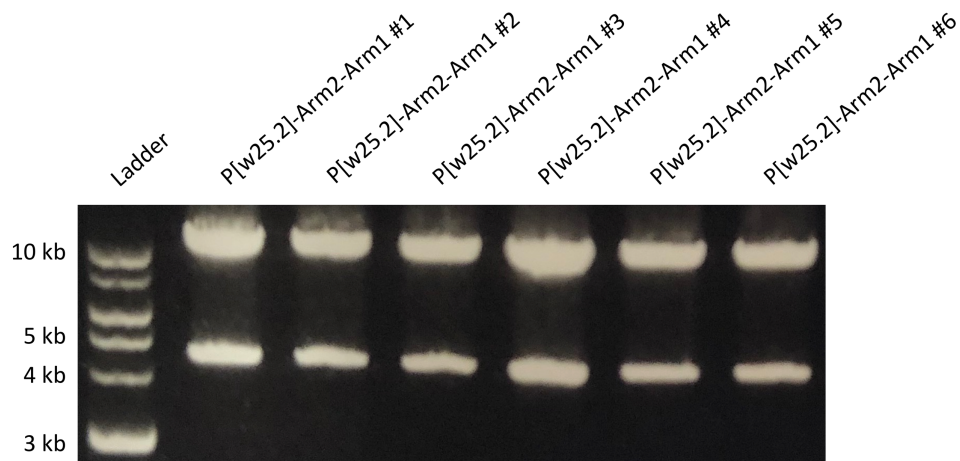
Figure 2.9 I-SceI Restriction Digestion of P[w25.2]-Arm2-Arm1

Six independent P[w25.2]-Arm2-Arm1 plasmids were restriction-digested with I-SceI, in order to confirm the presence of the correctly sized homology arms. I-SceI cuts 5' of Arm1 and 3' of Arm2, releasing a 10027 bp fragment that consists of these two homology arms and the mini-*white* gene located in between. Indeed, this band is present for each of the 6 P[w25.2]-Arm2-Arm1 plasmids. The second band corresponds to the P[w25.2] plasmid backbone, which is 4121 bp in size.

With the P[w25.2]-Arm2-Arm1 plasmid successfully generated (Figure 2.9), I introduced the E366G-causing A1097G point mutation into Arm2 (Figure 2.5). This point mutation will result in a codon change from GAG (glutamic acid) to GGG (glycine), recapitulating the GEPD genotype (Du et al., 2005). To this end, I replaced the 5' 722 bp of Arm2 with a 722 bp fragment that is identical in sequence with the exception of carrying the A1097G point mutation, via a cut-and-paste approach using restriction digestion and DNA ligation. This sequence replacement was performed in the P[w25.2]-Arm2 plasmid, thereby generating a novel plasmid carrying the E366G-containing Arm2 – this plasmid is denoted as P[w25.2]-Arm2^{E366G}. Upon successful generation of P[w25.2]-Arm2^{E366G}, I replaced wild-type Arm2 within P[w25.2]-Arm2-Arm1 with mutant Arm2^{E366G}, generating a P[w25.2] construct that carries wild-type Arm1 and mutant Arm2^{E366G}, denoted as P[w25.2]-Arm2^{E366G}-Arm1. To confirm the plasmid identity of P[w25.2]-Arm2^{E366G}-Arm1, I performed the same diagnostic restriction digestion with I-SceI as for P[w25.2]-Arm2-Arm1, demonstrating the successful generation of 11 independent plasmid preparations (Figure 2.10).
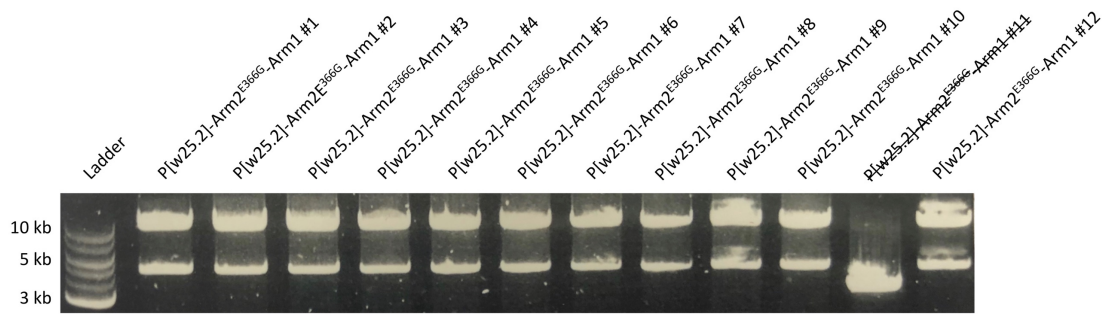
Figure 2.10 I-SceI Restriction Digestion of P[w25.2]-Arm2^{E366G}-Arm1

12 independent P[w25.2]-Arm2^{E366G}-Arm1 plasmid preparations were restriction-digested with I-SceI, in order to confirm the presence of the correctly sized homology arms, as described in Figure 2.9. 11 of the 12 plasmids showed the expected band arrangement.

Finally, I confirmed the absence of any unwanted mutations in the homology arms by Sanger sequencing of one P[w25.2]-Arm2^{E366G}-Arm1 plasmid preparation. Upon alignment of the Sanger sequencing results to the BDGP6 reference genome, no mutations could be detected apart from the GEPD-linked A1097G missense mutation, rendering P[w25.2]-Arm2^{E366G}-Arm1 suitable for embryonic injection (Figure 2.11).
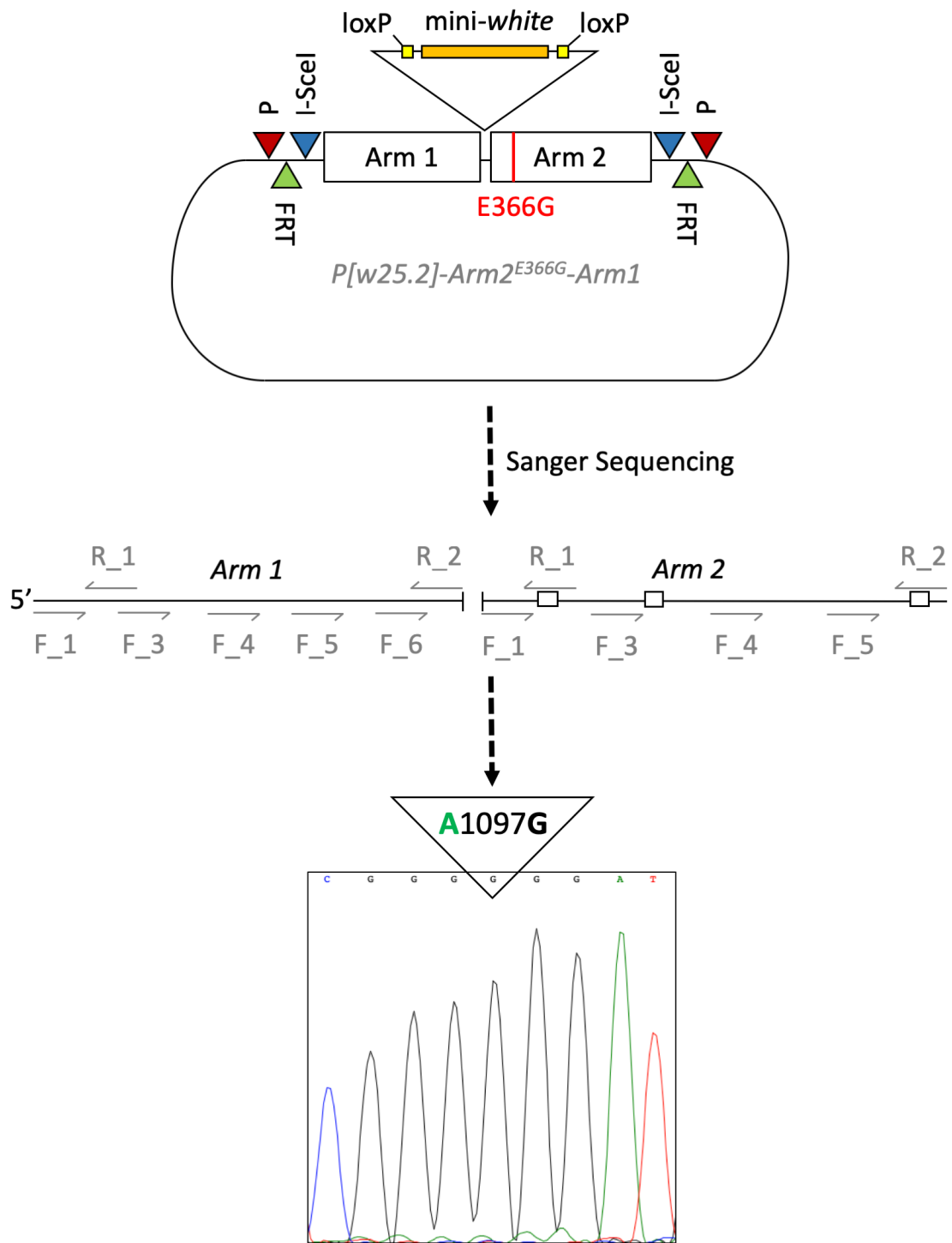
Figure 2.11 Sanger Sequencing of P[w25.2]-Arm2^{E366G}-Arm1

The two homology arms within P[w25.2]-Arm2^{E366G}-Arm1 (top schematic) were Sanger-sequenced in order to confirm the absence of any unwanted mutations. The approximate positions of the sequencing primers for both arms are shown in the middle as grey arrows. No unwanted mutations were detected in either arm. The presence of the E366G-causing A1097G point mutation in Arm2 was confirmed, as indicated in the electropherogram at the bottom.

At this stage, my protocol deviates from the one described in (Staber et al., 2011): usually, both plasmids, P[w25.2]-Arm2-Arm1 and P[w25.2]-Arm2^{E366G}-Arm1, would be injected separately into fly embryos, in order to generate the novel alleles *slo^{loxP}* and *slo^{E366G}*, respectively: *slo^{loxP}* only carries the 45-to-76-bp sequence replacement, including a loxP sequence, while *slo^{E366G}* carries this sequence replacement and the E366G mutation. The *slo^{loxP}* allele is required to account for any potential effects the sequence replacement alone might have. I reasoned that both alleles could be generated by injecting only the P[w25.2]-Arm2^{E366G}-Arm1 plasmid, because, depending on where along Arm2 HR occurs, the A1097G point mutation may or may not be integrated into the endogenous *slo* locus. Any HR event occurring 5' of the mutation will not introduce it into the endogenous genome, while any HR event 3' of the mutation will (Figure 2.13). Given a sufficiently large number of HR events, both alleles can, therefore, be generated from P[w25.2]-Arm2^{E366G}-Arm1. Hence, I decided to proceed with the protocol by injecting only P[w25.2]-Arm2^{E366G}-Arm1, disregarding P[w25.2]-Arm2-Arm1.

2.4.4 Generation of *slo$^{E366G[w+]}$* and *slo$^{loxP[w+]}$*

Once P[w25.2]-Arm2^{E366G}-Arm1 had been sequence-verified (Figure 2.11), this plasmid was injected into fly embryos. Balanced stocks of positive transformants are referred to as "donor flies": these flies carry a stably integrated P[w25.2]-Arm2^{E366G}-Arm1 transgene on chromosome 2, balanced over *CyO*. The presence of the integrated P[w25.2]-Arm2^{E366G}-Arm1 can be confirmed by orange eye colour, encoded by the mini-*white* gene present between the two homology arms (Figure 2.5). In order to generate *slo$^{E366G[w+]}$* and *slo$^{loxP[w+]}$* from the donor flies, the crossing scheme shown Figure 2.12 was performed. *slo$^{E366G[w+]}$* and *slo$^{loxP[w+]}$* flies still carry the floxed mini-*white* gene within the endogenous *slo* locus, as indicated by the *[w+]* superscript. The genetic mechanisms underlying this crossing scheme are illustrated in Figure 2.13. First, donor fly males were crossed to *y,w;hs-FLP,hs-I-SceI/CyO* virgin females. These flies carry heat shock-inducible FLP recombinase and heat shock-inducible I-SceI endonuclease on chromosome 2. The resulting offspring were heat-shocked as embryos and larvae at 48 h and 72 h after egg-laying, for 1 h each time at 38.5°C. The

increased temperature activates FLP recombinase and I-SceI endonuclease, which act to excise the P[w25.2]-Arm2^{E366G}-Arm1 transgene and linearise it, respectively. The resulting donor template can localise to- and recombine with its complementary sequence at the endogenous *slo* locus (Figure 2.13).
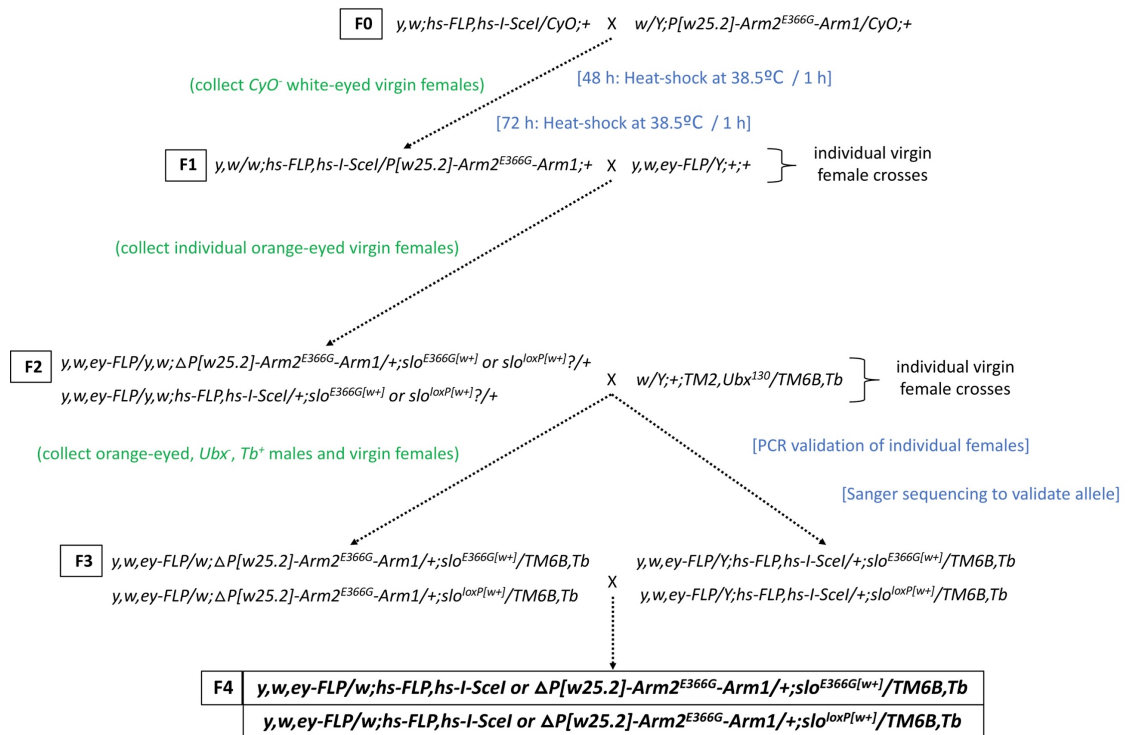
Figure 2.12 Crossing Scheme to Generate *slo$^{E366G[w+]}$* and *slo$^{loxP[w+]}$*

This diagram illustrates the genetic crosses involved in the generation of *slo$^{E366G[w+]}$*/*TM6B,Tb* and *slo$^{loxP[w+]}$*/*TM6B,Tb* stocks from donor flies, which carry the P[w25.2]-Arm2^{E366G}-Arm1 transgene on chromosome 2. Only the relevant genotypes are shown for simplicity. Fly collection criteria are marked in green, additional actions taken in blue. F0-F4 denote generation numbers. This figure was adapted from (Staber et al., 2011).

96
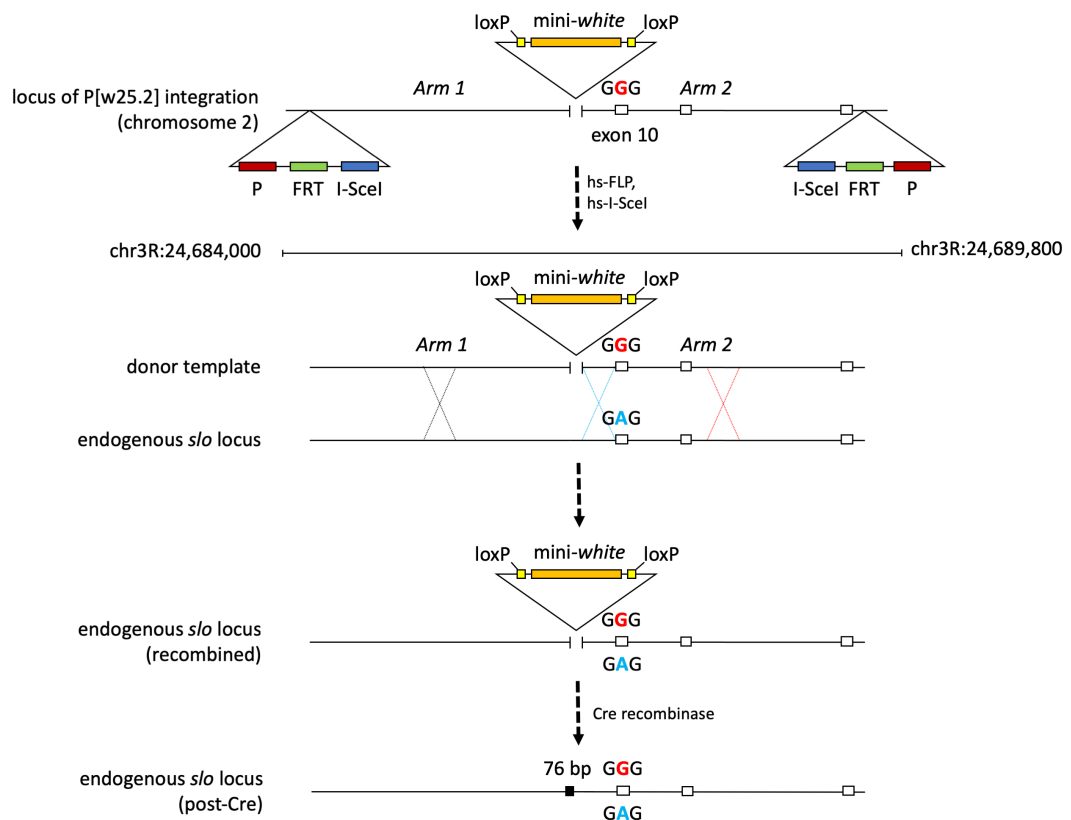
Figure 2.13 Genetics Underlying Ends-out Homologous Recombination

This schematic shows the genetic processes underlying ends-out HR. Donor flies carrying P[w25.2]-Arm2^{E366G}-Arm1 randomly integrated on chromosome 2 are shown on top. Flanking the homology arms of P[w25.2]-Arm2^{E366G}-Arm1 are P-element inverted repeats (maroon), FRT sites (green), and I-SceI recognition sequences (blue). Crossing the donor flies to flies expressing heat shock-inducible FLP and I-SceI (hs-FLP, hs-I-SceI) causes the excision of P[w25.2]-Arm2^{E366G}-Arm1 (via hs-FLP) and its linearisation (via hs-I-SceI), producing a donor template. The donor template can recombine with the endogenous *slo* locus, and, depending on where along Arm2 HR occurs, introduce the GEPD-linked A1097G missense mutation into the endogenous genome (**GG**G, red), or not (**GA**G, cyan). Positive recombinants still carry the floxed mini-*white* marker gene inside *slo*, which can be removed by crossing these flies to Cre-expressing stocks. This process leaves behind a 76 bp remnant vector sequence, consisting of AscI- and Acc65I restriction sites, two six-frame stop codons, and one residual loxP sequence (black).

The aim of the F0 cross in Figure 2.12 is for HR to occur in the germline of the developing F1 larvae and embryos, which will allow for the subsequent generation of stable stocks carrying the *slo$^{E366G[w+]}$* and *slo$^{loxP[w+]}$* alleles. Since germline events cannot directly be observed in the F1 progeny, their likelihood was assayed by somatic activity of FLP recombinase: efficient somatic excision of the P[w25.2]-Arm2^{E366G}-Arm1 transgene will lead to F1 adults with white eye

colour, due to the removal of the mini-*white* gene from a w^{1118} background (Figure 2.13). To this end, 150 F1 virgin females with white eye colour were collected and potential germline events assayed by setting up single-virgin crosses to *y,w,ey-FLP/Y* males (Figure 2.12). This cross distinguishes between non-excision events of the P[w25.2]-Arm2^{E366G}-Arm1 transgene and successful HR events: FLP driven by the *eyless* (*ey*) promoter excises the P[w25.2]-Arm2^{E366G}-Arm1 transgene in the eye by acting on the flanking FRT sites (Figure 2.13), resulting in white-eyed F2 progeny. Importantly, true recombinants will have lost their FRT sites upon HR into the endogenous genome, resulting in orange-eyed F2 progeny (Figure 2.13). Hence, orange-eyed F2 progeny are promising candidates for true HR events. Out of ~10,000 F2 adults screened, I retrieved 15 mini-*white*[+] virgin females (~0.15% efficiency). These flies were individually crossed to *TM2,Ubx^{130}/TM6B,Tb* males, in order to create stable lines balancing the potentially successful recombination event on chromosome 3 over *TM6B,Tb* (Figure 2.12).

2.4.5 Validation of Successful Homologous Recombination Events

To confirm that ends-out HR occurred at the correct genomic position in the 15 recombinants identified, I employed a PCR strategy that only yields an amplicon if the donor template has recombined with its complementary sequence within the endogenous *slo* locus: the forward primer is located within the mini-*white* gene, while the reverse primer is positioned 3' of Arm2. Using this strategy, I confirmed that all of the 15 orange-eyed F2 flies are true recombinants (Figure 2.14). The naming scheme for the recombinants consists of three numbers separated by dots: the first number is the number of the vial in which crosses between white-eyed *y,w;hs-FLP,hs-I-SceI/P[w25.2]-Arm2^{E366G}-Arm1* virgin females and *y,w,ey-FLP/Y* males were set up*;* since these crosses were flipped four times, the second number indicates the flip number; the third number indicates the number of the positive recombinant identified from that particular vile (Staber et al., 2011).
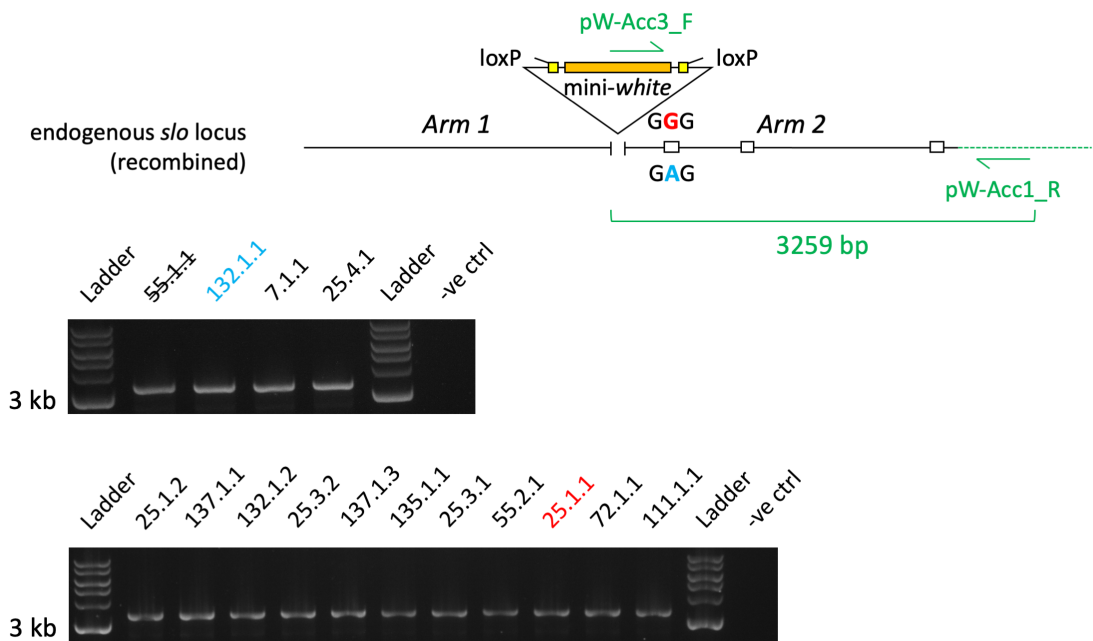
Figure 2.14 Confirmation of Positive Recombinants via PCR

To test for true HR events, a PCR strategy was employed that only yields an amplicon upon successful HR of the donor template with *slo* (Figure 2.13). The schematic at the top illustrates the design of the primer pair: the forward primer, pW-Acc3_F, is located within the mini-*white* gene (orange), while the reverse primer, pW-Acc1_R, is positioned 3' of Arm2 within *slo* (green dotted line). The gel images show that all 15 orange-eyed F2 flies were confirmed as true recombinants due to the presence of a 3259 bp amplicon. The negative control added to this experiment (-ve ctrl) was gDNA from donor flies, which did not yield an amplicon. The 55.1.1 stock later died and is hence struck through. 25.1.1 (red) and 132.1.1 (cyan) are the *slo*^E366G[w+] and *slo*^loxP[w+] stocks used for most downstream analyses, respectively.

I next sought to identify which recombination events integrated the A1097G point mutation into the endogenous *slo* locus and which ones did not (Figure 2.13). To this end, I performed the PCR strategy as shown in Figure 2.14 and gel extracted- and purified the 3259 bp amplicons, followed by Sanger sequencing. Altogether, I prepared 14 of the 15 recombinant stocks for sequencing because the 55.1.1 stock died (Figure 2.14). Of these 14 recombinant stocks, Sanger sequencing identified 4 to carry the *slo*^loxP[w+] allele (~29%) and 10 to carry the *slo*^E366G[w+] allele (~71%) (Figure 2.15).
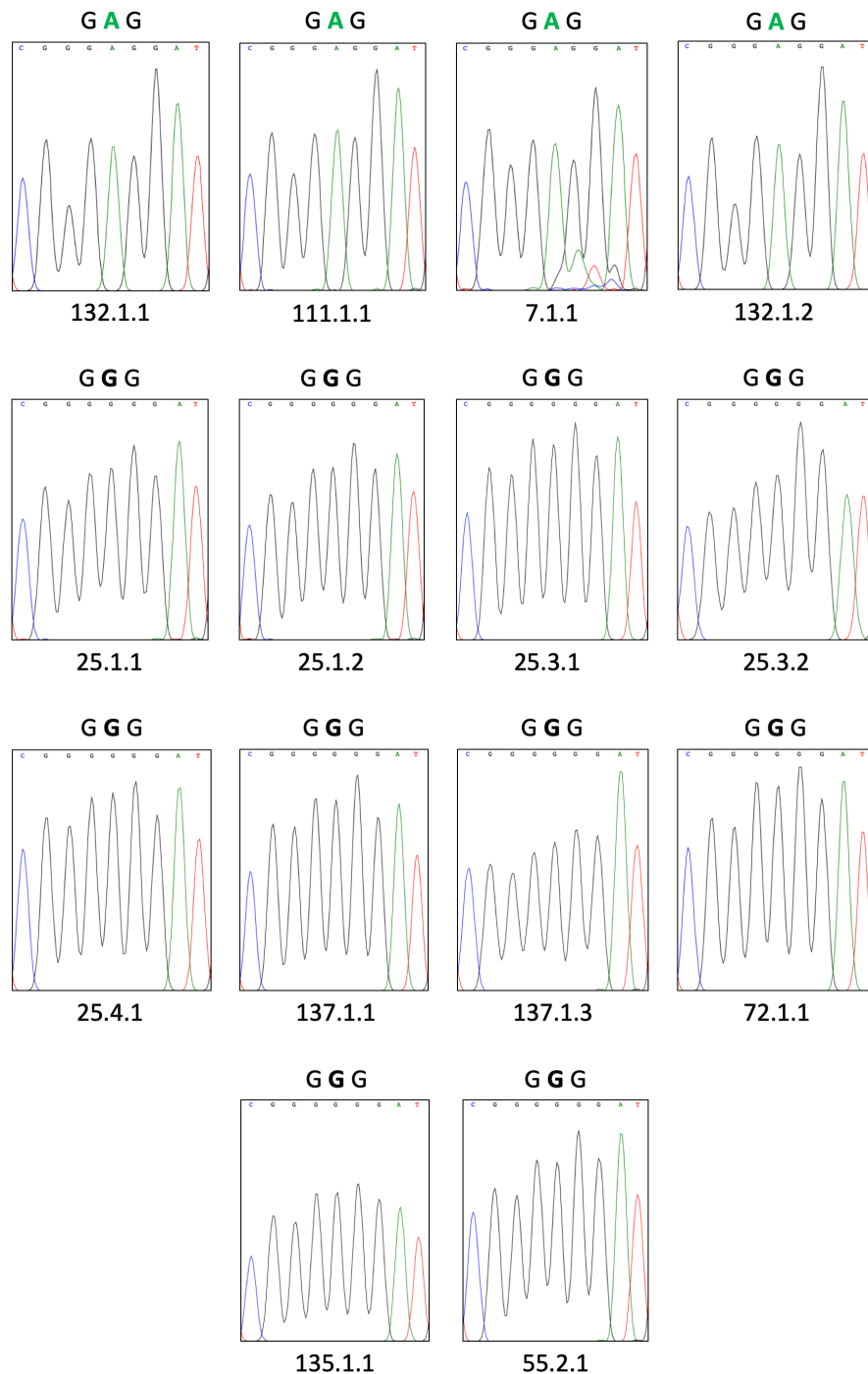
Figure 2.15 Sequence Validation of Successful Recombinants

The 14 surviving recombinant stocks were queried for the presence of the GEPD-linked A1097G mutation by Sanger sequencing. Depending on where along Arm2 HR occurs, this mutation may or may not be integrated into the endogenous genome (Figure 2.13). 4 of the 14 recombinants did not integrate the point mutation (top row, green), whereas 10 did (black). The respective codons are indicated as GAG for non-integration of the point mutation (glutamic acid) and GGG for successful integration (glycine).

Finally, four independent $slo^{loxP[w+]}$ recombinants (132.1.1, 111.1.1, 7.1.1, 132.1.2) and four independent $slo^{E366G[w+]}$ recombinants (25.1.1, 137.1.3, 135.1.1, 72.1.1) were outcrossed for 5 generations into isogenic background, as shown in Figure 2.16.

F0 $y,w,ey\text{-}FLP/y,w;\triangle P[w25.2]\text{-}Arm2^{E366G}\text{-}Arm1/+;slo^{E366G[w+]}$ or $slo^{loxP[w+]}/TM6B,Tb$
$y,w,ey\text{-}FLP/y,w;hs\text{-}FLP,hs\text{-}I\text{-}SceI/+;slo^{E366G[w+]}$ or $slo^{loxP[w+]}/TM6B,Tb$ X $w/Y;Sco/CyO;+$

(collect orange-eyed Tb^-, CyO^+ males)

F1 y,w or $y,w,ey\text{-}FLP/Y;\triangle P[w25.2]\text{-}Arm2^{E366G}\text{-}Arm1/CyO;slo^{E366G[w+]}$ or $slo^{loxP[w+]}/+$
y,w or $y,w,ey\text{-}FLP/Y;/y,w;hs\text{-}FLP,hs\text{-}I\text{-}SceI/CyO;slo^{E366G[w+]}$ or $slo^{loxP[w+]}/+$ X $w;+;+$

(collect orange-eyed CyO^+ males)

F2 $w/Y;+/CyO;slo^{E366G[w+]}$ or $slo^{loxP[w+]}/+$ X $w;+;+$

(collect orange-eyed CyO^- virgin females)

F3 $w;+;slo^{E366G[w+]}$ or $slo^{loxP[w+]}/+$ X $w/Y;+;+$ [repeat 5x to outcross genetic background]

F8 $w;+;slo^{E366G[w+]}$ or $slo^{loxP[w+]}/+$ X $w/Y;+;TM2,Ubx^{130}/TM6B,Tb$

(collect orange-eyed Tb^+ virgin females and males)

F9 $w;+;slo^{E366G[w+]}$ or $slo^{loxP[w+]}/TM6B,Tb$ X $w/Y;+;slo^{E366G[w+]}$ or $slo^{loxP[w+]}/TM6B,Tb$

F10 $w;+;slo^{E366G[w+]}/TM6B,Tb$ $w;+;slo^{loxP[w+]}/TM6B,Tb$

Figure 2.16 Crossing Scheme to Outcross $slo^{E366G[w+]}$ and $slo^{loxP[w+]}$

The $slo^{E366G[w+]}$ and $slo^{loxP[w+]}$ stocks generated as illustrated in Figure 2.12 might still carry chromosomes encoding transgenes or harbouring deletions. In 4 independent $slo^{E366G[w+]}$- and $slo^{loxP[w+]}$ stocks, these chromosomes were first exchanged with their isogenic homologues, before outcrossing these stocks into iso^{31} background for 5 generations. Green notes indicate fly collection criteria, blue notes additional actions taken. This figure was adapted from (Staber et al., 2011).

2.4.6 Establishing slo^{E366G} and slo^{loxP}

To remove the mini-*white* gene from the 14 $slo^{E366G[w+]}/TM6B,Tb$ and $slo^{loxP[w+]}/TM6B,Tb$ stocks (Figure 2.12), males from these stocks were separately crossed to $y,w,Cre;;D*/TM3,Sb$ virgin females, before establishing $TM6B,Tb$-balanced stocks of slo^{E366G} and slo^{loxP} (Figure 2.17).
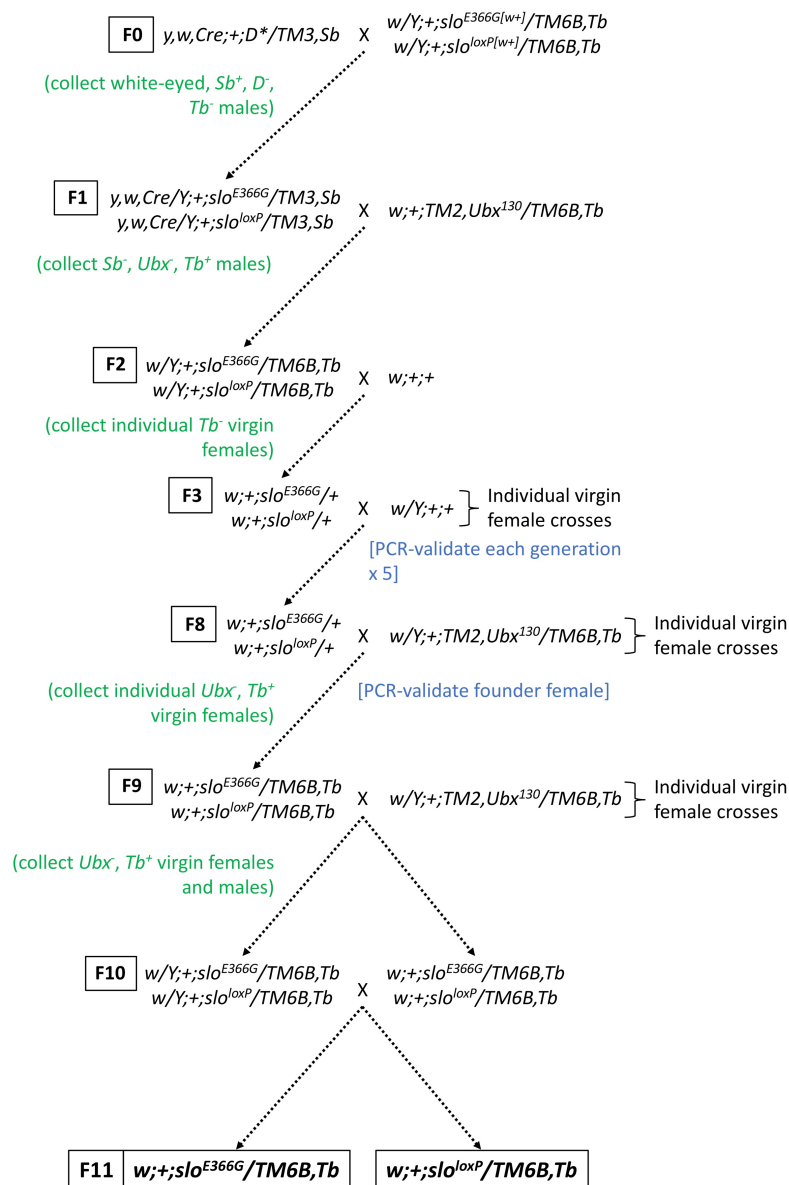
Figure 2.17 Crossing Scheme to Generate slo^{loxP} and slo^{E366G}

This crossing scheme was employed to remove the floxed mini-*white* gene via Cre recombinase activity, swap unwanted chromosomes, and outcross and balance the resulting slo^{loxP} and slo^{E366G} alleles. Green indicates fly collection criteria, blue additional actions taken. This figure was adapted from (Staber et al., 2011).

In order to account for possible genetic background effects that may influence future analyses of slo^{E366G} and slo^{loxP}, I outcrossed four independent slo^{E366G} recombinants (25.1.1, 137.1.3, 135.1.1, 72.1.1) and four independent slo^{loxP} recombinants (132.1.1, 111.1.1, 7.1.1, 132.1.2) into isogenic background (iso^{31}) for five generations (Figure 2.17). Since these post-Cre stocks have lost the eye-colour marker, I employed a PCR strategy to perform these outcrosses. For this strategy, the forward primer anneals to the 76 bp remnant sequence that is only present in recombinants, not in isogenic controls into which outcrossing was performed (Figure 2.18). I successfully validated this strategy on three independent recombinants (Figure 2.18).
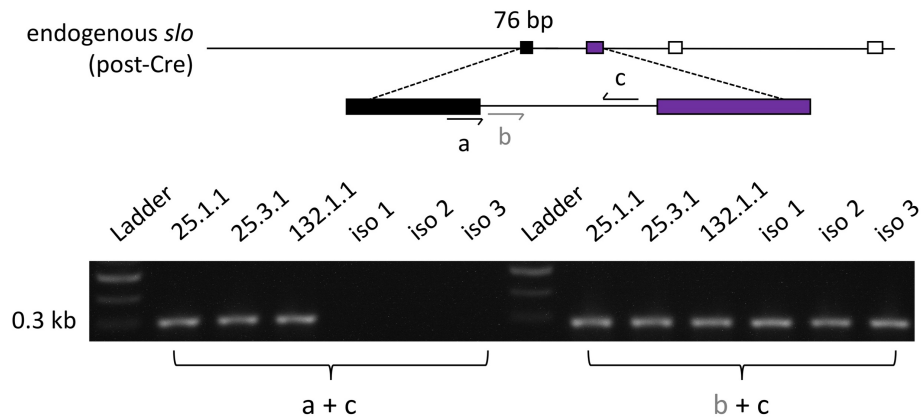
Figure 2.18 PCR-based Outcrossing of post-Cre Recombinants

The PCR strategy illustrated at the top was employed to outcross slo^{E366G} and slo^{loxP} flies into isogenic background: primers "a" and "c" (black arrows) will only yield an amplicon if the slo^{E366G} or slo^{loxP} allele is present because primer "a" anneals to the 76 bp remnant sequence that is not present in the isogenic (iso^{31}) background, into which outcrossing occurred. The gel at the bottom validates these primers: on the left, three separate recombinant lines and three independent iso^{31} negative controls were run after performing PCR using primers "a" and "c". No bands are present for iso^{31}, while all recombinants show a clear single band of expected size (301 bp). A separate forward primer (b, grey arrow in top schematic) confirmed that the gDNA used for this validation experiment was not degraded, as it successfully amplified a 283 bp amplicon together with primer "c" for all samples. Primers "a" and "c" were used to outcross post-Cre recombinants for five generations (Figure 2.17). In the schematic on top, the 76 bp remnant vector sequence is shown in black, while exon 10, carrying the E366 locus, is shown in violet.

2.4.7 Sequence Validation of *slo^E366G* and *slo^loxP*

Before performing experiments on the *slo^E366G* and *slo^loxP* alleles, it is necessary to confirm that the entire sequence of the *slo* locus spanned by the homology arms does not contain any unwanted mutations. Although the P[w25.2]-Arm2^E366G-Arm1 plasmid does not contain any such mutations (Figure 2.11), sequencing the endogenous *slo* locus of post-Cre recombinants is important to confirm that no unintended mutagenesis happened *in vivo*. To this end, I extracted gDNA from one *slo^E366G*/TM6B,Tb stock (*25.1.1/TM6B,Tb*, Figure 2.15) and one *slo^loxP*/TM6B,Tb stock (*132.1.1/TM6B,Tb*, Figure 2.15), PCR-amplified Arm1 and Arm2 separately, and gel-extracted and -purified the PCR products, followed by Sanger sequencing. Upon aligning the Sanger sequencing results to the BDGP6 *Drosophila melanogaster* reference genome, I identified 11 single-nucleotide polymorphisms (SNPs) and 1 insertion in Arm1, and 8 SNPs and 2 deletions in Arm2, in addition to the A1097G mutation in Arm2. In order to determine whether these variations are known to occur naturally, I queried published genome variation data on Ensembl for each of the sequence variants manually. Of note, Ensembl does not, to my knowledge, provide structural variation data for *Drosophila melanogaster*, preventing me from analysing the insertions and deletions directly. Instead, I analysed their respective genomic positions for the presence of SNPs, which would indicate that these loci show sequence variation. The results of this analysis are shown in Table 36 for Arm1 and in Table 37 for Arm2.

Table 36 Sequence Variation in Arm1

Class	Variation	Consequence	Genomic Location	Variant ID	Present in *25.1.1*	Present in *132.1.1*	Source
SNP	C>A	intron variant	3R:24684415	ENSVDME 05071548	yes	yes	DPGP
SNP	A>C	intron variant	3R:24685143	ENSVDME 05071589	yes	yes	DPGP
SNP	C>T	intron variant	3R:24685177	ENSVDME 05071594	yes	yes	DPGP
INS	A	intronic insertion	3R:24685501	-	yes	yes	-
SNP	A>C	intron variant	3R:24685666	ENSVDME 05071625	yes	yes	DPGP

Class	Variation	Consequence	Genomic Location	Variant ID	Present in 25.1.1	Present in 132.1.1	Source
SNP	T>C	intron variant	3R:24685784	ENSVDME 05071633	yes	yes	DPGP
SNP	A>T	intron variant	3R:24685813	ENSVDME 05071635	yes	yes	DPGP
SNP	T>C	intron variant	3R:24685845	ENSVDME 05071638	yes	yes	DPGP
SNP	C>T	intron variant	3R:24685848	ENSVDME 05071639	yes	yes	DPGP
SNP	T>G	intron variant	3R:24685849	ENSVDME 05071640	yes	yes	DPGP
SNP	C>A	intron variant	3R:24685874	ENSVDME 05071642	yes	yes	DPGP
SNP	T>A	intron variant	3R:24685875	ENSVDME 05071643	yes	yes	DPGP

Table 37 Sequence Variation in Arm2

Class	Variation	Consequence	Genomic Location	Variant ID	Present in *25.1.1*	Present in *132.1.1*	Source
DEL	CC	intronic deletion	3R:24687164 -24687169	ENSVDME 05071726- 05071729	no	yes	DPGP
-	A>G	exonic E366G missense mutation	3R:24687264	-	yes	no	-
SNP	C>A	intron variant	3R:24688025	ENSVDME 05071753	yes	yes	DPGP
SNP	G>C	intron variant	3R:24688138	ENSVDME 05071755	yes	yes	DPGP
SNP	A>T	intron variant	3R:24688292	ENSVDME 05071763	yes	yes	DPGP
SNP	T>G	intron variant	3R:24688426	ENSVDME 05071766	yes	yes	DPGP
SNP	C>A	intron variant	3R:24688440	ENSVDME 05071767	yes	yes	DPGP
SNP	G>A	intron variant	3R:24688625	ENSVDME 05071783	yes	yes	DPGP
DEL	TTT	intronic deletion	3R:24688631 -24688638	ENSVDME 05071786- 05071789	yes	yes	DPGP
SNP	T>A	intron variant	3R:24688642	ENSVDME 05071790	yes	yes	DPGP
SNP	C>A	intron variant	3R:24688900	ENSVDME 05071805	yes	yes	DPGP

All of the 11 SNPs present in Arm1 have been reported by the *Drosophila* Population Genomics Project (DPGP) and are annotated on Ensembl (Langley et al., 2012; Pool et al., 2012). All of these SNPs are intronic and present in both slo^{E366G} and slo^{loxP}. I identified one single-nucleotide insertion (adenine, A) at a position that shows no annotated sequence variation (Table 36). This insertion is located in an intronic stretch of 9 adenine residues and present in both alleles. Within the Arm2 sequence, I confirmed that the GEPD-linked A>G missense mutation is only present in slo^{E366G}. Moreover, all of the 8 SNPs in Arm2 have been reported by the DPGP, are intronic, and are present in both slo^{E366G} and slo^{loxP} (Table 37). I further identified a three-nucleotide deletion (3 x thymine, TTT) that is present in both alleles and is located within an intronic stretch of 8 consecutive thymine residues that shows considerable sequence variation: 4 of the 8 thymine residues exhibit annotated SNPs. Lastly, I identified a two-nucleotide deletion (2 x cytosine, CC) located within an intronic stretch of 6 consecutive cytosine residues that shows considerable sequence variation: 4 of these 6 cytosine residues exhibit annotated SNPs. This deletion is only present in the slo^{loxP} allele.

2.5 Discussion

This chapter describes the generation of a novel *Drosophila* knock-in model of GEPD. Using ends-out HR, an A1097G point mutation was introduced into *slo* – the fly orthologue of *KCNMA1* – resulting in an E366G amino acid change that is equivalent to the GEPD-linked D434G missense mutation in humans (Du et al., 2005). The *slo^{E366G}* allele is the first *in vivo* model of GEPD, facilitating the study of this PxD-epilepsy syndrome on a molecular, cellular, and behavioural level within a living organism.

2.5.1 Experimental Notes and Caveats

2.5.1.1 Functional Conservation of D434 in *Drosophila*

The human D434 amino acid residue (aspartic acid) is only functionally conserved in flies, which carry a glutamic acid residue (E) at the equivalent position (Figure 2.2). This could reflect a functional difference between mammalian and *Drosophila* BK channels, which would raise the question whether a missense mutation to glycine (G) would equally affect both channels. Importantly, electrophysiological data provide strong evidence for BK channels to be functionally similar in the presence of either aspartic- or glutamic acid at amino acid position 434 – as shown via expressing the D434G-equivalent murine D369G mutation in *Xenopous laevis* oocytes and recording macroscopic currents in the inside-out patch clamp mode (Yang et al., 2010). These experiments generated conductance-voltage (G-V) curves for a range of [Ca^{2+}], demonstrating that $V_{1/2}$ was shifted to more negative voltage ranges only for D369G BK channels, while D369E showed equivalent properties to D369D (Yang et al., 2010). Indeed, glycine was the only out of 7 amino acid residues tested that caused an increase in Ca^{2+} sensitivity, and molecular dynamics simulations suggested that this is due to a conformational change of the BK channel CTD that only occurs in the presence of glycine (Yang et al., 2010). Hence, I hypothesise that mammalian and *Drosophila* BK channels will be equally affected by this mutation, and that flies, therefore, represent a valid model system for GEPD.

2.5.1.2 Endogenous Sequence Replacement in slo^{E366G}

In addition to carrying the E366G missense mutation, the slo^{E366G} allele exchanges a 76 bp remnant vector sequence with 45 bp of endogenous gDNA. While the HR design ensures that these 45 bp are intronic and exhibit poor evolutionary conservation (Figure 2.3), this sequence can still be functionally important. For example, it has recently been shown that an intronic retroelement within *slo* affects the male *Drosophila* courtship song (Ding et al., 2016). In order to account for any potential effects of this sequence replacement, the slo^{loxP} allele was generated in parallel, which carries the 76 bp remnant vector sequence but not the E366G missense mutation (Figure 2.13). This allele serves as the control against which slo^{E366G} can be compared.

2.5.1.3 Sequence Variation in slo^{E366G} and slo^{loxP}

Extensive sequence variation within the *slo* locus of the slo^{E366G} and slo^{loxP} alleles was identified, as compared to the BDGP6 *Drosophila melanogaster* reference genome. However, via manual SNP analysis, I was able to show that all of the 19 point mutations present within the Arm1 and Arm2 regions of slo^{E366G} and slo^{loxP} – excluding A1097G – represent naturally occurring SNPs (Table 36 and Table 37). These SNPs are annotated on Ensembl and derive from the DPGP database, a large-scale genome sequencing effort covering >200 naturally occurring, mainly African, *Drosophila melanogaster* populations (Lack et al., 2016; Langley et al., 2012; Pool et al., 2012). Since P[w25.2]-Arm2^{E366G}-Arm1 was cloned from an iso^{31} genetic background, while embryonic injections were performed into a w^{1118} genetic background, it is likely that these SNPs represent sequence variation naturally present in the w^{1118} stock used by BestGene for embryonic injections. This would also explain the presence of all 19 SNPs in both alleles, slo^{E366G} and slo^{loxP}, as it is considered unlikely that independent mutagenic events occurring after embryonic injection result in precisely the same sequence variation. Further evidence for this hypothesis is provided by the presence of a two-nucleotide deletion (2 x cytosine, CC) only in the slo^{loxP} allele: for all slo^{loxP} alleles, the HR event on Arm2 must have happened 5' of the A1097G point mutation, in order not to introduce it into the endogenous *slo* locus (Figure 2.13). On the other hand, for all slo^{E366G} alleles, this event must have happened

3' of A1097G, in order to successfully integrate it. Hence, any sequence variation naturally present within the w^{1118} genetic background that is located 5' of A1097G on Arm2 can, by definition, only be present in the slo^{loxP} allele. Indeed, the deletion of two cytosine residues is the only sequence variant that is simultaneously 5' of A1097G on Arm2 and only present in slo^{loxP} – all other sequence- and structural variation, excluding A1097G, is present in both alleles (Table 36 and Table 37).

2.5.1.4   A Potential 5' Bias of Homologous Recombination

An interesting note with respect to ends-out HR is worth mentioning: assuming an equal probability of HR occurring along Arm2 and given that 14 HR events happened, one recombination event would be expected to occur every ~195 bp – this result is obtained by dividing the length of Arm2, 2731 bp, by the number of HR events, 14. Since the GEPD-linked A1097G mutation is located at position 402 (Figure 2.3), one would, therefore, expect 2 HR events amongst the 14 not to integrate the point mutation into the endogenous slo locus (Figure 2.13) – instead, I recovered 4. Hence, it might be the case that, within the scope of this experiment, HR has a 5' bias within Arm2.

2.5.2   Clinical Relevance

2.5.2.1   The First *in vivo* Model of GEPD

As discussed in Paragraph 1.4, BK channels show a complex pattern of expression and function (Bailey et al., 2019; Griguoli et al., 2016; Latorre et al., 2017). While *in vitro* studies of the D434G mutation have provided important biophysical insight (Yang et al., 2010), the organismal effects of this mutation are unknown. The novel slo^{E366G} allele presented in this chapter is the first *in vivo* model of GEPD and will facilitate the study of this disorder in a living organism. In particular, despite having evolutionarily diverged >700 million years ago (Hedges et al., 2006), the aim of this thesis is to discover pathological endophenotypes that are conserved between flies and humans (Lehner, 2013). Such cellular and molecular mechanisms would not only increase our understanding of GEPD, but might also reveal pathological principles that are applicable to PxD and epilepsy more generally.

2.5.3 Conclusion

The first *in vivo* model of GEPD has been generated via the introduction of the E366G missense mutation into *Drosophila slo*, replicating the human GEPD-linked D434G missense mutation (Du et al., 2005). The first step towards a mechanistic understanding of GEPD is a thorough phenotypic characterisation of the *slo*^{E366G} allele.

3   Phenotypic Characterisation of *slo*^{E366G}

3.1   Introduction

While electrophysiological studies have thoroughly described the biophysical effects of the GEPD-linked D434G missense mutation *in vitro* (Yang et al., 2010), its effects *in vivo* are unknown. As described in Paragraph 1.4.4, understanding how this mutation affects an entire organism might yield important and unexpected insights into the pathogenesis of GEPD. The newly established *slo*^{E366G} allele allows, for the first time, to study GEPD in a living organism. In this chapter, this task is approached on a cellular and behavioural level, including the video-tracking of *Drosophila* larvae and adults, electrophysiological recordings from the larval NMJ, and imaging of fixed- and live tissue.

      To this end, it is first established that the *slo*^{E366G} allele is homozygous lethal for post-pupal stages. Working with heterozygotes, it is shown that *slo*^{E366G}/+ larvae and adults exhibit severe locomotor defects, confirming the dominant nature of the *slo*^{E366G} allele. Pupal-, larval-, and adult morphology as well as adult life span are also markedly affected in *slo*^{E366G}/+ animals. Moreover, electrophysiological evidence is provided that *slo*^{E366G} is a gain-of-function allele *ex vivo*, exhibiting increased Ca^{2+} sensitivity in a manner similar to its murine D369G and human D434G equivalents (Du et al., 2005; Lee and Cui, 2009; Yang et al., 2010). Further cellular analyses of the larval nervous system, both electrophysiologically and via confocal imaging, revealed that the larval NMJ is structurally and functionally intact under physiological conditions, but that MNs in the ventral nerve cord (VNC) fire abnormally. Altogether, this chapter provides an in-depth characterisation of the *slo*^{E366G} allele and represents a first step towards identifying a pathogenic locus for GEPD in this *Drosophila* model.

3.2 Statement of Contribution

3.2.1 Direct Contributions

The video-tracking software AnimApp (Paragraph 3.4.2) was developed by Dr. Srinivasa Rao (code), Dr. Sam Olechnowicz (artwork, beta testing), Narayana Rao (code), and myself (beta testing), and is available on GitHub: https://github.com/sraorao/ (Rao et al., 2019). Dr. Srinivasa Rao and I wrote an R-based analysis script for the AnimApp tracking data, which is also available on GitHub: https://github.com/PatrickKratsch/. Confocal imaging of the larval NMJ, ensuing data analysis, and visualisation were performed by Dr. James Jepson (Paragraph 3.4.3). Electrophysiological recordings from the larval NMJ and corresponding data analyses were performed by Dr. Simon Lowe, while Dr. James Jepson visualised the data (Paragraphs 3.4.3, 3.4.4, and 3.4.5). Live-imaging of larval MNs was performed by both Dr. James Jepson and myself, each of us preparing and imaging 6 samples per genotype (Paragraph 3.4.5). Dr. James Jepson and I analysed the live-imaging data independently, but only the results from my own analyses are presented in this chapter (Paragraph 3.4.5). Table 38 lists these contributions and the corresponding figures in this chapter.

Table 38 Experimental Contributions to Chapter 3

Contributing Researcher	Corresponding Figure
Dr. Simon Lowe and Dr. James Jepson	Figure 3.10, Figure 3.11, Figure 3.12
Dr. James Jepson	Figure 3.9
Dr. James Jepson and Patrick Kratschmer	Figure 3.13, Figure 3.14, Figure 3.15

3.2.2 Indirect Contributions

Throughout the work described in this chapter, Dr. James Jepson and Dr. Ko-Fan Chen have provided invaluable intellectual input, without which the phenotyping of the slo^{E366G} allele would not have progressed as far as it has.

3.3 Materials and Methods

3.3.1 Genetic Nomenclature

The genotypes of flies used in this chapter are listed in Paragraph 3.3.2.
Nomenclature guidelines are described in Paragraph 2.3.1.

3.3.2 Fly Stocks

Table 39 Fly Stocks of Chapter 3

Genotype	Source
iso^{31}	Kind gift from Dr. Kyunghee Koh
$w;;slo^{E366G}/TM6B,Tb$	This thesis
$w;;slo^{loxP}/TM6B,Tb$	This thesis
$w;OK371\text{-}Gal4,UAS\text{-}GCaMP6M;$	Kind gift from Dr. Stefan Pulver

3.3.3 Fly Husbandry

Unless otherwise indicated, all fly stocks were maintained on standard fly food at
RT. The recipe of the standard fly food is shown in Table 4. All flies and larvae
used for behavioural experiments were maintained at 25ºC on a 12 h light:12 h
dark cycle.

3.3.4 Experimental Genotypes

Unless otherwise indicated, recombinant *25.1.1/TM6B,Tb* was used as a
representative for $slo^{E366G}/TM6B,Tb$, and recombinant *132.1.1/TM6B,Tb* as a
representative for $slo^{loxP}/TM6B,Tb$.

3.3.4.1 $slo^{E366G}/+$ and $slo^{loxP}/+$

$slo^{E366G}/+$ and $slo^{loxP}/+$ larvae and adults were generated by crossing
$slo^{E366G}/TM6B,Tb$ and $slo^{loxP}/TM6B,Tb$ to isogenic controls (iso^{31}), respectively.

3.3.4.2 Live-imaging

To generate *OK371-Gal4,UAS-GCaMP6M/+;slo^{E366G}/+* and *OK371-Gal4,UAS-
GCaMP6M/+;slo^{loxP}/+*, *OK371-Gal4,UAS-GCaMP6M* was crossed to
$slo^{E366G}/TM6B,Tb$ and $slo^{loxP}/TM6B,Tb$, respectively.

3.3.5 Pupal Morphology Analysis

Pupae were collected from vials kept at 25ºC, aligned above a ruler, and pictures taken with an iPhone 8 (Apple Inc.) through a stereomicroscope. Images were loaded into FIJI for analysis (Schindelin et al., 2012): width and length were measured in pixels and the results converted to mm in Microsoft Excel (Microsoft Excel for Mac, v 16.22). The data were loaded into RStudio (RStudio Inc., v. 1.2.1335), using R (v. 3.6.0) to perform statistical tests and data visualisation. The same versions of R and RStudio were used throughout this chapter.

3.3.6 Larval Video-recordings

Larvae were age-matched by restricting parental egg laying to a period of 24 h. 4 days after egg-laying, wandering L3 larvae were collected: the walls of food vials containing the larvae were cleared so as to avoid collecting pupariating larvae, before filling the vials with 20% sucrose solution (EMD Millipore, 5737-1KG), causing larvae to float to the surface due to buoyancy. After 10 min, larvae were poured into separate containers, gently collected with a paint brush, and cleaned with Milli-Q water. Following this, larvae were gently dried using Precision Wipes (KIMTECH SCIENCE, 7552) and placed onto a large surface coated with 2% agar (Sigma-Aldrich, A1296-1KG), located in an incubator (LSM) at 25ºC and a relative humidity between 50% and 55%. Videos of individual larvae were taken with the open-source Android Open Camera app (available at https://opencamera.sourceforge.io/) on a Samsung S5 mobile phone at 15 fps and 640x480 resolution. Videos were taken between 2:15 pm and 8:15 pm. The order in which genotypes were recorded was inverted between experimental repeats, to avoid circadian confounds.

3.3.7 Pre-processing of Larval Videos

Larval videos were cropped from 10 s to 70 s (duration = 1 min), allowing for 10 s of acclimatisation. The audio information was removed from videos in order to reduce file size. Cropping and removal of the audio information were performed on the Unix command line using the open-source software FFmpeg (v. 4.1.1, available at http://ffmpeg.org/) via the bash script shown in Table 40.

Table 40 Pre-processing of Larval Videos

```bash
#!/bin/bash
# for each video, remove sound
for i in $(echo *.mp4); do
  ffmpeg -i $i -an $j\_nosound.mp4
done
# for each silent video, crop from 10 s to 70 s
for i in $(echo *_nosound.mp4); do
  ffmpeg -i $i -ss 00:00:10.0 -t 00:01:00.0 \
  ./cropped/$i\_cropped.mp4
done
exit
```

For downstream analyses, it is important for each video to have the same number of frames. This was confirmed by using the bash script shown in Table 41, determining each video to consist of 900 frames.

Table 41 Retrieval of Video Frame Numbers

```bash
#!/bin/bash
# display frame number for each cropped video file
for i in $(echo *.mp4); do
  ffprobe -v error -select_streams v:0 -show_entries 3 \
  stream=nb_frames \
  -of default=nokey=1:noprint_wrappers=1 $i
done
exit
```

3.3.8 Tacking Larval Locomotion

Pre-processed larval videos were used for video-tracking with the desktop version of the AnimApp video tracker, available at https://github.com/sraorao/ (Rao et al., 2019). To execute Python scripts from the Unix command line, Python v. 2.7.15 was used (http://www.python.org). First, the optical threshold values for each genotype were identified via set_thresholds_v5.py. The code of

set_thresholds_v5.py adjusts the hue, saturation, and value (HSV) for each of the videos, in order to establish the maximum contrast between the larvae and the background, facilitating accurate tracking. The HSV values used are shown in Table 42.

Table 42 HSV Values for Larval Tracking

Parameter	Value
Hue Lower	0
Saturation Lower	0
Value Lower	176
Hue Upper	179
Saturation Upper	255
Value Upper	255

These values were used as input parameters for the tracking function opencv_colour_tracking_v12.py, whose output, including x- and y-positions over time, was used for the analysis of larval locomotion (Paragraph 3.3.9).

3.3.9 Analysis of Larval Locomotion

A customised R script was used to analyse the video-tracking data generated by AnimApp (Paragraph 3.3.8). This script is available on GitHub: https://github.com/PatrickKratsch/. It loads the AnimApp output files (CSV files) for each genotype into R, binds the x- and y-positions into a single data object, and confirms via exploratory plotting of the x- and y-values that each larva was accurately tracked. It then calculates the Euclidean distance travelled between consecutive frames via the Pythagorean Theorem as shown in Table 43.

Table 43 Calculation of Larval Locomotion

$$distance\ travelled = \sqrt{(x_2 - x_1)^2 + (y_2 - y_1)^2}$$
$$(x_1, y_1) = initial\ position\ of\ larva$$
$$(x_2, y_2) = larval\ position\ upon\ displacement\ between\ two\ frames$$

Total larval displacement is then calculated as the sum of consecutive frame displacements. This value was converted from pixels (default) to mm by interactively measuring a reference scale of 3 cm using the function set_thresholds_v5.py. For the videos analysed in this chapter, 3 cm correspond to 109 pixels. Hence, dividing the total distance in pixels by 3.63 pixels/mm yields the total distance in mm. In order to plot normalised paths for each larva, larval starting positions were subtracted from individual (x, y) positions for each frame. For the analysis of larval lengths and widths, the frame-wise length and width values of the tracked object were extracted from the AnimApp output data. The mean lengths and widths were calculated by taking the average of the larval lengths and widths over the course of the whole 1-min video recordings. Larval peristalsis was visualised by extracting the larval length via the same means and plotting it over time. Turning behaviour was calculated by dividing larval width by larval length, generating a novel parameter that increases prior to larval turning. By manually inspecting 30 videos, I identified a threshold value of 0.4 for the width:length ratio as a reliable indicator for larval turning. The width:length ratio was then plotted over time, and I manually counted how often the 0.4 threshold was crossed for each larva. This analysis was performed blinded to genotype.

3.3.10 Larval Morphology Analysis

To analyse larval length and width manually, wandering L3 larvae were collected and snap-frozen at -80°C for 30 min. Using fine forceps (#5, Dumont, 0103-5-PO), larvae were gently stretched to their maximum length from anterior (mouth hooks) to posterior (spiracles). All larvae were dead at this stage. Data analysis was performed as described in Paragraph 3.3.5 for pupal morphology.

3.3.11 Live-imaging of Larval Motoneurons

Wandering L3 larvae of genotypes *OK371-Gal4,UAS-GCaMP6M/+;slo^{E366G}/+* and *OK371-Gal4,UAS-GCaMP6M/+;slo^{loxP}/+* were collected from within the food and dissected in the recording solution shown in Table 44 (pH = 7.15), as adapted from (Pulver et al., 2015) and (Streit et al., 2016).

Table 44 Recording Solution for Live-imaging

Reagent	Concentration (mM)
NaCl	135
KCl	5
MgCl$_2$	4
CaCl$_2$	2
TES	5
Sucrose	36

Larvae were submerged in the recording solution during the dissection. Using fine forceps, the entire larval CNS (consisting of two brain lobes, the subesophageal zone, and the VNC) was gently removed and attached to a glass-bottom dish (CELLview, GBO, 627860) coated with poly-L-lysine (Sigma Aldrich, P4832-50mL). The glass-bottom dish contained the same recording solution as described in Table 44. Because an inverted confocal microscope was used for image acquisition, the dorsal side of the larval VNC was oriented to face the poly-L-lysine-covered bottom of the glass-bottom dish – this is necessary due to the dorsal location of MNs within the VNC. Larval dissections were performed immediately prior to image acquisition, and samples were imaged within 5 min after dissection. Image acquisition was performed on a Zeiss LSM 710 confocal microscope, using the Zen software (Zeiss). 5-min time series were recorded at 20x magnification, using the EC "Plan-Neofluar" 20x/0.50 M27 air objective (Zeiss, 420350-9900-000). The frame size was 256x256 pixels and the bit depth 8 bit. The scan time was 390.98 ms per frame, with 200 ms intervals between scans. The pinhole was maximally opened, so as to capture fluorescence from multiple focal planes. An Argon laser at 488 nm (A488) was used to excite GCaMP6M, which has an excitation wavelength of 450-490 nm (Chen et al., 2013).

3.3.12 Analysis of Live-imaging Data

Live-imaging data analysis was performed blinded to genotype and adapted from (Pulver et al., 2015) and (Streit et al., 2016). To analyse MN activity, using FIJI (Schindelin et al., 2012), regions of interest (ROIs) were drawn around MN axon

bundles innervating segments 7 and 4 on each side of the VNC (left and right), and fluorescence activity measured over time. The ROI area was kept constant at 115.809 μm^2. The background fluorescence was measured via an additional ROI placed at the upper left-hand corner of the image. The resulting fluorescence values were exported from FIJI into Microsoft Excel for further analysis (Microsoft Office 365, v. 16.24). First, the background fluorescence was subtracted from all other fluorescence values. Next, the frame number was converted into time (in ms) by multiplying it by 590.98 ms, the duration of each frame (Paragraph 3.3.11), resulting in fluorescence time series for ROIs from 4 segments: ROI 4 left (4L), ROI 4 right (4R), ROI 7 left (7L), and ROI 7 right (7R). To visualize the data and prepare them for analysis, the following five ROI fluorescence values were plotted over time: (1) 4L, (2) 4R, (3) 4L and 4R, (4) 4L and 7L, and (5) 4R and 7R – generating 5 individual plots. Using a manual counting approach, 4 parameters were analysed: (1) the fluorescence amplitude of Ca^{2+} spikes in segment 4 that occurred during forward peristaltic movements – forward peristaltic movements were identified as synchronous Ca^{2+} spikes on both sides of segment 4 that were preceded by synchronous Ca^{2+} spikes on both sides of segment 7 (posterior-to-anterior Ca^{2+} activity); (2) the frequency of Ca^{2+} spikes identified in (1); (3) the time interval between Ca^{2+} spikes in segments 7 and 4 during forward peristaltic movements; (4) the number of turn initiations, as identified by anti-correlated Ca^{2+} fluorescence between each side of segment 4. Parameters (1) and (3) were quantified for each side of the VNC (left and right) separately. For these analyses, only the first 508 video frames were used, which corresponds to 300217.84 ms. For simplicity, this duration is referred to as 5 min, ignoring the additional 217.84 ms.

3.3.13 Scoring Wing Inflation

Pictures of adult flies were taken with an iPhone 8 (Apple Inc.) through a stereomicroscope. Three separate wing phenotypes were scored and quantified manually: (1) non-inflated wings, (2) semi-inflated wings, and (3) fully inflated wings.

3.3.14 Adult Video Recordings

Flies were video-recorded inside 65-mm long, food-containing glass tubes (TriKinetics), which were attached to an even surface using Blu Tack (Bostik). To prepare the glass tubes with food, a solution of 2% agar (w/v, Sigma Aldrich, L2897-1KG) and 4% sucrose (w/v, EMD Millipore, 5737-1KG) was homogenised by heating in a microwave, followed by pouring it into a plastic tray, into which clean glass tubes were placed vertically. Once the food had cooled and solidified, the food-containing glass tubes were cleaned and the food-containing sides sealed with liquified paraffin wax (Sigma Aldrich, 327204-1KG). Flies were anaesthetised on CO_2 pads (Flystuff, Genesee Scientific) and loaded into the prepared glass tubes, which were then sealed with cotton. Loaded glass tubes were positioned in an incubator (LMS) and videos recorded using a USB-webcam (Logitech c920 HD pro) at a 12 h light:12 h dark regime at 25°C and an average humidity of 65% to 70%. The infrared filter of this webcam was manually removed to allow for recordings in darkness. Flies were acclimatised to the new environment for at least 24 h. Flies were between 3 and 6 days old at the time of recording.

3.3.15 Tracking Adult Locomotion

Adult video-tracking was performed with the *Drosophila* ARousal Tracker (DART) system, a MATLAB-based offline video-tracker (Faville et al., 2015), using videos recorded as described in Paragraph 3.3.14 as input files. The tracking algorithm outputs CSV files containing the x- and y-positions for each fly over time.

3.3.16 Analysis of Adult Locomotion

A customised R script was used to analyse the DART video-tracking data, which is available on GitHub: https://github.com/PatrickKratsch/. This script first creates an "offset table" from the DART tracking data, obtained by subtracting successive x- and y-values. Hence, the offset table defines the displacement for each fly between consecutive frames. The total distance travelled between consecutive frames was calculated for each fly as described for the analysis of larval locomotion, using the Pythagorean Theorem (Table 43). Summing all frame-to-frame displacements over 12 h yielded the total distance travelled during this

period. Flies that did not move during the second half of the experiment (hours 7 to 12) were identified as dead and excluded from further analysis. Of note, the precise duration analysed was 716 min (11 h and 56 min) due to the removal of 2 min post-lights-on and 2 min pre-lights-off, during which the lighting conditions prevented appropriate video-tracking. For simplicity, I refer to 716 min as 12 h. The analyses of movement parameters other than total distance travelled are based on a period of 1 h after the dark-light transition (9:02 am – 10:02 am). To analyse the distribution of locomotor speed, empirical cumulative distribution plots were generated based on 1-s movement bins (3600 bins for a 1-h period). To analyse movement initiation, a sliding window of length 2 quantified how often a 1-s bin of non-movement was followed by a 1-s bin of movement. To analyse the mean bout length, the fly movement data were transformed into a binary matrix, with 1's indicating movement and 0's non-movement. Subsequently, the lengths of movement streaks (streaks of 1's) were extracted and averaged.

3.3.17 Adult Life Span Analysis

110 $slo^{E366G}/+$ and 100 $slo^{loxP}/+$ males were age-matched by emptying parental vials < 12 h prior to the start of the experiment. These males were then housed with an excess number of females for 48 h before the start of the experiment, increasing the probability of mating. $slo^{E366G}/+$ and $slo^{loxP}/+$ males were then separately placed into standard food vials in groups of 10. These vials were flipped onto fresh food every 2 days, counting dead flies in the process.

3.3.18 Statistics

Statistical tests were performed in R using RStudio. For comparisons between two groups, Mann-Whitney-Wilcoxon tests were performed using the function `wilcox.test`. For multiple comparisons, Kruskal-Wallis tests were performed to confirm a difference between groups, using the `kruskal.test` function. A Dunn's post-hoc test was performed to identify which comparisons were significant, using the `dunnTest` function from the FSA package (Ogle, D.H. 2018. FSA: Fisheries Stock Analysis. R package, v. 0.8.20). To adjust p-values for multiple comparisons, the Holm method was used (default). To test for differences between two continuous distributions, a Kolmogorov-Smirnov test was

performed, using the `ks.test` function. For data not analysed by me, the figure caption indicates the analyses performed.

3.3.19 Data Visualisation

Figures were generated in R and RStudio, using the ggplot2 package (Wickham, ggplot2: Elegant Graphics for Data Analysis, 2016). Figures were arranged in Microsoft PowerPoint (Mac, v. 16.24, Office 365), and exported as JPG files at 300 dpi. Boxplots are drawn according to Tukey: the lower hinge corresponds to the first-, the upper hinge to the third quartile. The upper whisker reaches to the largest value less than or equal to 1.5-times the inter-quartile range (IQR) above the third quartile hinge. The lower whisker reaches to the smallest value larger than or equal to 1.5-times the IQR below the first quartile hinge. The median is marked within the box by an additional line. Figures generated by Dr. James Jepson plot the mean and standard error of the mean (SEM).

3.4 Results

3.4.1 *slo^{E366G}/slo^{E366G}* Alters Pupal Morphology

In order to study the effects of the *slo^{E366G}* allele at the organismal level, I first undertook a morphological examination of homozygotes for the mutant allele. Homozygous *slo^{E366G}/slo^{E366G}* larvae were very rare. Under good stock conditions, occasional *slo^{E366G}/slo^{E366G}* larvae developed to the L3 stage and successfully pupated. However, these pupae looked misshapen compared to *slo^{loxP}/slo^{loxP}*. Moreover, *slo^{E366G}/slo^{E366G}* pupae were significantly longer and thinner than their *slo^{loxP}/slo^{loxP}* counterparts (Figure 3.1). Importantly, none of the *slo^{E366G}/slo^{E366G}* pupae eclosed, rendering the *slo^{E366G}* allele homozygous lethal by the adult stage. A conventional parameter used to describe pupal dimensions is the axial ratio – pupal length divided by pupal width – and it has been reported that the popular wild-type strains *w^{1118}* and *Oregon R* have a mean axial ratio of 3.0 ± 0.1 (Guan et al., 2006). The axial ratio of *slo^{E366G}/slo^{E366G}* pupae was significantly greater than the axial ratio of *slo^{loxP}/slo^{loxP}* pupae, with a median axial ratio of 4.4 (*slo^{E366G}/slo^{E366G}*) compared to 3.2 (*slo^{loxP}/slo^{loxP}*) – the latter being close to the reported wild-type average (Figure 3.1) (Guan et al., 2006).
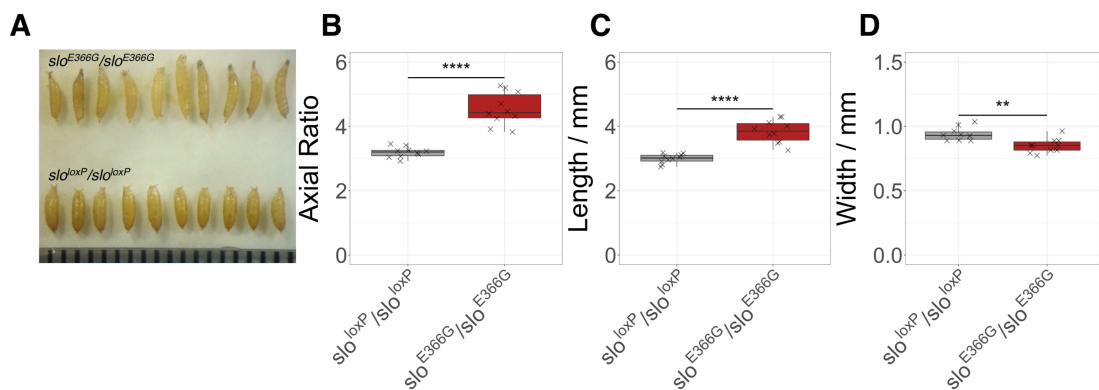
Figure 3.1 *slo^{E366G}/slo^{E366G}* Alters Pupal Morphology

Homozygous *slo^{E366G}/slo^{E366G}* pupae exhibit severe morphological abnormalities, as shown in **A**. The ruler at the bottom in **A** indicates steps in mm. (**B**) *slo^{E366G}/slo^{E366G}* pupae showed a significantly increased axial ratio, defined as pupal length divided by pupal width. Looking at these parameters in isolation showed that *slo^{E366G}/slo^{E366G}* pupae were significantly thinner (**C**) and longer (**D**) than *slo^{loxP}/slo^{loxP}* (**B**). (n = 10; Mann-Whitney-Wilcoxon test; **** = p < 0.0001, ** = p < 0.01)

3.4.2 slo^{E366G}/+ Affects Larval Locomotion

GEPD patients exhibit PxD and/or epilepsy in the presence of a heterozygous *KCNMA1^{D434G}* allele (Du et al., 2005). Hence, a key question is whether motor control is also affected in the GEPD fly model. To investigate this possibility, I performed video-tracking of individual age-matched slo^{E366G}/+ and slo^{loxP}/+ L3 larvae and compared the total distances travelled during 1 min. Three independent recombinants per genotype were used for these experiments, in order to account for potential genetic background effects. The following slo^{E366G}/+ recombinants were used: *25.1.1/+*, *137.1.3/+*, and *72.1.1/+*. For slo^{loxP}/+, the following three recombinants were used: *132.1.1/+*, *111.1.1/+*, and *7.1.1/+* (Figure 2.15). To analyse the video-recordings, a novel video-tracking software called AnimApp was used (Rao et al., 2019), as illustrated in Figure 3.2.
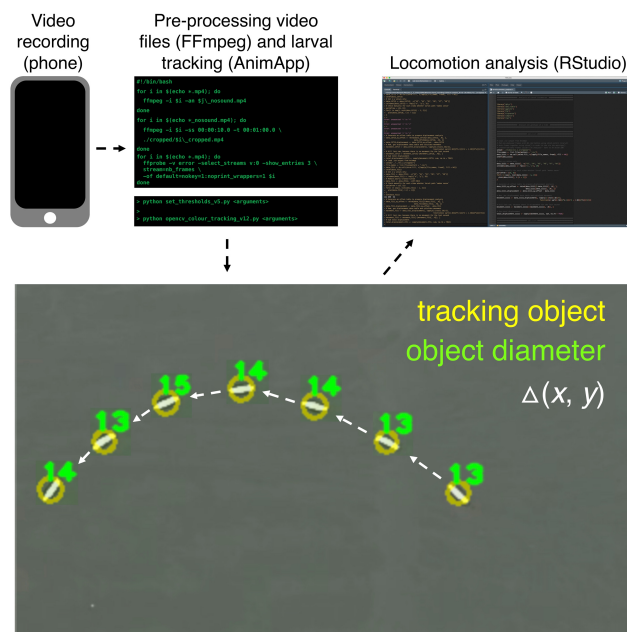
Figure 3.2 Pipeline for Larval Video-tracking

This figure illustrates how larval videos were taken (using a mobile phone), pre-processed (on the Unix command line using FFmpeg), how larvae were tracked (with the AnimApp software), and the resulting tracking data analysed (using customised R scripts in RStudio). At the bottom, the movement of a single larva is shown. The green numbers represent the larval diameter in pixels. White arrows indicate the larval trajectory. The larval genotype shown is slo^{loxP}/+ (recombinant *132.1.1/+*). The AnimApp video-tracking algorithm is available at https://github.com/sraorao/ (Rao et al., 2019).

L3 larvae were individually recorded for 1 min, and the resulting video files pre-processed on the Unix command line, before tracking larval movement using AnimApp (Figure 3.2) (Rao et al., 2019). The output CSV files contain the larval x-y positions for each video frame – amongst other information, such as the length and width of the tracked object. In order to confirm that the larvae had been properly tracked, I plotted their x-y trajectories manually and appraised whether they were physically possible (Figure 3.3). Only 1 out of 164 larvae was not tracked properly, and this larva, of genotype *72.1.1/+*, was excluded from further analyses (Figure 9.1).
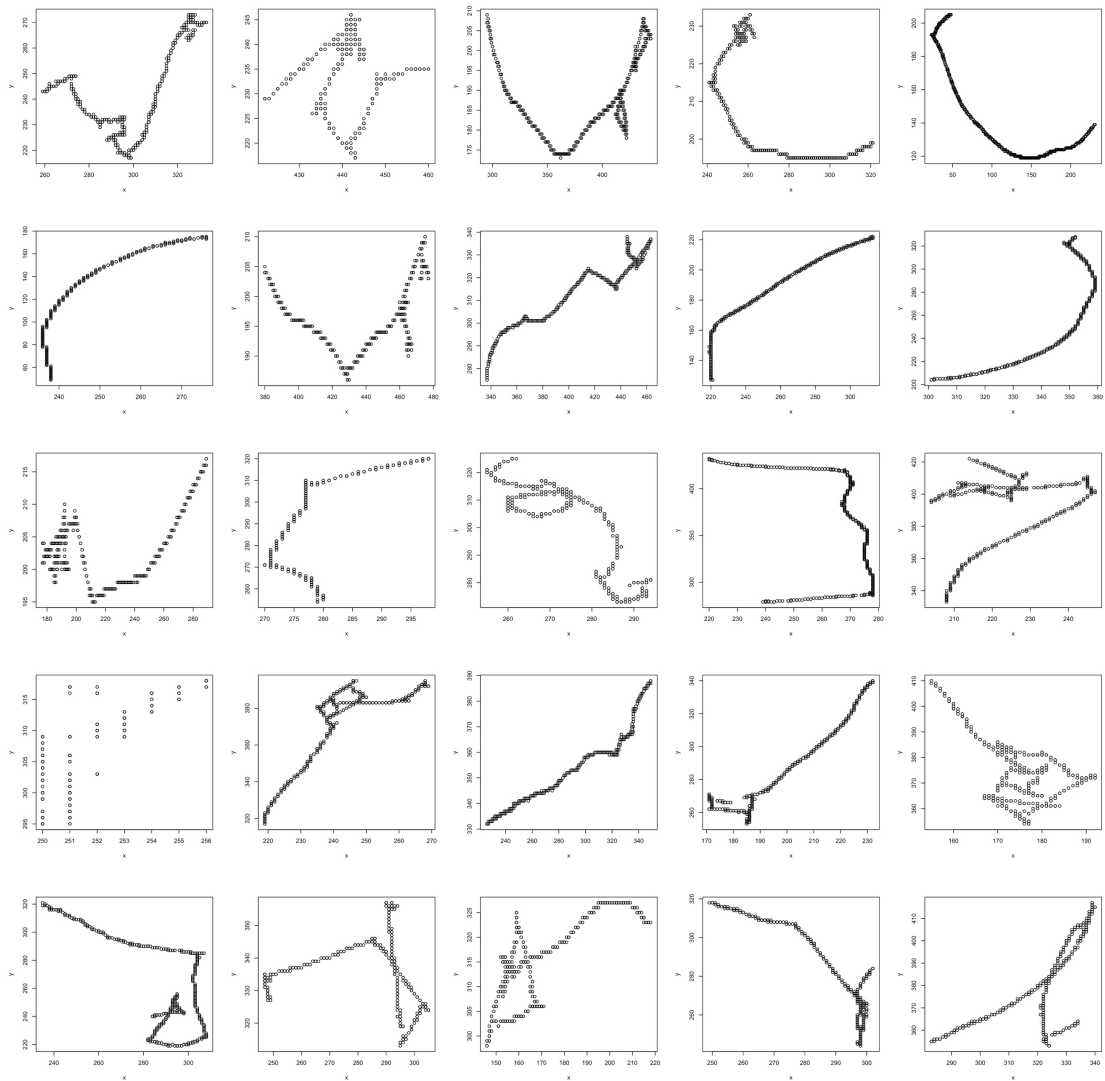
Figure 3.3 Exploratory Analysis of Larval Locomotion

Larval trajectories for each of the 164 recorded larvae were plotted in order to confirm proper tracking. This figure illustrates the procedure for 25 larvae of genotype $slo^{loxP}/+$ (recombinant *132.1.1/+*). Each graph plots larval x-y positions in pixels. The duration of each path is 1 min. 1 out of 164 larvae was identified as poorly tracked and excluded from further analyses (Figure 9.1).

The remaining 163 larvae were used for the quantification of total distance travelled during 1 min, demonstrating that $slo^{E366G}/+$ larvae moved significantly shorter distances than $slo^{loxP}/+$ larvae, while no within-genotype differences were observed (Figure 3.4). The reduction in mean travelling distance exhibited by $slo^{E366G}/+$ larvae was ~2-fold after pooling the recombinants by genotype (32.9 mm for $slo^{E366G}/+$ vs 66.3 mm for $slo^{loxP}/+$). Plotting the normalised trajectories of two representative recombinants per genotype, *25.1.1/+* for $slo^{E366G}/+$ and

132.1.1/+ for *slo^{loxP}/+*, illustrates the locomotor defect of *slo^{E366G}/+* larvae (Figure 3.4). Of note, the directionality of larval movement for each genotype appears to be random, suggesting a sufficiently homogenous recording environment (Figure 3.4).
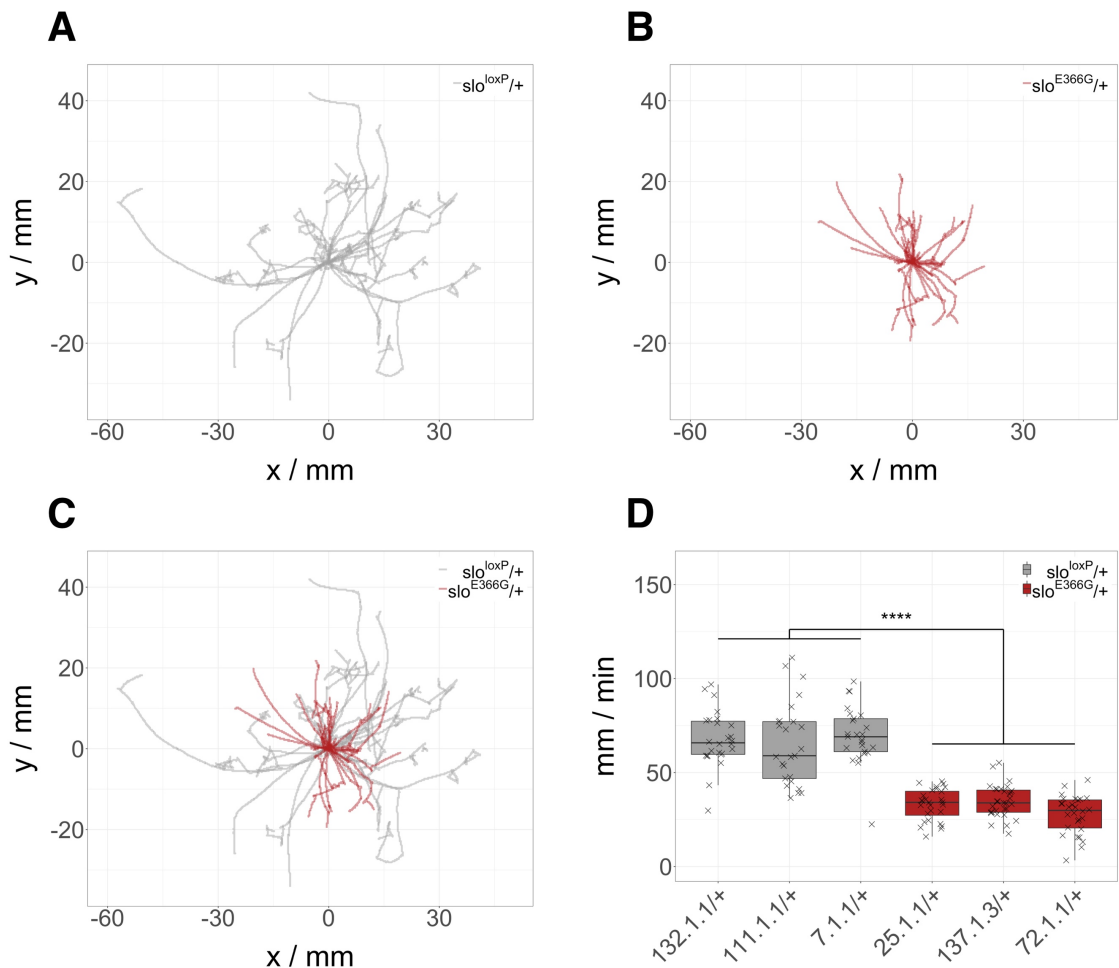
Figure 3.4 *slo^{E366G}/+* Reduces Larval Travelling Distance

Normalised larval trajectories of two representative recombinants per genotype are illustrated: (**A**) *slo^{loxP}/+* (recombinant *132.1.1/+*, 28 larvae) and (**B**) *slo^{E366G}/+* (recombinant *25.1.1/+*, 26 larvae), illustrating that *slo^{loxP}/+* larvae travel farther than *slo^{E366G}/+* larvae (**C**). (**D**) Total distance travelled during 1 min was quantified for three separate *slo^{loxP}/+* and three separate *slo^{E366G}/+* recombinants. *slo^{E366G}/+* larvae moved significantly shorter distances than *slo^{loxP}/+* larvae. No within-genotype differences were observed. Data from two independent experimental repeats were pooled. (n= 25-31; Kruskal-Wallis multiple comparison with Dunn's post-hoc test; **** = $p < 0.0001$)

I proceeded to investigate whether the *slo^{E366G}* allele affects larval peristalsis. To this end, I manually plotted larval length over time for each of the 163 larvae and

inspected the resulting graphs for qualitative differences. The change of larval length over time was used as an indicator for larval peristalsis because larval contractions and expansions occur along the direction of this axis. A similar parameter, larval area over time, was recently used for the same purpose (Otto et al., 2018). Figure 3.5 shows representative examples for one $slo^{E366G}/+$ larva (*25.1.1/+*) and one $slo^{loxP}/+$ larva (*132.1.1/+)*, suggesting that the peristaltic frequency of the $slo^{E366G}/+$ larva is reduced, which would provide a possible explanation for the reduction in travelling distance (Figure 3.4). However, these traces also suggest that the peristaltic amplitude of the $slo^{E366G}/+$ larva is increased, which would have the opposite effect. Hence, quantitative analyses need to be performed, in order to draw definitive conclusions about changes in peristaltic behaviour.
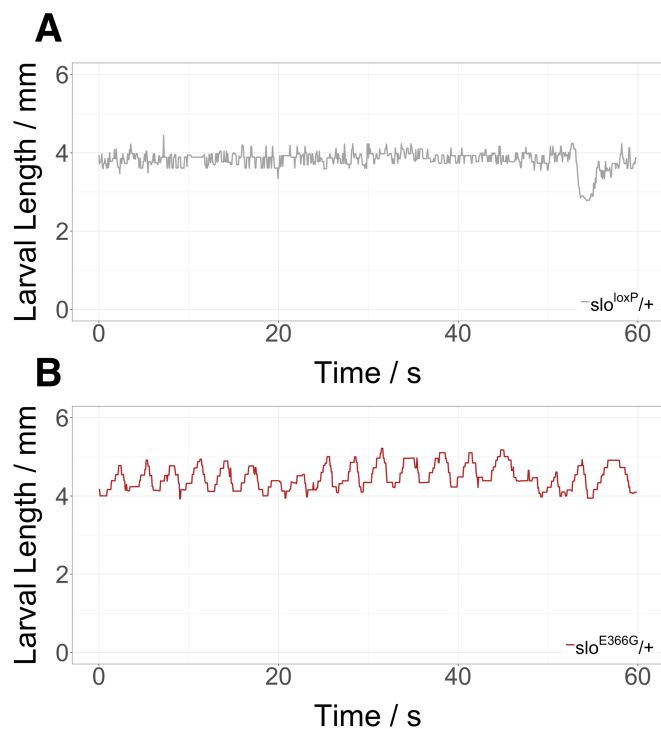
Figure 3.5 $slo^{E366G}/+$ Might Affect Larval Peristalsis

Larval length is plotted over time for one representative $slo^{loxP}/+$ larva (**A**, recombinant *132.1.1/+*) and one representative $slo^{E366G}/+$ larva (**B**, recombinant *25.1.1/+*). These traces suggest that $slo^{E366G}/+$ larvae exhibit a reduced peristaltic frequency and an increased peristaltic amplitude. The dip at the end of trace **A** represents the initiation of a larval turn, which is preceded by a decrease in larval length due to larval retraction.

Careful inspection of Figure 3.5 suggests that *slo^{E366G}/+* larvae have an increased baseline length compared to *slo^{loxP}/+*. A difference in larval size could indicate that the *slo^{E366G}* allele affects larval metabolism. GLUT1-DS and PED are both linked to mutations in *SLC2A1*, associating glucose metabolism with PxD and epilepsy (De Giorgis and Veggiotti, 2013) (Paragraph 1.2.1.3). Hence, I wondered whether there could be a link between altered metabolism and GEPD that affects larval size. To investigate this possibility, I extracted the median larval lengths and widths from the AnimApp tracking data for each larva, before pooling these values by genotype for statistical comparison. Indeed, *slo^{E366G}/+* larvae exhibited a significantly greater median length than *slo^{loxP}/+* larvae (Figure 3.6). There is also a non-significant trend towards an increased median width of *slo^{E366G}/+* larvae (Figure 3.6).
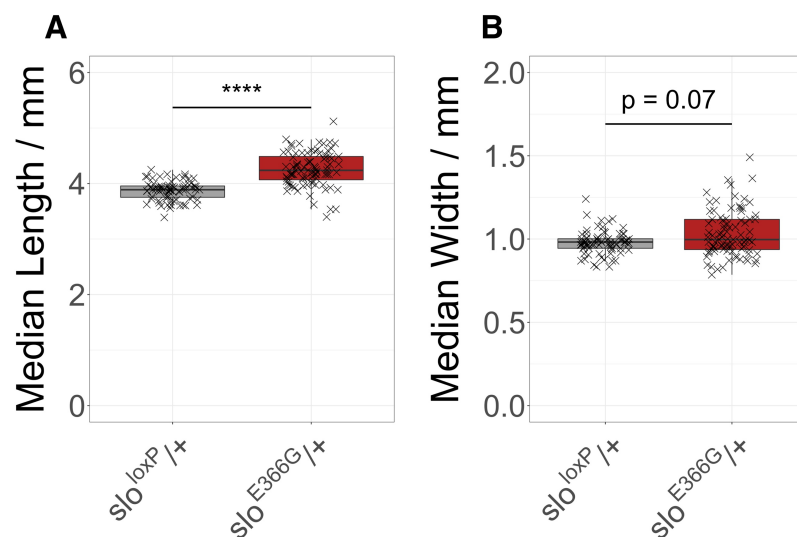
Figure 3.6 *slo^{E366G}/+* Alters Larval Dimensions

The median larval lengths and widths for three separate *slo^{loxP}/+* recombinants (*132.1.1/+, 111.1.1/+, 7.1.1/+*) and three separate *slo^{E366G}/+* recombinants (*25.1.1/+, 137.1.3/+, 72.1.1/+*) were calculated from the AnimApp video-tracking data, and pooled by genotype. *slo^{E366G}/+* larvae exhibit a significantly greater median length than *slo^{loxP}/+* larvae (**A**), in addition to a non-significant trend towards increased width (**B**). (n = 76-87; Mann-Whitney-Wilcoxon test, **** = p < 0.0001)

Figure 3.6 raises the question whether *slo^{E366G}/+* larvae are actually larger than *slo^{loxP}/+*, or whether the difference observed via video-tracking is due to an effect of the *slo^{E366G}* allele on larval contractility. One could imagine that an inability of

larval MNs to properly contract body wall muscles might result in more outstretched larvae. To address this question, I measured the lengths and widths of wandering slo^{E366G}/+ and slo^{loxP}/+ larvae manually. As shown in Figure 3.7, the quantified results are congruent with Figure 3.6, suggesting that the increase in slo^{E366G}/+ larval dimensions is due to an actual difference in size between genotypes.
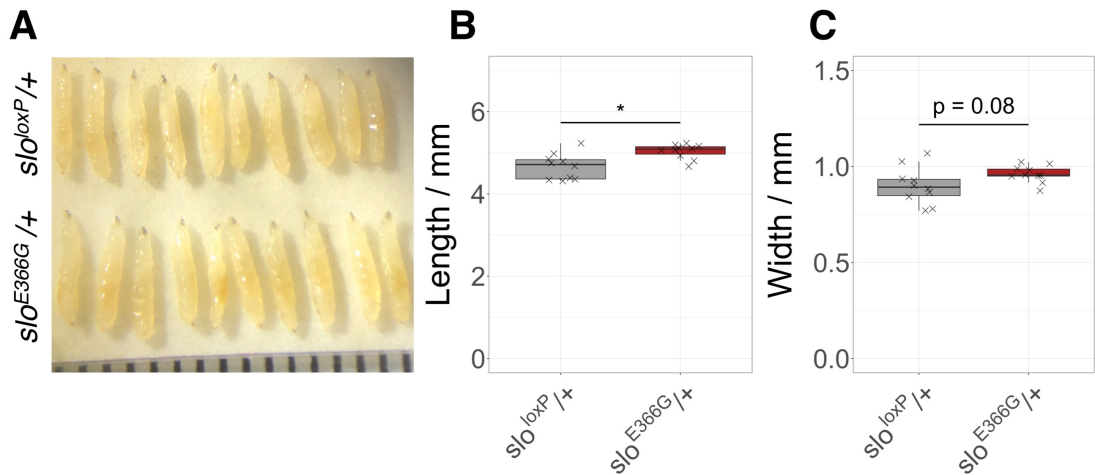
Figure 3.7 slo^{E366G}/+ Alters Larval Dimensions: Additional Evidence

(**A**) Wandering L3 larvae of genotypes slo^{loxP}/+ and slo^{E366G}/+ were snap-frozen at -80ºC and manually stretched to their maximal length. A ruler at the bottom marks steps in mm. (**B**) slo^{E366G}/+ larvae were significantly longer than slo^{loxP}/+ larvae, with a non-significant trend towards increased width of slo^{E366G}/+ larvae as well (**C**). (n = 10; Mann-Whitney-Wilcoxon test; * = p < 0.05)

Careful inspection of the larval traces in Figure 3.4 further suggests that slo^{E366G}/+ larvae might turn less frequently than slo^{loxP}/+. Since turning is a form of action selection, investigating this behaviour has clinical relevance due to its impairment in dyskinesia and other movement disorders (Kandel et al., 2013; Ryan et al., 2018). As it proved difficult to manually count turns from larval traces shown in Figure 3.4, I resorted to take another approach: larvae decrease in length before turning, because they retract before advancing into a different direction. Dividing the larval width by larval length yields a parameter that increases prior to turning events – due to a decreasing denominator. To identify a larval width:length ratio that can serve as a reliable indicator for larval turning, I manually counted larval turns in 30 video-recordings and found that a threshold value of 0.4 correlated

well with larval retraction prior to turning. Hence, I quantified the number of times the larval width:length ratio crossed a threshold of 0.4 during 1 min. As shown in Figure 3.8, $slo^{loxP}/+$ larvae exhibit significantly more turns than $slo^{E366G}/+$ larvae, while there are no within-genotype effects. These data suggest that action selection is impaired in $slo^{E366G}/+$ larvae.
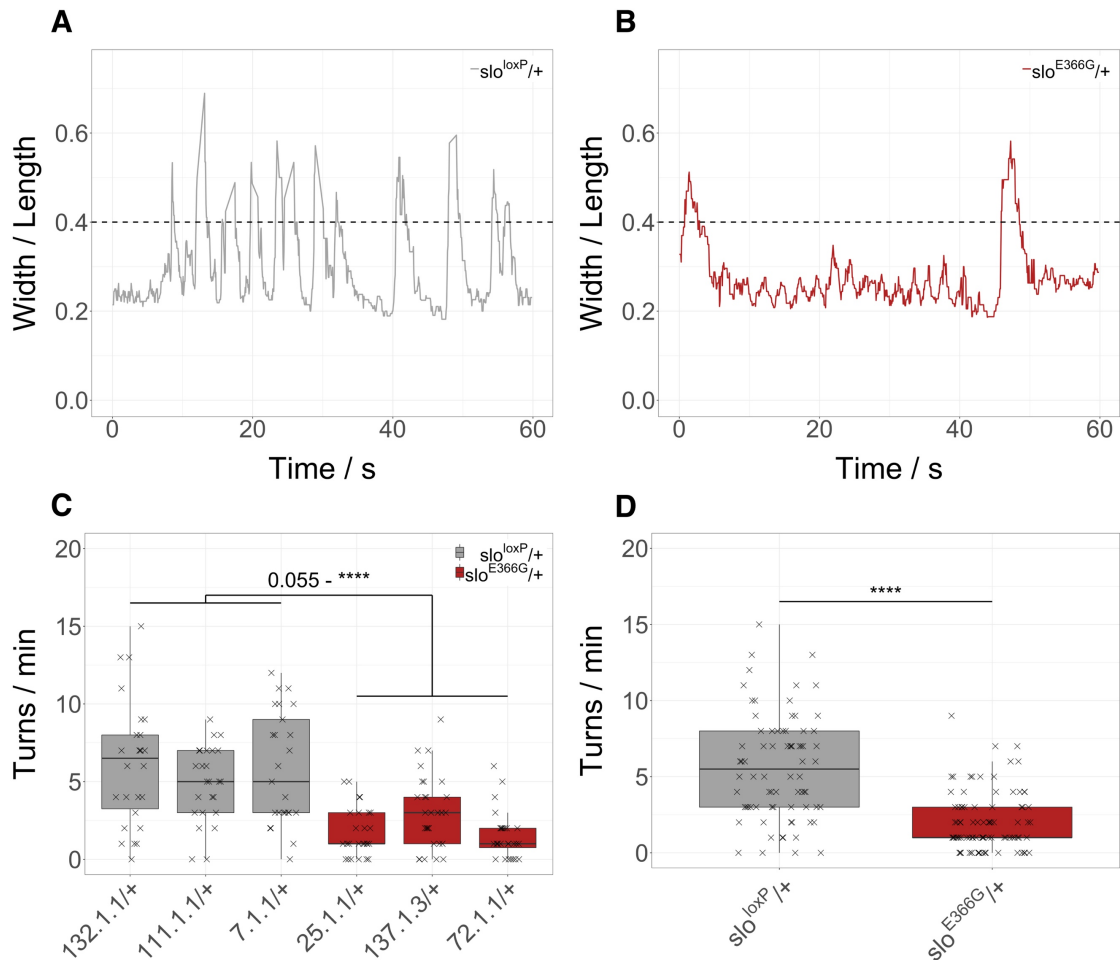
Figure 3.8 $slo^{E366G}/+$ Decreases the Number of Larval Turns

The larval width:length ratio was used to score turning behaviour. Representative traces for this parameter are shown for one $slo^{loxP}/+$ larva (*132.1.1/+*) in **A** and one $slo^{E366G}/+$ larva (*25.1.1/+*) in **B**. Peaks crossing a width:length ratio of 0.4 (dashed line) were defined as turning events and manually counted. The $slo^{loxP}/+$ larva shown exhibited 12 turns (**A**), the $slo^{E366G}/+$ larva exhibited 2 (**B**). (**C**) $slo^{E366G}/+$ larvae turned significantly less frequently than $slo^{loxP}/+$ larvae – with the exception of the comparison between *137.1.3/+* and *111.1.1/+* (p = 0.055). (n = 25-31; Kruskal-Wallis multiple comparison with Dunn's post-hoc test; **** = p < 0.0001). (**D**) Pooled $slo^{E366G}/+$ larvae turned significantly less frequently than pooled $slo^{loxP}/+$ larvae. Analyses were performed blinded to genotype. (n = 76-87; Mann-Whitney-Wilcoxon test, **** = p < 0.0001)

3.4.3 *slo^E366G/+* Does not Change NMJ Structure and Function

The decreased larval locomotion exhibited by *slo^E366G/+* (Figure 3.4) could imply larval NMJ abnormalities. Since loss of *slo* has previously been shown to affect NMJ morphology (Jepson et al., 2014; Lee and Wu, 2010) (Paragraph 1.5.3.2), the *slo^E366G/+* NMJ was investigated via confocal microscopy. Wandering *slo^E366G/+* and *slo^loxP/+* L3 larval NMJs were immuno-labelled for horseradish peroxidase (HRP), staining neuronal membrane, and Discs-large (DLG), staining post-synaptic termini. Three parameters were quantified: (1) total synapse size, (2) synaptic bouton number, and (3) synaptic bouton area – none of which showed a significant difference between genotypes (Figure 3.9).
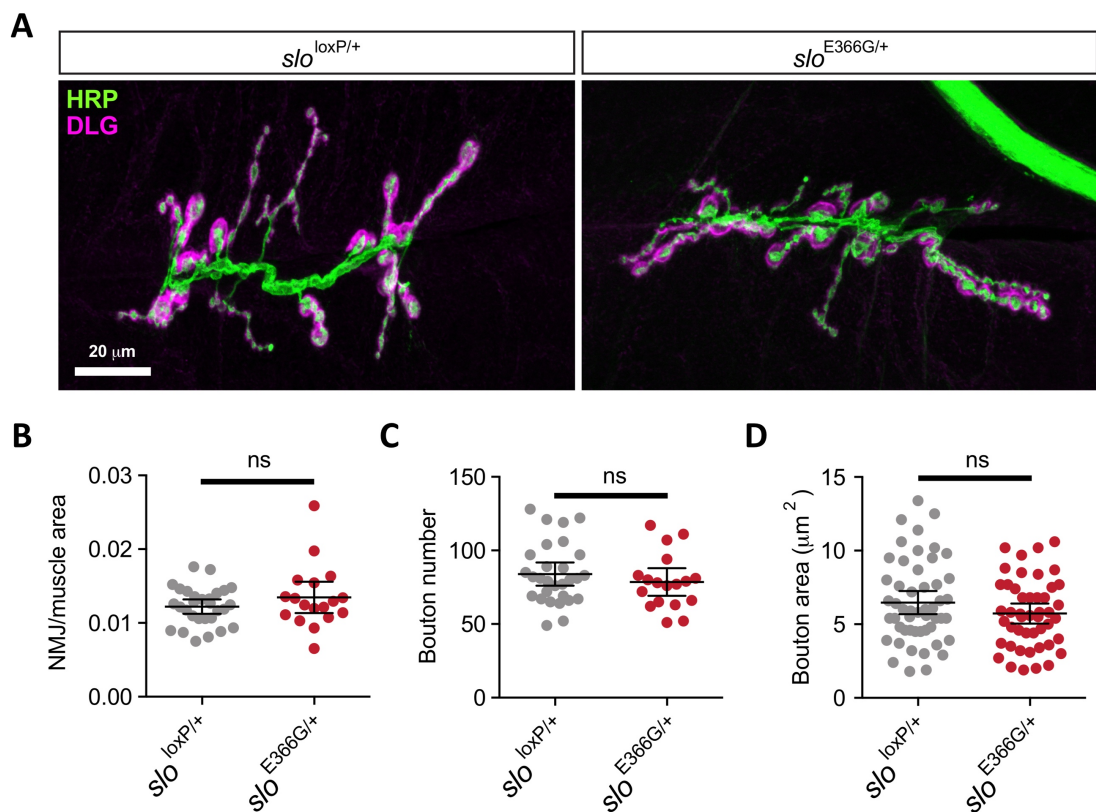
Figure 3.9 *slo^E366G/+* Does not Affect NMJ Morphology

(**A**) NMJs of wandering *slo^loxP/+* and *slo^E366G/+* L3 larvae were immuno-labelled with antibodies against HRP (green) and DLG (magenta). (**B**) Total synapse size, (**C**) synaptic bouton number, and (**D**) synaptic bouton area showed no significant differences between genotypes. The white scale bar indicates 20 μm. Data acquisition, analysis, and visualisation were performed by Dr. James Jepson. (B, C: n = 19-29; D: n = 47-51; Mann-Whitney-Wilcoxon test, ns = $p > 0.05$)

Despite an unchanged morphology for the parameters tested (Figure 3.9), $slo^{E366G}/+$ NMJs might function abnormally. As described in Paragraph 1.5.3.2, loss of *slo* has been linked to electrophysiological abnormalities at the NMJ (Ford and Davis, 2014; Jepson et al., 2014; Lee et al., 2008, 2014; Warbington et al., 1996). To investigate $slo^{E366G}/+$ NMJ function, sharp-electrode intracellular recordings from larval body wall muscles 6/7 were performed in modified HL3.1 saline at an extracellular $[Ca^{2+}]$ of 1 mM, quantifying two events: (1) excitatory junction potentials (EJPs), evoked by electrically stimulating the severed motor nerve, and (2) spontaneously occurring miniature excitatory junction potentials (mEJPs) – neither of which differed between genotypes (Figure 3.10). These data provide strong evidence for NMJ functionality to be unaffected in $slo^{E366G}/+$ larvae.
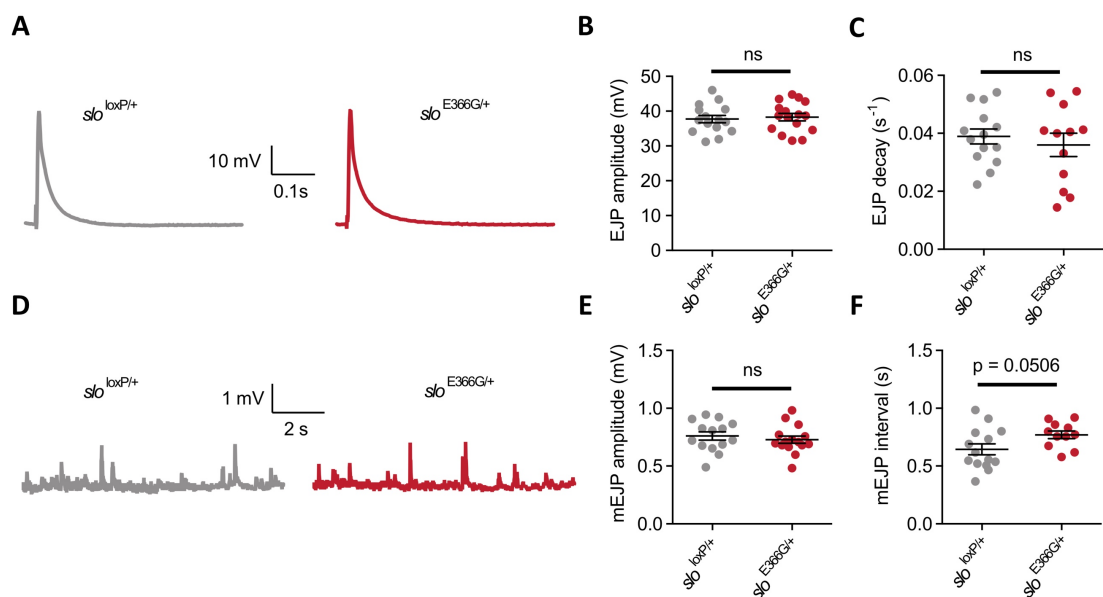
Figure 3.10 $slo^{E366G}/+$ Does not Affect NMJ Function

(**A**) Representative EJP traces from the L3 larval NMJ of $slo^{loxP}/+$ and $slo^{E366G}/+$ are shown. Neither EJP amplitude (**B**) nor EJP decay rate (**C**) differed significantly between genotypes. (**D**) Representative traces of mEJPs for both genotypes are shown. Neither mEJP amplitude (**E**) nor interval (**F**) showed significant differences between genotypes. Recordings were performed at an extracellular $[Ca^{2+}]$ of 1 mM. Data acquisition and analysis were performed by Dr. Simon Lowe. Dr. James Jepson visualised the data. (B: n = 15-16; C: n = 12-14; E: n = 14-15; F: n = 11-14; Mann-Whitney-Wilcoxon test, ns = p > 0.05)

3.4.4 *slo^E366G* is a Gain-of-function Allele *ex vivo*

It was surprising to find that the *slo^E366G* allele does not affect NMJ function (Figure 3.10), because the equivalent murine D369G mutation in *KCNMA1* has been shown to cause a gain-of-function by increasing the sensitivity of BK channels to Ca^{2+} (Yang et al., 2010). In neurons, BK channels link Ca^{2+} influx through Ca_v channels to K^+ efflux, contributing to the repolarisation of the AP (Bean, 2007). Hence, the initial hypothesis had been that this coupling of Ca^{2+} influx to K^+ efflux would be potentiated in *slo^E366G/+* MNs. This would lead to a decrease in AP width, resulting in an overall reduction of pre-synaptic Ca^{2+} influx and decreased neurotransmitter release, a Ca^{2+}-dependent process (Südhof, 2012). A decrease in neurotransmitter release from MNs was predicted to decrease the EJP amplitude in the muscle. This was not observed (Figure 3.10). However, it is possible that a gain-of-function effect of the E366G mutation is masked under an extracellular $[Ca^{2+}]$ of 1mM, used for the recordings in Figure 3.10, because both mutant and wild-type Slo might be maximally potentiated at this $[Ca^{2+}]$. Indeed, macroscopic current recordings in inside-out patch clamp mode have shown that the murine D369G mutation does not affect BK channel function at nominal zero- or saturating (100 μM) intracellular $[Ca^{2+}]$ (Yang et al., 2010). Instead, an increased Ca^{2+} sensitivity was only observed at intermediate intracellular $[Ca^{2+}]$ (Yang et al., 2010). To investigate a Ca^{2+}-dependent effect in *slo^E366G/+*, larval NMJ recordings were performed as described in Paragraph 3.4.3, but at varying extracellular $[Ca^{2+}]$: 0.15 mM, 0.25 mM, and 1 mM. Indeed, at 0.25 mM, a significant decrease in EJP amplitude was detected in *slo^E366G/+* when compared to *slo^loxP/+*, while no significant difference was observed at 1 mM (Figure 3.11). A non-significant trend towards a decreased EJP amplitude was also detected at an extracellular $[Ca^{2+}]$ of 0.15 mM (Figure 3.11).
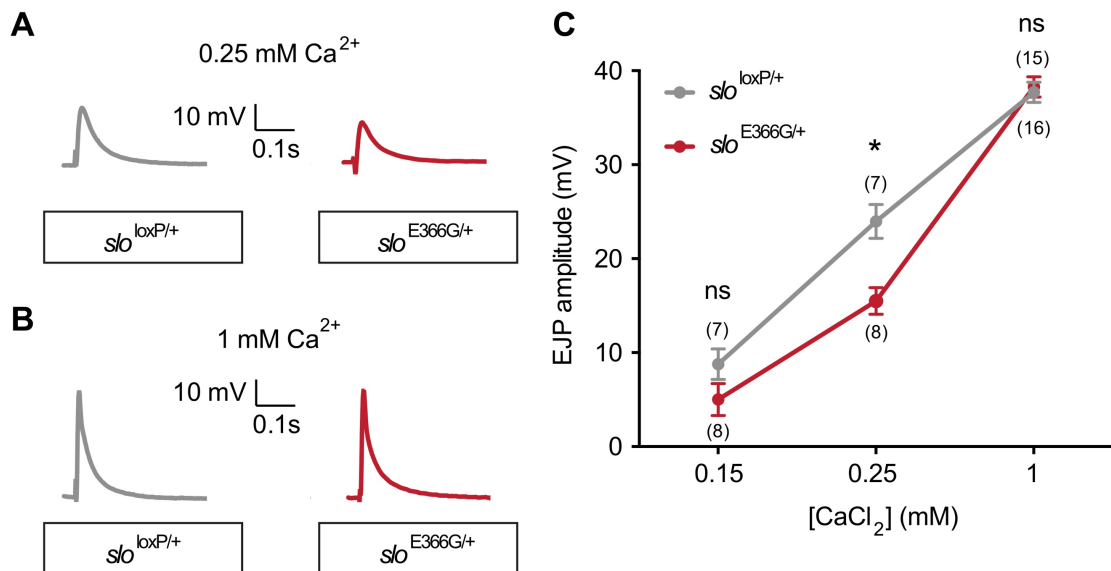
Figure 3.11 slo^{E366G} is a Gain-of-function Allele *ex vivo*

Example EJP traces from the L3 larval NMJ of $slo^{loxP}/+$ and $slo^{E366G}/+$ at (**A**) 0.25 mM- and (**B**) 1 mM extracellular [Ca^{2+}] are shown. (**C**) A significant decrease in EJP amplitude was detected at 0.25 mM extracellular [Ca^{2+}] for $slo^{E366G}/+$. Data acquisition and analysis were performed by Dr. Simon Lowe. Dr. James Jepson visualised the data. (n = 7-16; ns = p > 0.05, * = p < 0.05; Mann-Whitney-Wilcoxon test with Bonferroni correction)

A significant decrease in EJP amplitude would be the expected effect of a pre-synaptically expressed gain-of-function *slo* allele, as described above. Hence, these data strongly suggest that slo^{E366G} is a gain-of-function allele *ex vivo*, consistent with its murine and human orthologues *in vitro* (Du et al., 2005; Lee and Cui, 2009; Yang et al., 2010).

3.4.5 $slo^{E366G}/+$ Affects Endogenous NMJ- and Motoneuron Activity

Having demonstrated normal NMJ morphology and function under physiological conditions (Paragraph 3.4.3), it is conceivable that the larval locomotor phenotype is caused by abnormal activity of MNs innervating the NMJ. For electrophysiological analyses in Figure 3.10, the MNs innervating muscles 6/7 were severed. This is common practice in NMJ electrophysiology in order to allow for controlled current injections into the innervating nerve (Zhang and Stewart, 2010). While the NMJ itself is intact in this setup, any pre-synaptic input from endogenous MN activity is lost. In order to investigate whether endogenous MN activity was affected in $slo^{E366G}/+$ larvae, electrophysiological recordings were

performed from the NMJ with intact CNS efferents to the muscle at an extracellular [Ca^{2+}] of 1 mM. Interestingly, while all of the $slo^{loxP}/+$ NMJs showed normal burst firing (n = 11), more than half of the $slo^{E366G}/+$ NMJs were completely silent (14/26 = 54 %) – another 27% of $slo^{E366G}/+$ NMJs exhibited uncoordinated firing (7/26), while only 19% showed burst firing (5/26) (Figure 3.12). These data suggest that, while the $slo^{E366G}/+$ larval NMJ can function normally (Paragraph 3.4.3), it receives aberrant endogenous input. This strongly supports the hypothesis that pre-synaptic MN activity at the larval NMJ is affected in $slo^{E366G}/+$.
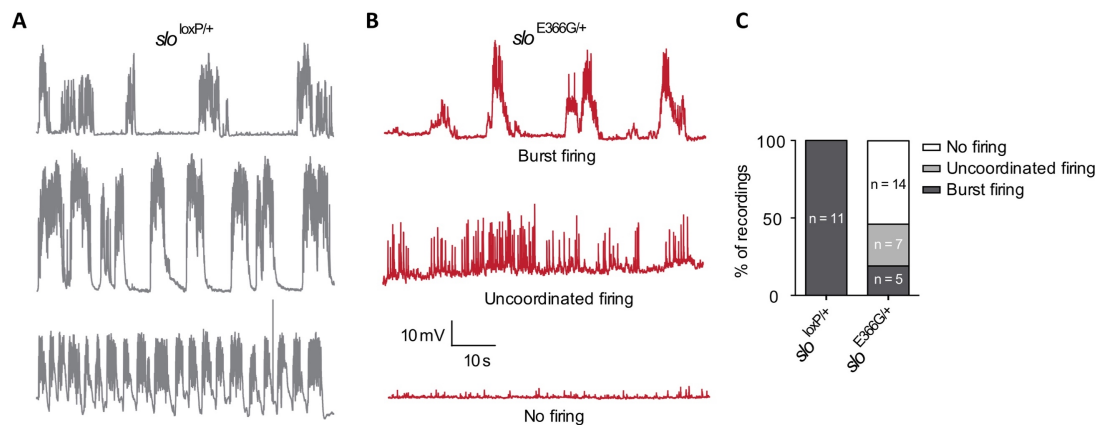
Figure 3.12 $slo^{E366G}/+$ Affects Endogenous NMJ Activity

Electrophysiological recordings of endogenous L3 larval NMJ activity with intact MN efferents were performed. (**A**) All intact recordings from $slo^{loxP}/+$ NMJs (n = 11) showed normal burst firing – three examples are shown to illustrate the variability in cycle period. (**B**) NMJs of $slo^{E366G}/+$ larvae (n = 26) showed three different endogenous activity patterns: burst firing (5), uncoordinated firing (7), and no firing (14). Recordings were performed at an extracellular [Ca^{2+}] of 1 mM. Data acquisition and analysis were performed by Dr. Simon Lowe. Dr. James Jepson visualised the data.

In order to directly investigate MN activity, live-imaging of larval MNs was performed using the GECI GCaMP6M (Chen et al., 2013), as described in (Pulver et al., 2015). GCaMP6M was expressed in $slo^{E366G}/+$ and $slo^{loxP}/+$ using the *OK371-Gal4* driver, an enhancer trap line that expresses *Gal4* under the control of an enhancer of the *Drosophila* vesicular glutamate transporter (*CG9887*), resulting in an expression pattern that limits *Gal4* transcription mainly to MNs within the larval VNC (Mahr and Aberle, 2006). The experimental genotypes were *OK371-Gal4,UAS-GCaMP6M/+;slo^{E366G}/+* and *OK371-Gal4,UAS-*

GCaMP6M/+;slo^loxP/+. Specifically, the fluorescence activity of MN axon bundles innervating abdominal segments 4 and 7 of the larval VNC was measured, as described in (Pulver et al., 2015) and illustrated for segment 4 in Figure 3.13. 12 CNS preparations per genotype were imaged on a confocal microscope on two separate days, in batches containing 6 preparations per genotype. Each recording lasted 5 min, which represents a trade-off between maximising information retrieval and minimising photobleaching.
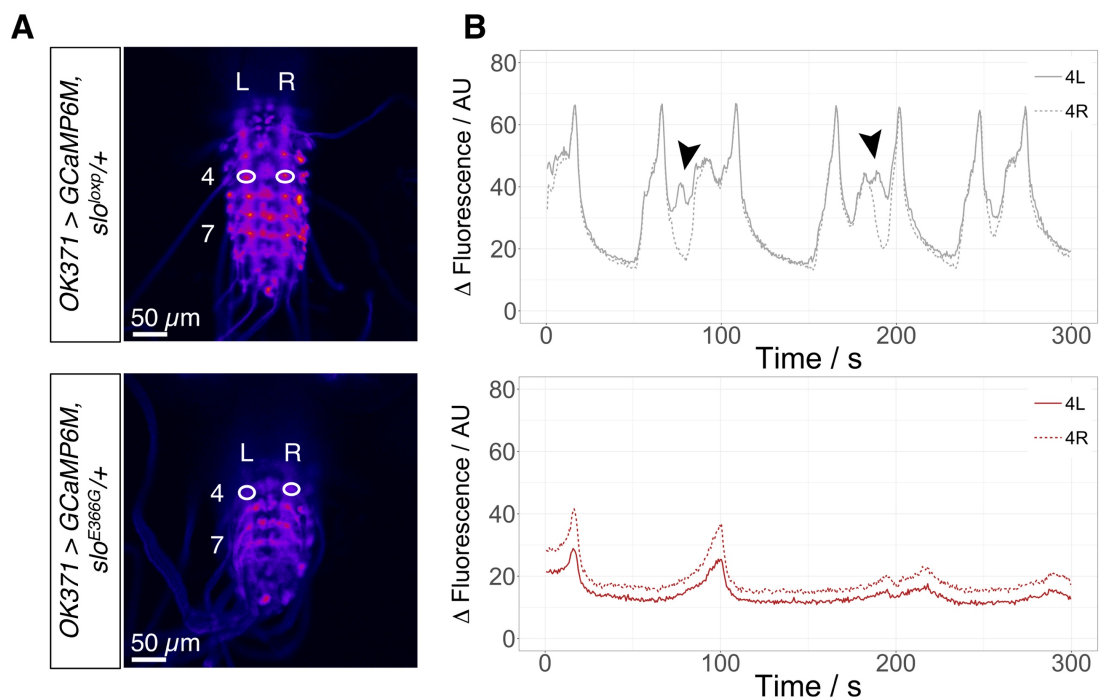
Figure 3.13 Live-imaging of Larval Motoneurons

MN activity in *slo^loxP/+* and *slo^E366G/+* VNCs was measured using GCaMP6M, as shown in **A**: L and R indicate the left and right side of the VNC, respectively, while 4 and 7 denote abdominal VNC segments. ROIs were drawn around MN axon bundles innervating segment 4 for illustrative purposes, but segment 7 was also included in downstream analyses. (**B**) The corresponding fluorescence traces for these preparations during 5 min-recordings are shown for segments 4L and 4R in both genotypes. The black arrowheads in the upper panel indicate anti-correlated MN activity on either side of segment 4, which was interpreted as larval turning.

4 parameters from the live-imaging data were quantified: (1) the frequency of forward peristaltic waves, (2) the amplitude of Ca^{2+} spikes during forward peristaltic waves, (3) the forward wave propagation time from segment 7 to segment 4, and (4) the number of anti-correlated Ca^{2+} spikes in segment 4, which

were interpreted as turning events – these parameters are illustrated in Figure 3.14. Parameters 2 and 3 were quantified for each side of the VNC separately.
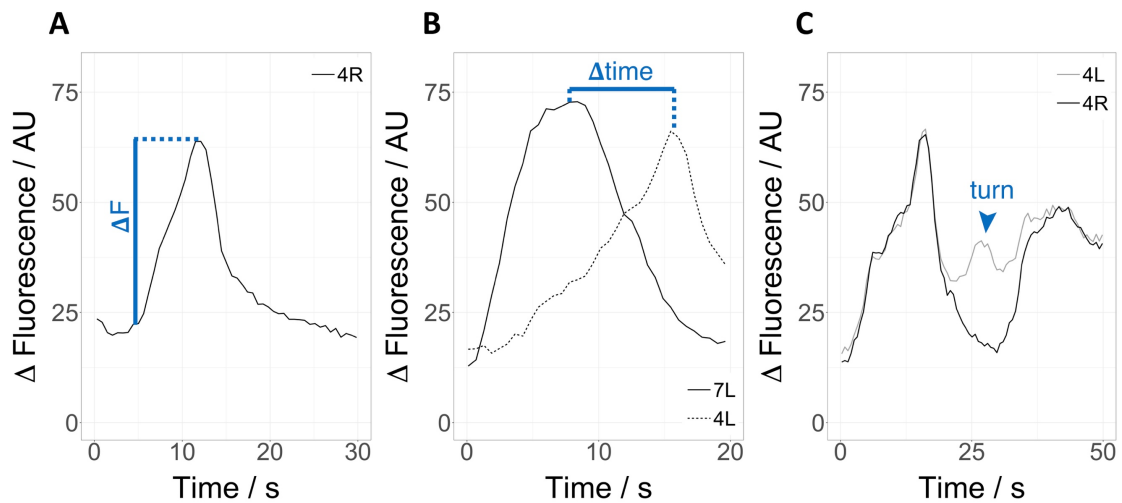
Figure 3.14 Live-imaging Parameter Illustration

Live-imaging of larval MNs was performed using GCaMP6M, and the resulting data analysed according to 4 parameters: (**A**) the frequency and amplitude of Ca^{2+} spikes in segment 4 during forward peristaltic waves, (**B**) the propagation time of forward peristaltic waves between segment 7 and segment 4, and (**C**) the frequency of turning events, defined as anti-correlated Ca^{2+} activity between the left and right sides of segment 4. The amplitude of Ca^{2+} spikes and the propagation time of forward peristaltic waves were quantified for each side of the VNC separately. All traces shown are derived from *slo^loxP/+*.

Analyses of the live-imaging data revealed altered *slo^E366G/+* MN activity according to each of the four parameters investigated: *OK371-Gal4,UAS-GCaMP6M/+;slo^E366G/+* MNs showed (1) a decreased frequency of forward peristaltic waves, (2) a decreased amplitude of Ca^{2+} spikes during forward peristaltic waves, (3) a decreased wave propagation time from segment 7 to segment 4, and (4) a decreased number of turning events (Figure 3.15).
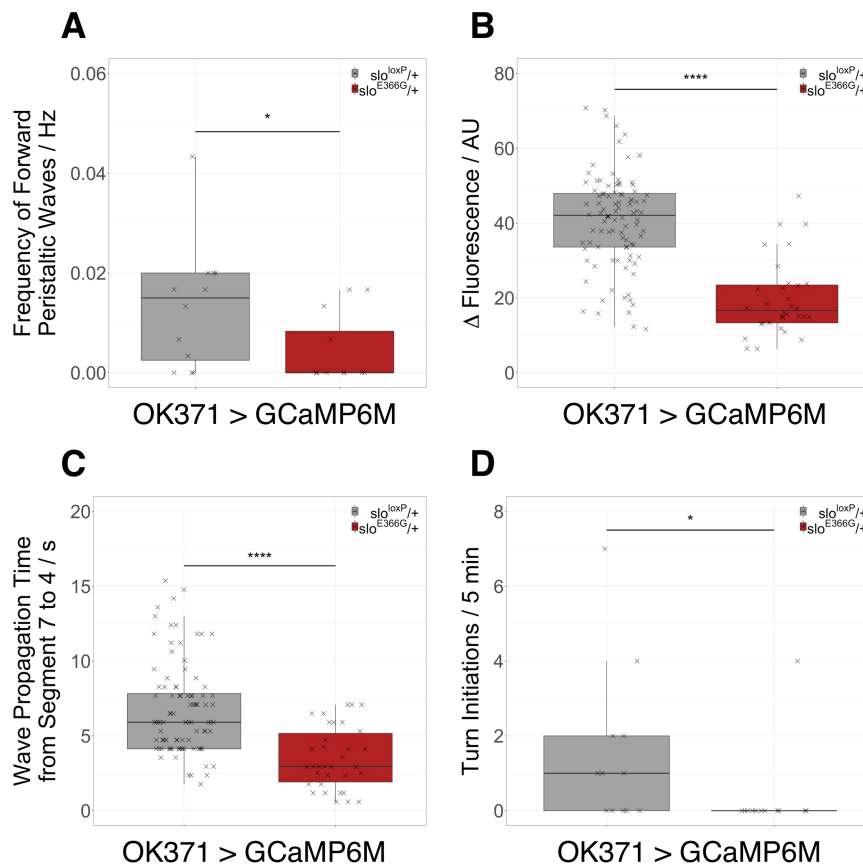
Figure 3.15 *slo^E366G/+* Alters Endogenous Motoneuron Activity

Live-imaging of *slo^loxP/+* and *slo^E366G/+* MN activity was performed using GCaMP6M. *slo^E366G/+* MNs showed (**A**) a decreased number of forward peristaltic waves as well as (**B**) a decreased amplitude of Ca^{2+} fluorescence peaks. (**C**) Peristaltic forward waves of Ca^{2+} activity travelled faster in *slo^E366G/+*. (**D**) *slo^E366G/+* MNs exhibited a decreased number of turning events. The recording time was 5 min. Data from two independent experimental repeats were pooled and analyses performed blinded to genotype. The data were acquired by both Dr. James Jepson and myself. (Mann-Whitney-Wilcoxon test, * = $p < 0.05$, **** = $p < 0.0001$)

The data shown in Figure 3.15 strongly support the hypothesis that endogenous MN activity is affected in *slo^E366G/+* larvae. I next sought to characterise the effect of *slo^E366G/+* in adults.

3.4.6 *slo^E366G /+* Partially Suppresses Wing Inflation

Similar in chronology to phenotyping *slo^E366G/+* larvae, I began the phenotypic characterisation of adult *slo^E366G/+* flies by investigating morphological abnormalities. It was evident that some *slo^E366G/+* flies exhibited a non-inflated wing phenotype, which was absent in *slo^loxP/+* controls. Moreover, even when the

wings had properly inflated, they often appeared brittle and slightly curled. To quantify this phenotype, I collected 92 slo^{E366G}/+ males and 96 slo^{E366G}/+ females, scoring wing inflation as follows: (1) fully inflated wings, (2) semi-inflated wings, and (3) non-inflated wings. ~15% of male- and ~11% of female slo^{E366G}/+ flies had non-inflated wings, while ~4% of male- and ~15% of female slo^{E366G}/+ flies had semi-inflated wings (Figure 3.16). In contrast, I collected 219 slo^{loxP}/+ males and 185 slo^{loxP}/+ females, none of which showed a non-inflated wing phenotype, whereas 1 male (~0.5%) and 3 females (~2%) showed semi-inflated wings.
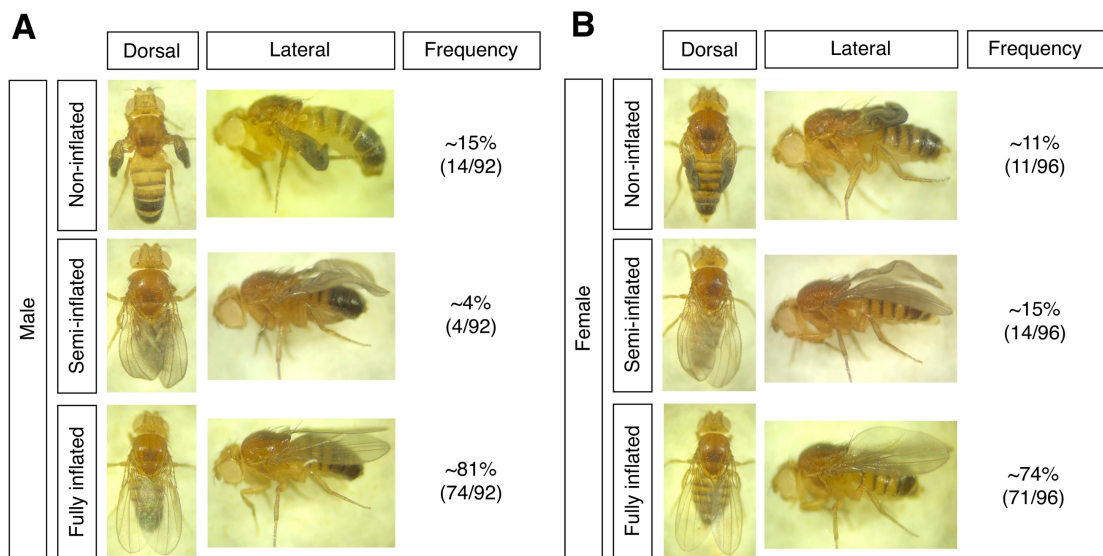
Figure 3.16 slo^{E366G}/+ Partially Suppresses Wing Inflation

Wing inflation of 92 slo^{E366G}/+ males (**A**) and 96 slo^{E366G}/+ females (**B**) was scored according to three categories: non-inflation of wings, semi-inflation of wings, and fully inflated wings. Of note, even fully inflated wings of slo^{E366G}/+ flies appeared brittle and slightly curled.

3.4.7 slo^{E366G}/+ Affects Adult Locomotion

Having observed a significant decrease in travelling distance of slo^{E366G}/+ larvae (Figure 3.4), I wondered whether this behaviour was conserved in adults. To this end, I used the DART system to video-track adult fly locomotion (Faville et al., 2015). This system tracks adult flies within glass tubes that mainly allow for movement along one axis. For these experiments, I used slo^{E366G}/+ and slo^{loxP}/+ virgin adults of both sexes from three independent recombinant lines each,

analogous to the larval locomotor analysis (Figure 3.4): *25.1.1/+*, *137.1.3/+*, and *72.1.1/+* for $slo^{E366G}/+$, and *132.1.1/+*, *111.1.1/+*, and *7.1.1/+* for $slo^{loxP}/+$. Importantly, I only used flies with fully inflated wings (Figure 3.16). In a 12 h light:12 h dark cycle, I recorded fly movement for a whole day period of 12 h. Figure 3.17 shows that both male and female $slo^{E366G}/+$ flies moved significantly shorter distances than their $slo^{loxP}/+$ counterparts. In fact, the effect size of this decrease was greater than observed for larvae: $slo^{E366G}/+$ males and females showed an ~3-fold decrease in mean locomotion compared to $slo^{loxP}/+$ flies (5 m vs 16.9 m for males, respectively; 5.7 m vs 18.2 m for females).
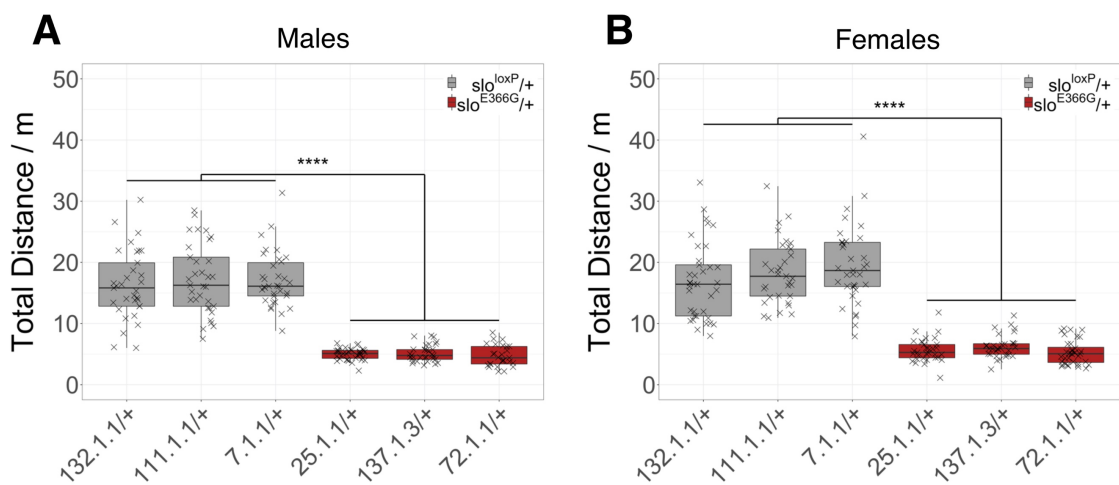
Figure 3.17 $slo^{E366G}/+$ Decreases Adult Locomotion

(**A**) $slo^{E366G}/+$ males (*25.1.1/+*, *137.1.3/+*, and *72.1.1/+*) showed a significant decrease in locomotion compared to $slo^{loxP}/+$ males (*132.1.1/+*, *111.1.1/+*, and *7.1.1/+*). (**B**) A similar reduction in total distance travelled was observed for $slo^{E366G}/+$ females. No within-genotype differences were observed for either sex. Total distance is measured in metres during 12 h lights-on. Data from three independent experimental repeats were pooled. (n = 27-37; Kruskal-Wallis multiple comparison with Dunn's post-hoc test; **** = p < 0.0001)

Due to a lack of within-genotype differences in locomotion (Figure 3.17), I pooled the DART data by genotype and sex for the analysis of more specific locomotor parameters. One possible explanation for a decrease in locomotion could be a decrease in locomotor speed, which I proceeded to quantify. Due to its crepuscular nature, *Drosophila* is most active during dusk and dawn (Peschel and Helfrich-Förster, 2011). Hence, in order to obtain a representation of their capacity to move at high speeds, I analysed locomotion of $slo^{E366G}/+$ and $slo^{loxP}/+$

flies during a period of 1 h after the dark-light transition. Indeed, Figure 3.18 shows a significant decrease in speed exhibited by slo^{E366G}/+ males and females compared to slo^{loxP}/+, illustrating that slo^{loxP}/+ flies achieved speeds within a range that is not reached by slo^{E366G}/+ (Figure 3.18).
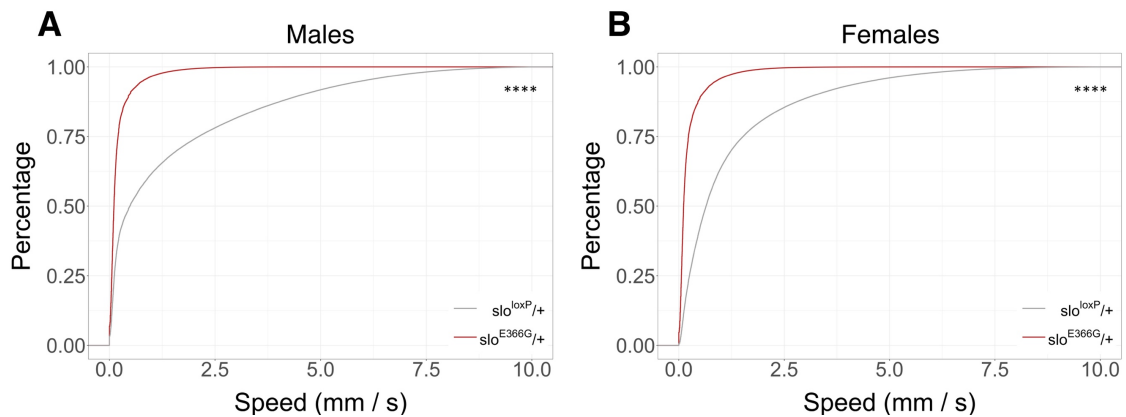
Figure 3.18 slo^{E366G}/+ Decreases Locomotor Speed

Adult slo^{E366G}/+ and slo^{loxP}/+ males (**A**) and females (**B**) were analysed for their cumulative distribution of locomotor speeds, measured as the distance in mm travelled during 1-s bouts for a period of 1 h after the dark-light transition. For both sexes, slo^{E366G}/+ flies exhibited significantly lower locomotor speeds than slo^{loxP}/+ flies. (n = 94-105; Kolmogorov-Smirnov test, **** = $p < 0.0001$)

Moving at lower speeds could potentially explain the decrease in travelling distance observed in slo^{E366G}/+ flies (Figure 3.17). It might also indicate that slo^{E366G}/+ flies exhibit impaired movement execution, a phenotype linked to basal ganglia dysfunction in a variety of movement disorders (Kandel et al., 2013) (Paragraph 1.2.2). Another important role of the basal ganglia is action selection (Kandel et al., 2013; Ryan et al., 2018), which was found to be impaired in slo^{E366G}/+ larvae (Figure 3.8). The larval readout for action selection was turning initiation, which could not be measured in adults due to the one-dimensional recording environment of the DART system. Instead, I quantified the number of movement initiations during a period of 1 h after the dark-light transition. As shown in Figure 3.19, slo^{E366G}/+ flies initiated movement significantly more often during this time than slo^{loxP}/+ flies, resulting in more staccato locomotion.
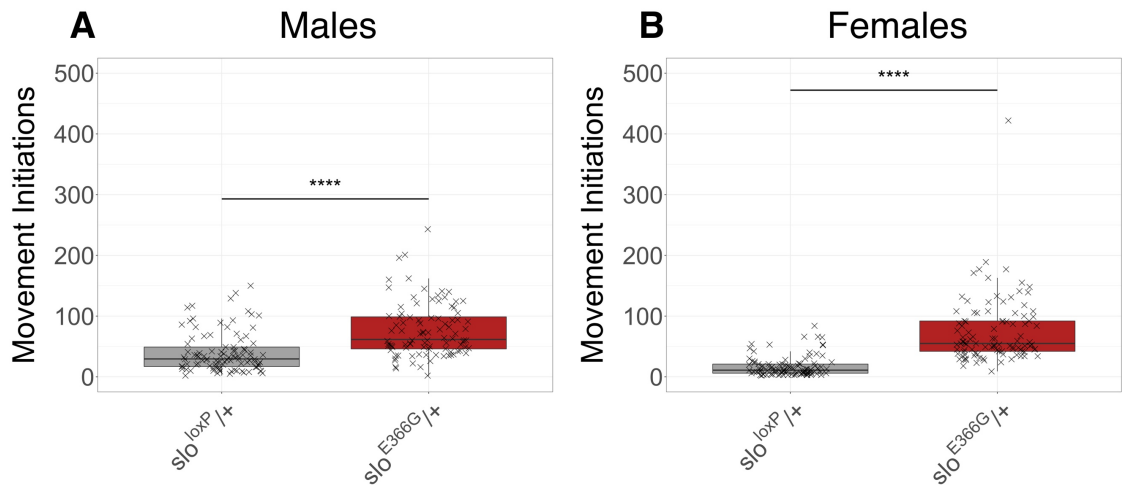
Figure 3.19 *slo^E366G^/+* Increases the Number of Movement Initiations

slo^E366G^/+ and *slo^loxP^/+* flies were analysed for the total number of movement initiations during a period of 1 h after the dark-light transition. *slo^E366G^/+* males (**A**) and females (**B**) initiated movement significantly more often than *slo^loxP^/+*. (n = 94-105; Mann-Whitney-Wilcoxon test; **** = $p < 0.0001$)

To confirm the data provided in Figure 3.19, I quantified the mean durations of sustained movement bouts – termed "mean bout length" – exhibited by *slo^E366G^/+* and *slo^loxP^/+* flies. A staccato movement pattern would predict that *slo^E366G^/+* flies fail to sustain movement for as long as *slo^loxP^/+*. As for Figure 3.18 and Figure 3.19, this analysis was performed for a period of 1 h after the dark-light transition. Indeed, *slo^E366G^/+* flies exhibited a significant decrease in mean bout lengths (Figure 3.20). These data indicate that *slo^E366G^/+* flies do not sustain movement for as long as *slo^loxP^/+* flies, which is congruent with an increased number of movement initiations (Figure 3.19). Together, these data provide strong evidence that action selection in *slo^E366G^/+* is impaired at both larval and adult stages.
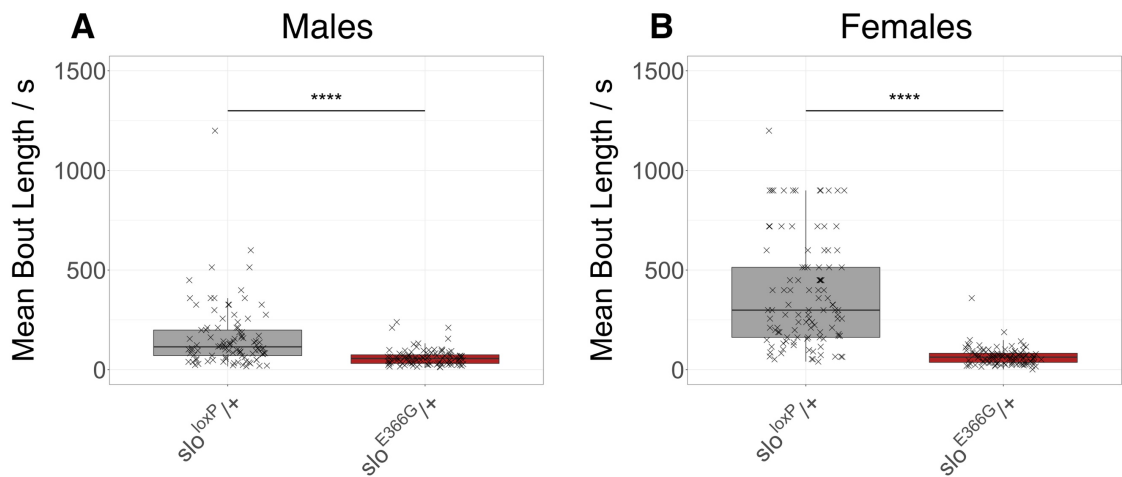
Figure 3.20 *slo^E366G^/+* Decreases the Length of Movement Bouts

The mean lengths of movement bouts were analysed for *slo^E366G^/+* and *slo^loxP^/+* flies during a period of 1 h after the dark-light transition. *slo^E366G^/+* males (**A**) and females (**B**) exhibited significantly decreased periods of sustained movement compared to *slo^loxP^/+*. (n = 94-105; Mann-Whitney-Wilcoxon test; **** = p < 0.0001)

3.4.8 *slo^E366G^/+* Flies Are Not Bang- But Temperature-sensitive

While this chapter has focussed on movement abnormalities of *slo^E366G^/+* larvae and adults, some GEPD patients also present with epilepsy, either in isolation or in combination with PxD (Du et al., 2005). As described in Paragraph 1.5.2, the bang-sensitive *Drosophila* mutants exhibit paralysis and seizures upon being subjected to a mechanical stimulus (Cunliffe et al., 2015; Parker et al., 2011). Hence, I investigated whether *slo^E366G^/+* flies exhibit bang-sensitivity. This was not the case with a variety of mechanical stimuli employed, such as vibration or tapping.

As described in Paragraph 1.5.2, *Drosophila* knock-in models of DS and GEFS+ exhibit temperature-induced seizures: exposing these flies to 40°C for 2 min induced leg twitching, wing flapping, and abdominal curling (Schutte et al., 2014; Sun et al., 2012). I replicated this experimental protocol but did not observe temperature-induced seizures in *slo^E366G^/+* flies. However, once vials containing *slo^E366G^/+* flies had been removed from 40°C, *slo^E366G^/+* flies remained motionless for an extended period of time, lasting from 30 min to more than 1 h. An extended recovery time upon exposure to increased temperature has also been described

for the GEFS+ knock-in flies (Sun et al., 2012) and is reminiscent of the sticky-feet phenotype observed in *slo* null homozygotes (Atkinson et al., 2000; Elkins et al., 1986). As this phenotype might indicate an extended state of aberrant neural activity (Atkinson et al., 2000), it warrants future investigation.

3.4.9 *slo^{E366G}/+* Reduces Adult Life Span

While GEPD is not explicitly linked to a decrease in patient life span (Du et al., 2005), the locomotor defect of *slo^{E366G}/+* flies is chronic, not paroxysmal. Hence, I wondered whether this continuous effect of the *slo^{E366G}* allele on *Drosophila* health might affect longevity. Indeed, analysing 110 *slo^{E366G}/+* males and 100 *slo^{loxP}/+* males uncovered a significant difference in life span (Figure 3.21). While *slo^{loxP}/+* males showed a sudden onset of mortality around day 40, *slo^{E366G}/+* males started dying during the first week of the experiment (Figure 3.21).
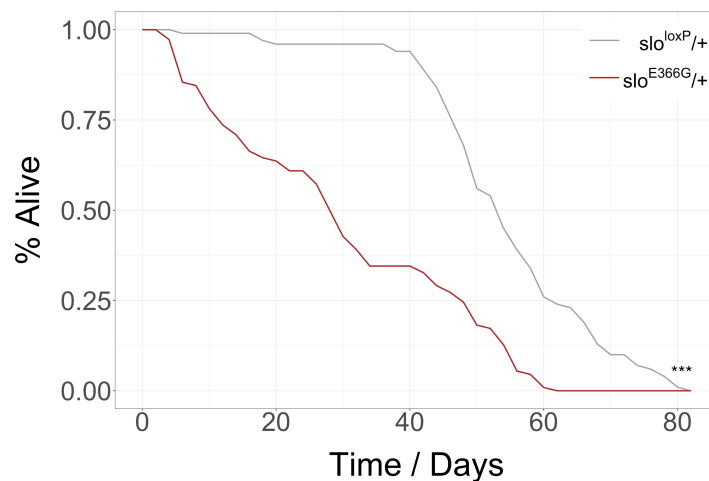
Figure 3.21 *slo^{E366G}/+* Reduces Adult Life Span

slo^{E366G}/+ males show a marked decrease in life span compared to *slo^{loxP}/+* males. The last *slo^{E366G}/+* male died between days 60 and 62, the last *slo^{loxP}/+* male between days 80 and 82. While *slo^{E366G}/+* males are steadily dying, *slo^{loxP}/+* males exhibit a sudden drop in survival at day 40. (n = 100-110; Kolmogorov-Smirnov Test, *** = p < 0.001)

3.5 Discussion

This chapter addresses the first question set out in the project aim: what are the organismal effects of the D434G-equivalent mutation in flies? The slo^{E366G} allele was found to be homozygous lethal by the adult stage, and $slo^{E366G}/+$ larvae and adults showed severe locomotor abnormalities, most notably a decrease in travelling distance and impaired action selection. Electrophysiological recordings from the larval NMJ provided evidence that the slo^{E366G} allele increases the Ca^{2+} sensitivity of Slo. While $slo^{E366G}/+$ NMJ function under physiological conditions was found to be unaffected, electrophysiological recordings from the intact NMJ and live-imaging of larval MNs provide strong evidence for altered endogenous MN activity in $slo^{E366G}/+$. Altogether, this chapter provides an in-depth phenotypic characterisation of the slo^{E366G} allele at the cellular and behavioural level.

3.5.1 Experimental Notes and Caveats

3.5.1.1 Slo^{E366G} Might Alter the Function of *CCAP*-positive Neurons

It has recently been shown that the over-expression of *wake* in *CCAP*-positive neurons causes a wing-inflation defect similar to the one observed in $slo^{E366G}/+$ (Figure 3.16) (Tabuchi et al., 2018). This Wake-induced phenotype could be rescued by the simultaneous knock-down of *slo* in *CCAP*-positive neurons (Tabuchi et al., 2018). Since Wake is a positive regulator of Slo, the over-expression of *wake* is functionally similar to the expression of a gain-of-function *slo* allele (Tabuchi et al., 2018). Hence, these data suggest that Slo^{E366G} might act as a gain-of-function allele in *CCAP*-positive neurons, which would be consistent with its function at the larval NMJ (Figure 3.11). This increased Slo function in *CCAP*-positive neurons might cause the wing-inflation defect observed in $slo^{E366G}/+$ (Figure 3.16).

3.5.2 Clinical Relevance

3.5.2.1 slo^{E366G} is a Gain-of-function Allele *ex vivo*

Macroscopic current recordings *in vitro* have previously shown that the D434G-equivalent murine D369G mutation in *KCNMA1* causes an increased BK channel Ca^{2+} sensitivity (Yang et al., 2010). This gain-of-function was strongest around

146

an intracellular $[Ca^{2+}]$ of 1 μM, but absent at nominal zero- and saturating (100 μM) intracellular $[Ca^{2+}]$ (Yang et al., 2010). Similarly, electrophysiological recordings at the $slo^{E366G}/+$ larval NMJ showed that the EJP amplitude decreases at an extracellular $[Ca^{2+}]$ of 0.25 mM, but not at a physiological concentration of 1 mM (Figure 3.11). This decrease in EJP amplitude in $slo^{E366G}/+$ larvae is likely caused by a gain of Slo function at the pre-synaptic terminus, which would decrease Ca^{2+} influx and glutamate release. Hence, these data provide strong evidence that slo^{E366G} acts as a gain-of-function allele *ex vivo*. To definitively test this hypothesis, *in vivo* patch clamp recordings could be performed from neurons known to express Slo, such as the DN1p clock neurons (Tabuchi et al., 2018). A Slo gain-of-function would be expected to increase I_{CF} in these neurons.

Importantly, the Ca^{2+}-dependence of this effect suggests variable consequences of this mutation for different neuronal subpopulations, as pre-synaptic termini exhibiting low intracellular $[Ca^{2+}]$ or weak coupling between BK- and Ca_v channels are expected to be most affected (Griguoli et al., 2016). At these synapses, an increased Ca^{2+} sensitivity of BK channels might decrease the probability of neurotransmitter release, potentially affecting neuronal circuit function and plasticity. On the other hand, synapses exhibiting high intracellular $[Ca^{2+}]$ or strong coupling between BK- and Ca_v channels would be less affected in GEPD, because the abundance of Ca^{2+} might maximally potentiate both mutant and wild-type BK channels. Such differential effects of the D434G mutation in different brain areas might explain the specific phenotypes of GEPD, despite the broad expression pattern of BK channels (Bailey et al., 2019; Griguoli et al., 2016; Latorre et al., 2017) (Paragraph 1.4.2).

3.5.2.2 $slo^{E366G}/+$ Induces Aberrant Motoneuron Activity

Electrophysiological recordings at an extracellular $[Ca^{2+}]$ of 1 mM showed that synaptic transmission at the $slo^{E366G}/+$ larval NMJ was normal upon severing the innervating nerve but exhibited severe abnormalities when MN efferents were preserved (Figure 3.10, Figure 3.12). These data suggest that the $slo^{E366G}/+$ larval NMJ can function normally but receives aberrant endogenous input from MNs. Indeed, this hypothesis was confirmed via live-imaging of larval MNs, which revealed altered endogenous MN activity in $slo^{E366G}/+$ larvae (Figure 3.15). This

change in MN firing might either indicate dendritic defects of MNs, or a dysregulation of neural activity upstream of MNs. Two previous studies support the latter hypothesis: (1) *ex vivo* patch clamp recordings from homozygous *slo* null larval MNs detected an increased peristaltic frequency-like activity (Kadas et al., 2015) – the opposite to what was observed in *slo^{E366G}/+* larvae (Figure 3.5, Figure 3.12). However, RNAi-mediated knock-down of *slo* specifically in MNs did not mimic this effect, suggesting that peristaltic frequency is regulated by *slo* upstream of MNs (Kadas et al., 2015) – potentially by neural populations also involved in mediating the *slo^{E366G}/+* locomotor defect. (2) By surgically removing specific regions of the larval CNS prior to GCaMP3-mediated live-imaging of VNC MNs, it could be shown that descending inputs from the brain lobes to the VNC are required for modulating both the cycle period of peristaltic Ca^{2+} waves and fictive turning behaviour (Pulver et al., 2015). Since both of these parameters are affected in *slo^{E366G}/+* (Figure 3.15), these data suggest neuronal populations in the larval brain to mediate the *slo^{E366G}/+* locomotor defect – such as the central pattern generator (CPG), a neuronal network innervating MNs and providing rhythmic synaptic drive that allows for coordinated muscle contractions and movement (Kadas et al., 2015; Marder and Bucher, 2001; Pulver et al., 2015).

3.5.2.3 *slo^{E366G}/+* Induces a Potential Cellular Seizure Phenotype

While no behavioural seizure phenotype could be observed in *slo^{E366G}/+* flies, live-imaging of larval MNs revealed a decreased inter-segmental time delay of Ca^{2+} activity, analogous to more synchronous MN firing (Figure 3.15). Using a similar experimental approach, an increased synchronicity of MN activity has recently been observed in the bang-sensitive *bss^1* larvae as well as in *para^{K1270T}* larvae, a model of the human epilepsy syndrome GEFS+ (Streit et al., 2016; Sun et al., 2012). This increased synchronicity of MN activity could be rescued by feeding AEDs to *bss^1* larvae, suggesting this phenotype to be a cellular readout for epileptic seizures (Streit et al., 2016). Hence, future experiments might test whether AEDs can also rescue the increased synchronicity of MN firing in *slo^{E366G}/+* larvae, which would suggest the presence of a cellular seizure phenotype in this GEPD model.

3.5.2.4 In Search of a Behavioural Seizure Phenotype in *slo^{E366G}/+*

GEPD patients present with PxD, epilepsy, or combined PxD-epilepsy (Du et al., 2005), illustrating variable expressivity of the D434G mutation that might depend on environmental and genetic background effects. *slo^{E366G}/+* flies exhibit severe locomotor abnormalities but no seizure-like behaviour, rendering this GEPD model more dyskinesia- than epilepsy-like. However, it is possible that triggers other than mechanical stimulation and temperature are required to induce seizures in *slo^{E366G}/+* flies, and this will be tested in future experiments. Moreover, outcrossing the *slo^{E366G}* allele into different genetic backgrounds might unmask seizure-like behaviour.

3.5.2.5 *slo^{E366G}/+* Induces a Chronic Locomotor Defect

Both *slo^{E366G}/+* adults and larvae exhibit severe locomotor defects, which manifest as a decrease in travelling distance and aberrant action selection (Figure 3.4, Figure 3.17, Figure 3.8, Figure 3.19). This locomotor defect is chronic, not paroxysmal, differentiating it from its human counterpart (Du et al., 2005). This difference might be explained by the absence of regulatory β- and γ-subunits in flies (Griguoli et al., 2016) (Paragraph 1.4.3). Not only do these subunits affect wild-type BK channel function, a previous study also demonstrated that β-subunits differentially modulate the effect of the D434G mutation, as shown via inside-out patch clamp recordings *in vitro* (Lee and Cui, 2009). Indeed, the presence of the β3b-subunit almost entirely abolished the increase in BK channel Ca^{2+} sensitivity associated with the D434G mutation (Lee and Cui, 2009). Since β-subunits are expressed in a tissue- and neuronal subtype-specific manner (Griguoli et al., 2016; Latorre et al., 2017) (Paragraph 1.4.3), these data suggest that some human tissues and brain regions would be more affected by the D434G mutation than others. The lack of this additional layer of functional modulation in flies might explain the more severe locomotor phenotype observed compared to humans.

3.5.2.6 *slo^{E366G}/+* Alters Action Selection

A specific movement phenotype investigated in this chapter is action selection. Both larval video-tracking and live-imaging of MNs suggest that *slo^{E366G}/+* larvae

exhibit a decrease in turning behaviour, a form of action selection (Figure 3.8, Figure 3.15). The adult readout for action selection was also affected, with $slo^{E366G}/+$ adults exhibiting a significant increase in the number of movement initiations, leading to more staccato locomotor patterns (Figure 3.19, Figure 3.20). Impaired action selection might indicate an involvement of pre-motor circuits in $slo^{E366G}/+$, which is consistent with the electrophysiological- and live-imaging data, suggesting that the pathogenic locus of $slo^{E366G}/+$ lies within the CNS (Paragraph 3.5.2.2). In dyskinesia patients, action selection is thought to be affected by a pathological imbalance between direct- and indirect striatopallidal pathway activity in the basal ganglia (Figure 1.1) (Kandel et al., 2013; Ryan et al., 2018). Striatopallidal connections are formed by GABAergic MSNs in the striatum (Kandel et al., 2013; Ryan et al., 2018). Interestingly, a recent study on a mouse model of LID identified a subpopulation of MSNs of the direct pathway whose firing rates positively correlated with dyskinesia severity, as measured via single-unit recordings in awake behaving mice (Ryan et al., 2018). Moreover, optogenetic activation of direct pathway MSNs was sufficient to evoke dyskinetic attacks in control mice (Ryan et al., 2018). Hence, it would be intriguing to investigate whether functionally analogous brain structures and neuronal subtypes mediate the $slo^{E366G}/+$ locomotor defect in flies.

3.5.2.7 A Potential Metabolic Component in $slo^{E366G}/+$

Identifying a significant increase $slo^{E366G}/+$ larval body size might indicate metabolic disturbances in this mutant (Figure 3.6, Figure 3.7). GLUT1-DS and PED patients experience seizures and PxD due to abnormal glucose metabolism (De Giorgis and Veggiotti, 2013), making conceivable the notion that GEPD, too, might have a metabolic component. Indeed, an increased larval body size might implicate dysregulated insulin signalling in GEPD, as broad over-expression of *dilp2,* one of eight insulin-like peptides (*dilps*) in *Drosophila,* has been shown to increase adult *Drosophila* body size (Brogiolo et al., 2001).

3.5.3 Conclusion

A phenotypic characterisation of $slo^{E366G}/+$ larvae and adults identified severe locomotor abnormalities in these animals and suggests a causal role for neural

circuits upstream of MNs. To test this hypothesis, the expression of the slo^{E366G} allele must be restricted to neuronal subpopulations.

4 Spatial Dissection of *slo^E366G^/+* Pathogenesis

4.1 Introduction

As described in Paragraph 1.4.2, *KCNMA1* is broadly expressed throughout the human body, and, within the CNS, in a variety of brain areas, including the basal ganglia, thalamus, and cerebellum, all of which have been implicated in movement disorders (Bailey et al., 2019). On a cellular level, *KCNMA1* is expressed by a variety of neuronal subtypes, including glutamatergic-, GABAergic-, and cholinergic neurons (Griguoli et al., 2016) (Paragraph 1.4.2). Moreover, due to alternative splicing, post-translational modifications, and the co-expression of regulatory subunits, BK channel function varies between cells and tissues (Griguoli et al., 2016; Latorre et al., 2017) (Paragraph 1.4.3). As a result, it is difficult to predict where the D434G mutation in *KCNMA1* exerts its pathogenic effects that lead to GEPD. Importantly, Chapter 3 provided strong evidence for pre-motor circuits in the larval brain to induce the *slo^E366G^/+* locomotor defect. The aim of this chapter is to test this hypothesis by spatially restricting Slo expression.

Via the selective re-expression of *dysc* in *dysc* null homozygotes – Dysc is a positive post-transcriptional regulator of Slo (Jepson et al., 2012) (Paragraph 1.5.3) – Slo expression was restricted to various cellular subpopulations. Using this strategy, it is demonstrated that the brain-specific activity of Slo^E366G^ is sufficient to induce the *slo^E366G^/+* locomotor defect, while its selective activity in muscle tissue does not affect locomotion. By further restricting Slo expression, it is shown that the activity of Slo^E366G^ in cholinergic neurons is sufficient to decrease locomotion, an effect not observed in glutamatergic MNs and other neuronal subpopulations. These data support the hypothesis, proposed in Chapter 3, that neuronal circuits in the central brain define the pathogenic locus of GEPD, and suggest that cholinergic neurons are important mediators of the *slo^E366G^/+* locomotor defect.

4.2 Statement of Contribution

4.2.1 Direct Contributions

Dr. James Jepson and I conceived of the genetic strategy for the spatial dissection of the $slo^{E366G}/+$ locomotor defect together, and Dr. James Jepson's intellectual input was invaluable. As acknowledged in Paragraph 3.2.1, Dr. Srinivasa Rao and Dr. Sam Olechnowicz are the main developers of the AnimApp video-tracking software (Rao et al., 2019).

4.2.2 Indirect Contributions

Dr. James Jepson and Dr. Ko-Fan Chen provided invaluable intellectual input for the behavioural experiments performed with adult flies.

4.3 Materials and Methods

4.3.1 Genetic Nomenclature

The genotypes of flies used in this chapter are listed in Paragraph 4.3.2.

Nomenclature guidelines are described in Paragraph 2.3.1.

4.3.2 Fly Stocks

Table 45 Fly Stocks of Chapter 4

Genotype	Source
iso^{31}	Kind gift from Dr. Kyunghee Koh
w;;TM2,Ubx^{130}/TM6B,Tb	Kind gift from Dr. Kyunghee Koh
w;Sco/CyO;	Kind gift from Dr. Kyunghee Koh
w;;slo^{E366G}/TM6B,Tb	This thesis
w;;slo^{loxP}/TM6B,Tb	This thesis
w;UAS-sloRNAi/CyO;	VDRC: 104421
w;;nSyb-Gal4/TM2,Ubx^{130}	Kind gift from Dr. Kyunghee Koh
w;UAS-sloRNAi/CyO;slo^{E366G}/TM6B,Tb	This thesis
w;UAS-sloRNAi/CyO;slo^{loxP}/TM6B,Tb	This thesis
w;;dysc^{s168}/TM6B,Tb	Kind gift from Dr. Kyunghee Koh
w;;slo^{E366G},dysc^{s168}/TM6B,Tb	This thesis
w;;slo^{loxP},dysc^{s168}/TM6B,Tb	This thesis
w;;da-Gal4/TM6B,Tb	BDSC: 55850
w;UAS-dysc;	Kind gift from Dr. Kyunghee Koh
w;UAS-dysc/CyO;slo^{E366G},dysc^{s168}/TM6C,Sb	This thesis
w;UAS-dysc/CyO;slo^{loxP},dysc^{s168}/TM6C,Sb	This thesis
w;;da-Gal4,dysc^{s168}/TM6B,Tb	This thesis
w;;nSyb-Gal4,dysc^{s168}TM6B,Tb	This thesis
w;;Mef2-Gal4/TM6B,Tb	BDSC: 27390
w;;Mef2-Gal4,dysc^{s168}/TM6B,Tb	This thesis
w;UAS-CD8::GFP;	Kind gift from Dr. Kyunghee Koh
w;OK371-Gal4/CyO;	Kind gift from Dr. Kyunghee Koh
w;OK371-Gal4/CyO;dysc^{s168}/TM6B,Tb	This thesis
w;c929-Gal4/CyO;	Kind gift from Dr. Kyunghee Koh
w;c929-Gal4/CyO;dysc^{s168}/TM6B,Tb	This thesis

w;GAD-Gal4/CyO;	Kind gift from Dr. Kyunghee Koh
w;GAD-Gal4/CyO;dysc^{s168}/TM6B,Tb	This thesis
w;ChAT-Gal4/CyO;	Kind gift from Dr. Kyunghee Koh
w;ChAT-Gal4/CyO;dysc^{s168}/TM6B,Tb	This thesis

4.3.3 Fly Husbandry

Unless otherwise indicated, all fly stocks were maintained on standard fly food at RT. The fly food recipe is shown in Table 4. All flies and larvae used for behavioural experiments were raised in an incubator (LMS) at 25°C and a 12 h light:12 h dark cycle.

4.3.4 Experimental Genotypes

Unless otherwise indicated, recombinant *25.1.1/TM6B,Tb* was used as a representative for *slo^{E366G}/TM6B,Tb*, and recombinant *132.1.1/TM6B,Tb* as a representative for *slo^{loxP}/TM6B,Tb*.

4.3.4.1 *slo^{E366G}/+* and *slo^{loxP}/+*

slo^{E366G}/+ and *slo^{loxP}/+* flies were generated by crossing *slo^{E366G}/TM6B,Tb* and *slo^{loxP}/TM6B,Tb* to isogenic controls (*iso^{31}*), respectively.

4.3.4.2 RNAi-mediated Knock-down of *slo*

The experimental genotypes *UAS-sloRNAi/+;nSyb-Gal4/slo^{E366G}* and *UAS-sloRNAi/+;nSyb-Gal4/slo^{loxP}* were generated by crossing *UAS-sloRNAi/CyO;slo^{E366G}/TM6B,Tb* and *UAS-sloRNAi/CyO;slo^{loxP}/TM6B,Tb* to *nSyb-Gal4/TM6B,Tb*, respectively. *nSyb-Gal4/+* and *UAS-sloRNAi/+* were generated by crossing *nSyb-Gal4/TM6B,Tb* and *UAS-sloRNAi/CyO* to *iso^{31}*, respectively.

4.3.4.3 *slo^{E366G},dysc^{s168}/dysc^{s168}* and *slo^{loxP},dysc^{s168}/dysc^{s168}*

slo^{E366G},dysc^{s168}/dysc^{s168} and *slo^{loxP},dysc^{s168}/dysc^{s168}* flies were generated by crossing *slo^{E366G},dysc^{s168}/TM6B,Tb* and *slo^{loxP},dysc^{s168}/TM6B,Tb* to *dysc^{s168}/TM6B,Tb*, respectively.

4.3.4.4 Immuno-staining

UAS-CD8::GFP/+;Mef2-Gal4/+ and *UAS-CD8::GFP/+;nSyb-Gal4/+* flies were generated by crossing *UAS-CD8::GFP* to *Mef2-Gal4/TM6B,Tb* and *nSyb-Gal4/TM2,Ubx^{130}*, respectively.

4.3.4.5 Dysc-mediated Spatial Dissection

All experimental genotypes used for Dysc-mediated spatial dissection experiments were generated by crossing *UAS-dysc/CyO;slo^{E366G},dysc^{s168}/TM6C,Sb* and *UAS-dysc/CyO;slo^{loxP},dysc^{s168}/TM6C,Sb* to the *Gal4* driver lines shown in Table 46.

Table 46 Experimental Genotypes for Spatial Dissection

Gal4 Driver	Experimental Genotype
da-Gal4,dysc^{s168}/TM6B,Tb	*UAS-dysc/+;da-Gal4,dysc^{s168}/slo$^{E366G/loxP}$,dysc^{s168}*
nSyb-Gal4,dysc^{s168}/TM6B,Tb	*UAS-dysc/+;nSyb-Gal4,dysc^{s168}/slo$^{E366G/loxP}$,dysc^{s168}*
Mef2-Gal4,dysc^{s168}/TM6B,Tb	*UAS-dysc/+;Mef2-Gal4,dysc^{s168}/slo$^{E366G/loxP}$,dysc^{s168}*
OK371-Gal4/CyO;dysc^{s168}/TM6B,Tb	*OK371-Gal4/UAS-dysc;dysc^{s168}/slo$^{E366G/loxP}$,dysc^{s168}*
c929-Gal4/CyO;dysc^{s168}/TM6B,Tb	*c929-Gal4/UAS-dysc;dysc^{s168}/slo$^{E366G/loxP}$,dysc^{s168}*
GAD-Gal4/CyO;dysc^{s168}/TM6B,Tb	*GAD-Gal4/UAS-dysc;dysc^{s168}/slo$^{E366G/loxP}$,dysc^{s168}*
ChAT-Gal4/CyO;dysc^{s168}/TM6B,Tb	*ChAT-Gal4/UAS-dysc;dysc^{s168}/slo$^{E366G/loxP}$,dysc^{s168}*

Crossing the *Gal4* drivers to *slo^{E366G},dysc^{s168}/TM6B,Tb* and *slo^{loxP},dysc^{s168}/TM6B,Tb* generated the driver controls shown in Table 47.

Table 47 Driver Controls for Spatial Dissection

Gal4 Driver	Driver Control
da-Gal4,dysc^{s168}/TM6B,Tb	*da-Gal4,dysc^{s168}/slo$^{E366G/loxP}$,dysc^{s168}*
nSyb-Gal4,dysc^{s168}/TM6B,Tb	*nSyb-Gal4,dysc^{s168}/slo$^{E366G/loxP}$,dysc^{s168}*
Mef2-Gal4,dysc^{s168}/TM6B,Tb	*Mef2-Gal4,dysc^{s168}/slo$^{E366G/loxP}$,dysc^{s168}*
OK371-Gal4/CyO;dysc^{s168}/TM6B,Tb	*OK371-Gal4/+;dysc^{s168}/slo$^{E366G/loxP}$,dysc^{s168}*
c929-Gal4/CyO;dysc^{s168}/TM6B,Tb	*c929-Gal4/+;dysc^{s168}/slo$^{E366G/loxP}$,dysc^{s168}*
GAD-Gal4/CyO;dysc^{s168}/TM6B,Tb	*GAD-Gal4/+;dysc^{s168}/slo$^{E366G/loxP}$,dysc^{s168}*
ChAT-Gal4/CyO;dysc^{s168}/TM6B,Tb	*ChAT-Gal4/+;dysc^{s168}/slo$^{E366G/loxP}$,dysc^{s168}*

Crossing *UAS-dysc/CyO;slo^{E366G},dysc^{s168}/TM6C,Sb* and *UAS-dysc/CyO;slo^{loxP},dysc^{s168}/TM6C,Sb* to *dysc^{s168}/TM6B,Tb* generated the

transgene controls *UAS-dysc/+;slo^{E366G},dysc^{s168}/dysc^{s168}* and *UAS-dysc/+;slo^{loxP},dysc^{s168}/dysc^{s168}*, respectively.

4.3.5 Adult Fly Behavioural Tracking

To track adult locomotion, the Drosophila Activity Monitor (DAM) system was used (DAM2, TriKinetics). This system consists of individual monitors containing 32 channels, into which the same glass tubes were inserted as described for the DART system in Paragraph 3.3.14. The glass tubes were prepared, and flies loaded, as described in Paragraph 3.3.14. Flies used for this experiment were between 2 and 6 days old at the time of recording. Fly-containing glass tubes were placed into DAM monitors and the monitors positioned in an incubator (LMS) at 25ºC, 65%-70% relative humidity, and a 12 h light:12 h dark regime. Flies were acclimatised to the new environment for at least 24 h, followed by recording of a whole 12 h light:12 h dark period (24 h) from 9 am to 9 am the following day.

4.3.6 Behavioural Tracking Analysis

DAM data were analysed using a customised R script (R v. 3.6.0), which is available on GitHub: https://github.com/PatrickKratsch/. This script reads the DAM output (TXT files) for each monitor into separate data objects and extracts the relevant experimental time. It then extracts the beam break data for each fly and sums the corresponding values over 24 h, yielding the total number of beam breaks per fly. Flies that did not move at all (0 beam breaks) during the second 12 h of the experiment were identified as dead and removed from further analyses.

4.3.7 Scoring Wing Inflation

Adult wing inflation was scored as described in Paragraph 3.3.13.

4.3.8 Antibody Staining of Adult Brains

Adult flies were anaesthetised on CO_2 pads (Flystuff, Genesee Scientific) and dissected using fine forceps (#5, Dumont, 0103-5-PO) in 0.3% PBT (0.3% Triton in Phosphate-buffered saline). Dissected brains were transferred into 0.5 mL

eppendorf tubes containing 450 μL of 4% PFA solution in 0.3% PBT on ice (Alfa Aesar, 43368). Fixation in 4% PFA was performed while shaking the samples at 4°C for 1.5 h. The 4% PFA was washed off with three quick washes (pipetting off the solution contained within the 0.5 mL eppendorf tubes, followed by adding 450 μL of 0.3% PBT) and three long washes (same procedure as quick washes but with an additional 15 min of shaking at RT upon addition of 450 μL of 0.3% PBT). Following the third long wash, the 450 μL of 0.3% PBT were pipetted off and replaced with 450 μL of 5% goat serum in 0.3% PBT (Thermo Fisher Scientific, 16210064). The fixed brains were blocked with 5% goat serum while shaking at RT for 1 h. The 5% goat serum was then pipetted off and replaced with 450 μL of a 5% goat serum solution containing a 1:200 dilution of a primary mouse anti-Bruchpilot antibody (DSHB, AB_2314866) and a 1:1000 dilution of a primary chicken anti-GFP antibody (Thermo Fisher Scientific, AB_2534023). Primary antibody staining was then performed by shaking these samples at 4°C for 16 h. The primary antibody-containing 5% goat serum solution was then washed off with three quick and three long washes, as described above, before adding 450 μL of a 5% goat serum solution containing a 1:1000 dilution of a secondary goat anti-mouse Alexa Fluor 555 antibody (Thermo Fisher Scientific, AB_2536164) and a 1:1000 dilution of a secondary goat anti-chicken Alexa Fluor 488 antibody (Thermo Fisher Scientific, AB_2534096). Samples were covered in aluminium foil to prevent photobleaching and left shaking at 4°C for 16 h. The secondary antibody-containing 5% goat serum solution was then washed off with three quick and three long washes, as described above, before adding 50 μL of Slowfade to each sample (Thermo Fisher Scientific, S36936). The brains suspended in Slowfade were stored in -20°C until the day of imaging.

4.3.9 Confocal Imaging of Adult Brains

For bridge mounting, two coverslips (VWR, 631-0121) were glued onto each side of a microscopy slide (Thermo Fisher Scientific, 49514), creating a gap in between. Into this gap, the brain-containing Slowfade solution (containing 3-6 brains per sample) was pipetted, before the gap was covered with a third coverslip. The edges around the coverslips were sealed with nail polish. Brains

were imaged on a Zeiss LSM 710 confocal microscope, using Zen software (Zeiss) and the EC "Plan-Neofluar" 20x/0.50 M27 air objective (Zeiss, 420350-9900-000) at a resolution of 1024x1024 and a 16-bit bit depth. An argon laser at 488 nm was used to excite the goat anti-chicken Alexa Fluor 488 fluorophore, while a wavelength of 568 nm was used to excite the goat anti-mouse Alexa Fluor 555 fluorophore. For all images, z-stacks from the most anterior to the most posterior brain signals were acquired.

4.3.10 Analysis of Confocal Imaging Data

Confocal imaging data were loaded into FIJI (Schindelin et al., 2012), where the two channel colours (488 nm and 568 nm) were merged and maximum z-projections, including scale bars, generated.

4.3.11 Larval Video-recordings

Larval video recordings were performed as described in Paragraph 3.3.6. An iPhone 8 (Apple Inc.) was used to take the videos for this chapter, at a resolution of 1080x1920 and a frame rate of 30 fps.

4.3.12 Pre-processing of Larval Videos

Larval videos were pre-processed as described in Paragraph 3.3.7, with the following differences: (1) videos were cropped from 13 s to 73 s, and (2) due to a higher frame rate, each 1-min video was composed of 1800 frames.

4.3.13 Tacking Larval Locomotion

Larval video-tracking was performed using the desktop version of AnimApp (Rao et al., 2019), as described in Paragraph 3.3.8. The HSV values used for the videos analysed in this chapter are shown in Table 48.

Table 48 HSV Values for Larval Tracking

Parameter	Value
Hue Lower	0
Saturation Lower	0
Value Lower	254

Hue Upper	180
Saturation Upper	255
Value Upper	255

4.3.14 Analysis of Larval Locomotion

The larval video-tracking output was analysed as described in Paragraph 3.3.9. The pixel-to-mm conversion was performed by dividing the distance travelled in pixels by 10.3 pixels / mm, because 3 cm correspond to 309 pixels with the video resolution used in this chapter.

4.3.15 Data Visualisation

The data were visualised as described in Paragraph 3.3.19, with boxplots drawn according to Tukey.

4.3.16 Statistics

Statistical analyses were performed using R (v. 3.6.0) and RStudio (RStudio Inc., v. 1.2.1335), as described in Paragraph 3.3.18.

4.4 Results

4.4.1 The DAM System Detects the *slo^{E366G}/+* Locomotor Defect

The aim of this chapter is to identify subpopulations of cells sufficient to induce the *slo^{E366G}/+* locomotor defect – a process referred to as "spatial dissection". Although the cellular characterisation of the *slo^{E366G}* allele was performed in larvae (Paragraphs 3.4.3, 3.4.4, and 3.4.5), adults were used for the spatial dissection experiments because larval video-tracking does not lend itself to high-throughput analyses. To measure adult locomotion, I used the DAM system, which infers activity from the number of times flies break an infrared beam (Pfeiffenberger et al., 2010). This system does not require the pre-processing of large video files and offline video-tracking, making it suitable for large-scale experiments. However, it first needed to be confirmed that the DAM system is sensitive enough to detect the reduction in travelling distance of *slo^{E366G}/+* adults, as observed using the DART system (Figure 3.17). To this end, two independent recombinants of *slo^{E366G}/+* and *slo^{loxP}/+* were tested: *25.1.1/+* and *137.1.3/+* for *slo^{E366G}/+* and *132.1.1/+* and *111.1.1/+* for *slo^{loxP}/+*. Indeed, the DAM system detected the *slo^{E366G}/+* locomotor defect in 24-h recordings at a 12 h light:12 h dark cycle (Figure 4.1) – these are the recording conditions used for all DAM experiments throughout this chapter.
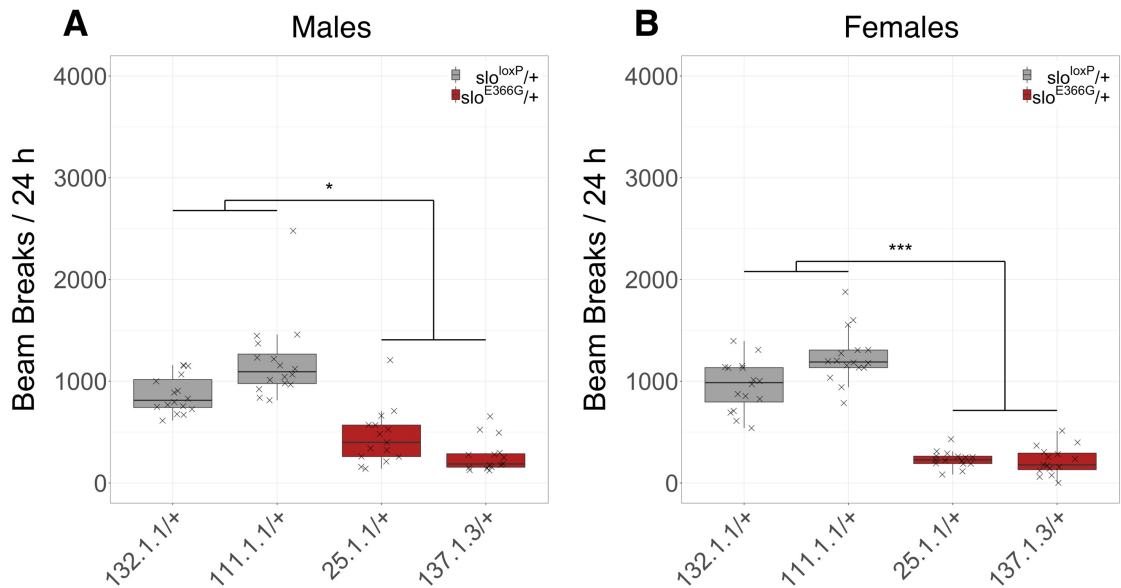
Figure 4.1 Validation of the DAM System for Locomotor Tracking

The DAM system detected a significant decrease in locomotion of slo^{E366G}/+ (*25.1.1/+* and *137.1.3/+*) males (**A**) and females (**B**), compared to slo^{loxP}/+ (*132.1.1/+* and *111.1.1/+*). No within-genotype differences were detected. (n = 15-16; Kruskal-Wallis multiple comparison with Dunn's post-hoc test, * = p < 0.05, *** = p < 0.001)

Figure 4.1 confirms that the DAM system can be used for the spatial dissection of the slo^{E366G}/+ locomotor phenotype. As a reduction in locomotion was detected for both sexes, I proceeded by focussing exclusively on males. First, a strategy needed to be designed that allows for the spatially restricted modification of Slo activity.

4.4.2 *slo* Knock-down does not Affect Locomotion

A common approach to downregulate the expression of target genes is RNA interference (RNAi)-mediated knock-down, which induces the degradation or translational inhibition of specific target mRNAs (Heigwer et al., 2018). Due to the gain-of-function nature of the slo^{E366G} allele (Figure 3.11), I hypothesised that RNAi-mediated knock-down of *slo* should rescue the slo^{E366G}/+ locomotor defect by scaling Slo function back to more physiological levels. In order to test this hypothesis, I expressed *slo-RNAi* pan-neuronally under the control of the *nSyb-Gal4* driver, using the Gal4/UAS system (Figure 1.3) (Brand and Perrimon, 1993). *nSyb-Gal4* drives *Gal4* expression in cells expressing neuronal Synaptobrevin, a

vesicle-associated membrane protein (VAMP) that is required for the secretion of synaptic vesicles and expressed specifically by neurons (Bhattacharya et al., 2002). To perform pan-neuronal knock-down of *slo* in the background of *slo^{E366G}/+* and *slo^{loxP}/+*, I generated the novel fly lines *UAS-sloRNAi/CyO;slo^{E366G}/TM6B,Tb* and *UAS-sloRNAi/CyO;slo^{loxP}/TM6B,Tb* according to Figure 4.2. This crossing scheme was used throughout this chapter to combine two constructs on the second and third chromosomes in a single *Drosophila* line.

w;+;TM2,Ubx^{130}/TM6B,Tb   X   *w;Sco/CyO;+*

w/Y;+/Sco;+/TM6B,Tb   X   *w/w;**A**/CyO;+*   *w;+;**B**/TM6B,Tb*   X   *w;+/CyO;+/TM2,Ubx^{130}*

*w/Y;**A**/Sco;+/TM6B,Tb*   X   *w/w;+/CyO;**B**/TM2,Ubx^{130}*

*w;**A**/CyO;**B**/TM6B,Tb*
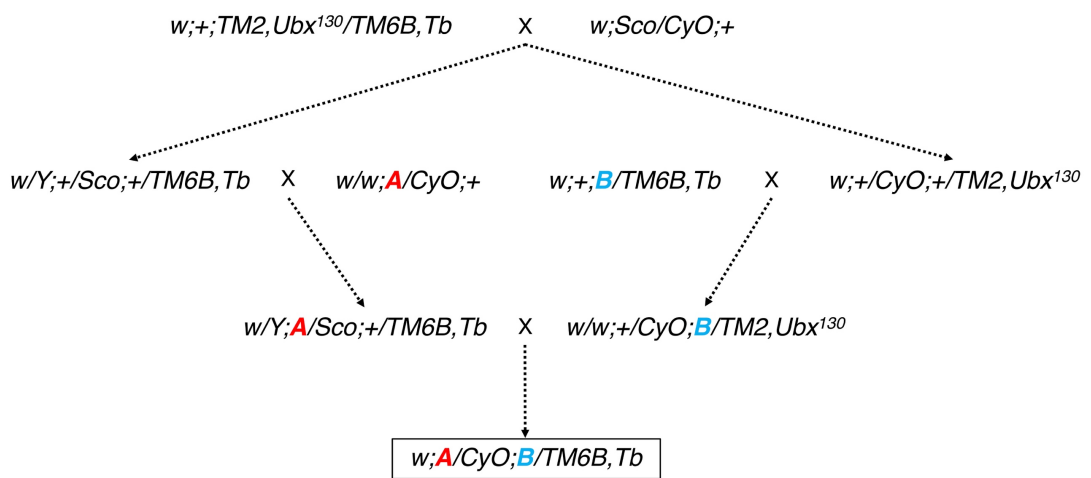
Figure 4.2 Combining Constructs on Chromosomes 2 and 3

This generic crossing scheme illustrates how novel fly stocks were generated by bringing together constructs located on the second (**A**, red) and third (**B**, cyan) chromosomes into a single fly stock.

The novel stocks *UAS-sloRNAi/CyO;slo^{E366G}/TM6B,Tb* and *UAS-sloRNAi/CyO;slo^{loxP}/TM6B,Tb* were used to generate the experimental genotypes *UAS-sloRNAi/+;nSyb-Gal4/slo^{E366G}* and *UAS-sloRNAi/+;nSyb-Gal4/slo^{loxP}*, which induce the pan-neuronal knock-down of *slo* in the background of *slo^{E366G}/+* and *slo^{loxP}/+*, respectively. Pan-neuronal knock-down of *slo* did not rescue the *slo^{E366G}/+* locomotor defect (Figure 4.3). In a *slo^{E366G}/+* background, the control genotype *nSyb-Gal4/slo^{E366G}* alone increased the number of beam breaks to a degree indistinguishable from the experimental genotype (Figure 4.3).
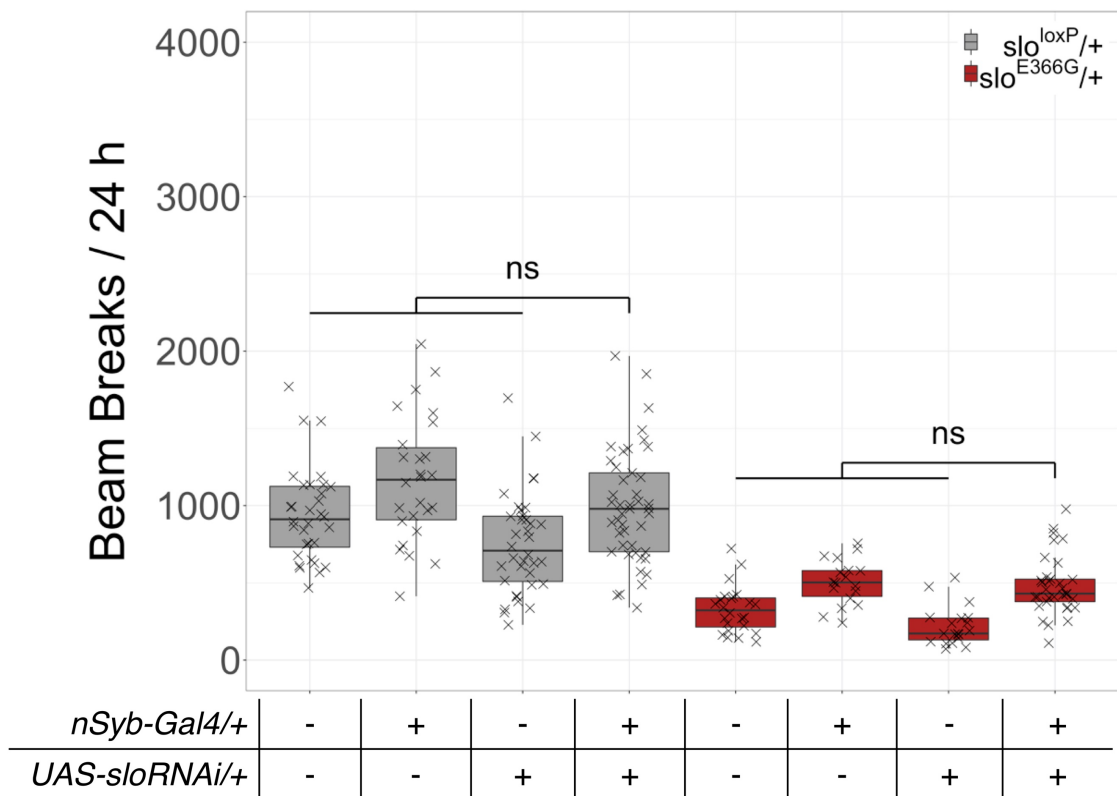
Figure 4.3 Pan-neuronal Knock-down of *slo* does not Affect Locomotion

Pan-neuronal knock-down of *slo* did not rescue the *slo^E366G/+* locomotor defect. Similarly, locomotion in a *slo^loxP/+* background was unaffected. Data from three independent experimental repeats were pooled. (n = 18-45; Kruskal-Wallis multiple comparison with Dunn's post-hoc test, ns = p > 0.05)

4.4.3 Selective Expression of Slo via Dysc

Why did the pan-neuronal RNAi-mediated knock-down of *slo* fail to rescue the *slo^E366G/+* locomotor defect (Figure 4.3)? It is possible that the *slo*-RNAi construct used for these experiments exhibits inefficient knock-down of *slo*, which could be tested via qPCR and the use of alternative *slo*-RNAi constructs. However, a general drawback of the RNAi strategy is that it induces an indiscriminate knock-down of both the wild-type and the mutant *slo* allele in a *slo^E366G/+* background. Maybe the preservation of relative expression levels prevents a behavioural rescue. Rather than optimising this experimental design, I opted to take another approach. Recently, it was shown that *dysc* encodes a PDZ domain-containing scaffolding protein (Dysc) that is required for the post-transcriptional expression of Slo (Jepson et al., 2012) (Paragraph 1.5.3). In homozygous *dysc* null flies, Slo

expression in the adult brain was almost entirely lost, and *dysc* null neurons exhibited a reduction in Slo-dependent K^+ currents (Jepson et al., 2012). Furthermore, Dysc and Slo were shown to regulate each other's expression via direct protein-protein interactions (Jepson et al., 2012). This dependence of Slo function upon Dysc could potentially be harnessed for the selective expression of Slo in specific subpopulations of cells if the following two hypotheses could be confirmed:

1. A homozygous *dysc* null background should rescue the $slo^{E366G}/+$ locomotor defect, since the expression of Slo^{E366G} should be greatly reduced.

2. The selective re-introduction of *dysc* in *dysc* null homozygotes should allow for Slo to be expressed wherever *dysc* is expressed, while the rest of the fly body should mostly lack Slo expression. If *dysc* is re-introduced in a $slo^{E366G}/+$ background, both Slo and Slo^{E366G} should be expressed, which should re-instate the $slo^{E366G}/+$ locomotor defect.

To test the first hypothesis, I compared the locomotor behaviour of $slo^{E366G}/+$ to $slo^{E366G}/+$ in a homozygous *dysc* null background. *dysc* is located on the third chromosome and expresses two major isoforms, a short and a long one, and it has been shown that the long isoform, which contains 3 C-terminal PDZ domains, is necessary and sufficient for normal locomotor behaviour in adult flies (Jepson et al., 2012). I hence performed this experiment using the $dysc^{s168}$ allele, a hypomorphic P-element insertion within the *dysc* locus that results in the selective loss of the long isoform, while leaving the short isoform intact (Jepson et al., 2012). The novel lines $slo^{E366G},dysc^{s168}/TM6B,Tb$ and $slo^{loxP},dysc^{s168}/TM6B,Tb$ were generated according to Figure 4.4, which illustrates in general terms how third chromosome recombinants were made throughout this chapter.

$w;+;$ ***A****/TM6B,Tb*   X $w;+;$ ***B****/TM6B,Tb*

$w/w;+;$ ***A****/****B***   X $w/Y;+;TM2,Ubx^{130}/TM6B,Tb$

$w/Y;+;$ ***A****,****B****/TM6B,Tb*   X $w/w;+;TM2,Ubx^{130}/TM6B,Tb$

$\boxed{w;+;\textbf{\textit{A}},\textbf{\textit{B}}/TM6B,Tb}$

Figure 4.4 Generating Third Chromosome Recombinants

This crossing scheme illustrates how constructs **A** (red) and **B** (cyan) were recombined on the third chromosome.

The $slo^{E366G},dysc^{s168}/TM6B,Tb$ and $slo^{loxP},dysc^{s168}/TM6B,Tb$ recombinants were used to generate the experimental genotypes $slo^{E366G},dysc^{s168}/dysc^{s168}$ and $slo^{loxP},dysc^{s168}/dysc^{s168}$, whose locomotion was compared to $slo^{E366G}/+$ and $slo^{loxP}/+$, respectively. Strikingly, homozygous $dysc^{s168}$ completely rescued the $slo^{E366G}/+$ locomotor defect, while also significantly increasing locomotion in a $slo^{loxP}/+$ background (Figure 4.5). The latter effect is consistent with previous reports that $dysc^{s168}$ homozygotes exhibit increased day- and night-time activity (Jepson et al., 2012). Interestingly, locomotion is also increased in $slo^{E366G},dysc^{s168}/dysc^{s168}$ when compared to $slo^{loxP},dysc^{s168}/dysc^{s168}$ (Figure 4.5). These data confirm the first hypothesis, as outlined above: loss of *dysc* completely rescues the $slo^{E366G}/+$ locomotor defect, rendering the $dysc^{s168}$ allele a recessive suppressor of this phenotype.
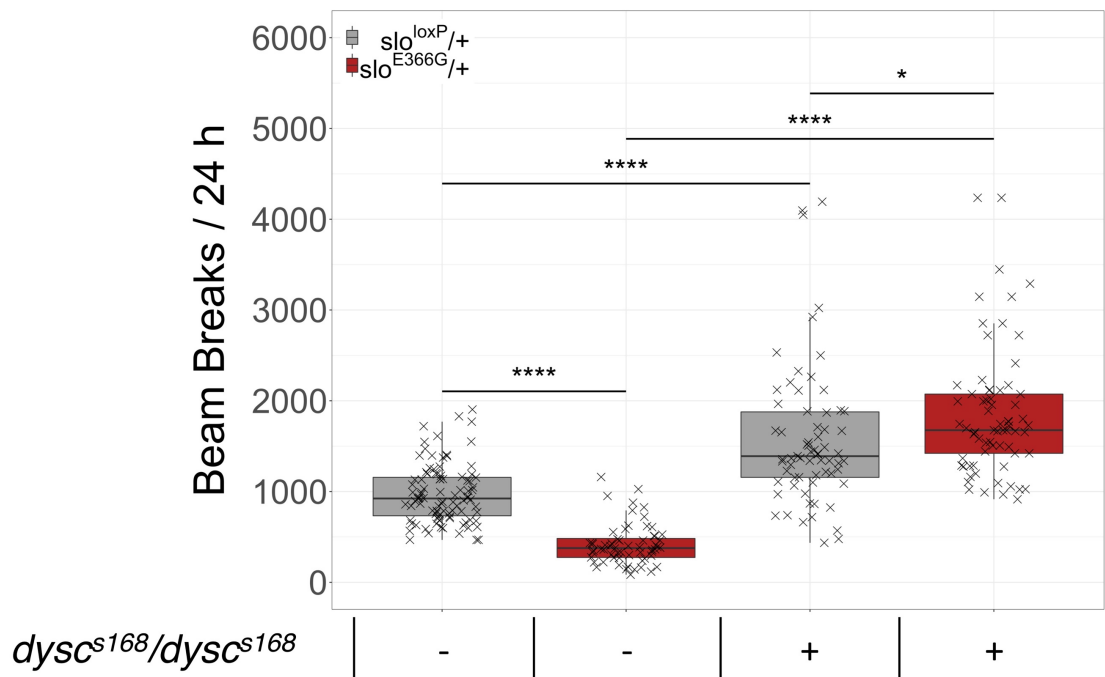
Figure 4.5 *dysc^s168^/dysc^s168^* Rescues the *slo^E366G^/+* Locomotor Defect

The *slo^E366G^/+* locomotor defect was completely rescued in *dysc^s168^* homozygotes, while locomotion was significantly increased in a *slo^loxP^/+* background as well. A significant difference in locomotion could also be observed between *dysc^s168^* homozygotes of either genetic background. Data from six independent experimental repeats were pooled. (n = 60-96; Kruskal-Wallis multiple comparison with Dunn's post-hoc test, * = p < 0.05, **** = p < 0.0001)

I proceeded to test whether the re-introduction of *dysc* in *slo^E366G^,dysc^s168^/dysc^s168^* could re-instate the *slo^E366G^/+* locomotor defect. To this end, I used *da-Gal4* to drive *dysc* expression (Wodarz et al., 1995): Daughterless (Da) is a TF involved in processes ranging from nervous system development to sex determination, showing a broad expression pattern that becomes detectable during embryonic stages (http://flybase.org/reports/FBgn0267821). Hence, this driver will induce *dysc* expression widely throughout the *Drosophila* body, starting early in development. In order to perform this experiment, the stocks *UAS-dysc/CyO;slo^E366G^,dysc^s168^/TM6C,Sb* and *UAS-dysc/CyO;slo^loxP^,dysc^s168^/TM6C,Sb* were generated according to Figure 4.2. Of note, the *UAS-dysc* construct drives the expression of the wild-type long isoform of *dysc*, which is lost in *dysc^s168^/dysc^s168^*. In order to establish homozygosity for *dysc^s168^*, the *da-Gal4,dysc^s168^/TM6B,Tb* recombinant line was made according to

Figure 4.4. Figure 4.6 illustrates the experimental design for the Dysc-mediated spatial dissection strategy – these crossing schemes were used throughout this chapter to generate experimental genotypes with different *Gal4* drivers.

A

w;UAS-dysc/CyO;slo^{E366G},dysc^{s168}/TM6C,Sb   X   *w;X-Gal4,dysc^{s168}/TM6B,Tb*

| *w;UAS-dysc/+;slo^{E366G},dysc^{s168}/X-Gal4,dysc^{s168}* |

B

w;UAS-dysc/CyO;slo^{E366G},dysc^{s168}/TM6C,Sb   X   *w;X-Gal4/CyO;dysc^{s168}/TM6B,Tb*

| *w;UAS-dysc/X-Gal4;slo^{E366G},dysc^{s168}/dysc^{s168}* |
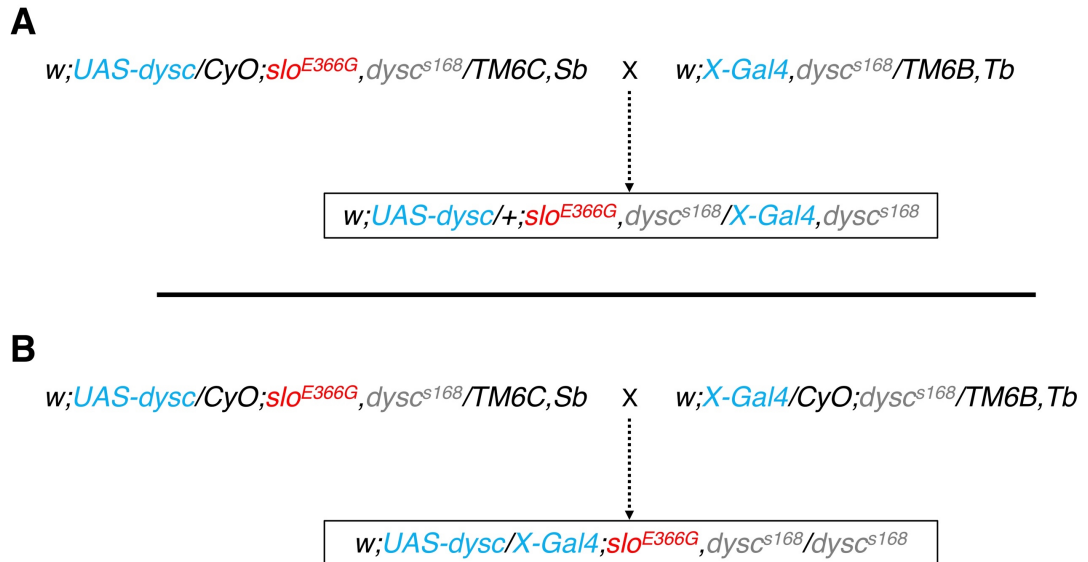
Figure 4.6 Dysc-mediated Spatial Dissection Strategy

This figure illustrates the genotypes required for the conditional re-introduction of *dysc* (cyan) in an otherwise *dysc* null background (grey) that also harbours the heterozygous *slo^{E366G}* allele (red). For simplicity, this strategy is only shown for the *slo^{E366G}* allele, but it equally applies to *slo^{loxP}*. **A** illustrates this strategy for *Gal4* drivers located on chromosome 3, while **B** shows the genotypes involved for *Gal4* drivers located on chromosome 2. The conditional re-introduction of *dysc* induces Slo expression in specific subpopulations of cells, while every cell not expressing *dysc* will mostly lack Slo expression. The *UAS-dysc* construct drives the expression of the wild-type long isoform of *dysc,* which is lost in *dysc^{s168}* homozygotes.

As shown in Figure 4.7, the broad re-introduction of *dysc* using the *da-Gal4* driver significantly decreased the number of beam breaks in a *slo^{E366G}/+* background, while not affecting locomotion in a *slo^{loxP}/+* background (Figure 4.7). These data confirm the second hypothesis, as stated above: the re-introduction of *dysc* in *dysc^{s168}* homozygotes re-instates the *slo^{E366G}/+* locomotor defect. Hence, this strategy can be used for the spatial dissection of this phenotype.

dysc^{s168}/dysc^{s168}	+	+	+	+	+	+	+	+
da-Gal4/+	-	+	-	+	-	+	-	+
UAS-dysc/+	-	-	+	+	-	-	+	+
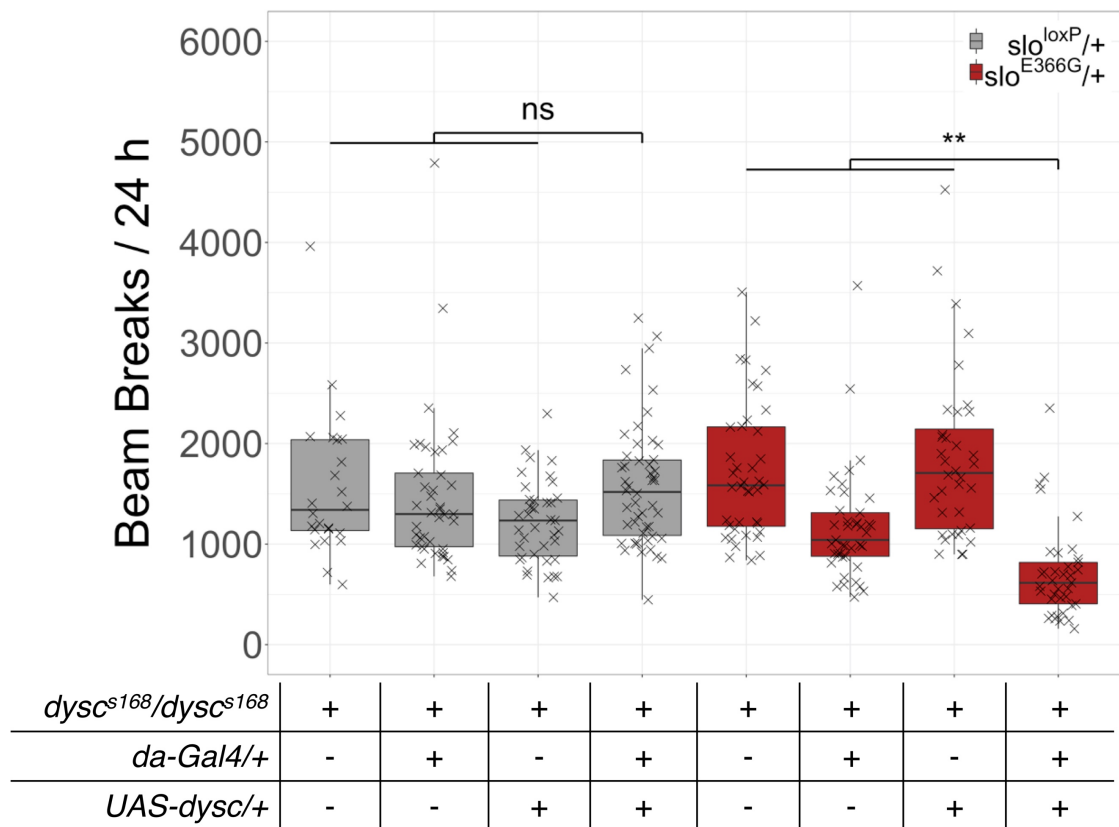
Figure 4.7 Broad Expression of Slo^{E366G} Decreases Locomotion

The broad re-introduction of *dysc* in *dysc^{s168}* homozygotes via *da-Gal4* significantly decreased locomotion in a *slo^{E366G}/+* background – an effect not observed in a *slo^{loxP}/+* background. Data from three independent experimental repeats were pooled. (n = 24-50; Kruskal-Wallis multiple comparison with Dunn's post-hoc test, ns = p > 0.05, ** = p < 0.01)

4.4.4 Neuronal Slo^{E366G} Induces the *slo^{E366G}/+* Locomotor Defect

The selective re-introduction of *dysc* in *dysc^{s168}* homozygotes mediates the selective expression of Slo. In a *slo^{E366G}/+* background, this leads to the expression of both Slo^{E366G} and Slo, while in a *slo^{loxP}/+* background, only Slo is expressed. Using the broad driver *da-Gal4*, the *slo^{E366G}/+* locomotor defect could be re-instated in a *slo^{E366G}/+* genetic background (Figure 4.7). I next investigated the selective expression of Slo in the nervous system and muscle tissue. To express *dysc* pan-neuronally, the *nSyb-Gal4* driver was used, as described in Paragraph 4.4.2 (Bhattacharya et al., 2002). To selectively target muscle tissue, I used *Mef2-Gal4*. *Mef2* is a TF involved in muscle differentiation, and the *Mef2-Gal4* line has been generated by cloning *Mef2* enhancer- and promoter elements

169

that allow for *Gal4* expression in somatic-, visceral-, and cardiac muscle (Ranganayakulu et al., 1998). For these experiments, the novel genotypes *nSyb-Gal4,dysc^{s168}/TM6B,Tb* and *Mef2-Gal4,dysc^{s168}/TM6B,Tb* were generated according to Figure 4.4, the experimental genotypes according to Figure 4.6. Strikingly, pan-neuronal re-introduction of *dysc* in a *slo^{E366G}/+* background recapitulated the *da-Gal4*-mediated locomotor defect, while locomotion in a *slo^{loxP}/+* background was unaffected (Figure 4.8).

$dysc^{s168}/dysc^{s168}$	+	+	+	+	+	+	+	+
nSyb-Gal4/+	-	+	-	+	-	+	-	+
UAS-dysc/+	-	-	+	+	-	-	+	+
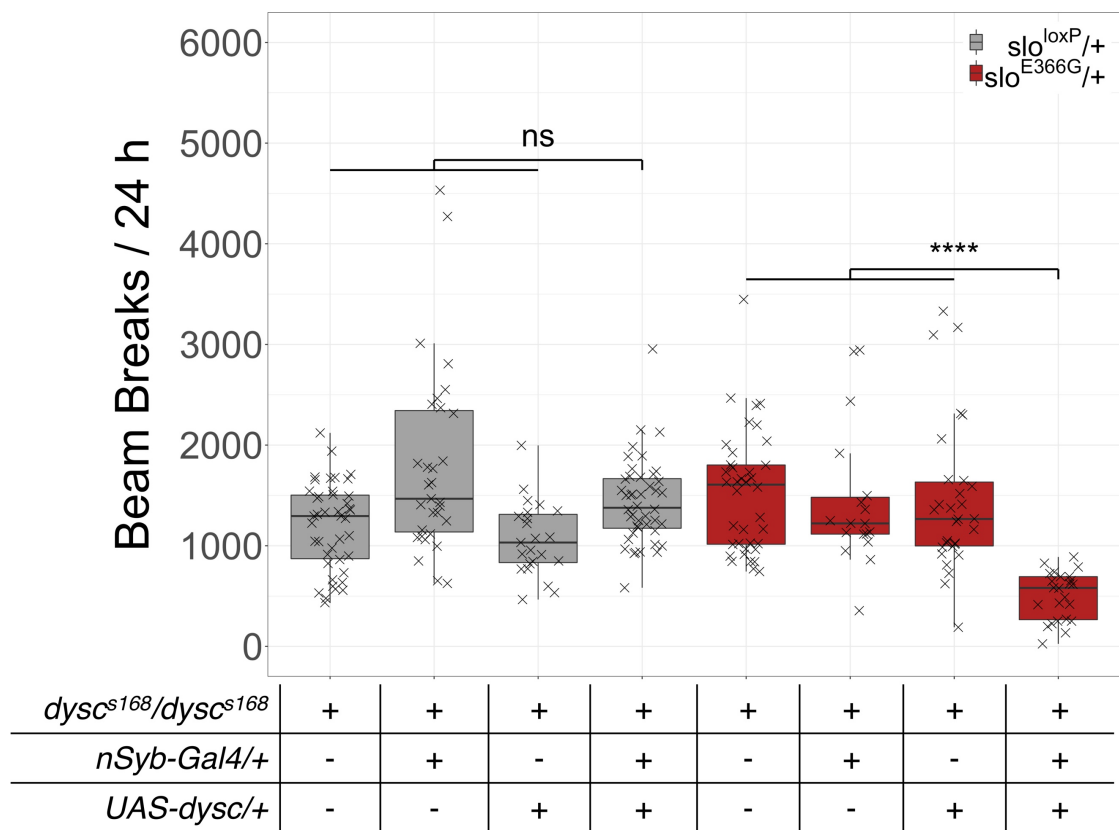
Figure 4.8 Pan-neuronal Expression of Slo^{E366G} Decreases Locomotion

The pan-neuronal re-introduction of *dysc* in *dysc^{s168}* homozygotes via *nSyb-Gal4* induced a significant decrease in locomotion in a *slo^{E366G}/+* background – an effect not observed in a *slo^{loxP}/+* background. Data from four independent experimental repeats were pooled. (n = 18-44; Kruskal-Wallis multiple comparison with Dunn's post-hoc test, ns = $p > 0.05$, **** = $p < 0.0001$)

The similar effects of pan-neuronal- (Figure 4.8) and broad (Figure 4.7) expression of Slo^{E366G} on locomotion suggested muscle tissue not to be involved in *slo^{E366G}/+* pathogenesis. Indeed, *Mef2-Gal4*-mediated re-introduction of *dysc* did not affect locomotion in a *slo^{E366G}/+* background (Figure 4.9). Together, these

data provide strong evidence that the pathogenic locus of the $slo^{E366G}/+$ locomotor defect lies within the nervous system.

$dysc^{s168}/dysc^{s168}$	+	+	+	+	+	+	+	+
Mef2-Gal4/+	-	+	-	+	-	+	-	+
UAS-dysc/+	-	-	+	+	-	-	+	+
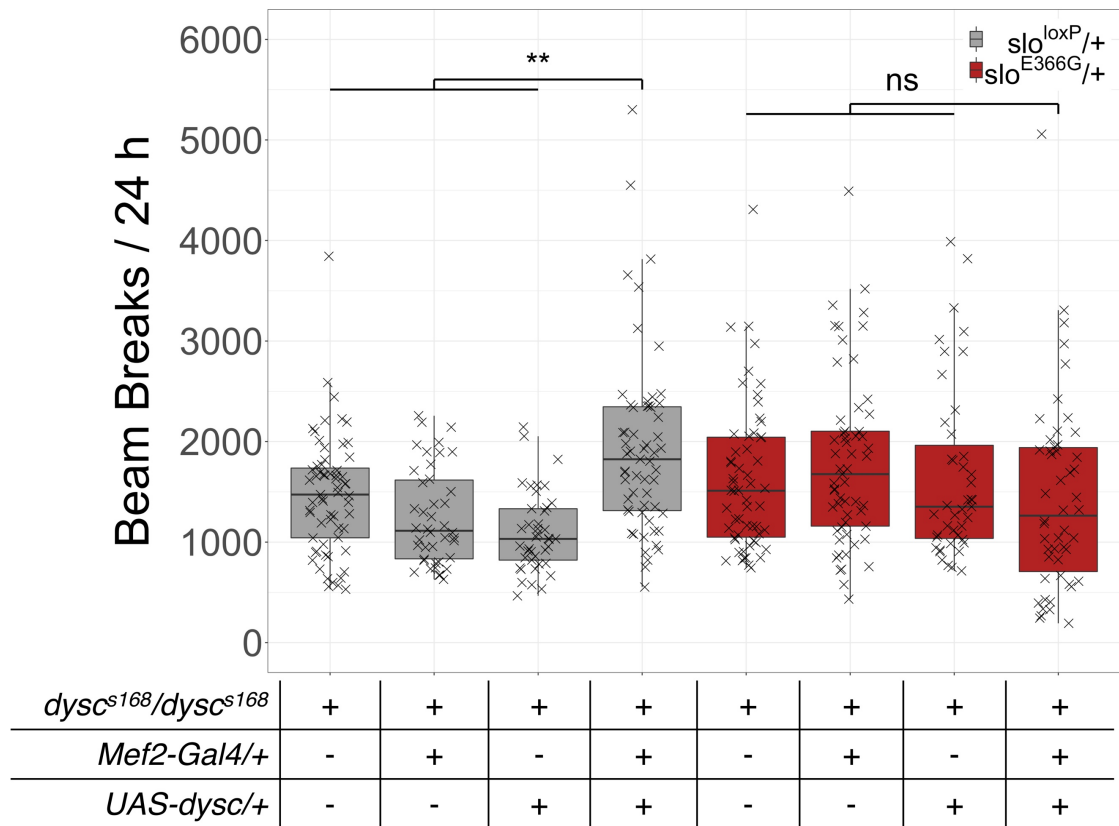
Figure 4.9 Slo^{E366G} in Muscle Tissue does not Affect Locomotion

Mef2-Gal4-mediated muscle-specific re-introduction of *dysc* in *dysc^{s168}* homozygotes did not affect locomotion in a *slo^{E366G}/+* background, while an increase could be observed in a *slo^{loxP}/+* background. Data from four independent experimental repeats were pooled. (n = 41-63; Kruskal-Wallis multiple comparison with Dunn's post-hoc test, ns = $p > 0.05$, ** = $p < 0.01$)

Why did the muscle-specific re-introduction of *dysc* cause an increase in locomotion in a *slo^{loxP}/+* background, but not in a *slo^{E366G}/+* background (Figure 4.9)? One possibility is that Slo and Slo^{E366G} have a pro-locomotive effect when selectively expressed in muscle tissue, but the *Mef2-Gal4* driver might show some expression in the brain as well. As a result, the locomotion-decreasing activity of Slo^{E366G} in the brain might offset its pro-locomotive activity in the muscle, specifically affecting the *slo^{E366G}/+* background. I tested this hypothesis by visualising the expression pattern of *Mef2-Gal4* in *UAS-CD8::GFP/+;Mef2-Gal4/+* adult brains. CD8-GFP is a fusion protein that links the mouse membrane-

tethered protein CD8 to GFP, facilitating the visualisation of the plasma membrane (Lee and Luo, 1999). The *Mef2-Gal4* expression pattern was compared to *UAS-CD8::GFP/+;nSyb-Gal4/+*, which is expected to label the brain pan-neuronally. The brain neuropil was visualised by co-staining against Bruchpilot (BRP), a pre-synaptic cytoskeletal protein (Rein et al., 2002). Interestingly, while *nSyb-Gal4* showed broad GFP expression throughout the brain, *Mef2-Gal4*-mediated GFP expression could also be detected, particularly in the PI and the ellipsoid body (EB, Figure 4.10). Hence, it is possible that the activity of Slo^{E366G} in these neurons suppresses its pro-locomotive effect in the muscle (Figure 4.9).
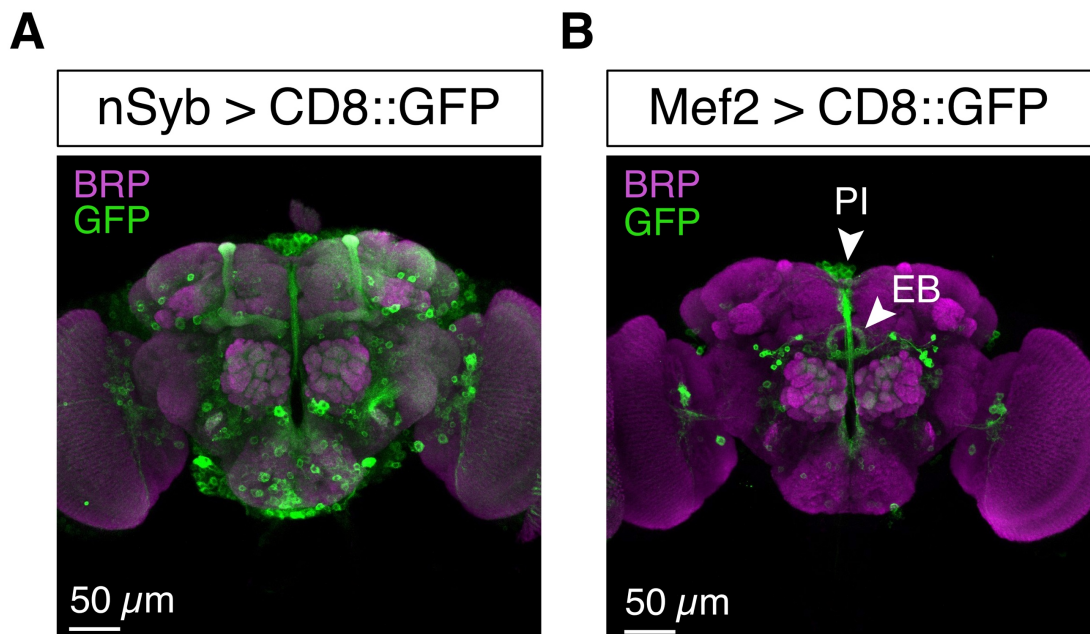
Figure 4.10 *Mef2-Gal4* Expression in the Adult *Drosophila* Brain

UAS-CD8::GFP/+;nSyb-Gal4/+ and *UAS-CD8::GFP/+;Mef2-Gal4/+* adult male brains were stained for GFP and the pre-synaptic marker BRP. (**A**) *nSyb-Gal4* is widely expressed throughout the brain. (**B**) *Mef2-Gal4* shows a more restricted expression pattern, with strong staining in the PI and the EB (white arrowheads). Scale bars indicate 50 μm.

4.4.5 Expression of Slo^{E366G} in Neuronal Subpopulations

Having shown that pan-neuronal re-introduction of *dysc* in a $slo^{E366G}/+$ background is sufficient to induce the $slo^{E366G}/+$ locomotor defect (Figure 4.8), I

investigated more restricted neuronal subpopulations. While cellular analyses demonstrated abnormal MN activity in $slo^{E366G}/+$ larvae (Figure 3.15), it remained unclear whether Slo^{E366G} induces this effect by altering dendritic excitability of MNs or by acting in neuronal populations upstream of MNs (Paragraph 3.5.2.2). I addressed this question in $slo^{E366G}/+$ adults by re-introducing *dysc* specifically in MNs using the glutamatergic *OK371-Gal4* driver described in Paragraph 3.4.5 (Mahr and Aberle, 2006). The novel line *OK371-Gal4/CyO;dysc^{s168}/TM6B,Tb* was generated according Figure 4.2, the experimental genotypes according to Figure 4.6. Interestingly, the re-introduction of *dysc* in MNs had no effect on locomotion, suggesting that Slo^{E366G} does not act autonomously in MNs to induce the $slo^{E366G}/+$ locomotor defect (Figure 4.11).

dysc^{s168}/dysc^{s168}	+	+	+	+	+	+	+	+
OK371-Gal4/+	-	+	-	+	-	+	-	+
UAS-dysc/+	-	-	+	+	-	-	+	+
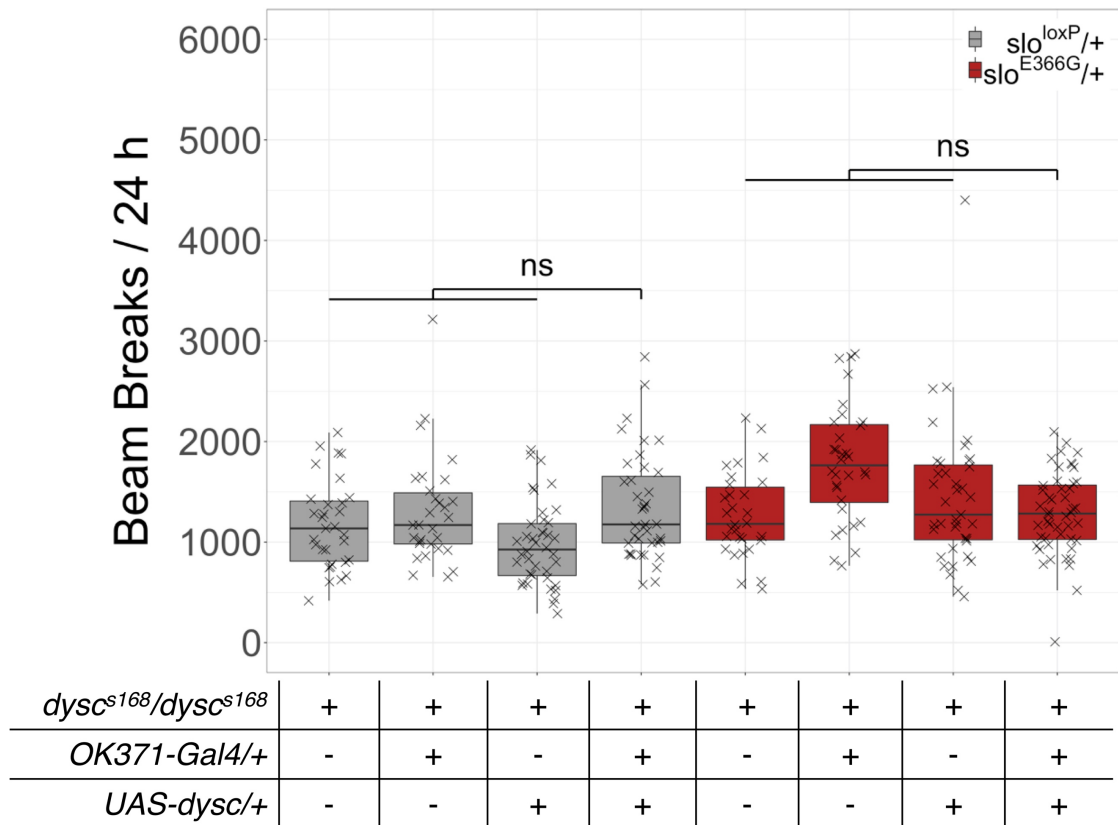
Figure 4.11 Slo^{E366G} in Motoneurons does not Affect Locomotion

The MN-specific re-introduction of *dysc* in *dysc^{s168}* homozygotes via *OK371-Gal4* did not affect locomotion in either a *slo^{E366G}/+* or a *slo^{loxP}/+* background. Data from two independent experimental repeats were pooled. (n = 30-48; Kruskal-Wallis multiple comparison with Dunn's post-hoc test, ns = p > 0.05)
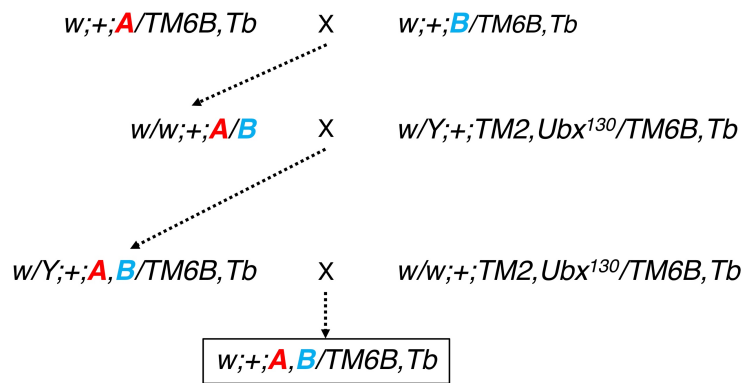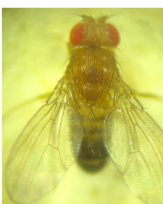
I proceeded to investigate alternative subpopulations of neurons. Since the non-inflated wing phenotype observed in $slo^{E366G}/+$ adults might be caused by altered peptidergic signalling involving *CCAP*-positive neurons (Tabuchi et al., 2018) (Paragraph 3.5.1.1), I hypothesised that altered peptidergic signalling might also be involved in eliciting the $slo^{E366G}/+$ locomotor defect. Hence, I re-introduced *dysc* in peptidergic neurons using the *c929-Gal4* driver. *c929-Gal4* is an enhancer trap line located within the locus of the pro-secretory TF *dimmed*, labelling most peptidergic neurons in the CNS (Hewes et al., 2003). The novel line *c929-Gal4/CyO;dysc^{s168}/TM6B,Tb* was generated according to Figure 4.2, the experimental genotypes according to Figure 4.6. No locomotor defect was observed upon re-introduction of *dysc* in peptidergic neurons (Figure 4.12).

dysc^{s168}/dysc^{s168}	+	+	+	+	+	+	+	+
c929-Gal4/+	-	+	-	+	-	+	-	+
UAS-dysc/+	-	-	+	+	-	-	+	+
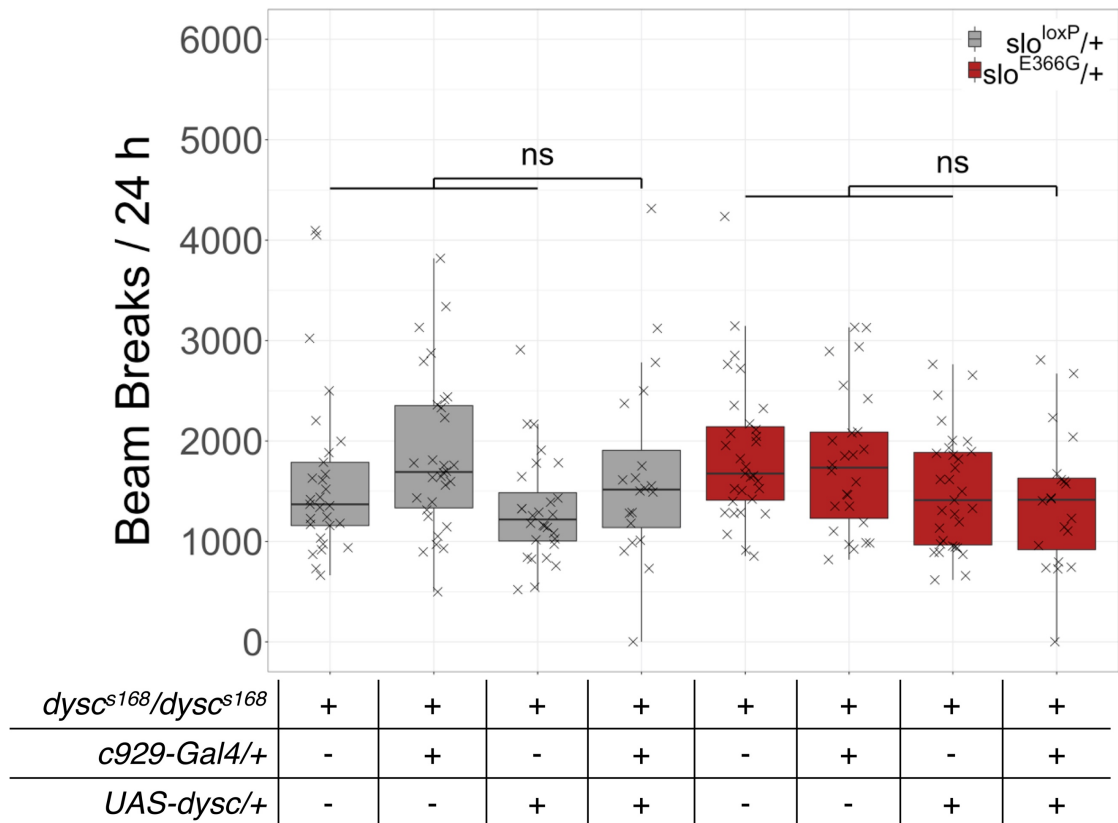
Figure 4.12 Slo^{E366G} in Peptidergic Neurons does not Affect Locomotion

The re-introduction of *dysc* in peptidergic neurons of *dysc^{s168}* homozygotes via *c929-Gal4* did not affect locomotion in either a *slo^{E366G}/+* or a *slo^{loxP}/+* background. Data from two independent experimental repeats were pooled. (n = 20-31; Kruskal-Wallis multiple comparison with Dunn's post-hoc test, ns = p > 0.05)

Although not affecting locomotion, the re-introduction of *dysc* in peptidergic neurons of *dysc^s168* homozygotes induced the non-inflated wing phenotype observed in *slo^E366G/+* (Figure 3.16): ~26% (6/23) of males exhibited non-inflated wings in a *slo^E366G/+* background, a phenotype that was not observed in a *slo^loxP/+* background (0/20) (Figure 4.13). Of note, only flies with fully inflated wings were used for the behavioural experiments shown in Figure 4.12.

		Dorsal	Lateral	Frequency
Male	Non-inflated			~26% (6/23)
	Semi-inflated			~9% (2/23)
	Fully inflated			~65% (15/23)

Figure 4.13 Peptidergic Slo^E366G Partially Suppresses Wing Inflation

23 *UAS-dysc/c929-Gal4;slo^E366G,dysc^s168/dysc^s168* males were scored according to wing inflation: non-inflation of wings, semi-inflation of wings, and fully inflated wings. While the peptidergic re-introduction of dysc induced a non-inflated wing phenotype in ~26% of these flies (6/23), none of 20 males exhibited this phenotype in a *slo^loxP/+* background.

These data dissociate the wing- from the locomotor phenotype, suggesting that the activity of Slo^E366G in peptidergic neurons specifically induces the former. In order to identify a neuronal subpopulation capable of recapitulating the *slo^E366G/+* locomotor defect, I next re-introduced *dysc* in GABAergic neurons with the *GAD-Gal4* driver. *GAD-Gal4* drives *Gal4* expression under the control of upstream regulatory sequences of *GAD1*, a gene encoding the enzyme Glutamic acid decarboxylase 1 (GAD1), which is involved in the synthesis of GABA and hence

expressed in all GABAergic neurons (Ng et al., 2002). The novel line *GAD-Gal4/CyO;dysc^{s168}/TM6B,Tb* was generated according to Figure 4.2, experimental genotypes according to Figure 4.6. As shown in Figure 4.14, the re-introduction of *dysc* in GABAergic neurons did not affect locomotion in a *slo^{E366G}/+* background, while causing a significant increase in a *slo^{loxP}/+* background. However, in contrast to the muscle-specific re-introduction of *dysc* (Figure 4.9), a trend towards increased locomotion in a *slo^{E366G}/+* background could be observed (Figure 4.14), suggesting that GABAergic neurons do not play a major role in eliciting the *slo^{E366G}/+* locomotor defect.

dysc^{s168}/dysc^{s168}	+	+	+	+	+	+	+	+
GAD-Gal4/+	-	+	-	+	-	+	-	+
UAS-dysc/+	-	-	+	+	-	-	+	+
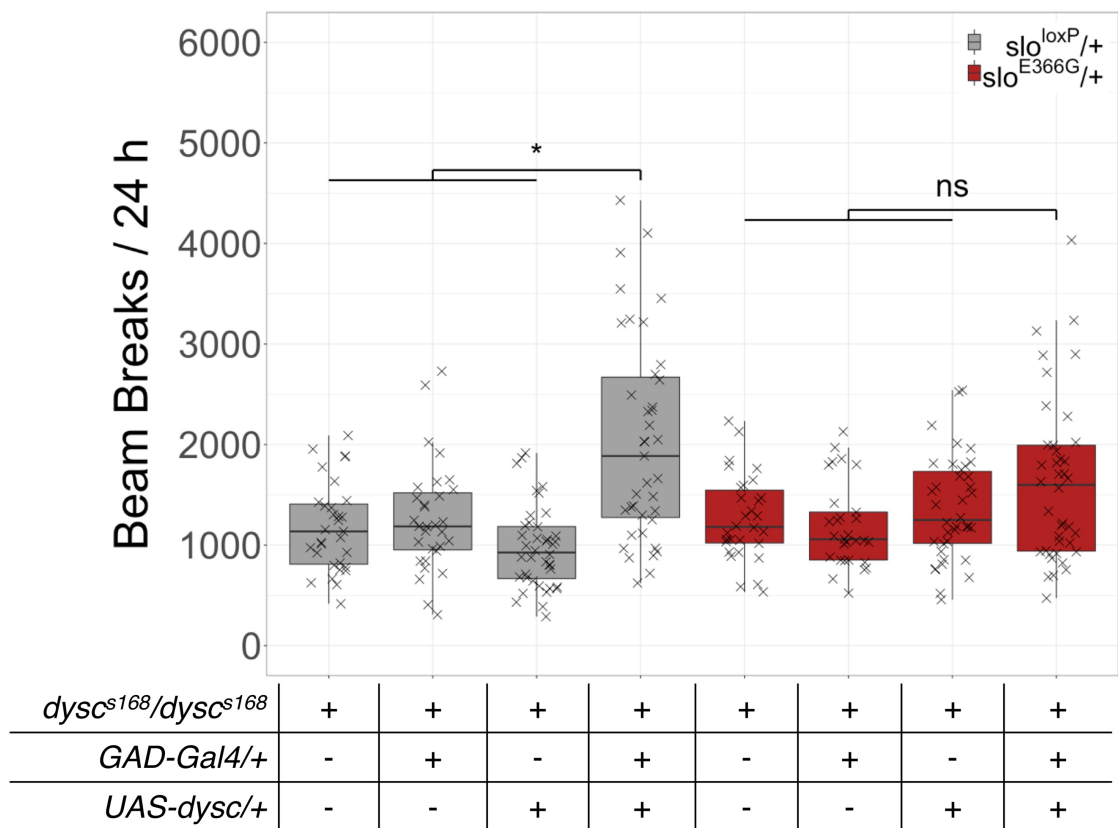
Figure 4.14 Slo^{E366G} in GABAergic Neurons does not Affect Locomotion

The re-introduction of *dysc* in GABAergic neurons of *dysc^{s168}* homozygotes via *GAD-Gal4* did not affect locomotion in a *slo^{E366G}/+* background, while significantly increasing it in a *slo^{loxP}/+* background. Data from two independent experimental repeats were pooled. (n = 30-40; Kruskal-Wallis multiple comparison with Dunn's post-hoc test, ns = $p > 0.05$, * = $p < 0.05$)

4.4.6 Cholinergic Slo^{E366G} Induces the *slo^{E366G}/+* Locomotor Defect

Cholinergic neurons release the neurotransmitter ACh and are prominently expressed throughout the *Drosophila* brain (Yasuyama and Salvaterra, 1999). Hence, I tested whether cholinergic re-introduction of *dysc* might affect locomotion, using the *ChAT-Gal4* driver. *ChAT-Gal4* drives *Gal4* expression under the control of a 7.4 kb DNA region 5' of the *Drosophila* cholinergic locus, and has been shown to label the vast majority of cholinergic neurons (Salvaterra and Kitamoto, 2001). The novel line *ChAT-Gal4/CyO;dysc^{s168}/TM6B,Tb* was generated according to Figure 4.2, the experimental genotypes according to Figure 4.6. Indeed, cholinergic re-introduction of *dysc* significantly decreased the number of beam breaks only in a *slo^{E366G}/+* background (Figure 4.15).

dysc^{s168}/dysc^{s168}	+	+	+	+	+	+	+	+
ChAT-Gal4/+	-	+	-	+	-	+	-	+
UAS-dysc/+	-	-	+	+	-	-	+	+
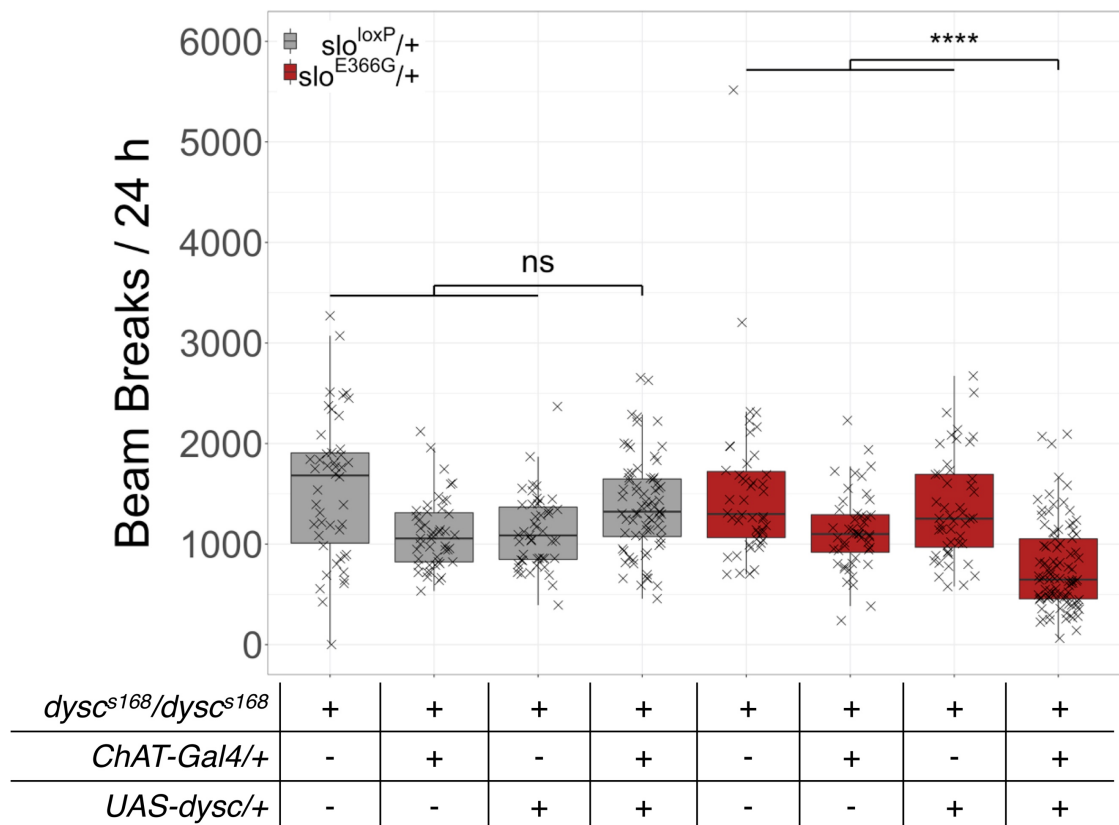
Figure 4.15 Slo^{E366G} in Cholinergic Neurons Decreases Locomotion

The re-introduction of *dysc* in cholinergic neurons of *dysc^{s168}* homozygotes via *ChAT-Gal4* significantly reduced locomotion in a *slo^{E366G}/+* background, while not affecting locomotion in a *slo^{loxP}/+* background. Data from three independent experimental repeats were pooled. (n = 46-93; Kruskal-Wallis multiple comparison with Dunn's post-hoc test, ns = p > 0.05, **** = p < 0.0001)

These data strongly suggest a role for cholinergic neurons in eliciting the $slo^{E366G}/+$ locomotor defect in adults. To test whether such an effect could also be observed in larvae, I repeated this experiment using the AnimApp video-tracking pipeline, which is illustrated in Figure 3.2 (Rao et al., 2019). As shown in Figure 4.16, the cholinergic re-introduction of *dysc* in larvae failed to induce the $slo^{E366G}/+$ locomotor defect.

$dysc^{s168}/dysc^{s168}$	+	+	+	+	+	+	+	+
ChAT-Gal4/+	-	+	-	+	-	+	-	+
UAS-dysc/+	-	-	+	+	-	-	+	+
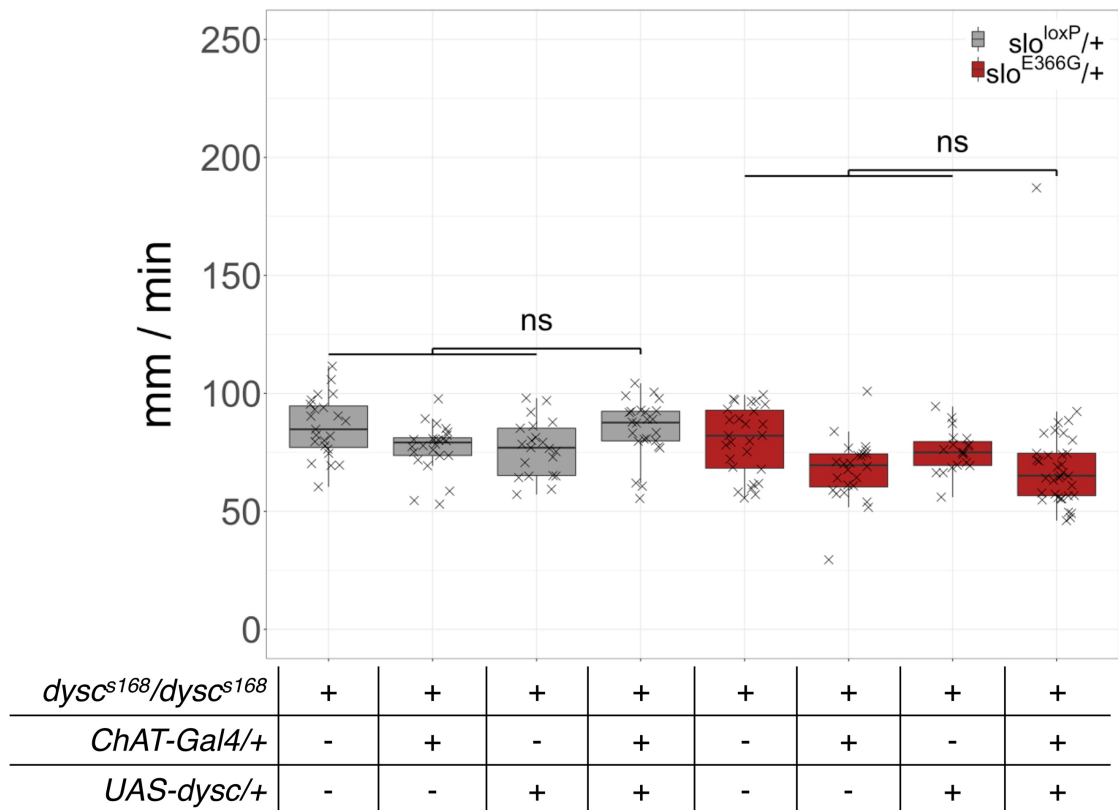
Figure 4.16 Cholinergic Slo^{E366G} does not Affect Larval Locomotion

The re-introduction of *dysc* in cholinergic neurons of $dysc^{s168}$ homozygotes via *ChAT-Gal4* did not affect larval locomotion in either a $slo^{E366G}/+$ or a $slo^{loxP}/+$ background. Larval video-recordings were performed for 1 min per larva. Data from two independent experimental repeats were pooled. (n = 19-35; Kruskal-Wallis multiple comparison with Dunn's post-hoc test, ns = $p > 0.05$)

4.5 Discussion

This chapter addresses the second question set out in the project aim: where is the slo^{E366G} allele required to exert its pathogenic effects? Using a targeted *dysc* re-introduction strategy into *dysc* null homozygotes, *in vivo* evidence is provided that the specific expression of Slo^{E366G} in the nervous system is sufficient to induce the $slo^{E366G}/+$ locomotor defect. Furthermore, the data presented in this chapter support the hypothesis, as outlined in Chapter 3, that this phenotype is caused by altered neural activity upstream of MNs. Specifically, cholinergic neurons are shown to contain the pathogenic locus of $slo^{E366G}/+$. Altogether, these data suggest a neuroanatomical basis for GEPD pathogenesis.

4.5.1 Experimental Notes and Caveats

4.5.1.1 Experimental Design of the Spatial Dissection Strategy

In order to restrict Slo expression to subpopulations of cells, *dysc* was conditionally expressed in a *dysc* null homozygous background. Due to the dependence of Slo expression upon Dysc (Jepson et al., 2012), this strategy allows for the expression of Slo specifically in cells into which *dysc* has been re-introduced. Indeed, the $slo^{E366G}/+$ locomotor defect was completely suppressed in *dysc^{s168}* homozygotes but could be re-instated by broadly re-introducing *dysc* (Figure 4.7). However, these data also show that homozygous *dysc^{s168}* increases locomotion in a *slo^{loxP}/+* background (Figure 4.5). This result demonstrates that the genetic background used for this spatial dissection strategy independently affects locomotion. Since *slo* null homozygotes (*slo^1* and *slo^4*) have been shown to exhibit normal overall activity levels (Ceriani et al., 2002), the increased locomotion of *dysc^{s168}* homozygotes illustrates the pleitropic nature of *dysc*, being involved in cellular processes other than the regulation of Slo expression. Indeed, immuno-staining detected Dysc in areas with little or no Slo expression, including parts of the antennal lobes, mushroom body, and ellipsoid body, suggesting that in these brain areas, Dysc performs cellular functions independent of Slo (Jepson et al., 2012). To control for these effects, it is important that the spatial dissection results presented in this chapter are independently confirmed. For example, RNAi-mediated knock-down experiments in a *slo^{E366G}/+* background could be

179

performed, targeting genes that Slo function depends on, such as *dysc*, or genes encoding Ca$_v$ channels (Griguoli et al., 2016) (Paragraph 1.4.3.1). Alternatively, the RNAi-mediated knock-down of *slo* could be optimised by testing alternative RNAi lines, doubling the dose of *slo*-RNAi, or co-expressing *Dicer2*, which encodes a dsRNA-specific endonuclease involved in the RNAi pathway that increases RNAi efficacy (Perrimon et al., 2010). Using *ChAT-Gal4* to drive these RNAi constructs, a rescue of the *slo^{E366G}/+* locomotor defect would confirm the results obtained via the Dysc-mediated expression of Slo.

4.5.1.2 Discrepant Results in Larvae and Adults

It is unclear why the expression of Slo^{E366G} in cholinergic neurons did not induce the *slo^{E366G}/+* locomotor defect in larvae (Figure 4.16). Electrophysiological and optical live-imaging evidence suggest that larval peristaltic frequency is affected by neurons upstream of MNs (Kadas et al., 2015; Pulver et al., 2015), including the CPG, which, as described in Paragraph 3.5.2.1, implicates pre-motor circuits in the *slo^{E366G}/+* larval locomotor defect. Moreover, it has recently been shown, via serial section TEM, that the majority of pre-MNs in L1 larvae are cholinergic (Zarin et al., 2019). These data support the hypothesis that in larvae, too, cholinergic neurons might be involved in mediating the *slo^{E366G}/+* locomotor defect. Importantly, Dysc has been shown to interact with Slo at the larval NMJ to regulate synapse- and AZ morphology as well as neurotransmission (Jepson et al., 2014). Moreover, it has been shown via immuno-staining that homozygous *dysc* null larvae lack Slo expression in the VNC (Jepson et al., 2014). These data strongly suggest that the dependence of Slo expression upon Dysc is conserved between L3 larvae and adults. Nonetheless, re-introducing *dysc* more broadly in larvae via *da-Gal4*, as performed in adults, will be necessary to validate this experimental strategy in larvae.

4.5.1.3 Slo^{E366G} in *CCAP*-positive Neurons Might Cause Wing-inflation Defect

The peptidergic re-introduction of *dysc* in a *slo^{E366G}/+* background induced the non-inflated wing phenotype observed in *slo^{E366G}/+* adults (Figure 4.13, Figure 3.16), while leaving locomotion unaffected (Figure 4.12), thereby dissociating the two phenotypes. These data strengthen the hypothesis outlined in Paragraph 3.5.1.1, suggesting that the *slo^{E366G}/+* wing-inflation defect might be caused by

the activity of Slo^{E366G} in *CCAP*-positive neurons. Indeed, the *c929-Gal4* driver, used for the peptidergic re-introduction of *dysc*, labels a subset of 14 *CCAP*-expressing neurons that directly release bursicon into the haemolymph – a hormone critical for wing expansion and cuticle tanning (Luan et al., 2006). Hence, I hypothesise that bursicon release from these 14 neurons is dysregulated in *slo^{E366G}/+*, resulting in the non-inflated wing phenotype – a hypothesis that could be tested by re-introducing *dysc* specifically in *CCAP*-expressing neurons using the *CCAP-Gal4* driver (Park et al., 2003).

4.5.2 Clinical Relevance

4.5.2.1 Cholinergic Neurons as a Pathogenic Locus for GEPD

As described in Paragraph 1.4.2, *KCNMA1* is expressed broadly throughout the human body, suggesting that the D434G mutation is likely to affect BK channel function in a variety of organs and tissues (Bailey et al., 2019). The results presented in this chapter provide the first *in vivo* evidence that the expression of this mutation in the nervous system is sufficient to induce GEPD pathogenesis (Figure 4.8). Moreover, by further restricting Slo^{E366G} expression, evidence is provided that cholinergic neurons contain the pathogenic locus of GEPD (Figure 4.15). How do these results fit into the PxD and movement disorder literature? As shown in Figure 1.1, the striatum is the main input structure of the human basal ganglia, receiving afferent connections from cortical areas. The most common cell type in the striatum is the GABAergic MSN (Kandel et al., 2013), as introduced in Paragraph 3.5.2.6. This neuronal subtype sends inhibitory projections via the direct and indirect pathways to the GPi-SNr and GPe, respectively, as well as reciprocal connections to the dopaminergic SNc (Figure 1.1) (Kandel et al., 2013). Hence, MSNs are integral components of motor behaviours such as action selection and the preparation and execution of movement (Kandel et al., 2013). As such, the activity of MSNs is under intricate control from a variety of brain areas: cortical and thalamic afferents form glutamatergic connections-, afferents from the SNc dopaminergic connections with MSN dendrites (Kandel et al., 2013). Importantly, while small local interneurons modulate MSN activity via GABAergic synapses, large local

interneurons within the striatum form cholinergic connections with MSNs (Kandel et al., 2013).

4.5.2.2 Focus on Striatal Cholinergic Interneurons

Considering the role of the basal ganglia in PxD and other movement disorders (Kandel et al., 2013) (Paragraph 1.2.2), the data provided in this chapter suggest that altered activity of striatal cholinergic interneurons might be involved in GEPD pathogenesis via dysregulating the activity of striatal MSNs. This hypothesis is strengthened by the finding that action selection – a behaviour under striatal MSN control (Kandel et al., 2013) – was found to be perturbed in $slo^{E366G}/+$ (Paragraph 3.5.2.6). As described in Paragraph 3.5.2.6, a recent study on a mouse model of LID identified a correlation between the firing rate of direct pathway striatal MSNs and dyskinesia severity, while also showing that the optogenetic activation of these neurons is sufficient to induce dyskinetic attacks in control mice (Ryan et al., 2018). These data illustrate the importance of striatal MSN activity in dyskinesia. Further evidence for their importance in regulating movement is provided by studies of DYT1 dystonia, a severe form of inherited dystonia linked to a deletion in *TOR1A* (Ozelius et al., 1997), which was introduced in Paragraph 1.5.2. *Ex vivo* sharp microelectrode recordings from MSNs in a DYT1 knock-in mouse model showed a bidirectional impairment of synaptic plasticity at corticostriatal synapses: DYT1 mice exhibited a loss of long-term depression (LTD) and an increased long-term potentiation (LTP) amplitude (Maltese et al., 2014; Martella et al., 2014). In particular, it could be shown that synaptic depotentiation (SD), the process of reversing LTP with a train of low-frequency stimulation (LFS), was severely impaired at DYT1 corticostriatal synapses (Maltese et al., 2014; Martella et al., 2014). Intriguingly, SD was completely restored upon application of specific M_1 muscarinic ACh receptor (mAChR) antagonists, demonstrating the importance of cholinergic modulation of MSNs in dystonia (Maltese et al., 2014; Martella et al., 2014). Indeed, anticholinergic drugs can be used to treat generalised and segmental dystonia as well as Parkinsonian tremor clinically (Jankovic, 2006; Poewe et al., 2017).

Since cholinergic modulation of striatal MSNs is performed by striatal cholinergic interneurons, it is of interest whether these neurons express BK

channels, as this might suggest their function to be altered in GEPD. Indeed, whole-cell recordings in rat striatal slices have demonstrated that neostriatal cholinergic interneurons express BK channels (Bennett et al., 2000; Goldberg and Wilson, 2005). By pharmacologically blocking specific types of Ca_v channels, strong evidence was provided that BK channels in striatal cholinergic interneurons are coupled to P/Q-type Ca_v channels and negatively regulate AP width (Bennett et al., 2000; Goldberg and Wilson, 2005). Striatal cholinergic interneurons are tonically active and exhibit three distinct rhythmic firing patterns that are sustained *in vitro*: regular single-spiking, irregular single-spiking, and rhythmic bursting (Goldberg and Wilson, 2005; Goldberg et al., 2009). Interestingly, selective inhibition of specific types of Ca_v channels can cause a transition between these intrinsic firing patterns (Goldberg and Wilson, 2005). Moreover, electrophysiological recordings from cholinergic interneurons in the primate putamen demonstrated that parkinsonian symptoms are linked to a transition from tonic- to oscillatory activity exhibited by these neurons (Raz et al., 1996). Hence, it is possible that the D434G mutation modulates the firing behaviour of striatal cholinergic interneurons via altered BK channel function, leading to a perturbed modulation of striatal MSN activity, which in turn might contribute to GEPD pathogenesis.

4.5.3 Conclusion

This chapter presented a genetic approach to specifically express Slo^{E366G} in subpopulations of cells and identified cholinergic neurons as a potential pathogenic locus of GEPD. It is still unclear, however, how the D434G mutation in *KCNMA1* might exert its pathogenic effects on a molecular level.

5 Molecular Analysis of $slo^{E366G}/+$

5.1 Introduction

Chapter 4 provided strong evidence suggesting that the pathogenic locus of $slo^{E366G}/+$ encompasses cholinergic neurons. An outstanding question, however, is how the slo^{E366G} allele affects molecular and cellular function. In the presence of this mutant allele, it is conceivable that two scenarios take place: (1) physiological cellular function is perturbed, and (2) compensatory responses are aimed at counteracting this perturbation in a homeostatic manner, in order to re-establish physiological function. Both processes could affect behaviour and contribute to the $slo^{E366G}/+$ locomotor defect. This chapter aims at establishing a link between molecular function and behaviour by identifying cellular pathways perturbed in $slo^{E366G}/+$. While contributing to an increased molecular understanding of GEPD, this approach might also uncover pathological principles that apply to PxD and epilepsy more generally.

To experimentally link molecular mechanisms and behaviour, I performed RNA-sequencing (RNA-seq) of $slo^{E366G}/+$ and $slo^{loxP}/+$ adult fly heads – a strategy aimed at detecting transcriptomic changes between these genotypes that might uncover pathophysiological disturbances of cellular function. Bioinformatic analyses of 1036 differentially expressed genes (DEGs) demonstrate that $slo^{E366G}/+$ flies exhibit perturbed metabolic-, redox-, and immune function, while the TF Foxo is predicted to regulate almost half of the genes over-expressed in $slo^{E366G}/+$. Functionally testing these results via a dominant modifier screen based on locomotor behaviour identified a genetic interaction between *foxo* and slo^{E366G}, while also implicating dysregulated insulin signalling with the $slo^{E366G}/+$ locomotor defect. These results establish a first *in vivo* link between molecular function and behaviour in GEPD.

5.2 Statement of Contribution

5.2.1 Direct Contributions

Deborah Hughes operated the HiSeq 3000 sequencing system, while also performing the final Bioanalyzer run of pooled cDNA libraries. Together with Deborah Hughes, I generated a sample sheet used by Dr. Alan Pittman for de-multiplexing and file conversion of the sequencing data. Table 49 lists these contributions and indicates the figures generated based on the data.

Table 49 Experimental Contributions to Chapter 5

Contributing Researcher	Corresponding Figure
Deborah Hughes and Patrick Kratschmer	Figure 9.2
Dr. Alan Pittman	Table 55
Deborah Hughes and Patrick Kratschmer	Figure 5.4

5.2.2 Indirect Contributions

Dr. Ko-Fan Chen has been of great help during the initial stages of RNA extraction, sharing his expertise in molecular biology. Deborah Hughes has been of great help in setting up an experimental pipeline for the generation of cDNA libraries. Dr. Ko-Fan Chen and Tony Brooks have been of incredible help during the optimisation of the cDNA library preparation protocol. Dr. Alan Pittman has been a fantastic bioinformatics teacher and greatly contributed to my progress in programming. Dr. James Jepson provided invaluable intellectual input during the interpretation of the RNA-seq data.

5.3 Materials and Methods

5.3.1 Genetic Nomenclature

The genotypes of flies used in this chapter are listed in Paragraph 5.3.2.

The nomenclature guidelines described in Paragraph 2.3.1 were adjusted for the insulin-themed modifier screen: only mutations of interest are denoted in the main text, not every mutation deviating from iso^{31}. For example, $cn,chico^1/+;ry/slo^{E366G/loxP}$ is denoted as $chico^1/+;+/slo^{E366G/loxP}$.

5.3.2 Fly Stocks

Table 50 Fly Stocks of Chapter 5

Genotype	Source
iso^{31}	Kind gift from Dr. Kyunghee Koh
$w;;slo^{E366G}/TM6B,Tb$	This thesis
$w;;slo^{loxP}/TM6B,Tb$	This thesis
$w;;slo^{E366G[w+]}/TM6B,Tb$	This thesis
$w;;slo^{loxP[w+]}/TM6B,Tb$	This thesis
$w;;dilp1^1$	BDSC: 78055
$w;;dilp2^1$	BDSC: 30881
$w;;dilp3^1$	BDSC: 30882
$w;;dilp4^1$	BDSC: 30883
$w;;dilp5^1$	BDSC: 30884
$y,w,dilp6^{68};;$	BDSC: 30886
$w,dilp7^1;;$	BDSC: 30887
$y,w;;dilp8^{M727}$	BDSC: 33079
$w;;dilp2-3$	BDSC: 30888
$w;;dilp2-3,5^3/TM3,Sb$	BDSC: 30889
$y,w,dilp6^{68};;dilp2-3,5^3/TM3,Sb$	BDSC: 30891
$w,dilp7^1;;dilp2-3,5^3/TM3,Sb$	BDSC: 30893
$w;;dilp1-4,5^4/TM3,Sb$	BDSC: 30890
$w,dilp7^1;;dilp1-4,5^4/TM3,Sb$	BDSC: 30894
$;;ry,InR^{P45}/TM3,ry,Sb,Ser$	BDSC: 11661

;;InR^{E19}/TM2,Ubx^{130}	BDSC: 9646
;cn,chico^{1}/CyO;ry	BDSC: 10738
;;ry,Akt^{P4226}/TM3,ry,Sb,Ser	BDSC: 11627
w;;foxo^{Δ94}/TM6b,Tb	BDSC: 42220
w;;to^{P632}	BDSC: 10202
w;;ImpL2^{M4721}	BDSC: 24219

5.3.3 Fly Husbandry

Unless otherwise indicated, all fly stocks were kept on standard fly food at RT. The recipe of the standard fly food is shown in Table 4. All flies used for behavioural experiments were maintained at 25°C on a 12 h light:12 h dark cycle.

5.3.4 Experimental Genotypes

Unless otherwise indicated, recombinant *25.1.1/TM6B,Tb* was used as a representative for *slo^{E366G}/TM6B,Tb*, and recombinant *132.1.1/TM6B,Tb* as a representative for *slo^{loxP}/TM6B,Tb*.

5.3.4.1   *slo^{E366G}/+* and *slo^{loxP}/+*

slo^{E366G}/+ and *slo^{loxP}/+* flies were generated by crossing *slo^{E366G}/TM6B,Tb* and *slo^{loxP}/TM6B,Tb* to isogenic controls (*iso^{31}*), respectively.

5.3.4.2 Insulin-themed Modifier Screen

Experimental genotypes for the insulin-themed modifier screen were generated by crossing the BDSC-acquired stocks shown in Table 50 to *slo^{E366G}/TM6B,Tb* and *slo^{loxP}/TM6B,Tb*. Table 51 lists the experimental genotypes as well as the nature of the mutant alleles.

Table 51 Experimental Genotypes for Insulin-themed Modifier Screen

Experimental Genotype	Allele Type
dilp1^{1}/slo$^{E366G/loxP}$	Null allele[1]
dilp2^{1}/slo$^{E366G/loxP}$	Null allele[1]
dilp3^{1}/slo$^{E366G/loxP}$	Null allele[1]
dilp4^{1}/slo$^{E366G/loxP}$	Null allele[1]
dilp5^{1}/slo$^{E366G/loxP}$	Null allele[1]

$dilp6^{68}/Y;;+/slo^{E366G/loxP}$	Null allele[1]
$dilp7^1/Y;;+/slo^{E366G/loxP}$	Null allele[1]
$dilp8^{M727}/slo^{E366G/loxP}$	Hypomorphic allele[2]
$dilp2\text{-}3/slo^{E366G/loxP}$	Null alleles[1]
$dilp2\text{-}3,5^3/slo^{E366G/loxP}$	Null alleles[1]
$dilp6^{68}/Y;;dilp2\text{-}3,5^3/slo^{E366G/loxP}$	Null alleles[1]
$dilp7^1/Y;;dilp2\text{-}3,5^3/slo^{E366G/loxP}$	Null alleles[1]
$dilp1\text{-}4,5^4/slo^{E366G/loxP}$	Null alleles[1]
$dilp7^1/Y;;dilp1\text{-}4,5^4/slo^{E366G/loxP}$	Null alleles[1]
$InR^{P45}/slo^{E366G/loxP}$	Hypomorphic allele[3]
$InR^{E19}/slo^{E366G/loxP}$	Unknown
$chico^1/+;+/slo^{E366G/loxP}$	Null allele[4]
$Akt^{P4226}/slo^{E366G/loxP}$	Unknown
$foxo^{\Delta94}/slo^{E366G/loxP}$	Null allele[5]
$to^{P632}/slo^{E366G/loxP}$	Unknown
$ImpL2^{M4721}/slo^{E366G/loxP}$	Unknown

[1](Grönke et al., 2010), [2](Garelli et al., 2012), [3](Fernandez et al., 1995), [4](Naganos et al., 2012), [5](Slack et al., 2011)

5.3.5 Adult Head Isolation

$slo^{E366G}/+$ and $slo^{loxP}/+$ males were combined with an excess number of orange-eyed $slo^{E366G[w+]}/+$ and $slo^{loxP[w+]}/+$ females, respectively, for 48 h, in order to increase the probability of mating. Flies between the ages of 3 and 6 days were flash-frozen in 15 mL Falcon tubes pre-cooled in liquid nitrogen. Importantly, no anaesthetisation of flies with CO_2 was performed for at least 48 h prior to flash-freezing. The Falcon tubes containing the flash-frozen flies were vortexed at maximum speed with intermittend shaking, in order to mechanically dislocate fly heads from bodies. Fly heads were poured onto Petri dishes on dry ice and 16-20 heads per sample collected into 1.5 mL eppendorf tubes under a stereomicroscope. Male heads were identified by white eye colour, as all females had orange eyes. Once all samples had been collected, RNA extraction was performed immediately. Importantly, adult head isolation was always performed

between 4 pm and 6 pm, in order to account for circadian effects on gene expression.

5.3.6 RNA Extraction and DNase Treatment

Adult male *Drosophila* heads were isolated as described in Paragraph 5.3.5 and transferred onto wet ice, before adding 200 μL of TRIzol (Thermo Fisher Scientific, 15596026) to each sample. Head tissue was homogenised in TRIzol using a cordless motorised tissue grinder and pestles (Sigma Aldrich, Z359971-1EA and Z359947-100EA), before adding another 300 μL of TRIzol and transferring the samples to RT. The samples were shaken vigorously for 10 s and incubated at RT for 5 min, before adding 50 μL of BCP (Sigma Aldrich, B9673-200ML) to each sample, followed by another 10 s of vigorous shaking and incubation at RT for 10 min. Samples were then centrifuged at 15000 x g and 4ºC for 15 min. Upon phase separation, 180 μL of the RNA-containing aqueous phase were carefully transferred into fresh 1.5 mL eppendorf tubes, and 450 μL of isopropanol (Sigma Aldrich, I9516-25ML) added to each sample, followed by gentle mixing by inversion and incubation at RT for 10 min. Samples were then centrifuged at 15000 x g and 4ºC for 8 min, the supernatant discarded, and 1 mL of freshly prepared, cold 75% ethanol added to the samples (Sigma-Aldrich, E7023-500ML). The RNA pallet was ethanol-washed by gentle inverse-mixing, followed by centrifugation at 7500 x g and 4ºC for 5 min. The ethanol supernatant was discarded, and the wash with 75% ethanol repeated. After the second wash, the ethanol supernatant was discarded, and the samples left uncapped at RT to facilitate ethanol evaporation (3-5 min). 89 μL of nuclease-free water were added to the dried RNA pallets and the samples dissolved at 65ºC for 5 min. In order to eliminate DNA contamination, DNase treatment with the TURBO DNA-*free* Kit (Thermo Fisher Scientific, AM1907) was performed, using the reaction mixture shown in Table 52.

Table 52 TURBO DNase Treatment

Reagent	Volume / μL
RNA in nuclease-free water	89
TURBO DNase Buffer (10 x)	10

TURBO DNase	1 (2 U)
Final volume	**100**

DNase treatment was performed at 37°C for 30 min, before adding 10 µL of the DNase Inactivation Reagent (Thermo Fisher Scientific, AM1907) to the reaction mixture and letting the samples incubate at RT for 5 min under constant pipette-mixing. The samples were then centrifuged at 10000 x g and 22°C for 1.5 min, and 80 µL of the supernatant containing the DNase-treated RNA carefully transferred to new 1.5 mL eppendorf tubes on wet ice. RNA concentrations were quantified (Paragraph 5.3.7), and samples stored at -80°C.

5.3.7 RNA and DNA Quantification

Throughout this chapter, the concentrations of RNA and DNA were quantified using a Qubit 2.0 Fluorometer (Thermo Fisher Scientific, Q32866). For RNA, the Qubit RNA HS Assay Kit (Thermo Fisher Scientific, Q32852) was used, while for DNA, the Qubit dsDNA HS Assay Kit (Thermo Fisher Scientific, Q32851) was used.

5.3.8 On-chip Gel Electrophoresis

On-chip gel electrophoresis was performed with an Agilent 2100 Bioanalyzer (Agilent Technologies). To test for RNA integrity, total RNA samples were run on an Agilent RNA 6000 Nano Chip (Agilent Technologies, 5067-1511), after heat-denaturing the samples for 2 min at 70°C, which minimises secondary structure formation. To analyse cDNA library quality, cDNA samples were run on a High Sensitivity DNA Chip (Agilent Technologies, 5067-4626). Screenshots of the Bioanalyzer results were taken to generate figures in this chapter.

5.3.9 cDNA Library Preparation

cDNA libraries were generated with the KAPA mRNA HyperPrep Kit (KAPA Biosystems Inc., KK8580), using protocol v. 4.17. Some parameters in this protocol are variable, and Table 53 lists the parameters I used as well as the relevant steps in the protocol.

Table 53 cDNA Library Preparation Parameters

Parameter	Value	Protocol Paragraph
Total RNA input	200 ng	2.8
mRNA fragmentation temperature	94ºC	3.3
mRNA fragmentation time	8 min	3.3
Adapter concentration	68.2 nM	6.2
Number of PCR amplification cycles	13	9.3

For adapter ligation, the KAPA Single-Indexed Adapter Sets A and B (KAPA Biosystems Inc., KK8710) were used. Table 54 lists the sample-index combinations as well as KAPA index IDs for the 18 cDNA libraries successfully generated and sequenced.

Table 54 Sample-Index Combinations of cDNA Libraries

cDNA Library Sample	Index Sequence	KAPA ID
17_GEPD1	ATCACG	1
17_GEPD2	TTAGGC	3
17_GEPD5	TAGCTT	10
17_loxP1	GTGGCCTT	20
17_loxP3	CGTACGTA	22
17_loxP6	ATTCCTTT	27
18_GEPD1	CGATGT	2
18_GEPD2	TGACCA	4
18_GEPD3	ACAGTG	5
18_GEPD4	GCCAAT	6
18_GEPD5	CAGATC	7
18_GEPD6	CTTGTA	12
18_loxP1	AGTCAACA	13
18_loxP2	AGTTCCGT	14
18_loxP3	ATGTCAGA	15
18_loxP4	CCGTCCCG	16
18_loxP5	GTCCGCAC	18

18_loxP6	GTGAAACG	19

Successfully prepared cDNA libraries were suspended in 20 μL of 10 mM Tris-HCl (pH = 8.0 – 8.5, Sigma Aldrich, T3038-1L) and stored at -20ºC. For this experiment, all instruments used, such as pipettes, tube racks, and ice buckets, were treated with RNAse*ZAP* RNase Decontamination Solution (Thermo Fisher Scientific, AM9780).

5.3.10 Bioinformatics

5.3.10.1 Operating Systems and Programming Languages

Computational operations up until and including the generation of BAM and BAI files (Paragraph 5.3.10.5) were performed on a cluster computer running Red Hat Enterprise Linux 6.6 (Santiago). BAM and BAI files were then transferred onto a local computer running macOS Mojave (v. 10.14.5) for further analysis. All analyses were performed on the Unix command line and in R (v. 3.6.0), using RStudio (v. 1.2.1335). Throughout this chapter, the following protocol was used as a guide for the RNA-seq analysis: (Love et al., 2016) – a more detailed description of this analysis pipeline is available at https://www.bioconductor.org/packages/devel/workflows/vignettes/rnaseqGene/inst/doc/rnaseqGene.html.

5.3.10.2 RNA-seq Data Retrieval

FASTQ files were generated from BCL files by Dr. Alan Pittman using the bcl2fastq conversion software provided by Illumina (v. 1.8.4) via the Unix command line arguments shown in Table 55.

Table 55 De-multiplexing RNA-seq Data

```
## BCL-to-FASTQ file format conversion for 8-bp indices
> ./bcltofastq --sample-sheet <sampleSheetName>.csv  \
--use-bases-mask Y75n,I8,I8,Y75n
## BCL-to-FASTQ file format conversion for 6-bp indices
> ./bcltofastq --sample-sheet <sampleSheetName>.csv  \
--use-bases-mask Y75n,I6,I6,Y75n
```

The sample sheets needed to specify sample-index information (`<sampleSheetName>.csv` in Table 55) were generated by Deborah Hughes and myself, and are shown in Figure 9.2. Sample-index information is used for de-multiplexing the sequencing reads. The `use-bases-mask` argument in Table 55 specifies to use the first 75 base calls for each read and to ignore the 76th base call (Y75n). `I8` and `I6` specify 8- and 6-bp index sequences, respectively, based on which de-multiplexing occurred.

5.3.10.3 Quality Control of FASTQ Data

The open-source software FASTQC was used to generate quality reports on FASTQ data (http://www.bioinformatics.babraham.ac.uk/projects/fastqc/). FASTQC was run on the Unix command line, using the command shown in Table 56.

Table 56 FASTQC Analysis

```
## Run FASTQC on each of the FASTQ files
> fastqc <FASTQ_file_name>.fastq
```

FASTQC outputs quality reports as HTML files, which were analysed by manual inspection. Screenshots of these HTML files were taken to generate the figures based on FASTQC data.

5.3.10.4 Alignment of RNA-seq Reads

RNA-seq reads in FASTQ file format were aligned to the BDGP6 *Drosophila melanogaster* reference genome using the STAR alignment software (v. 2.5.3a) (Dobin et al., 2013). Alignment with STAR occurs in two steps: first, genome index files are built, which are used during the mapping step (step two) as a reference for the splice-aware alignment of RNA-seq reads (Dobin, 2017). Genome index files were built based on the BDGP6 *Drosophila melanogaster* reference genome, using chromosomal, mitochondrial, and non-chromosomal DNA (dos Santos et al., 2014). As the bash script in Table 57 shows, the relevant genomic FASTA files of the BDGP6 reference genome were downloaded directly from the Ensemble FTP (Ensembl release 91), facilitating reproducibility (Zerbino et al., 2018). Similarly, the corresponding BDGP6 GTF file, which contains gene

structure information, was downloaded from the Ensemble FTP (Table 57). Allowing the alignment algorithm to access and extract splice-junction information from GTF files has been described to greatly increase mapping accuracy (Dobin, 2017).

Table 57 Retrieval of FASTA and GTF Files

```
## Download genomic FASTA files of BDGP6
> wget ftp://ftp.ensembl.org/pub/release-
91/fasta/drosophila_melanogaster/dna/*.dna.chromosome*
> wget ftp://ftp.ensembl.org/pub/release-
91/fasta/drosophila_melanogaster/dna/*.dna.nonchromosomal*
## Download GTF file for BDGP6
> wget ftp://ftp.ensembl.org/pub/release91/gtf/drosophila_
melanogaster/Drosophila_melanogaster.BDGP6.91.gtf.gz
## Unzip
> gunzip *.gz
```

STAR genome index files were built as shown in Table 58.

Table 58 Building STAR Genome Index Files

```
#!/usr/bin/bash
## Build STAR genome index files
$STAR --runThreadN $CPUS --runMode genomeGenerate \
--genomeDir $GENOMEDIR/STAR_index \
--genomeFastaFiles $GENOMEDIR/*.fa --sjdbGTFfile $GTF \
--sjdbOverhang 74 --genomeSAindexNbases 13
## Variable definitions
# $STAR        = full path to the STAR executable
# $CPUS        = number of CPU cores (24)
# $GENOMEDIR   = path to the directory containing the BDGP6
#                genome in FASTA format
# $GTF         = path to the BDGP6 GTF file
exit
```

194

Of note, the argument `genomeSAindexNbases` was set to 13 (default = 14), due to the *Drosophila melanogaster* genome size of 142573017 bp, as described in (Dobin, 2017). The argument `sjdbOverhang` was set to 74, as it is defined by the read length (75 bp) minus 1 (Dobin, 2017). Both of these arguments affect the structure of the resulting genome index files, which contain information about the genome sequence and corresponding splice junction coordinates as well as further information regarding chromosomes, genes, and transcripts (Dobin, 2017). Using these genome index files, RNA-seq reads in FASTQ format were aligned to the BDGP6 *Drosophila melanogaster* reference genome, as shown in Table 59. Of note, due to the paired-end nature of the RNA-seq experiment, read alignment was performed for paired-end reads.

Table 59 RNA-seq Read Alignment

```bash
#!/usr/bin/bash
## Run STAR alignment for every set of read pairs
$STAR --runThreadN $CPUS --alignIntronMax $MAXINTRON \
--alignIntronMin $MININTRON --genomeDir $GENOME \
--readFilesIn $FASTQ/<Read_1>.fastq $FASTQ/<Read_2>.fastq
## Variable definitions
# $STAR       = full path to the STAR executable
# $CPUS       = number of CPU cores (24)
# $MAXINTRON  = maximum intron size for alignments (26745)
# $MININTRON  = minimum intron size for alignments (51)
# $GENOME     = full path to genome index files
# $FASTQ      = full path to FASTQ files
exit
```

In order to determine the maximum and minimum intron sizes of *Drosophila melanogaster* (Table 59), I downloaded a FASTA file containing information on all annotated *Drosophila melanogaster* introns from the FlyBase FTP, as shown in Table 60.

Table 60 Retrieval of Intron Information

```bash
## Download all Drosophila introns
```

```
> wget ftp://ftp.flybase.net/genomes/Drosophila_melanogaster/
dmel_r6.21_FB2018_02/fasta/dmel-all-intron-r6.21.fasta.gz
## Unzip file
> gunzip *.gz
```

Using this file, intron lengths were extracted with the command line arguments shown in Table 61, generating a new file (`introns` in Table 61) that was loaded into R for further analysis.

Table 61 Retrieval of *Drosophila melanogaster* Intron Lengths

```
## Retrieve intron lengths and write to new file
> grep "^>" introns | cut -f7 -d ";" | cut -f2 -d "=" >
introns
```

Using R, the intron lengths at the 1st and 99th centiles were calculated, which correspond to 51 bp and 26745 bp, respectively. These values were then used as input to the STAR alignment software, as shown in Table 59. The output of the mapping process is provided in SAM file format, with read pairs from two FASTQ files generating a single SAM file due to the paired-end alignment mode.

5.3.10.5 Generation of Sorted BAM and BAI Files

The open-source software SAMtools (v. 1.9) was used to convert SAM files into sorted BAM files (Li et al., 2009). Indexing of BAM files, which generates BAI files, was performed simultaneously, as shown in Table 62.

Table 62 Generation of Sorted BAM and BAI Files

```
#!/usr/bin/bash
## Generate sorted BAM files from SAM files
$SAMTOOLS sort -@ $CPUS -o <BAM_file_name>.bam \
<SAM_file_name>.sam
## Generate BAI files by indexing sorted BAM files
$SAMTOOLS index -@ $CPUS <BAM_file_name>.bam
## Variable definitions
# $SAMTOOLS = full path to SAMtools executable
```

```
# $CPUS     = number of CPU cores (24)
exit
```

5.3.10.6 Investigating Alignment Statistics

Alignment statistics were retrieved from STAR LOG files, which are automatically generated by the STAR alignment software upon completion of the alignment process (Dobin and Gingeras, 2015).

5.3.10.7 Visualising Genomic Alignments

The Integrative Genomics Viewer (IGV) was used to visualise RNA-seq alignments (Robinson et al., 2011). BAM and BAI files were used as input files for this visualisation (Paragraph 5.3.10.5). Screenshots of IGV alignments were taken to generate figures in this chapter.

5.3.10.8 Gene Expression Quantification

BAM files containing RNA-seq alignment information for each sample (Paragraph 5.3.10.5) were loaded into R, alongside gene structure information in GTF file format (Paragraph 5.3.10.4). The GTF file was then used to generate a `GRangesList` object, which is a data class that stores every gene listed in the GTF file as a separate `GRanges` object, containing gene-specific exon information (Lawrence et al., 2013). Hence, the `GRangesList` object can be thought of as a "list of exons grouped by gene" (Love et al., 2016). To quantify gene expression, the `summarizeOverlaps` function was used, as shown in Table 63 (Lawrence et al., 2013).

Table 63 Quantification of Gene Expression

```
## Quantify gene expression
## Explanation for the preprocess.reads argument can be found
## on https://support.bioconductor.org/p/65844/
se <- summarizeOverlaps(features = ebg, reads = bamfiles,
                        mode = "Union",
                        singleEnd = FALSE,
                        ignore.strand = FALSE,
```

197

```
                              fragments = TRUE,
                              preprocess.reads = invertStrand)
## Variable definitions
# ebg      = "exons-by-gene" GRangesList object containing
             a list of all exons grouped by genes – generated
             based on the BDGP6 GTF file
# bamfiles = a list containing all BAM files generated from
#            RNA-seq alignment
```

The arguments used in the call to summarizeOverlaps (Table 63) specify that the RNA-seq alignment data derive from paired-end sequencing (singleEnd = FALSE), that the data are strand-specific (ignore.strand = FALSE and preprocess.reads = invertStrand), and that single reads without a mapped mate should be counted rather than discarded (fragments = TRUE). Algorithmically, this function identifies and counts overlaps between the RNA-seq alignments (stored in BAM files) and exons in the *Drosophila melanogaster* reference genome (stored in the GTF file), resulting in a matrix of sample-specific fragment counts per gene (se in Table 63) (Obenchain, 2016). Importantly, the measure of "fragment counts per gene" indicates that paired reads are quantified as single units for this analysis, rather than being counted separately. Moreover, each fragment is only counted once, even if it overlaps multiple exons of the same gene, and any fragment overlapping exons from multiple genes is discarded (Obenchain, 2016).

5.3.10.9 Computing Euclidean Distances Between cDNA Libraries

Gene counts stored within the DESeqDataSet R object class were transformed using the regularised logarithm (rlog) (Love et al., 2014), and the Euclidean distances between cDNA libraries calculated based on entire gene expression profiles using the dist function. The Euclidean distance calculation is shown for two cDNA library samples in Table 64.

Table 64 Euclidean Distance Calculation

$$d(S_1, S_2) = \sqrt{\sum_{i=1}^{n} (S_{1i} - S_{2i})^2}$$

$$d = Euclidean\ distance$$
$$S_1 = sample\ 1$$
$$S_2 = sample\ 2$$
$$S_{1i} = counts\ of\ gene\ i\ in\ sample\ 1$$
$$S_{2i} = counts\ of\ gene\ i\ in\ sample\ 2$$
$$n = total\ number\ of\ genes$$

5.3.10.10 Generating Heatmaps

All heatmaps in this chapter were generated using the `pheatmap` R package (https://cran.r-project.org/web/packages/pheatmap/index.html). The function call to generate heatmaps automatically performs agglomerative hierarchical sample clustering and visualises clustering results as dendrograms.

5.3.10.11 Principal Component Analysis

Principle component analysis (PCA) was performed using the `plotPCA` function in R, which performs standard PCA analysis and outputs the first and second principal components, including their percentage-variation.

5.3.10.12 Differential Gene Expression Analysis

The DESeq2 R package was used to analyse differential gene expression (DGE), performed via the `DESeq` function as shown in Table 65 (Love et al., 2014).

Table 65 Differential Gene Expression Analysis

```
## Perform DGE analysis based on gene expression data
DE <- DESeq(dds)
## Variable definitions
# dds = data object containing gene count information
```

The DESeq2 package is described in (Love et al., 2014). Briefly, `DESeq` first normalises raw gene counts by computing the natural logarithm ($\log_e$) of the ratio

of sample-specific gene counts to average gene counts across samples. This is done for all genes. Next, the median of this ratio is taken for each sample, and the results converted into a normal number, generating sample-specific scaling factors – a process known as "median-of-ratios" (Love et al., 2014). All gene counts are then divided by these sample-specific scaling factors, resulting in normalised counts. `DESeq` then estimates the dispersion of gene counts and builds a generalised linear model (GLM) for the expression of each gene. Log_2-fold-changes (LFCs) between genotypes are then estimated and a Wald test performed on these estimates. The resulting Wald test p-values are corrected for multiple comparisons by performing the Benjamini-Hochberg-adjustment (BH-adjustment), using independent filtering of genes to increase sensitivity (Love et al., 2014).

5.3.10.13   MA- and Volcano Plots

MA plots were generated in R using the `plotMA` function (Love et al., 2014). Volcano plots were generated in R using the `EnhancedVolcano` package (https://github.com/kevinblighe/EnhancedVolcano).

5.3.10.14   Gene Ontology Analysis

Gene ontology (GO) analysis was performed using DAVID (Huang et al., 2009). The complete list of 1036 DEGs was used as input to DAVID (v. 6.8), which applies a modified Fisher's Exact test in order to identify functional enrichment of GO terms compared to the *Drosophila melanogaster* reference genome. GO enrichments were retrieved at a cut-off p-value of 0.1. All p-values were then subjected to the BH correction to yield false discovery rates (FDRs).

5.3.10.15   KEGG Pathway Analysis

KEGG pathway analysis was performed with DAVID as described in Paragraph 5.3.10.14, using the KEGG PATHWAY database to identify functional enrichment (Kanehisa et al., 2017).

5.3.10.16   Visualisation of Gene Ontology and Pathway Analyses

GO and KEGG Pathway analyses were visualised in R using the `GOPlot` package (https://wencke.github.io/), following a protocol that I briefly describe below, and which is available at https://wencke.github.io/. The key feature the `GOPlot`

package is the `circ` function, which links DGE data (Paragraph 5.3.10.12) and GO or KEGG pathway data (Paragraphs 5.3.10.14 and 5.3.10.15) into a single data object containing information on gene identity, DGE, and functional annotation. The object also contains a z-score, which is calculated as shown in Table 66. Importantly, z-scores are annotation-specific, so each functional annotation term is attributed its own z-score. This data object was fed into `GOBubble`, a customised function for the generation of bubble plots.

Table 66 Calculation of z-scores

$$z = \frac{(up - down)}{\sqrt{count}}$$

$$up = number\ of\ genes\ upregulated\ in\ GEPD$$
$$down = number\ of\ genes\ downregulated\ in\ GEPD$$
$$count = total\ number\ of\ genes$$

Multi-dimensional string plots were also generated with the `GOPlot` package. First, all DEGs associated with a subset of enriched functional annotations were retrieved. Using the `chord_data` function, a novel data object was generated that combines gene- and associated LFC information in a binary matrix, indicating whether a gene is ("1") or is not ("0") associated with a given functional annotation. This data object was used as input to `GOChord`, a customised function for the generation string plots.

5.3.10.17   iRegulon Analysis

iRegulon is a Cytoscape plugin (https://cytoscape.org/, v. 2.8.3) available at http://iregulon.aertslab.org/index.html (Janky et al., 2014). To identify gene regulatory networks (GRNs) and associated TFs, a list of DEGs was loaded into Cytoscape, before the iRegulon plugin was used to apply motif enrichment analysis to the data. To predict regulators and targets, the default parameters for *Drosophila melanogaster* were used: a motif collection of 9713 position-weight matrices (PWMs) and a normalised enrichment score (NES) threshold of 2.5. GRNs were visualised in Cytoscape.

5.3.11 Adult Fly Behavioural Tracking

To track adult locomotion, the DAM system was used, as described in Paragraph 4.3.5.

5.3.12 Behavioural Tracking Analysis

Adult fly behavioural tracking analysis was performed as described in Paragraph 4.3.6. Total beam breaks were normalised to the median number of beam breaks exhibited by the relevant genetic background, $slo^{E366G}/+$ or $slo^{loxP}/+$. Hence, the resulting values indicate fold-changes of beam breaks compared to the relevant genetic background.

5.3.13 Data Visualisation

Data generated as part of the RNA-seq analysis pipeline were visualised as described in Paragraph 5.3.10. Figures for behavioural data were generated as described in Paragraph 3.3.19, with boxplots drawn according to Tukey.

5.3.14 Statistics

Statistical methods underlying RNA-seq data analysis are described in Paragraph 5.3.10. DAM behavioural data were analysed by performing Mann-Whitney-Wilcoxon tests between two groups. To account for multiple comparisons, the Bonferroni correction was applied to the resulting p-values.

5.4 Results

5.4.1 RNA Preparation from Adult *Drosophila* Head Tissue

In order to obtain a global overview of how the slo^{E366G} allele impacts a variety of molecular pathways, I compared the transcriptomes of $slo^{E366G}/+$ and $slo^{loxP}/+$ flies via RNA-seq. The analysis of DGE might implicate specific cellular pathways involved in the pathogenesis of GEPD, providing an entry point into the understanding of GEPD pathophysiology. The first step of any RNA-seq protocol is the extraction of high-quality RNA from the tissue of interest (Wang et al., 2009). I extracted total RNA from *Drosophila* head tissue, because the spatial dissection data in Chapter 4 provided strong evidence suggesting that the brain is the pathogenic locus of the $slo^{E366G}/+$ locomotor defect. However, due to the broad expression pattern of BK channels (Bailey et al., 2019) (Paragraph 1.4.2), it is possible that extra-cerebral tissues are involved in GEPD pathogenesis as well. In addition to the brain, the head capsule contains tissues such as the pericerebral fat body. Hence, isolating whole heads represents a trade-off between enriching for neuronal changes in gene expression and maintaining sensitivity for gene expression changes outside the brain.

Total RNA from $slo^{E366G}/+$ and $slo^{loxP}/+$ adult fly heads was extracted from 12 samples per genotype, each sample consisting of 16-20 individual heads. RNA extractions were performed in two independent batches on two separate days, each batch consisting of 6 $slo^{E366G}/+$ and 6 $slo^{loxP}/+$ samples, and all samples were treated with DNase, in order to prevent DNA contamination. A major determinant of RNA-seq data quality is RNA integrity, as degraded RNA leads to various biases, such as a 3' bias for the sequencing of mRNA (Kukurba and Montgomery, 2015). I measured RNA integrity using a Bioanalyzer, which employs on-chip gel electrophoresis to separate total RNA fragments based on size (Kukurba and Montgomery, 2015). The quality of total RNA is inferred from the quality of the 28S and 18S rRNAs, which present as sharp and distinct electrophoretic peaks at ~5 kb and ~2 kb in mammals, respectively. Based on these two peaks as well as other electrophoretic features, a trained artificial neural network has been developed to classify RNA integrity into 10 separate categories, from completely degraded (1) to intact (10) – a parameter known as

RNA Integrity Number (RIN) (Imbeaud et al., 2005). However, the 28S rRNA of insects has been shown to be thermolabile due to a "hidden break" in the molecule, which connects two similarly sized rRNA subunits via hydrogen bonds that readily break in response to increased temperature (Winnebeck et al., 2010). As a result, the rRNA profile in *Drosophila* is markedly different from the one observed in mammals: the individual 28S rRNA fragments (28Sa and 28Sb) migrate closely with the 18S rRNA fragment, resulting in electrophoretic peaks at ~2 kb (18S and 28Sb superimposed) and at ~1.7 kb (28Sa) (Long and Dawid, 1980; Winnebeck et al., 2010). This difference in rRNA composition renders *Drosophila* total RNA incompatible with the RIN algorithm described above. Instead, Drosophilists have to manually appraise total RNA integrity based on the sharpness of three peaks: the two peaks at ~2 kb and ~1.7 kb described above and an additional peak at ~120 bp, which corresponds to the 5.8S rRNA (Pavlakis et al., 1979). Indeed, Figure 5.1 shows that the 24 total RNA samples I extracted from *slo^{E366G}/+* and *slo^{loxP}/+* adult head tissue were of high quality, indicating the presence of all three peaks. Of note, whilst a shift towards increased fragment sizes can be observed for all samples, the consistency of this shift across the three rRNA peaks suggests an experimental artifact of either slowly running samples or a fast-running ladder. Hence, these 24 total RNA samples were considered to be of high enough quality to proceed to the next stage of the RNA-seq protocol: the generation of cDNA libraries.
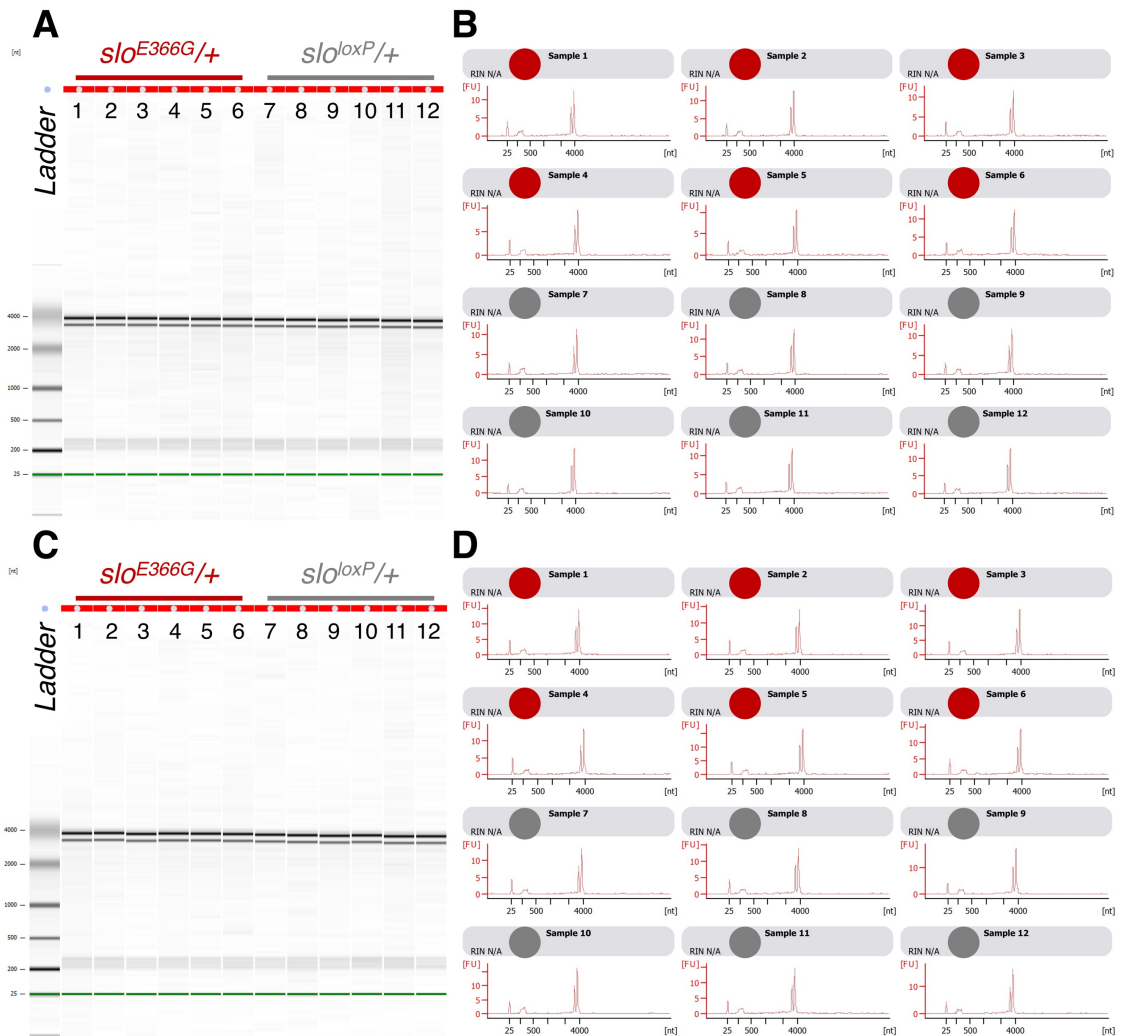
Figure 5.1 Quality Control of Total RNA

24 total RNA samples extracted from *slo^E366G^/+* and *slo^loxP^/+* adult fly heads were run on a Bioanalyzer. The first batch of total RNA samples is shown in **A** and **B**, the second batch in **C** and **D**. **A** and **C** show the resulting data as gel-like images, **B** and **D** as electropherograms. Three sharp peaks can be observed for all samples at 200-300 bp (5.8S rRNA), ~3.5 kb (28Sa rRNA), and ~4 kb (18S rRNA and 28Sb rRNA superimposed). These peaks are normally expected at ~120 bp, ~1.7 kb, and ~2 kb, respectively, but the consistency of the size shift suggests either slowly running samples or a fast-running ladder. A 25-bp peak indicates the marker. This figure was generated from screenshots of the Bioanalyzer results.

5.4.2 cDNA Library Preparation

RNA-seq is usually performed by sequencing cDNA, and multiple steps have to be taken in order to prepare cDNA libraries from total RNA samples for sequencing (Kukurba and Montgomery, 2015). I generated cDNA libraries from the 24 total RNA samples shown in Figure 5.1, performing these experiments in

two independent batches on two separate days, with each batch consisting of 6 slo^{E366G}/+ and 6 slo^{loxP}/+ samples. cDNA library preparation was performed using the KAPA mRNA HyperPrep Kit (KAPA Biosystems Inc., KK8580), which is optimised for the generation of cDNA libraries from mRNA. An mRNA-specific RNA-seq protocol was chosen because investigating DGE of protein-coding genes increases the probability of identifying molecular pathways perturbed in slo^{E366G}/+. It should be noted, however, that this experimental design precludes the analysis of other potential mediators of GEPD pathology, such as ncRNAs and miRNAs.

The main steps of the cDNA library preparation protocol are illustrated in Figure 5.2. First, mRNA was captured from total RNA via oligo-dT beads, which bind to the 3' poly-A tail of mRNA. Captured mRNA was fragmented in the presence of heat and Mg^{2+}, in order to render the cDNA libraries size-compatible with short-read sequencing platforms (Kukurba and Montgomery, 2015). Fragmented mRNA was reverse-transcribed to yield a cDNA:RNA hybrid, which was converted into dscDNA via second-strand synthesis, incorporating dUTP into the newly synthesised cDNA strand. A-tailing of the dscDNA 3' ends was performed in order to facilitate the subsequent ligation to the 3' poly-T tails of adapters. Adapters are DNA oligomers that (1) are required for the adhesion of the cDNA library fragments to the flow cell lane of the sequencing platform, and (2) carry DNA sequences (known as "indices") that allow for multiplexed sequencing (Kukurba and Montgomery, 2015) – unique adapters were ligated to each of the 24 samples. Finally, the cDNA fragments were PCR-amplified in a strand-specific manner because the dUTP-containing cDNA strand serves as an inefficient template for the DNA polymerase used in this protocol (Hrdlickova et al., 2017). As shown in Figure 5.2, the resulting cDNA libraries are strand-specific, being made up selectively of cDNA that is antisense (-) to the original mRNA.
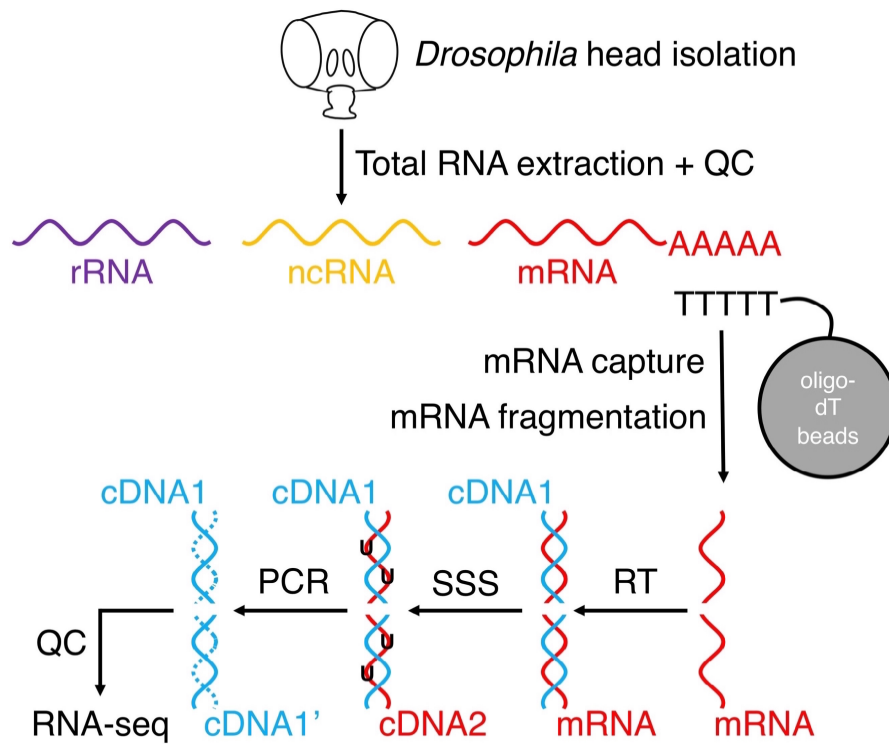
Figure 5.2 cDNA Library Preparation

Total RNA from *Drosophila* head tissue, having passed quality control (QC), was used as input material for the KAPA mRNA HyperPrep Kit, in order to generate mRNA-specific stranded cDNA libraries. First, oligo-dT beads capture mRNA poly-A tails, excluding other RNA species. mRNA is then fragmented and reverse-transcribed (RT), yielding a cDNA:RNA hybrid. Second-strand synthesis (SSS) is performed on the cDNA strand (cDNA1) to yield dscDNA. This step incorporates dUTP (U) into the newly formed cDNA strand (cDNA2), which prevents it from being PCR-amplified at the next step. This specific amplification of only one cDNA strand (cDNA1) generates strand-specific cDNA libraries, with all cDNA fragments being antisense (-) to the original mRNA fragments – illustrated by cyan and red colours, respectively. The dotted cyan line indicates the complementary cDNA strand to cDNA1 (cDNA1'). A-tailing during SSS and adapter ligation before PCR amplification are not shown for simplicity (Paragraph 5.4.2). QC of cDNA libraries is performed prior to RNA-seq.

From a total of 24 cDNA libraries, 20 were subjected to quality control using a Bioanalyzer, as described in Paragraph 5.4.1. 4 cDNA libraries were excluded prior to quality control, due to low concentrations upon library generation. Figure 5.3 shows that 18 cDNA libraries exhibit an even cDNA fragment size distribution around a mean of ~300 bp. These 18 cDNA libraries were used for RNA-seq. The other 2 cDNA libraries (hollow circles in the electropherograms of Figure 5.3) were excluded from downstream analyses because their cDNA fragment size

distributions were skewed towards larger values, suggesting problems during the mRNA fragmentation step (Figure 5.2).
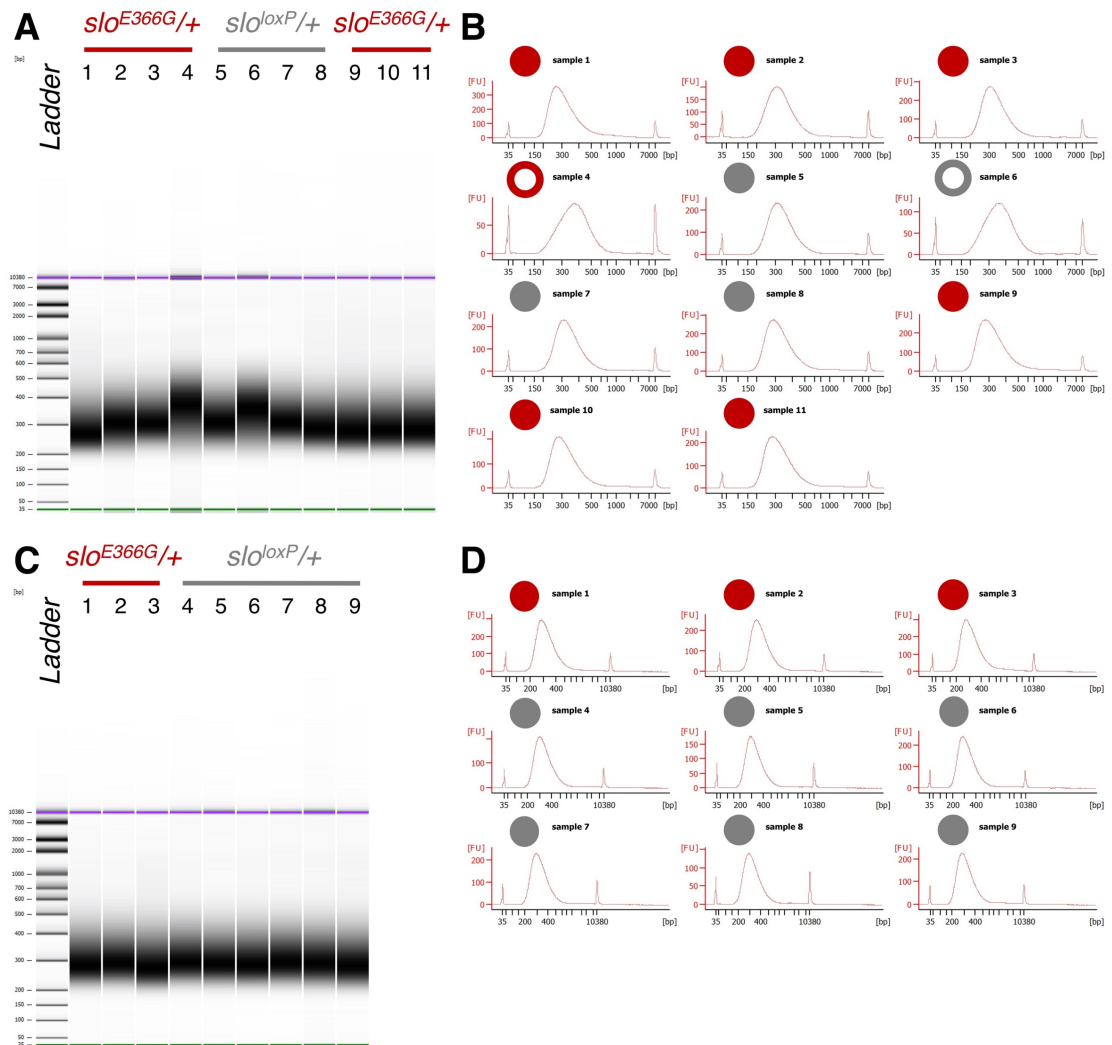
Figure 5.3 Quality Control of cDNA Libraries

20 cDNA libraries prepared from total RNA extracted from $slo^{E366G}/+$ and $slo^{loxP}/+$ adult fly heads were run a Bioanalyzer. The first batch of cDNA libraries is shown in **A** and **B** (samples 1-8), the second batch in **A** and **B** (samples 9-11) and in **C** and **D**. **A** and **C** show the resulting data as gel-like images, **B** and **D** as electropherograms. 18 cDNA libraries (filled circles in **B** and **D**) show an even cDNA fragment size distribution around a mean of ~300 bp. These samples passed the quality control. Samples 4 and 6 in **B** (hollow circles) were not used for RNA-seq, due to different size distributions of cDNA fragments. A 35-bp peak indicates the lower marker, a 10380 bp peak the upper marker. This figure was generated from screenshots of the Bioanalyzer results.

To allow for an even sequencing depth across samples, equal amounts of the 18 cDNA libraries that passed quality control (~37 ng, Figure 5.3) were pooled and

subsequently run on a Bioanalyzer, confirming high sample quality (Figure 5.4). The primer-dimers detected in this sample (Figure 5.4) will not affect sequencing quality, as these molecules lack the adapter sequences required to attach to the flow cell. Altogether, the pooled cDNA libraries passed the final quality control step and were used for the next step of the RNA-seq protocol: RNA-sequencing.
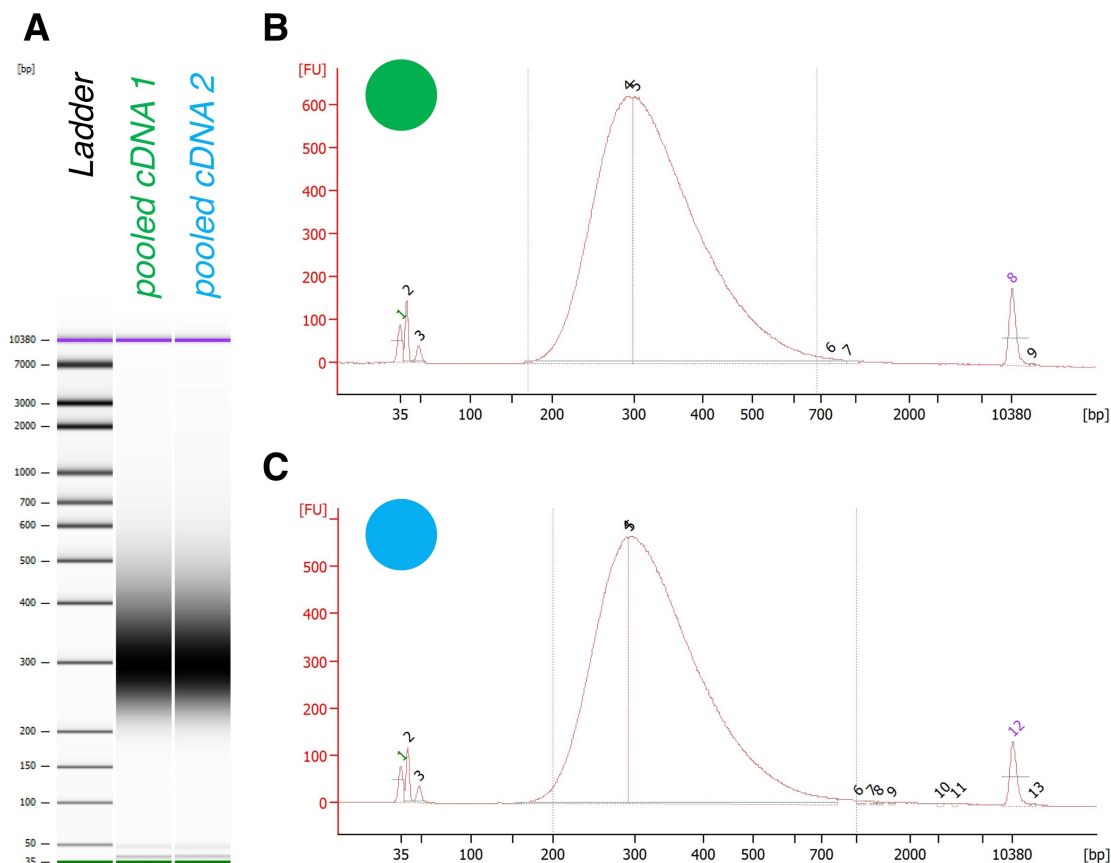
Figure 5.4 Quality Control of Pooled cDNA Libraries

The 18 cDNA libraries that passed quality control (Figure 5.3) were pooled and run on a Bioanalyzer as two replicates. **A** shows gel-like images of the samples, while **B** and **C** show their electropherograms, illustrating an even size distribution around a mean of ~300 bp. A 35-bp peak indicates the lower marker, a 10380 bp peak the upper marker. The two additional peaks close to the lower marker (40-50 bp) are likely primer-dimers. I prepared and pooled the cDNA libraries shown in this figure, while Deborah Hughes performed the Bioanalyzer run. This figure was generated from screenshots of the Bioanalyzer results.

5.4.3 RNA-seq of cDNA Libraries

The 18 pooled cDNA libraries, having passed quality control (Figure 5.4), were sequenced on an Illumina HiSeq 3000 sequencing system, which employs a

"sequencing-by-synthesis" approach – the cyclic reversible termination (CRT) method – to sequence cluster-amplified clones of individual cDNA fragments (Kukurba and Montgomery, 2015; Metzker, 2010). The 18 cDNA libraries were multiplexed for sequencing on a single flow cell lane. Paired-end sequencing was performed, producing two reads of 75 bp each for every cDNA fragment sequenced (Read1 and Read2). As shown in Figure 5.2, Read1 will generate the antisense (-) sequence of the original mRNA molecule, while Read2 will generate the sense (+) sequence. During the sequencing process, sequencing- and quality information for each base call is stored in BCL file format. For downstream analyses, these data need to be converted into FASTQ file format, which stores similar information about base call identity and quality, but organises it on a per-read- rather than per-cycle basis. Moreover, the sequencing data need to be de-multiplexed based on adapter-contained index sequences that are unique for each sample (Paragraph 5.4.2), in order to obtain sample-specific gene expression data. File conversion and de-multiplexing produced two FASTQ files per sample: one for Read1 and one for Read2. Hence, 36 FASTQ files were generated for the 18 cDNA libraries.

5.4.4 Quality Control of RNA-seq Data

Prior to DGE analysis, I performed quality control of the FASTQ data via the open-source software FASTQC (Conesa et al., 2016), focussing on two questions: (1) what is the overall sequence quality? (2) Are there any over-represented sequences in the data that cannot be explained by the experimental design (Kukurba and Montgomery, 2015)? Question (1) addresses problems that might occur during the sequencing run itself. In particular, for paired-end sequencing on Illumina short-read sequencing platforms, three important observations have been made: (a) the read-quality drops towards the 3' end of a read, (b) the quality of Read2 is significantly lower compared to Read1, and (c) Read2 sequence quality shows great variability between samples of the same sequencing run (Tan et al., 2019). Phasing errors have been suggested to underly (a) and (b), while (c) describes a phenomenon that has been attributed to the fragment size distribution of cDNA libraries (Tan et al., 2019). Hence, it is crucial to confirm that the FASTQ sequencing data exhibit high-confidence base calls throughout the

entire reads, both for Read1 and Read2, before analysing these data – low-quality sequencing reads might need to be trimmed prior to analysis (Kukurba and Montgomery, 2015). The FASTQC results for one representative cDNA library (18_GEPD1) illustrate that the overall read quality for all 18 cDNA libraries was high (Figure 5.5). The lowest mean base quality score, present at the 5' and 3' ends of Read2, is still around 30, which translates into a probability of ~0.1% that the base call at this position is incorrect.

A

Read 1

$$\text{Quality Score} = -10 \log_{10} P$$

P = Probability for a base call to be incorrect

Quality Score

Number of Reads

Read Position / bp

Quality Score

B

Read 2

Quality Score

Number of Reads

Read Position / bp

Quality Score
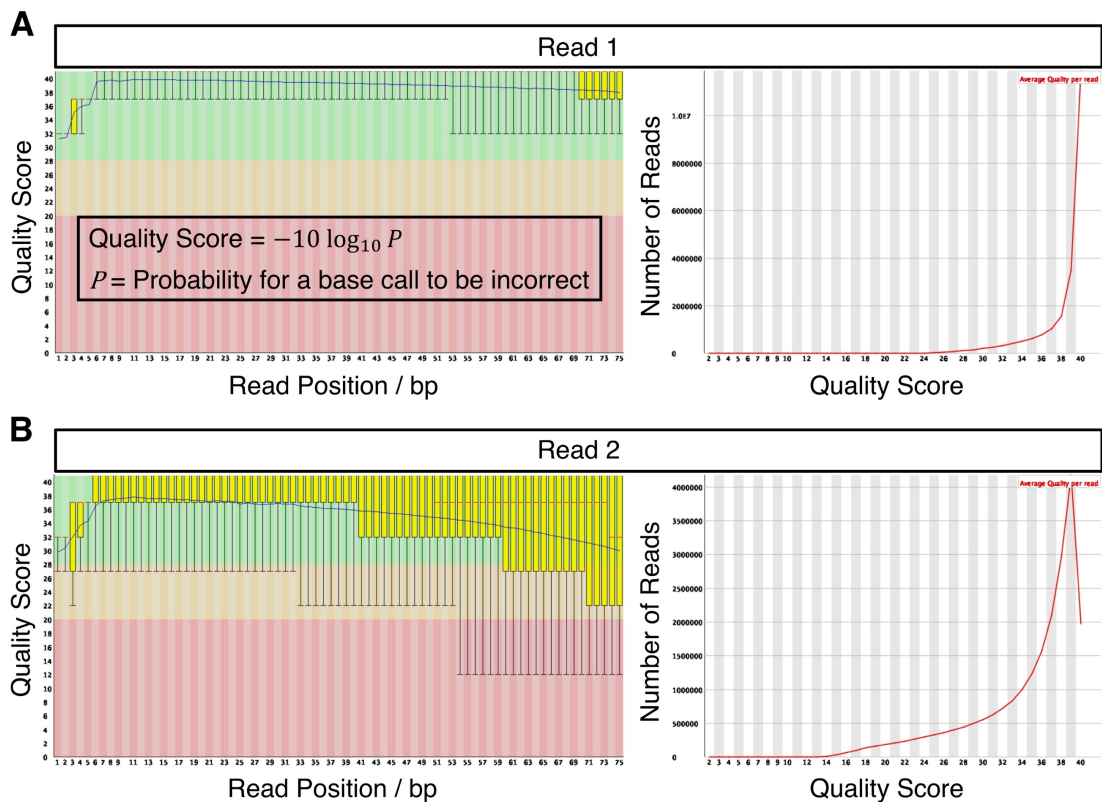
Figure 5.5 Sequence Quality of cDNA Libraries

FASTQ data quality control was performed using FASTQC for each of the 18 cDNA libraries, illustrated in this figure by one representative example (18_GEPD1). **A** shows the base qualities for Read1, **B** for Read2. The per-base quality scores (y-axis) for the 75-bp reads (x-axis) are shown on the left. The boxplots represent the median quality scores as red lines, the first-to-third quartile ranges as yellow boxes, and the ranges from 10% to 90% as whiskers. The mean quality scores are indicated by a blue line. Per-base quality scores are high, with ~30 being the lowest mean quality score. The formula underlying the base quality score is shown as an inset in **A**. The graphs on the right show the per-sequence quality scores for entire 75-bp reads. The mean quality score for most Read1 reads is 40 (**A**), while for Read2 reads it is 39 (**B**). This figure was generated from screenshots of the FASTQC results.

211

Observations (a) and (b) described above are confirmed in Figure 5.5: the base quality scores decrease towards the 3' end of both reads, and Read2 is of lower quality than Read1. However, the overall per-base sequence quality is considered to be high enough for downstream analyses without pre-processing. Importantly, FASTQC did not identify over-represented sequences in the data, defined as individual sequences that make up more than 0.1% of all sequences present in a sample. This finding illustrates the absence of rRNA and other contaminating sequences (Delhomme et al., 2014), confirming that poly-A selection during cDNA library preparation was successful (Figure 5.2). Of note, FASTQC did report that the base content along the sequencing reads is biased, both for Read1 and Read2. As Figure 5.6 illustrates, Read1 shows a consistent bias towards thymine, Read2 towards adenine. However, this is consistent with the nature of the cDNA libraries, which are prepared from poly-A-selected mRNA. Indeed, the specific bias towards thymine in Read1 and adenine in Read2 illustrates that the cDNA libraries consist of cDNA that is antisense (-) to the original mRNA molecules.
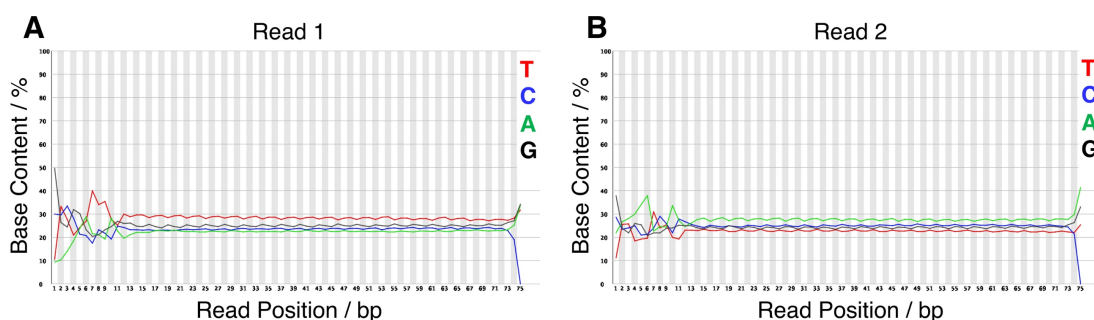
Figure 5.6 Per-base Sequence Bias in cDNA Libraries

FASTQC reported a per-base sequence bias for Read1 (**A**) and Read2 (**B**), as illustrated in this figure based on one representative cDNA library (18_GEPD1). The graphs in **A** and **B** plot the percentage base content (y-axis) over read length (x-axis) for Read1 and Read2, respectively. The bias towards thymine in Read1 (**A**) and adenine in Read2 (**B**) is consistent with the nature of the cDNA libraries, which were prepared from poly-A-selected mRNA. This figure was generated from screenshots of the FASTQC results.

Of note, the erratic nature of the graphs in Figure 5.6 for the first 12 bases is characteristic of Illumina RNA-seq data, and has been proposed to be due to biases introduced during reverse transcription (Delhomme et al., 2014).

Altogether, quality control of the FASTQ files did not indicate any problems with the data that would require pre-processing.

5.4.5 Genomic Alignment of RNA-seq Reads

Throughout this chapter, I followed a workflow available on Bioconductor to perform DGE analysis on the RNA-seq data, which is available at https://www.bioconductor.org/packages/devel/workflows/vignettes/rnaseqGene/inst/doc/rnaseqGene.html. The corresponding publication is (Love et al., 2016). Bioconductor is an open-source, R-based software environment that provides extensive computing resources to analyse high-throughput biological data (Gentleman et al., 2004; Huber et al., 2015). Figure 5.7 shows a schematic of the RNA-seq data analysis pipeline I employed, illustrating that the step following FASTQ quality control is the alignment of RNA-seq reads to the *Drosophila melanogaster* reference genome.

cDNA libraries

Next-generation sequencing

FASTQ data

FASTQC
Alignment to reference genome

SAM files

Conversion to sorted binary format
Indexing binary files

BAM files and BAI files

Alignment quality control
Alignment visualisation
Differential gene expression analysis

List of differentially
expressed genes

Gene Ontology analysis
Gene regulatory network analysis
Manual inspection

List of candidate
modifier genes

Figure 5.7 RNA-seq Data Analysis Pipeline

This schematic illustrates the RNA-seq data analysis pipeline, with methods employed shown in grey, and the resulting data shown in black. First, cDNA libraries were sequenced on an Illumina HiSeq 3000 short-read sequencing platform in paired-end mode, and quality control of the resulting FASTQ data performed via FASTQC. Sequencing reads were then aligned to the BDGP6 *Drosophila melanogaster* reference genome using the STAR aligner, producing SAM files. SAM files were converted to sorted BAM files, whose index information is stored in BAI files, allowing alignment data to be visualised using IGV. Alignment quality information was retrieved via STAR LOG files. DGE analysis was performed using DESeq2. The resulting list of DEGs was used for GO analysis with DAVID and GRN analysis with iRegulon. Results of these analyses were combined with manual inspection to yield a list of candidate modifier genes of the *slo^{E366G}/+* locomotor defect. References for the methods used are provided in the main text.

Read alignment was performed using the STAR alignment tool (Dobin et al., 2013). The mapping algorithm underlying STAR aligns non-contiguous reads to the reference genome via a Maximal Mappable Prefix (MMP) approach, which allows for the mapping of spliced mRNA to gDNA (Dobin et al., 2013). In order to

pre-empt confusion, some terminology needs to be clarified at this stage: while STAR aligns individual RNA-seq reads to the reference genome, it treats both reads of the same read pair (Read1 and Read2) as a single "fragment", since both reads derive from the same cDNA library molecule (Dobin and Gingeras, 2015). Hence, the term "fragment" is used to refer to paired-end reads, while the term "read" is used to refer to individual reads (Dobin and Gingeras, 2015). Aligning the FASTQ data of the 18 cDNA libraries to the BDGP6 *Drosophila melanogaster* reference genome yielded 18 files in SAM format, which were converted to sorted BAM files and indexed using the open-source software SAMtools (Li et al., 2009). BAM and SAM files contain equivalent information, but the former stores it in a compressed binary formant, which requires less computer memory. Upon alignment, it is of interest to retrieve information about the alignment process as a means of quality control. The STAR alignment software automatically generates LOG files, which contain various alignment statistics, two of which are listed in Table 67: (1) the percentage of fragments that uniquely mapped to the reference genome and (2) the total number of uniquely mapped fragments per sample. The former informs about alignment quality, while the latter serves as a measure of future experimental sensitivity (Conesa et al., 2016). The prefixes "17_" and "18_" in Table 67 identify the two different batches of cDNA libraries, generated on the 17th and 18th of December 2017, respectively.

Table 67 RNA-seq Alignment Statistics

Sample	Uniquely Mapped Fragments / %	# Mapped Fragments
17_GEPD1	92.47	14380590
17_GEPD2	91.58	14874699
17_GEPD5	93.20	17705943
17_loxP1	93.09	18386802
17_loxP3	92.74	15438189
17_loxP6	93.45	17989924
18_GEPD1	92.70	19985141
18_GEPD2	92.62	17149622
18_GEPD3	92.86	16277414

18_GEPD4	92.90	18966126
18_GEPD5	93.22	17622781
18_GEPD6	92.73	18389412
18_loxP1	93.16	18192140
18_loxP2	93.62	19201277
18_loxP3	93.03	16966936
18_loxP4	93.03	16711160
18_loxP5	92.99	18776976
18_loxP6	92.72	16252085

The percentages of uniquely mapped fragments shown in Table 67 are consistently above 90%, suggesting that both cDNA library quality and RNA-seq read alignment quality are high (Dobin and Gingeras, 2015). To visualise the RNA-seq alignments, the open-source software IGV was used (Robinson et al., 2011). Investigating read alignments at the *slo* locus showed that reads clustered within exons, as expected for mRNA-specific RNA-seq data (Figure 5.8). The exonic sequencing depth at exon 10 of *slo*, which harbours the E366 locus mutated in *slo*^{E366G}, was ~200 reads per base. Importantly, Figure 5.8 illustrates that both *slo* alleles are transcribed to similar degrees in *slo*^{E366G}/+, with 54% (112/206) of reads carrying the wild-type GAG codon (glutamic acid) and 46% (94/206) carrying the mutant GGG codon (glycine). Hence, there does not seem to be allele-specific expression (ASE) of *slo* in this fly model of GEPD (De La Chapelle, 2009).
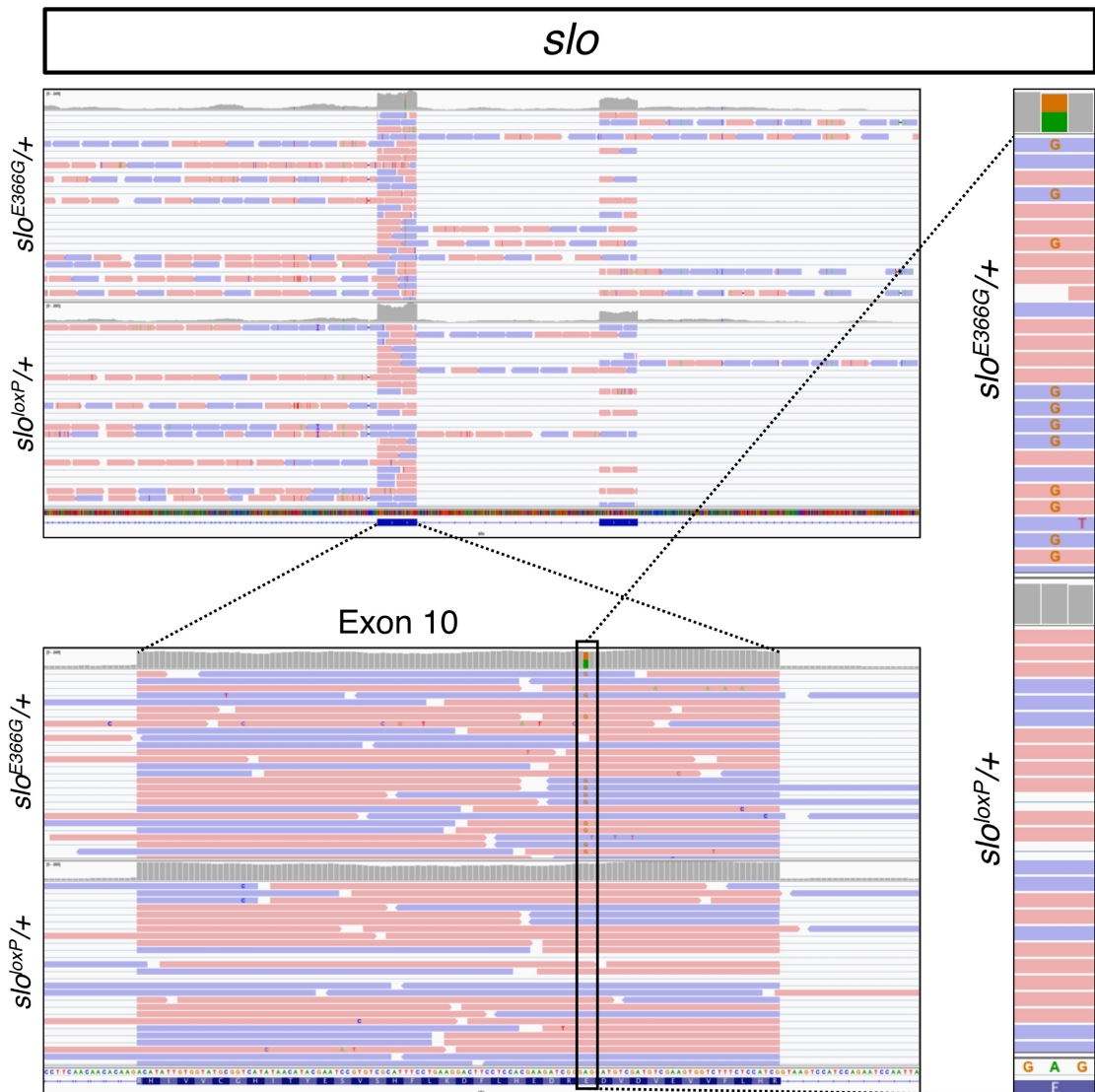
Figure 5.8 Visualising RNA-seq Alignments at the *slo* Locus

IGV was used to visualise RNA-seq read alignment at the *slo* locus, represented by one *slo^E366G^/+* (18_GEPD1) and one *slo^loxP^/+* (18_loxP1) sample. The top panel shows read alignments around exon 10, which harbours the E366 locus. Red and blue colours indicate forward (Read2) and reverse (Read1) reads, respectively. Reads are clustered within exons, as expected from mRNA-specific sequencing. Exon 10 is magnified in the bottom panel. While grey bars above the read alignments indicate wild-type bases, the brown/green-coloured bar in *slo^E366G^/+* represents the GEPD-linked A>G transition. A further level of magnification focusses on the amino acid E366, shown vertically on the right. The height of the vertical bars above the read alignments indicates sequencing depth, illustrating that transcription of the mutant (guanine, brown) and wild-type (adenine, green) alleles seems indiscriminate: 112 reads carry adenine (54%), 94 reads guanine (46%). This figure was generated from screenshots of IGV alignments.

217

5.4.6 Differential Gene Expression Analysis

As shown in Figure 5.7, the step following alignment visualisation is the quantification of gene expression and a concomitant analysis of DGE between $slo^{E366G}/+$ and $slo^{loxP}/+$. This task was performed as a continuation of the Bioconductor workflow introduced in Paragraph 5.4.5 (Love et al., 2016). The BAM files generated as described in Paragraph 5.4.5 were loaded into R, along with a GTF file that stores annotated gene structure information about the BDGP6 *Drosophila melanogaster* reference genome. The R package GenomicAlignments was used to count the number aligned RNA-seq fragments (stored in BAM files) that overlap exons of the BDGP6 *Drosophila melanogaster* reference genome (stored in the GTF file), resulting in a matrix containing the number of fragment counts per gene for each sample, referred to as a "count matrix" (Love et al., 2016; Obenchain, 2016). To provide an illustration of the count matrix, a screenshot from within R is provided in Figure 5.9. Of note, throughout this chapter, abbreviations for the genotypes $slo^{E366G}/+$ and $slo^{loxP}/+$ will be used: $slo^{E366G}/+$ is often referred to as "GEPD", while $slo^{loxP}/+$ is often referred to as "loxP". Another note on terminology: when describing DEGs throughout this chapter, up- and down-regulation always refer to the gene expression in $slo^{E366G}/+$ relative to $slo^{loxP}/+$, so that up-regulated genes are more strongly expressed in $slo^{E366G}/+$ when compared to $slo^{loxP}/+$, and down-regulated genes are more weakly expressed in $slo^{E366G}/+$ when compared to $slo^{loxP}/+$. Moreover, up- and down-regulation always imply a significance level of FDR < 0.05.

```
                17_GEPD1_S1_L001 17_GEPD2_S2_L001 17_GEPD5_S3_L001 17_loxp1_S1_L001 17_loxp3_S2_L001 17_loxp6_S3_L001
FBgn0000003                   84              231              142              102               76              121
FBgn0000008                  450              455              556              581              555              598
FBgn0000014                    0                0                0                0                0                2
FBgn0000015                    2                0                0                0                0                0
FBgn0000017                 3453             3305             4193             4247             3641             4266
FBgn0000018                  160              141              179              189              150              189
FBgn0000022                    0                0                0                0                0                0
FBgn0000024                 8669             8196            10615             9950             8512             9028
FBgn0000028                  358              299              372              378              302              359
FBgn0000032                  219              230              292              286              224              260
```

Figure 5.9 Count Matrix for Differential Gene Expression Analysis

This screenshot from within R illustrates the structure of the count matrix, which was obtained upon counting the number of aligned RNA-seq fragments that overlap exons of the BDGP6 *Drosophila melanogaster* reference genome. Genes are organised in rows, samples in columns. The numbers in the body of the matrix represent the fragment counts per gene (row) for each sample (column). Only the first 10 out of 17737 genes are shown for simplicity, and only the first 6 of the 18 samples.

Having generated the count matrix as shown in Figure 5.9, the total number of fragments counted per sample across all genes was calculated. This parameter is of interest because it provides a comparison to Table 67, which lists the number of fragments aligned to the reference genome for each sample. Hence, comparing these numbers reveals how many aligned fragments were excluded from the DGE analysis. Such exclusion occurs due to a violation of the counting algorithm. For example, fragments aligning to overlapping exons from different genes are discarded (Obenchain, 2016). Table 68 indicates that a substantial number of fragments (> 1 million) was removed from each sample, as calculated by subtracting the total number of fragments counted (Table 68) from the total number of fragments aligned (Table 67).

Table 68 Total Fragments Counted for RNA-seq Analysis

Sample	Total Fragment Counts	Discarded Fragments
17_GEPD1	13263469	1117121
17_GEPD2	13786109	1088590
17_GEPD5	16362239	1343704
17_loxP1	16953133	1433669
17_loxP3	14186909	1251280
17_loxP6	16686004	1303920
18_GEPD1	18445556	1539585

18_GEPD2	15915560	1234062
18_GEPD3	15174939	1102475
18_GEPD4	17619092	1347034
18_GEPD5	16363097	1259684
18_GEPD6	17051747	1337665
18_loxP1	16918410	1273730
18_loxP2	17983492	1217785
18_loxP3	15732874	1234062
18_loxP4	15586179	1124981
18_loxP5	17642913	1134063
18_loxP6	15181822	1070263

While the count matrix contains one row per gene for all genes of the *Drosophila melanogaster* genome (Figure 5.9), some rows will contain zero counts across samples because some genes are not expressed in head tissue, or expressed at such low levels so as to escape experimental sensitivity. In fact, the gene *FBgn0000022* (seventh row in Figure 5.9) is one such example. In order to reduce the object size of the count matrix and increase programming speed, the count matrix was filtered by removing all genes exhibiting less than 1 count across all 18 samples (Love et al., 2016). Following this minimal filtering, which removed ~13% of genes (2381/17737), I performed exploratory analysis of the count matrix data, in order to obtain general information about the cDNA libraries (Love et al., 2016).

Some exploratory data analysis approaches, such as sample clustering, have been shown to work best on homoskedastic data – data with uniform variance across data points – because using heteroskedastic data results in highly variable data points dominating the results, while less variable data points contribute disproportionately little (Love et al., 2016). The variance of RNA-seq counts is greatest for highly expressed genes, enabling them to contribute more strongly to exploratory data analysis results than lowly expressed genes (Love et al., 2016). A simple logarithmic transformation of gene counts inverts this influence, generating greater variance for lowly expressed genes (Love et al.,

2016). As a possible solution to this problem, a $\log_2$-like transformation termed rlog has been developed (Love et al., 2014, 2016). This transformation yields similar results to the $\log_2$-transformation for high gene counts, while shrinking low gene counts towards a reference value, therefore stabilising the overall variance, rendering the count data homoskedastic, and allowing all genes to contribute equally to the results of exploratory data analyses (Love et al., 2014, 2016). Importantly, rlog-transformed data are only used for exploratory data analysis, not for statistical testing of DGE, for which raw counts are required, as described later in this chapter. In order to investigate the differences between cDNA libraries, I calculated the Euclidean distances between their rlog-transformed gene counts and visualised the resulting distance matrix as a heatmap (Figure 5.10). Moreover, hierarchical clustering of the cDNA libraries was performed, and the resulting cluster agglomerations visualised with dendrograms connected to the heatmap – proximity within the dendrograms represents similarity between cDNA libraries (Figure 5.10). Splitting the heatmap into the two main horizontal and vertical clusters reveals that the cDNA libraries cluster based on genotype, an important confirmation of systematic differences in gene expression (Figure 5.10). Interestingly, one of the $slo^{E366G}/+$ samples, 18_GEPD2, appears to exhibit substantial differences to the other GEPD samples, rendering it a potential outlier – no such outlier was detected in the loxP samples (Figure 5.10).
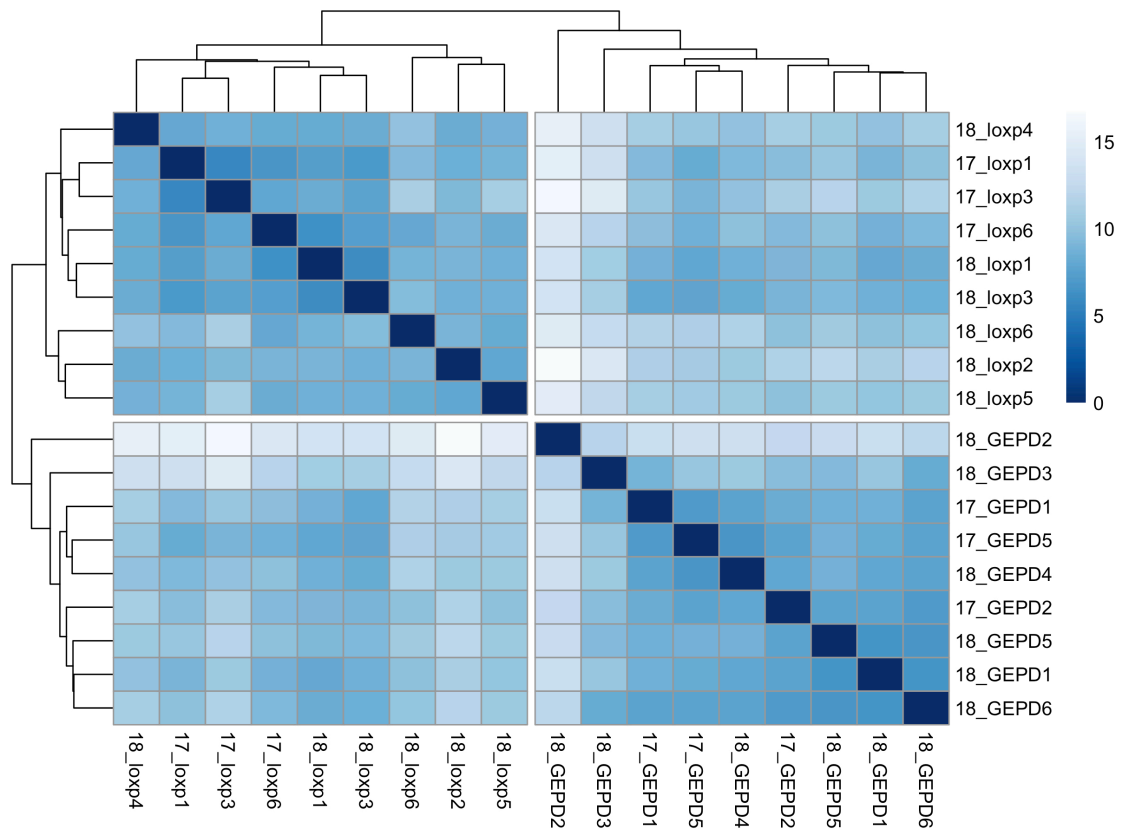
Figure 5.10 Euclidean Distance Between cDNA Libraries

The Euclidean distances between cDNA libraries were calculated and visualised as a heatmap. The legend on the right indicates that no difference between samples is represented by the darkest shade of blue, with increasingly lighter shades illustrating increasing differences. The results of hierarchical clustering are represented as dendrograms on the left and top – proximity within the dendrograms represents similarity between cDNA libraries. The heatmap was split into two horizontal and two vertical clusters, based on the hierarchical clustering results, illustrating that the samples cluster by genotype. Sample 18_GEPD2 appears to be an outlier.

Another approach to illustrate the relationships between samples is PCA, a method used to visualise the differences between multi-dimensional data objects in 2-dimensional space. Performing PCA on the cDNA libraries confirmed the results of Figure 5.10: cDNA libraries cluster by genotype into one $slo^{E366G}/+$ cluster and one $slo^{loxP}/+$ cluster (Figure 5.11). Notably, PCA also confirmed that sample 18_GEPD2 is an outlier, as it strongly segregated from both clusters – hence, it was removed from the ensuing DGE analysis. No batch effect could be observed in the data.
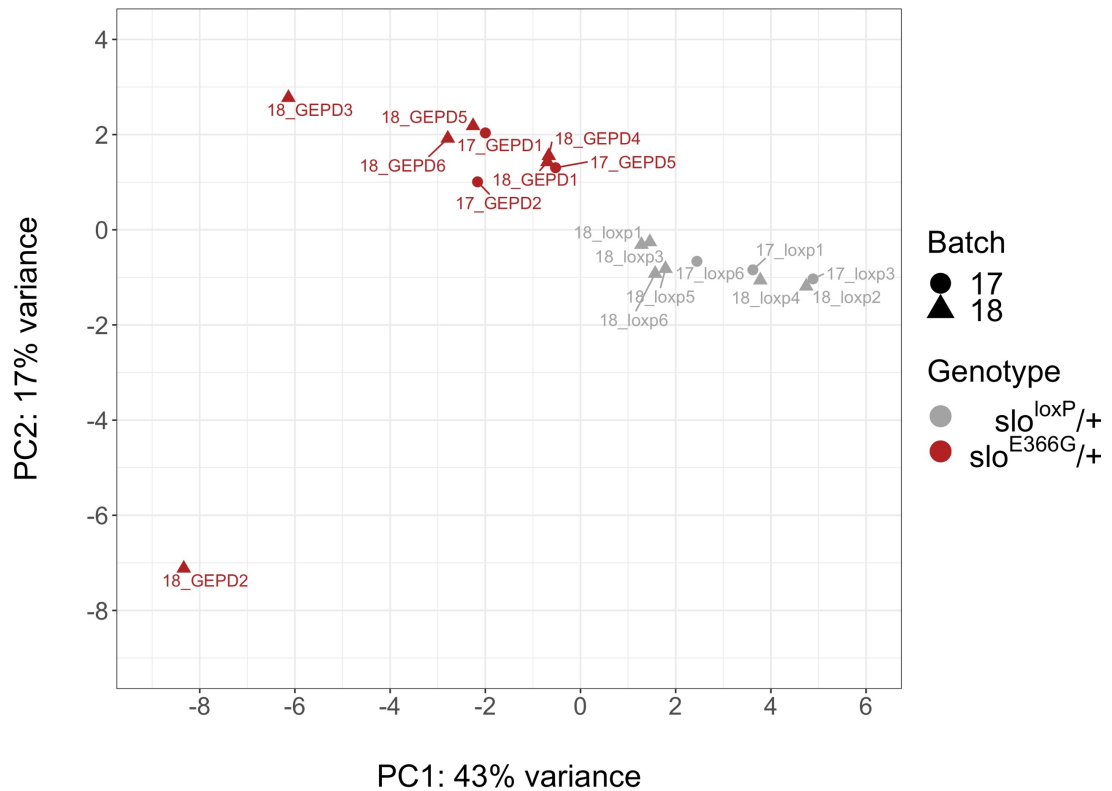
Figure 5.11 Principle Component Analysis of cDNA Libraries

PCA was performed on the 18 cDNA library samples and the results visualised with the first principal component on the x- (PC1) and the second principal component on the y-axis (PC2). The amount of variance each principal component accounts for is provided in the axis labels. Genotypes are colour-coded, while the two batches (17 and 18) can be identified by shape. Two main clusters separate by genotype. Sample 18_GEPD2 appears to be an outlier and was removed from further analyses. No batch effect could be observed.

After discarding sample 18_GEPD2, I performed DGE analysis between $slo^{E366G}/+$ (8 cDNA libraries) and $slo^{loxP}/+$ (9 cDNA libraries), using the R package DESeq2 (Love et al., 2014). This analysis was performed for each of the 15356 genes that survived the low-count filtering described above. DESeq2 is mathematically complex, but conceptually, it operates in five steps, as described in more detail in (Love et al., 2014): (1) the count data are normalised based on library size – this is a different procedure from rlog-transformation, and it is important to stress that raw counts are used for DGE analysis, not rlog-transformed counts. Normalisation of raw counts based on library size is necessary because increased sequencing depth proportionally scales gene

counts, which could result in between-sample differences that are biologically meaningless. (2) DESeq2 estimates the dispersion for the expression of each gene, which is a measure of the variability of gene counts across samples. (3) GLMs are built to describe the gene expression data. (4) LFCs of gene expression between genotypes are estimated and a Wald test for significance performed on these LFCs. (5) Due to the high number of comparisons, multiple-testing correction is performed by calculating BH-adjusted p-values, also known as FDRs, from the Wald test p-values (Love et al., 2014). The final result of this analysis is a matrix-like data object containing gene identifiers, mean levels of gene expression, LFCs between genotypes, and FDRs, amongst other parameters. A screenshot of this data object is shown in Figure 5.12.

	baseMean	log2FoldChange	lfcSE	stat	pvalue	padj
	<numeric>	<numeric>	<numeric>	<numeric>	<numeric>	<numeric>
FBgn0031176	102.395416437552	8.93290083369926	1.61310434575654	5.53770799588899	3.06455643695797e-08	2.50717583387516e-06
FBgn0032505	254.248703894283	8.61035968338767	1.19085310892254	7.23041290220768	4.81527734511823e-13	1.07404802137994e-10
FBgn0266455	11.8874963398865	6.74323834220586	1.65232699184306	4.08105561156767	4.4831625969754e-05	0.00134754950877595
FBgn0263762	6.46597086114069	5.8929275975809	1.50156163898193	3.9245325963284	8.68982929578961e-05	0.00227841042331293
FBgn0053109	20.5447343563465	5.77447280336704	1.14418225523974	5.04681205893823	4.49242868180635e-07	2.40798603382931e-05
FBgn0265103	41.3836880244215	3.34807337933085	0.555630888743782	6.02571499741575	1.68363641026733e-09	1.86935181429784e-07
FBgn0050371	7.60757797024104	3.27026076768755	0.824795825479602	3.964933704394	7.3416348552078e-05	0.00202238807239281
FBgn0265577	17.9151707546379	2.8531798749457	0.744116654059515	3.83431799218607	0.000125913164848471	0.00303782959360579
FBgn0063496	15.3632416066408	2.58644719149673	0.910817585381163	2.83969834685871	0.00451562125289262	0.0481238735090349
FBgn0028583	221.959883488409	2.57749971341849	0.618355426570395	4.16831421325784	3.06860730848673e-05	0.000996701973840123

Figure 5.12 Differential Gene Expression Results Data Structure

DESeq2 was used to perform DGE analysis between $slo^{E366G}/+$ (8 cDNA libraries) and $slo^{loxP}/+$ (9 cDNA libraries). A screenshot from within R showing the resulting matrix-like data object is shown in this figure. Row names denote FlyBase gene IDs, while columns contain mean gene expressions across samples (baseMean), LFCs between genotypes (log2FoldChange), standard errors associated with LFC estimates (lfcSE), Wald test statistics (stat), Wald test p-values (pvalue), and BH-adjusted p-values known as FDRs (padj). This data object has been sorted by decreasing LFC, showing the 10 most strongly DEGs at a significance level of FDR < 0.05.

Using an FDR threshold of FDR < 0.05, 514 (3.3%) of the analysed genes were found to be significantly up-, and 522 (3.4%) genes to be significantly down-regulated in $slo^{E366G}/+$ compared to $slo^{loxP}/+$. The whole list of 1036 DEGs is provided in Table 69. To visualise global patterns of DGE, MA plots are often used, which represent the LFC on the y-, and the mean gene expression on the x-axis (Dudoit et al., 2002). A complementary visualisation is the volcano plot, which plots the logarithmically transformed FDR on the y-, and the LFC on the x-axis. Both plots are shown in Figure 5.13.
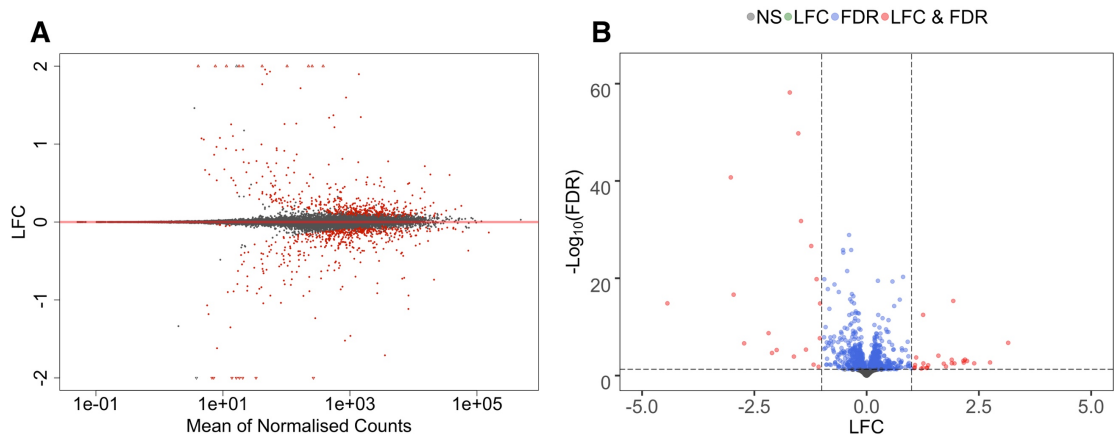
Figure 5.13 Global Gene Expression Patterns

DGE results for 15356 genes are visualised as an MA plot (**A**) and a volcano plot (**B**), with each gene represented by a dot. (**A**) The MA plot indicates the LFC on the y-, and the mean gene expression on the x-axis. DEGs at FDR < 0.05 are coloured red. Triangles at the top and bottom indicate genes that lie outside the y-axis boundaries of the plot. (**B**) The volcano plot indicates the negative logarithm of the FDR on the y-, and the LFC on the x-axis. The colouring scheme illustrates genes that are not significantly (FDR >= 0.05) differentially expressed (grey, "NS"), genes that are significantly (FDR < 0.05) differentially expressed (blue, "FDR"), and genes that are significantly differentially expressed with an up- or downregulation of at least 2-fold (red, "LFC & FDR"). Green dots would indicate genes that show a non-significant up- or downregulation of at least 2-fold, but none were present. Dashed lines in **B** represent FDR = 0.05 (horizontal) and LFC = +/- 1 (vertical). LFCs in both graphs represents the gene expression of $slo^{E366G}/+$ relative to $slo^{loxP}/+$.

An observation that can be made from both plots in Figure 5.13 is that, within the set of significantly DEGs, high fold-changes are rare. Moreover, both plots illustrate that significantly DEGs are evenly split between up- and downregulation. In order to visualise the expression pattern of the 40 most significantly DEGs, I retrieved their rlog-transformed count data from the original count matrix (Figure 5.9) and generated a heatmap (Figure 5.14).
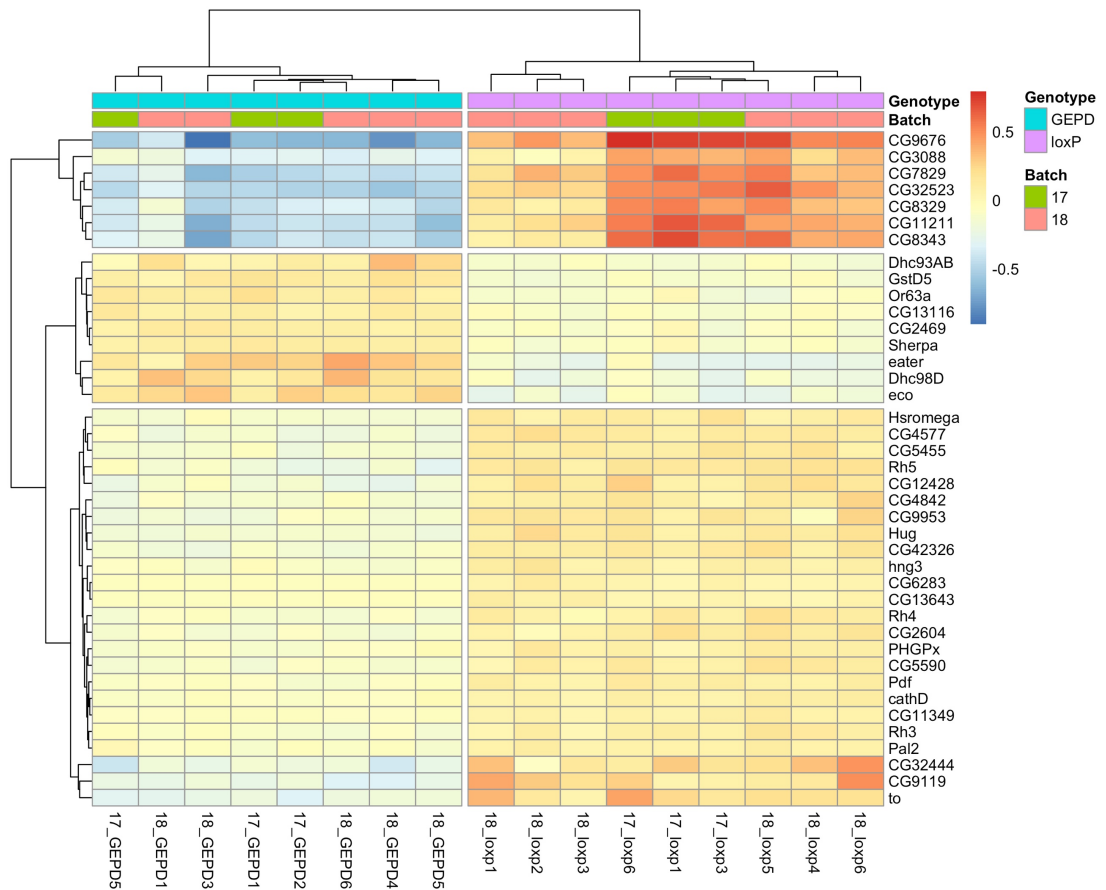
Figure 5.14 Most Significant Gene Expression Pattern

The expression pattern of the 40 most significantly DEGs is visualised as a heatmap. Each tile represents the expression level of one gene (row) per sample (column). Gene expression levels are indicated as the difference between sample-specific gene expression and mean gene expression across samples, as quantified by rlog-transformed counts. This measure gives an indication of how strongly sample-specific gene expression deviates from mean gene expression across samples. Positive numbers, represented by shades of red, indicate above-average gene expression, negative numbers, represented by shades of blue, below-average gene expression. Both genes and samples were hierarchically clustered, resulting in two main horizontal and three main vertical clusters, which are illustrated by cuts through the heatmap. Dendrograms visualise the clustering results. Samples naturally cluster by genotype, whereas no batch effect could be observed.

The heatmap in Figure 5.14 illustrates that hierarchical clustering separates the 17 cDNA libraries based on genotype without indicating the presence of a batch effect, which is congruent with Figure 5.10 and Figure 5.11. Three main clusters were established based on gene expression profiles, two of which contain genes down-regulated- (top and bottom clusters), a third one contains genes up-regulated in $slo^{E366G}/+$ (middle cluster). While visualisations such as MA plots,

volcano plots, and heatmaps provide a good overview over large data sets, with a total of 1036 DEGs, it is important to obtain a better functional understanding of the transcriptomic differences between $slo^{E366G}/+$ and $slo^{loxP}/+$.

5.4.7 Functional Analysis of RNA-seq Data

High-throughput data sets, such as the DGE data generated in Paragraph 5.4.6, harbour a wealth of latent information, and it is a major challenge to extract biological meaning from them (Huang et al., 2009). A common entry point is to perform GO analysis. The Gene Ontology project aims to classify genes systematically into three groups: (1) cellular component (CC), describing cellular location, (2) molecular function (MF), describing gene function on a molecular level, and (3) biological process (BP), describing higher-order functions a gene is involved in (The Gene Ontology Consortium, 2007). By performing GO analysis on the set of DEGs between $slo^{E366G}/+$ and $slo^{loxP}/+$, my aim was to identify biological themes that might be involved in GEPD pathogenesis, which could allow for the generation of testable hypotheses. In order to perform GO analysis, I used the open-source software DAVID (Huang et al., 2009), addressing the following question: does the set of 1036 DEGs contain any GO terms that are significantly enriched compared to the *Drosophila melanogaster* reference genome? Conceptually, DAVID operates by first annotating each of the 1036 DEGs with GO terms (CC, MF, and BP), before statistically testing for functional enrichment against the *Drosophila melanogaster* reference genome via a modified Fisher's Exact test (Huang et al., 2009). Upon completion of the GO analysis, I extracted the results from DAVID and loaded them into R, in order to visualise the enriched GO terms (Figure 5.15).
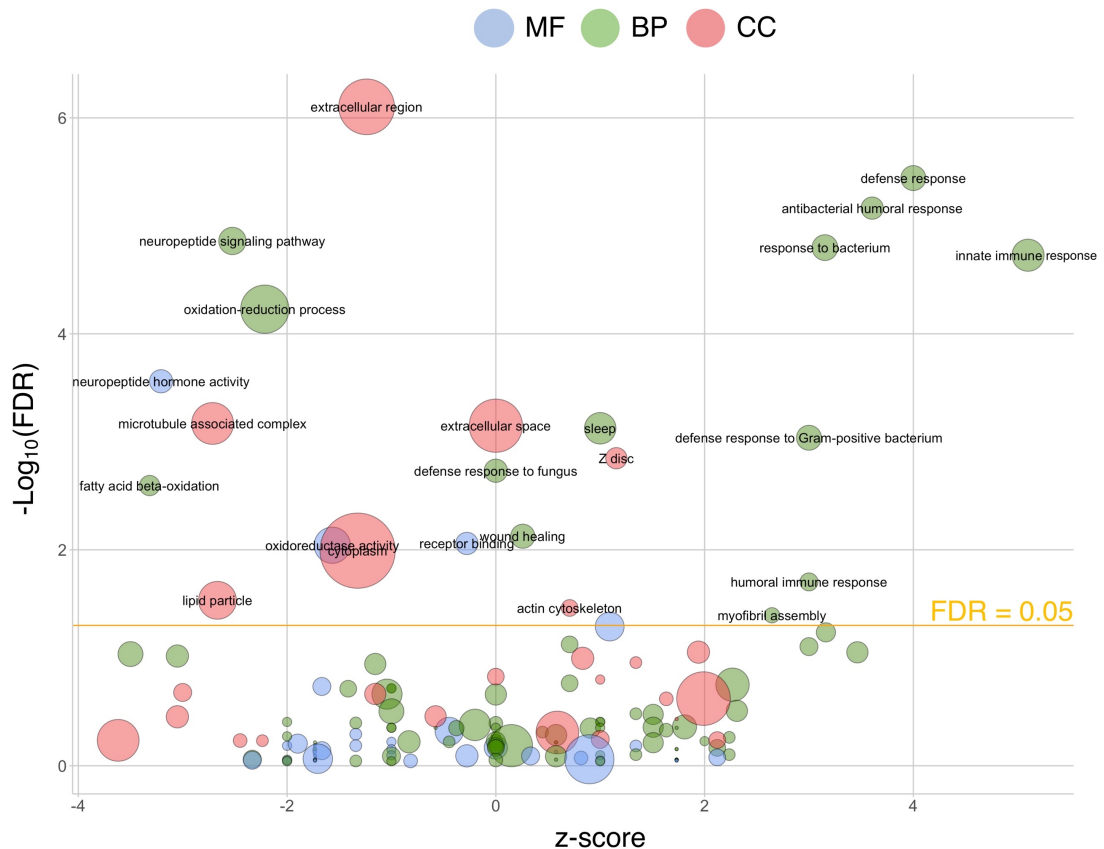
Figure 5.15 Gene Ontology Analysis

GO analysis was performed on the set of 1036 DEGs between $slo^{E366G}/+$ and $slo^{loxP}/+$. The enriched GO terms are visualised as a bubble plot, with each bubble representing a different colour-coded GO term (MF = molecular function; BP = biological process; CC = cellular component). The bubble size is proportional to the gene number contained within bubbles. The y-axis plots the negative logarithm of the FDR, with greater numbers indicating smaller FDRs and, hence, greater significance. The x-axis plots the z-score, which is a measure of whether the genes within a particular GO term are up- (positive values) or down-regulated (negative values) in $slo^{E366G}/+$ compared to $slo^{loxP}/+$. An orange line demarcates the FDR threshold of 0.05, above which GO terms are labelled. The major themes emerging are metabolism, oxidation-reduction, and immunity.

The bubble plot in Figure 5.15 is multidimensional, providing simultaneous insight into GO term identity, significance of GO term enrichment, the number of genes contained within individual GO terms, and whether these genes are up- or down-regulated in $slo^{E366G}/+$ compared to $slo^{loxP}/+$. Three biological themes stand out: metabolism, oxidation-reduction, and immunity, suggesting that these physiological processes could be involved in GEPD pathogenesis. In addition to GO annotations, DAVID interfaces with other databases as well, such as the

KEGG PATHWAY database, which is of particular interest because it contains manually curated pathway information based on biochemical evidence (Kanehisa et al., 2017). Complementing the GO analysis, I used DAVID to test for enriched KEGG pathways within the set of 1036 DEGs. Figure 5.16 illustrates the results of this analysis as described for Figure 5.15. Interestingly, enriched KEGG pathways are almost exclusively metabolic in nature, supporting the hypothesis that metabolism is a biological theme affected in GEPD. However, caution must be applied, because the KEGG PATHWAY database is more thoroughly curated for, and therefore more sensitive towards the detection of, metabolic- over other biological pathways (Kanehisa et al., 2017).
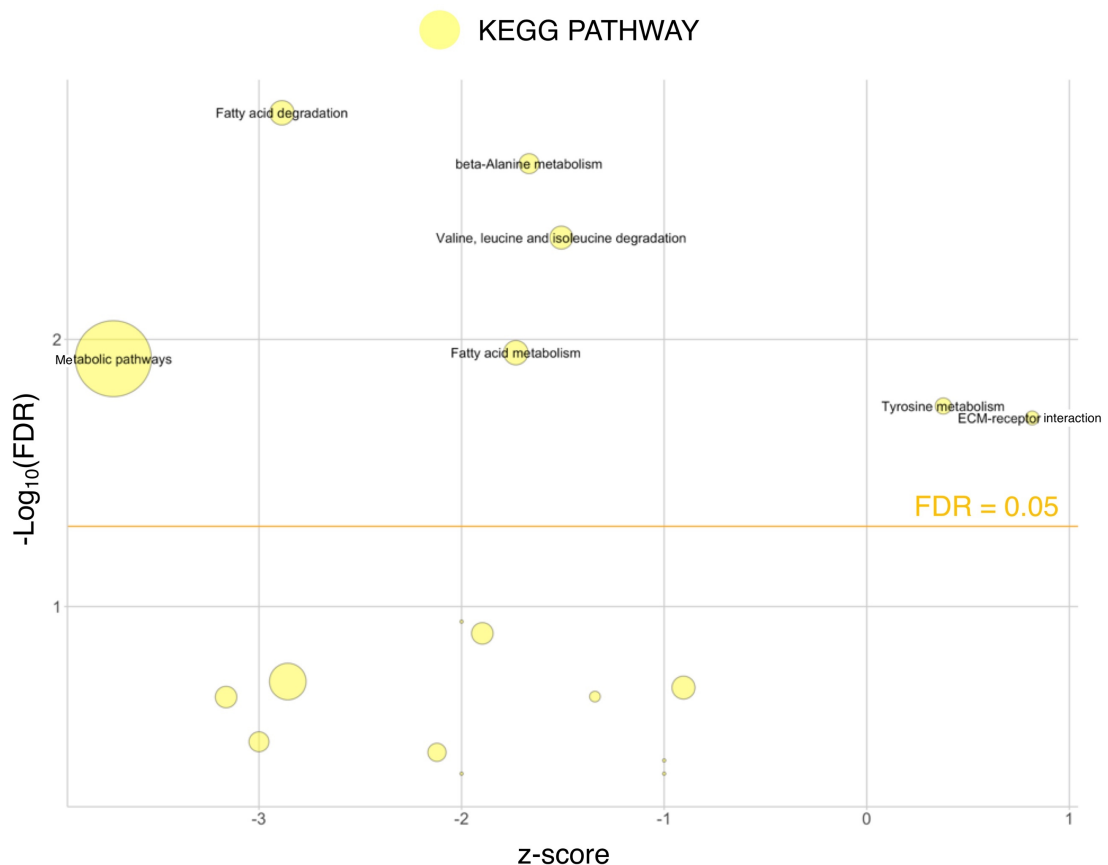
Figure 5.16 KEGG PATHWAY Analysis

The KEGG PATHWAY database was used to analyse the 1036 DEGs between $slo^{E366G}/+$ and $slo^{loxP}/+$ for enriched KEGG pathway annotations, and the results are visualised as outlined for Figure 5.15. Most identified pathways are down-regulated in $slo^{E366G}/+$ and pertain to metabolism.

Apart from strengthening the hypothesis that metabolism is a potential biological theme involved in GEPD pathogenesis, Figure 5.16 lists specific metabolic pathways affected in slo^{E366G}/+, such as fatty acid- and amino acid metabolism. However, bubble plots lack resolution about the nature of individual genes affected in slo^{E366G}/+. To gain such insight, I extracted the gene information from a set of metabolic KEGG PATHWAY annotations at FDR < 0.05 for visualisation in a multi-dimensional string plot that combines information about functional annotations and gene expression levels (Figure 5.17).
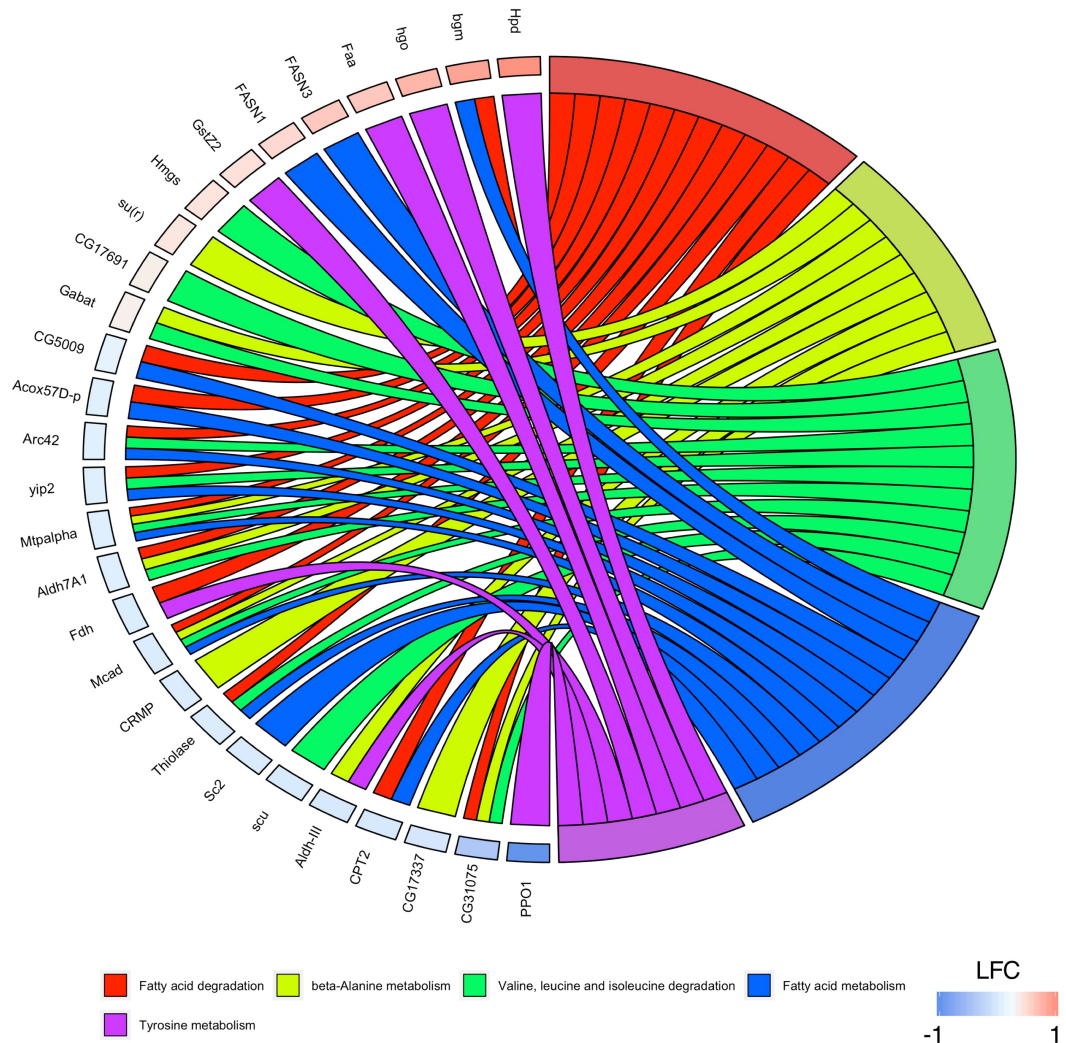
Figure 5.17 Metabolic Gene Relationships

This string plot illustrates KEGG PATHWAY-gene expression relationships. The genes associated with five significantly enriched KEGG PATHWAY annotations (shown in the bottom legend) were extracted from the set of 1036 DEGs. These 28 genes were sorted according to LFC, with genes up-regulated in $slo^{E366G}/+$ represented by shades of red and genes down-regulated in $slo^{E366G}/+$ represented by shades of blue, before being linked to KEGG pathways via coloured strings.

Figure 5.17 provides novel insight into the differential regulation of metabolic pathways in $slo^{E366G}/+$ and $slo^{loxP}/+$. While Figure 5.16 suggested that most metabolic pathways are down-regulated in $slo^{E366G}/+$, Figure 5.17 provides a more nuanced picture, in which every metabolic KEGG PATHWAY annotation contains both up- and down-regulated genes, suggesting a dys-, rather than general down-regulation of these metabolic processes. It would be of great

interest to identify regulatory genes that have the potential to affect the transcriptional landscape to elicit such a dysregulation – a task I approached by using the open-source software iRegulon (Janky et al., 2014). iRegulon aims to identify GRNs, defined as sets of genes regulated by single TFs, within a list of DEGs (Janky et al., 2014). Conceptually, iRegulon operates in three steps, as described in more detail in (Janky et al., 2014): (1) using large databases of TF binding motifs, it first builds an associative database between *cis*-regulatory elements (CREs) and all genes in the *Drosophila melanogaster* reference genome, thereby establishing genomic co-localisations between genes and CREs. (2) The algorithm then analyses which CREs can recover the greatest proportion of genes from an input list of DEGs, thereby identifying CRE enrichment within the DGE data. (3) Finally, iRegulon identifies TFs that are predicted to bind to enriched CREs, thereby generating a list of "master regulators" that are capable of inducing large-scale transcriptional changes (Janky et al., 2014).

For this analysis, I split the list of 1036 DEGs into one list of 514 up-, and a second list of 522 down-regulated genes. Both lists were analysed separately for TF binding site enrichment. Upon analysing the list of 514 up-regulated genes, the TF Foxo was predicted to bind to two separate groups of enriched TF binding motifs. Foxo is an interesting candidate because it is functionally implicated in metabolism, oxidation-reduction, and immunity (Becker et al., 2010; Eijkelenboom and Burgering, 2013), three major biological themes identified to be dysregulated in $slo^{E366G}/+$ (Figure 5.15, Figure 5.16). Based on the iRegulon analysis, Foxo is predicted to bind to TF binding sites associated with ~47% of up-regulated genes (234/514), and its interaction map is shown in Figure 5.18.
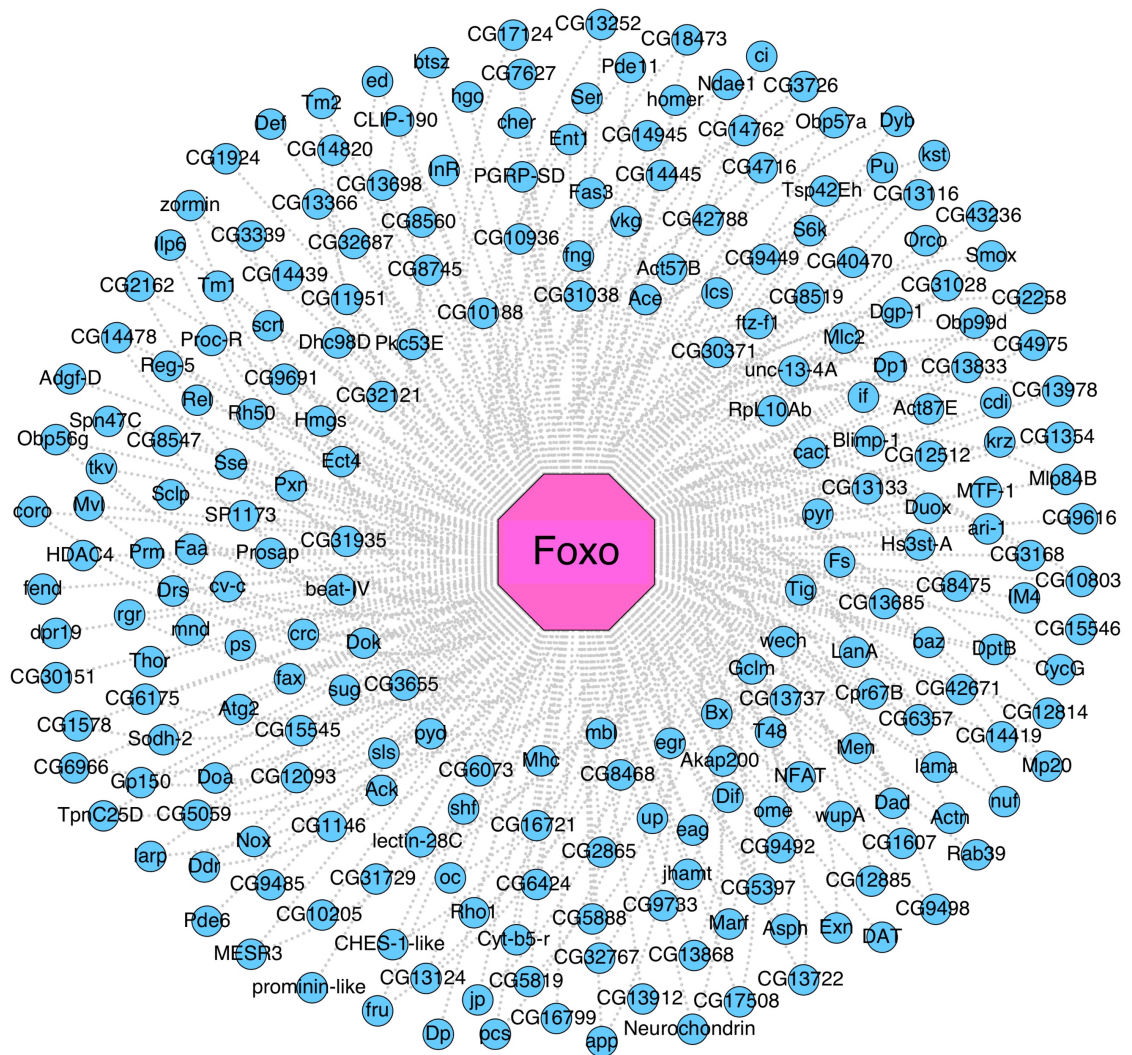
Figure 5.18 Foxo Gene Regulatory Network

iRegulon was used to analyse all 514 differentially up-regulated genes in $slo^{E366G}/+$ for enriched TF binding motifs. Enriched binding motifs were then linked to TFs that are predicted to bind to them. Foxo was identified as a TF that is predicted to bind to ~47% of differentially up-regulated genes (234/514), shown as a network diagram in this figure, with Foxo as a pink octagon at the centre. Grey dotted edges connect Foxo to the genes it regulates, illustrated as blue circles. The 514 up-regulated genes were enriched for two independent groups of Foxo TF binding motifs, and this network diagram represents both. Hence, some genes are innervated by two edges, indicating that these genes are associated with both motifs, while other genes are innervated by a single edge, indicating that these genes are associated with one of the two motifs.

Further analysis showed that Foxo is not predicted to bind to the 522 down-regulated genes, supporting the hypothesis that its activity might be increased in $slo^{E366G}/+$. An interesting TF specifically linked to the down-regulated genes is CrebB. As for Foxo and the set of up-regulated genes, two separate groups of CrebB binding motifs were found to be enriched in the set of down-regulated

genes. CrebB was found to bind to ~46% of down-regulated genes (239/522), a value strinkingly similar to the one ascribed to Foxo and the up-regulated genes. The GRN associated with CrebB is shown in Figure 5.19.

Figure 5.19 CrebB Gene Regulatory Network

iRegulon analysis was performed as described in Figure 5.18, using all 522 differentially down-regulated genes in *sloE366G/+*. CrebB was identified as a TF that is predicted to bind to ~46% of differentially down-regulated genes (239/522). The 522 down-regulated genes were enriched for two independent groups of TF binding motifs CrebB is predicted to bind, and this network diagram represents these interactions as described in Figure 5.18.

Due to the identification of Foxo as a TF predicted to bind specifically to a subset of up-regulated genes, and CrebB as a TF predicted to bind specifically to a subset of down-regulated genes, one might expect their respective GRNs to recover the GO annotations associated with the entire set of 1036 DEGs. In

particular, one would expect the Foxo-specific GRN to recover up-regulated GO terms and the CrebB-specific GRN to recover down-regulated GO terms. Indeed, this is exactly what I found: GO analysis with the Foxo- and CrebB-specific GRNs identified the GO terms "immune response" (GO:0006955) and "innate immune response" (GO:0045087) as significantly enriched in the Foxo-specific GRN (FDR = 0.0053 and FDR = 0.0069, respectively), and the GO terms "oxidation-reduction process" (GO:0055114) and "neuropeptide signaling pathway" (GO:0007218) as significantly enriched in the CrebB-specific GRN (FDR = 0.014 and FDR = 0.025, respectively). These data suggest that differential regulation of Foxo and CrebB in $slo^{E366G}/+$ might elicit the metabolic-, redox-, and immune dysregulation observed in this fly model of GEPD. Hence, one might predict a modulation of Foxo and CrebB activity in $slo^{E366G}/+$ to affect locomotor behaviour, the main phenotype associated with $slo^{E366G}/+$ animals (Figure 3.4, Figure 3.17).

5.4.8 RNA-seq-informed Behavioural Modifier Screen

Foxo is activated by oxidative stress, inhibited by insulin signalling, and has been shown to induce the innate immune response via the expression of anti-microbial peptides (AMPs) (Becker et al., 2010; Eijkelenboom and Burgering, 2013). These functional implications are well aligned with the main GO annotations associated with the gene expression changes between $slo^{E366G}/+$ and $slo^{loxP}/+$: oxidation-reduction, metabolism, and immunity (Figure 5.15). Intriguingly, manual curation of the DGE data revealed that four components of the insulin signalling pathway are differentially regulated between $slo^{E366G}/+$ and $slo^{loxP}/+$: the insulin-like peptides *dilp6* and *dilp2* are up- and down-regulated in $slo^{E366G}/+$, respectively, while insulin receptor (*InR*) and its adapter *chico* are up-regulated in $slo^{E366G}/+$. The differential expression of these genes and the prediction of their downstream target Foxo to bind to almost half of the up-regulated genes in $slo^{E366G}/+$ suggest a role for insulin signalling in GEPD pathogenesis. I tested this hypothesis by performing an insulin-themed dominant modifier screen. Using locomotor activity as a readout, dominant suppressors of the $slo^{E366G}/+$ locomotor defect are predicted to cause an increase in locomotion, while dominant enhancers should cause a decrease. To detect additive effects, this screen was simultaneously

performed in a $slo^{loxP}/+$ background. A schematic of insulin- and Foxo signalling in *Drosophila* is shown in Figure 5.20.
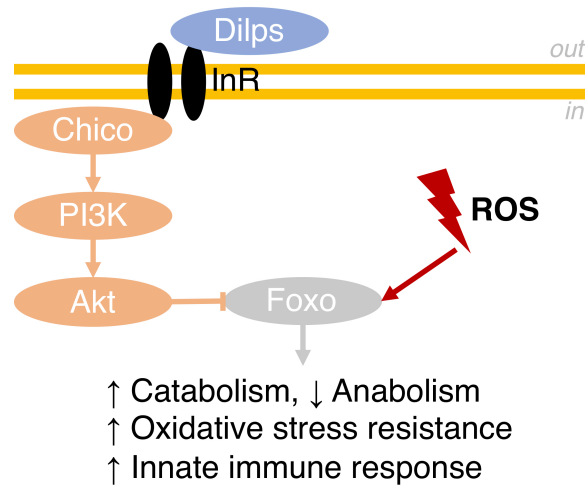
Figure 5.20 Insulin- and Foxo Signalling in *Drosophila*

The *Drosophila* genome encodes 8 Dilps via the genes *dilp1-8*, which bind to InR, inducing a signalling cascade involving Chico, PI3K, Akt, and the inhibition of the TF Foxo. Foxo activity is regulated by multiple upstream processes apart from insulin signalling, such as oxidative stress, which activates Foxo (ROS = reactive oxygen species). This figure was adapted from the following publications: (Eijkelenboom and Burgering, 2013; Garofalo, 2002; Nässel et al., 2015).

For this modifier screen, I tested alleles of the 8 *dilps* the *Drosophila* genome encodes (*dilp1-8*), different combinations of *dilps* simultaneously, two *InR* alleles, and alleles of *chico*, *Akt*, *foxo*, *to*, and *ImpL2*. Most of these alleles are reportedly hypo- or amorphic, as listed in Table 51. *to* and *ImpL2* were included in this screen because both genes are down-regulated in $slo^{E366G}/+$, while also being implicated in insulin signaling: ImpL2 has been shown to bind to secreted Dilps antagonistically (Figueroa-Clarevega and Bilder, 2015; Kwon et al., 2015), while To mediates downstream metabolic and behavioural effects of insulin signalling (Sheldon et al., 2011). The mutant alleles were crossed into $slo^{E366G}/+$ and $slo^{loxP}/+$ genetic backgrounds and locomotion measured over 24 h at a 12 h light:12 h dark cycle. For locomotor analysis, total beam breaks over 24 h were normalised to the $slo^{E366G}/+$ and $slo^{loxP}/+$ genetic backgrounds, as shown in Figure 5.21.
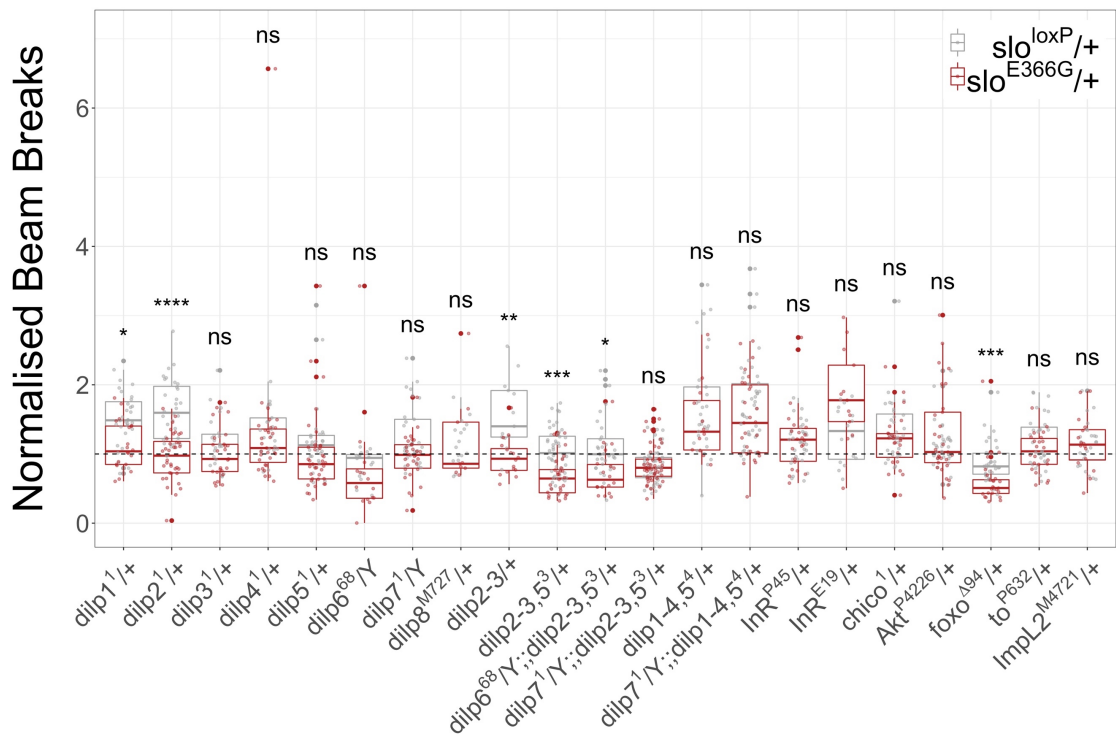
Figure 5.21 Insulin-themed Dominant Modifier Screen

This figure illustrates the results of an insulin-themed dominant modifier screen. The mutant alleles tested are shown on the x-, and their locomotion on the y-axis. Locomotion was normalised to genetic background, which is indicated in red for $slo^{E366G}/+$ and in grey for $slo^{loxP}/+$. A dashed line demarcates a fold-change of 1 with respect to the genetic backgrounds. Between 1 and 3 independent experimental repeats per genotype were performed, and the resulting data pooled. (n = 9-99; Mann-Whitney-Wilcoxon tests with Bonferroni correction; **** = p < 0.0001, *** = p < 0.001, ** = p < 0.01, * = p < 0.05, ns = p > 0.05)

The behavioural data in Figure 5.21 indicate that some mutant alleles increase locomotion in $slo^{loxP}/+$, but do not affect it in $slo^{E366G}/+$ ($dilp1^1$, $dilp2^1$, and $dilp2,3$), while others do not affect locomotion in $slo^{loxP}/+$, but decrease it in $slo^{E366G}/+$ ($dilp2,3,5^3$, $dilp6^{68}$;;$dilp2,3,5^3$, and $foxo^{\Delta94}$). Intriguingly, the $foxo$ null allele $foxo^{\Delta94}$ enhances the $slo^{E366G}/+$ locomotor defect, consistent with its potential role as a master regulator in GEPD pathogenesis (Figure 5.18). In order to confirm this result, I performed an experimental repeat with $foxo^{\Delta94}$, using the independent $slo^{E366G}/+$ and $slo^{loxP}/+$ recombinants $137.1.3/+$ and $111.1.1/+$, respectively. Indeed, the data confirm that partial loss of $foxo$ enhances the $slo^{E366G}/+$ locomotor defect, indicative of a genetic interaction (Figure 5.22).
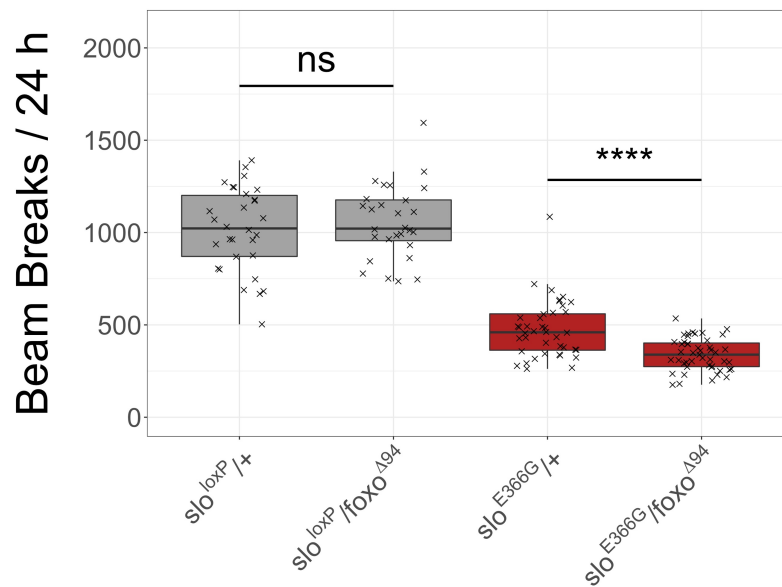
Figure 5.22 Partial Loss of *foxo* Enhances the *slo^E366G^/+* Locomotor Defect

Partial loss of *foxo* significantly decreased locomotion in *slo^E366G^/+*, while not affecting *slo^loxP^/+* locomotor activity, indicative of a genetic interaction. Data from two independent experimental repeats were pooled. (n = 28-47; Mann-Whitney-Wilcoxon test; **** = p < 0.0001, ns = p > 0.05)

5.5 Discussion

This chapter addresses the third question set out in the project aim: what are the molecular mechanisms underlying GEPD? In order to investigate GEPD pathophysiology on a molecular level, I performed RNA-seq of slo^{E366G}/+ and slo^{loxP}/+ adult male head tissue. The transcriptomic differences between these genotypes point towards potential roles for dysregulated metabolic-, redox-, and immune function in slo^{E366G}/+. Furthermore, behavioural evidence is provided that partial loss of *foxo* enhances the slo^{E366G}/+ locomotor defect, while also suggesting a potential role for insulin signalling in modulating this phenotype. Altogether, the results presented in this chapter serve as an entry point towards an increased molecular understanding of GEPD, while simultaneously focussing attention on specific pathophysiological mechanisms.

5.5.1 Experimental Notes and Caveats

5.5.1.1 Interpreting RNA-seq Data

It is important to scrutinise from first principles how the RNA-seq data were generated, and how the process of sample preparation might affect their interpretability. Could it be, for example, that slo^{E366G}/+ flies are more prone to infection, which might explain the up-regulation in immune-related genes (Figure 5.15)? Similarly, being a weak genotype, might poor stock conditions of slo^{E366G}/+ flies prevent proper feeding, resulting in a differential expression of genes involved in metabolism (Figure 5.15, Figure 5.16)? These questions illustrate the fundamental importance of the quality of starting material in RNA-seq experiments (Conesa et al., 2016). Indeed, I took multiple measures to reduce the number of confounding variables affecting gene expression: (1) all males used for RNA-seq were age-matched with a resolution of 2 days (4-6 days old). (2) All males were housed with an excess number of females for 48 h prior to head isolation, in order to increase the probability of mating. (3) Head isolation was always performed during the same time of day – between 4 pm and 6 pm – due to the circadian cycling of *slo* expression (Ceriani et al., 2002). (4) None of the flies were anaesthetised with CO_2 for 48 h prior to head isolation. (5) All flies were transferred onto fresh food every day prior to head isolation, in order to

prevent a build-up of mould and bacteria, which could affect nutritional- and infectious status. Despite this rigorous effort to minimise the number of confounding variables, some could not be controlled for, such as potential effects of the slo^{E366G} allele on the biophysical properties of the male *Drosophila* courtship song (Ding et al., 2016; Peixoto and Hall, 1998), which could in turn affect mating success, or the chronically reduced locomotion of $slo^{E366G}/+$ flies, which might result in transcriptomic changes as well. Hence, the RNA-seq data likely represent a chimera of primary transcriptional changes induced by the presence of the slo^{E366G} allele and secondary changes that occur in response to altered molecular-, cellular-, and organismal function of $slo^{E366G}/+$ animals. To identify primary, disease-relevant changes, functional studies, such as the behavioural screen presented in this chapter, are required (Figure 5.21, Figure 5.22).

5.5.1.2 Validation of Behavioural Data

Before discussing the behavioural data presented in this chapter, it has to be stressed that these data are preliminary and require independent experimental validation (Figure 5.21, Figure 5.22). None of the alleles, including $foxo^{Δ94}$, were outcrossed, making it impossible to exclude genetic background effects from affecting behaviour. Hence, it will be important to repeat these experiments with outcrossed modifier alleles. To confirm the genetic interaction between *foxo* and slo^{E366G}, conditional over-expression and knock-down of *foxo* in a $slo^{E366G}/+$ background might be employed as well.

5.5.2 Clinical Relevance

5.5.2.1 Foxo as a Potential Master Regulator in GEPD

It is possible that multiple parallel processes induce the transcriptional changes between $slo^{E366G}/+$ and $slo^{loxP}/+$. Alternatively, a small number of TFs might orchestrate them. This hypothesis was tested via CRE enrichment analysis (Janky et al., 2014), identifying Foxo as a TF predicted to bind to ~47% of genes up-regulated in $slo^{E366G}/+$ (Figure 5.18). While this analysis also identified CrebB as a TF predicted to bind to ~46% of down-regulated genes, I focussed on Foxo due to its role as a molecular integrator of insulin signalling and oxidative stress

(Eijkelenboom and Burgering, 2013), processes captured by the enriched GO- and KEGG PATHWAY annotations (Figure 5.15, Figure 5.16). Indeed, a dominant modifier screen identified the *foxo* null allele *foxo^{Δ94}* as a genetic enhancer of the *slo^{E366G}/+* locomotor defect (Figure 5.22), suggesting that increased Foxo activity might be a homeostatic response to the presence of the *slo^{E366G}* allele.

Further evidence for an involvement of Foxo in GEPD pathogenesis is provided by its downstream transcriptional signature. Foxo has previously been shown to induce the expression of AMPs, which are integral components of the innate immune response in *Drosophila* (Becker et al., 2010). Strikingly, the authors identified a Foxo-mediated increase in the expression of 8 AMPs, 6 of which are also up-regulated in *slo^{E366G}/+*: *Atta*, *Drs*, *Dpt*, *Dro*, *Cec*, and *Def* (Becker et al., 2010). These data provide further evidence for Foxo to be involved in mediating the transcriptional changes observed in *slo^{E366G}/+*, implicating its activity with each of the main GO annotations enriched in the DGE data: metabolism, oxidation-reduction, and immunity (Figure 5.15).

While the *Drosophila* genome encodes a single Foxo isoform, the mammalian genome encodes four: FoxO1, FoxO3, FoxO4, and FoxO6 (Salih and Brunet, 2008). The regulation of both *Drosophila* and mammalian Foxo is complex and involves a variety of upstream signalling pathways as well as post-translational modifications of Foxo, including phosphorylation, methylation, ubiquitylation, and acetylation (Eijkelenboom and Burgering, 2013). Fundamentally, Foxo acts as a convergence point of insulin signalling and oxidative stress, which act antagonistically to inhibit and activate Foxo, respectively (Figure 5.20) (Salih and Brunet, 2008). Insulin signalling induces the phosphorylation of Foxo, inhibiting it via cytoplasmic retention, while oxidative stress induces activation of Foxo by mediating its translocation into the nucleus and facilitating the transcription of Foxo target genes (Eijkelenboom and Burgering, 2013). Hence, Foxo functions as a "homeostatic regulator", inducing transcriptional responses to counteract oxidative- and metabolic stress as well as growth factor deprivation (Eijkelenboom and Burgering, 2013). These transcriptional responses are aimed at mitigating the stress Foxo was activated

by, affecting metabolism, protein homeostasis, cell fate decisions, damage repair, and stress resistance (Eijkelenboom and Burgering, 2013; Salih and Brunet, 2008). Hence, identifying $foxo^{\Delta 94}$ as a genetic modifier of the $slo^{E366G}/+$ locomotor defect strongly suggests that $slo^{E366G}/+$ flies experience a state of stress and depend on the homeostatic activity of Foxo. On the other hand, $slo^{loxP}/+$ flies might tolerate a partial loss of $foxo$ because they do not experience this stressful state (Figure 5.22). Investigating potential stressors that induce Foxo activity in $slo^{E366G}/+$ might, therefore, represent a strategy to identify upstream molecular pathways that are perturbed in this genotype, facilitating the discovery of the $prima\ causa$ of GEPD. Following this approach, I focussed on a potential role for insulin signalling GEPD.

5.5.2.2 Altered Insulin Signalling in GEPD

GLUT1-DS is linked to mutations in $SLC2A1$ (De Giorgis and Veggiotti, 2013). As described in Paragraph 1.2.1.3, $SLC2A1$ encodes GLUT1, a glucose transporter facilitating the transport of glucose across the BBB (De Giorgis and Veggiotti, 2013). The clinical symptoms of GLUT1-DS – including dyskinesia, seizures, and a variety of comorbidities – are due to unmet neuronal energy demands as a result of hypoglycorrhachia (Brockmann, 2009; De Giorgis and Veggiotti, 2013). Both GO- and KEGG PATHWAY analyses identified altered metabolism in $slo^{E366G}/+$ (Figure 5.15, Figure 5.16), indicating a metabolic component to GEPD as well – an unexpected but intriguing finding.

　　　Four lines of evidence suggest that insulin signalling might be involved in mediating the $slo^{E366G}/+$ locomotor defect: (1) perturbed insulin signalling could lead to the metabolic disturbances identified via GO- and KEGG PATHWAY analyses (Figure 5.15, Figure 5.16); (2) perturbed insulin signalling could be the upstream mechanism affecting Foxo activity (Eijkelenboom and Burgering, 2013) (Paragraph 5.5.2.1); (3) manual curation of the RNA-seq data identified 4 genes of the insulin signalling pathway to be differentially expressed between $slo^{E366G}/+$ and $slo^{loxP}/+$: $dilp6,\ InR$, and $chico$ are up-, while $dilp2$ is down-regulated in $slo^{E366G}/+$; (4) dysregulated insulin signalling would be congruent with the increased larval body size and decreased adult life span observed in $slo^{E366G}/+$ animals (Figure 3.6, Figure 3.7, Figure 3.21), as broad $dilp2$ over-expression has

been shown to increase adult *Drosophila* body size (Brogiolo et al., 2001), while loss of *dilp2* extended *Drosophila* life span (Grönke et al., 2010). Indeed, via an insulin-themed dominant modifier screen, I identified differential effects of altered insulin signalling on slo^{E366G}/+ and slo^{loxP}/+ locomotion – suggesting a potential role for insulin signalling in GEPD (Figure 5.21).

While $dilp1^1$/+, $dilp2^1$/+, and $dilp2$-3/+ specifically increased slo^{loxP}/+ locomotion, $dilp2,3,5^3$/+ and $dilp6^{68}$/Y;;$dilp2,3,5^3$/+ specifically reduced slo^{E366G}/+ locomotion (Figure 5.21). Dilp2, Dilp3, and Dilp5 are released from 14 median neurosecretory cells (MNCs) in the PI, termed insulin-producing cells (IPCs), implicating a role for dysregulated cerebral insulin signalling in slo^{E366G}/+ locomotion (Nässel et al., 2015). However, since insulin signalling negatively regulates Foxo activity (Figure 5.20), reducing *dilp* levels should increase Foxo activity and would, therefore, be expected to result in a behavioural rescue – instead, simultaneously reducing *dilp2-, dilp3-, and dilp5* levels enhanced the slo^{E366G}/+ locomotor defect (Figure 5.21).

These contradictory results might be explained by a complex transcriptional network regulating *dilp* expression, which could lead to unexpected transcriptional changes in response to $dilp2,3,5^3$/+ and $dilp6^{68}$/Y;;$dilp2,3,5^3$/+. For example, homozygosity for $dilp2^1$ leads to increased *dilp3* and *dilp5* expression, while loss of *dilp3* increases *dilp2* and *dilp5* expression (Grönke et al., 2010). Moreover, ablation of *dilp5* is linked to an increase in *dilp3-*, and ablation of *dilp6* to a decrease in *dilp3* expression (Grönke et al., 2010). Hence, without molecular analysis, it is difficult to predict actual changes of *dilp* expression in the presence of $dilp2,3,5^3$/+ and $dilp6^{68}$/Y;;$dilp2,3,5^3$/+. Moreover, *dilp* expression has been shown not to directly correlate with Dilp release (Nässel et al., 2015; Park et al., 2014), further complicating the results. Hence, additional experiments are required to confirm a role for insulin signalling in GEPD pathogenesis.

5.5.3 Conclusion

This chapter provided a preliminary link between dysregulated insulin signalling, increased Foxo activity, and GEPD pathogenesis. Further investigation of these

findings might lead towards a better understanding of the molecular mechanisms underlying this PxD-epilepsy syndrome.

6 Concluding Remarks

This thesis described the generation, characterisation, and functional analysis of a novel *Drosophila* model of GEPD, which recapitulates the human GEPD-linked D434G missense mutation in form of the novel slo^{E366G} allele (Du et al., 2005). Prior to this work, *in vitro* studies had defined the biophysical effects of the GEPD-linked mutation, as described in Paragraph 1.4.1.2 (Yang et al., 2010). The *in vivo* and *ex vivo* data on $slo^{E366G}/+$ animals presented in this thesis complement those results and incorporate them into an organismal framework.

First, this thesis provides supporting evidence for the hypothesis that the increased Ca^{2+} sensitivity exhibited by the murine (D369G) and human (D434G) mutations *in vitro* is conserved *ex vivo* in *Drosophila* harbouring the equivalent mutation (E366G) (Figure 3.11) (Du et al., 2005; Yang et al., 2010). Characterising the effects of this mutation at the organismal level revealed that $slo^{E366G}/+$ larvae and adults exhibit severe locomotor abnormalities, most notably a decrease in travelling distance and altered action selection (Figure 3.4, Figure 3.17, Figure 3.8, Figure 3.19). Importantly, in adults, these defects could be localised to cholinergic neurons (Figure 4.15). Further, transcriptomic analyses identified potential roles for altered metabolic-, redox-, and immune function in GEPD pathogenesis. Based on these data, preliminary evidence is provided that insulin signalling might be perturbed- (Figure 5.21), and *foxo* differentially regulated in GEPD (Figure 5.22).

Altogether, these data address the three questions set out in the project aim (Paragraph 1.6): (1) what are the organismal effects of the D434G-equivalent mutation in flies? (2) Where is the mutation required to exert its pathogenic effects? (3) What are the molecular mechanisms underlying GEPD? This thesis does not exhaustively (1) or definitively (2, 3) answer these questions, but it provides a wealth of data that lay the foundation for a better understanding of GEPD pathogenesis. Based on these data, three main strands of future investigation are of particular interest: (1) a more restricted pathogenic locus of GEPD might be identified; (2) experiments might be conducted to confirm and further investigate a role for insulin signalling in GEPD; (3) other experimental

avenues might be explored that could lead to an increased understanding of GEPD pathogenesis.

6.1 Future Directions

6.1.1 Restricting the Pathogenic Locus of GEPD

In order to validate the spatial dissection results presented in Chapter 4, Paragraph 4.5.1.1 suggested to perform an RNAi-based screen in a $slo^{E366G}/+$ background, targeting either slo itself, or genes that Slo function depends on, such as $dysc$ and genes encoding Ca_v channels (Griguoli et al., 2016; Jepson et al., 2012). A knock-down of these genes in cholinergic neurons would be predicted to rescue the $slo^{E366G}/+$ locomotor defect, strengthening the hypothesis that cholinergic neurons contain the pathogenic locus of GEPD. Notably, cholinergic neurons are the main neuronal subtype in the *Drosophila* nervous system, as illustrated by the detection of ChAT immunoreactivity in almost the entire adult brain neuropil (Yasuyama and Salvaterra, 1999).

Indeed, cholinergic neurons can be found in both the central and peripheral nervous system (Salvaterra and Kitamoto, 2001; Yasuyama and Salvaterra, 1999), and both populations might contribute to the $slo^{E366G}/+$ locomotor defect – which may be thought of as a compound phenotype consisting of various pathological processes acting in parallel. Via selectively targeting the central and peripheral nervous system with the two spatial dissection strategies outlined in Chapter 4, their relative contributions to the $slo^{E366G}/+$ locomotor defect could be determined – this approach might further be applied to test individual sensory modalities that are known to involve cholinergic signalling, such as audition (Ishikawa et al., 2017; Sanes and Hildebrand, 1976). Similarly, more restricted cholinergic subpopulations in the CNS could be investigated.

Moreover, it is possible that, despite not affecting locomotion by themselves (Figure 4.12), peptidergic neurons modulate the $slo^{E366G}/+$ locomotor phenotype – potentially via an involvement in the metabolic dysregulation observed in $slo^{E366G}/+$ (Figure 5.15, Figure 5.16), which would be consistent with their role in mediating the wing-inflation defect (Figure 4.13). This hypothesis

could be tested by simultaneously targeting peptidergic and cholinergic neurons with the spatial dissection strategies described in Chapter 4.

Instead of targeting neurons based on neurotransmitter identity, a complementary approach could target specific brain areas based on neuroanatomy. Since $slo^{E366G}/+$ animals exhibit severe locomotor defects, this approach might commence by targeting locomotor centres in the CNS. Of particular interest would be the fly central complex, because this central brain structure has been suggested to be homologous to the vertebrate basal ganglia (Strausfeld and Hirth, 2013), whose involvement in movement disorders, including dyskinesia, is widely appreciated (Wichmann and Dostrovsky, 2011). The central complex consists of the fan-shaped body, the ellipsoid body, the protocerebral bridge, and the paired noduli, and its disruption has been linked to a variety of locomotor defects, including decreases in locomotor speed and -bout length (Strauss, 2002) – reminiscent of the $slo^{E366G}/+$ adult locomotor defect (Figure 3.18, Figure 3.20). Hence, applying the RNAi- and Dysc-mediated spatial dissection strategies to sub-compartments of the central complex would elucidate whether aberrant activity within this network contributes to the $slo^{E366G}/+$ locomotor defect. In Paragraph 4.5.2.2, I ascribed an important role in GEPD pathogenesis to striatal cholinergic interneurons, due to their involvement in modulating MSN activity (Kandel et al., 2013). Using the spatial dissection strategies to target the homologous neurons in the central complex would allow for this hypothesis to be tested in flies. Indeed, local interneurons in the fan-shaped body have been described as homologous to striatal cholinergic interneurons (Strausfeld and Hirth, 2013). Hence, if appropriate *Gal4*-drivers can be identified, an ideal future experiment would target these interneurons in the fan-shaped body to assess their role in mediating the $slo^{E366G}/+$ locomotor defect.

6.1.2 Investigating Insulin Signalling in GEPD

An RNA-seq-informed modifier screen suggested a potential role for insulin signalling in GEPD pathogenesis (Figure 5.21). However, further evidence is required to confirm these results (Paragraphs 5.5.1.2 and 5.5.2.2). In order to definitively test whether insulin signalling is involved in GEPD pathogenesis, two questions must be answered: (1) is insulin signalling altered in $slo^{E366G}/+$, and (2)

does experimental modulation of insulin signalling affect $slo^{E366G}/+$ behaviour? Dilp secretion can be measured directly via a tagged *dilp2* construct that allows for ELISA-based quantification of secreted Dilp2 from the *Drosophila* haemolymph at picomolar concentrations (Park et al., 2014). Using this experimental strategy, Dilp2 release could be compared between $slo^{E366G}/+$ and $slo^{loxP}/+$, revealing whether IPC-mediated insulin signalling is dysregulated in this fly model of GEPD. To modulate Dilp release *in vivo*, the activity of IPCs could be manipulated. Interestingly, it has recently been shown that IPC-targeted expression of *Kir2.1*, encoding a hyperpolarising inward-rectifying K^+ channel (Baines et al., 2001), significantly reduces Dilp2 secretion (Park et al., 2014). Performing an analogous experiment with the *UAS-TrpA1* construct, which encodes a depolarising temperature- and voltage-gated cation channel (Hamada et al., 2008; Pulver et al., 2009), would increase IPC activity and Dilp release *in vivo*. Dilp release can also be manipulated pharmacologically: direct sensing of extracellular leucine by IPCs has been shown to induce Dilp2- and Dilp5 release in *Drosophila* larvae (Manière et al., 2016), while the chemical inhibitor SecinH3 decreases insulin signalling in *Drosophila* larvae and adults (Fuss et al., 2006; Hafner et al., 2006). Together, quantifying endogenous levels of Dilp secretion and manipulating Dilp secretion *in vivo* would provide strong evidence to demonstrate or refute an involvement of insulin signalling in GEPD. If insulin signalling can be confirmed to participate in GEPD pathogenesis, it would be of great interest to investigate it in more detail.

Insulin signalling is pleitropic and targets virtually all mammalian cells, including myocytes, adipocytes, hepatocytes, and neurons (Haeusler et al., 2018). Via neurons, it affects anorexigenic and locomotor behaviour, while stimulating glucose uptake in myocytes and adipocytes by increasing GLUT4 expression on the plasma membrane (Haeusler et al., 2018). Furthermore, insulin signalling stimulates protein synthesis in muscle tissue, decreases lipolysis in adipose tissue, and increases glucose utilisation and triglyceride synthesis in the liver, where it also inhibits glucose production (Haeusler et al., 2018). Hence, if Foxo activation in $slo^{E366G}/+$ occurs via dysregulated insulin signalling (Paragraph 5.5.2.1), this genotype is predicted to cause wide-ranging metabolic disturbances, including altered glucose metabolism.

Hence, it would be intriguing to investigate whether altering metabolism via a change in diet could modulate the $slo^{E366G}/+$ locomotor defect. Subjecting $slo^{E366G}/+$ flies to the ketogenic diet would be of particular interest, since this dietary intervention is an effective treatment for PED and GLUT1-DS (De Giorgis and Veggiotti, 2013), while also decreasing seizures in a *Drosophila* model of mitochondrial encephalomyelopathies (MEs), a seizure-associated group of metabolic disorders (Fogle et al., 2016) – illustrating its efficacy in disorders independent of *SLC2A1* mutations. To specifically investigate a role for altered glucose metabolism in GEPD, the cellular glucose availability in $slo^{E366G}/+$ could be reduced by performing a dominant modifier screen with hypomorphic *Glut1* alleles – if $slo^{E366G}/+$ flies exhibit dysregulated glucose metabolism, they might be more sensitive to a reduction in *Glut1* transcription. This screen could be accompanied by conditional over-expression and knock-down experiments targeting *Glut1*. Moreover, circulating glucose levels in the haemolymph could be quantified spectrophotometrically, as previously demonstrated in *Drosophila* larvae (Ugrankar et al., 2018). If these experiments were to yield positive results, large-scale metabolic shifts between $slo^{E366G}/+$ and $slo^{loxP}/+$ could be investigated using an unbiased metabolomics approach (Tennessen et al., 2014). Indeed, the availability of both metabolomic and transcriptomic datasets would allow for data analysis approaches aimed at linking pathogenic gene expression changes to metabolic dysregulation, further elucidating GEPD pathogenesis.

6.1.3 Unexplored Mechanisms Linked to GEPD

6.1.3.1 Dopamine Signalling in GEPD

The spatial dissection data presented in Chapter 4 suggest a role for striatal cholinergic interneurons in GEPD pathogenesis (Paragraph 4.5.2.2). Since these neurons express BK channels (Bennett et al., 2000; Goldberg and Wilson, 2005), it is possible that the D434G mutation alters their intrinsic firing properties (Paragraph 4.5.2.2). Hence, Paragraph 6.1.1 suggests to specifically re-introduce Slo or knock-down *slo* in homologous neurons in *Drosophila*. A complementary strategy could investigate a role for dopaminergic modulation of striatal cholinergic interneurons in GEPD pathogenesis. In the DYT1 dystonia

mouse model described in in Paragraph 4.5.2.2, the response of striatal cholinergic interneurons to the dopamine receptor D2 (D2R) agonist quinpirole was found to be altered: while not affecting the firing properties of these neurons in wild-type controls, quinpirole induced a persistent increase in firing rate in DYT1 mice (Martella et al., 2014). These data suggest that an altered response of striatal cholinergic interneurons to dopaminergic nigrostriatal projections might be involved in DYT1 pathogenesis.

To test whether dopaminergic modulation of striatal cholinergic interneurons might also be involved in GEPD pathogenesis, RNAi-mediated knock-down of *Drosophila* dopamine receptors (*Dop1R1*, *Dop1R2*, *Dop2R*, and *DopEcR*) in cholinergic neurons – or subpopulations thereof – could be performed. If aberrant dopaminergic modulation of striatal cholinergic interneurons is involved in GEPD pathogenesis, knock-down of the relevant dopamine receptor in cholinergic neurons should modulate the $slo^{E366G}/+$ locomotor defect. Of note, the mechanisms underlying dopaminergic modulation in the insect central complex have been suggested to be homologous to nigrostriatal dopaminergic modulation in the vertebrate basal ganglia (Strausfeld and Hirth, 2013), supporting this experimental approach.

6.1.3.2 Oxidative Stress in GEPD

While Foxo is inhibited by insulin signalling, it is activated by oxidative stress either via Jun N-terminal kinase (JNK) signalling or by direct oxidation of its own amino acid residues (Figure 5.20) (Eijkelenboom and Burgering, 2013). Hence, in addition to confirming and further exploring insulin signalling in GEPD pathogenesis (Paragraph 6.1.2), future experiments might also investigate an involvement of oxidative stress. A potential role for oxidative stress in GEPD pathogenesis is supported by the expression of mtBK channels on the IMM, as described in Paragraph 1.4.3.2 (Li and Gao, 2016). Mitochondria are the site of aerobic respiration, a process that generates ROS – including superoxide radicals ($O_2\bullet^-$), hydrogen peroxide (H_2O_2), and hydroxyl radicals ($\bullet OH$) – as metabolic by-products (Turrens, 2003). As discussed in Paragraph 1.4.3.2, ROS levels have been found to be increased in murine $KCNMA1^{-/-}$ cardiomyocytes in post-anoxic conditions, associating altered mtBK channel function with oxidative

stress (Soltysinska et al., 2014). Hence, dysregulated mitochondrial Slo function in $slo^{E366G}/+$ animals might lead to increased levels of ROS production, which would, in turn, activate Foxo so as to counteract oxidative stress (Figure 5.20).

If oxidative stress is involved in GEPD pathogenesis, one would predict different ROS levels between $slo^{E366G}/+$ and $slo^{loxP}/+$. Hence, it would be of interest to quantify ROS levels in these genotypes, which can be done fluorometrically, as demonstrated previously in *Drosophila* (Chakrabarti et al., 2014). In order to address whether oxidative stress might be causally linked to the $slo^{E366G}/+$ locomotor defect, *in vivo* modulation of ROS levels would be required. Pharmacologically, oxidative stress can be increased *in vivo* via injection or feeding of the herbicide paraquat, which increases the production of $O_2 \bullet^-$ (Cochemé and Murphy, 2008; Hill et al., 2018), or via feeding of H_2O_2, which induces $\bullet OH$ production and has been shown to alter *Drosophila* locomotor behaviour (Grover et al., 2009; Hill et al., 2018). In order to decrease ROS levels *in vivo*, *Gal4*-mediated over-expression of the antioxidant genes *catalase*, *Sod1*, and *Sod2* could be performed (Hill et al., 2018): Superoxide dismutase (Sod) catalyses the disproportionation/dismutation of $O_2 \bullet^-$ into O_2 and H_2O_2, while catalase catalyses the reaction of H_2O_2 to H_2O and O_2 (Chelikani et al., 2004; Hayyan et al., 2016), both counteracting oxidative stress. If oxidative stress contributes to GEPD pathogenesis, increasing it would be predicted to enhance-, while decreasing it would be predicted to suppress the $slo^{E366G}/+$ locomotor defect.

6.2 Classifying GEPD

As described in Paragraph 1.2.1.4, PxDs, with or without epilepsy, have been classified using a tripartite system comprising channelopathies, synaptopathies, and transportopathies (Erro et al., 2017). Since PRRT2 and PNKD are implicated in synaptic function, their associated forms of PxD – PKD and PNKD, respectively – have been classified as synaptopathies (Erro et al., 2017; Gardiner et al., 2015). Similarly, the transporter function of GLUT1 led to the classification of *SLC2A1*-linked PED as a transportopathy (Erro et al., 2017). Since *KCNMA1* encodes the α-subunit of the BK channel, GEPD was classified as a channelopathy,

suggesting that altered neuronal excitability causes PNKD and epilepsy (Erro et al., 2017; Shen et al., 2015). However, the possible involvement of perturbed metabolic-, redox-, and immune function in GEPD pathogenesis suggests additional nuance to this pathological framework (Figure 5.15, Figure 5.16) – a proposition strengthened by a suggested role for PNKD in regulating cellular redox state in addition to pre-synaptic neurotransmitter release (Shen et al., 2011). Hence, although the GEPD-linked D434G mutation in *KCNMA1* has been shown to lead to a gain of BK channel function *in vitro* (Yang et al., 2010) and *ex vivo* (Figure 3.11), changes in neuronal excitability might contribute to-, but not represent the whole picture of GEPD pathogenesis. Indeed, while cholinergic neurons might contain the pathogenic locus of GEPD (Figure 4.15), the expressivity of this disorder could be dependent on additional modulatory effects, such as insulin signalling and glucose metabolism (Figure 5.21). As such, the data presented in this thesis warrant a multi-systems approach to GEPD, and potentially other forms of PxD and PxD-epilepsy syndromes – which might, ultimately, lead to improved treatment strategies.

7 Acknowledgements

I could not have attempted, let alone completed, a PhD without the support of many a person. Words are insufficient to express my gratitude, but, briefly, I would like to thank:

- My parents, who have always encouraged me to pursue my ambitions
- My family, who has always supported my decisions
- My friends, collectively, for their interest in my life
- Dieter Wiedenhöft, whose support in high school laid the foundation for everything that came thereafter
- Prof. Robert Wilkins, who has always believed in me
- Dr. Srinivasa Rao, who has shown nothing but patience and kindness
- Prof. David Attwell, whom I could always rely on
- The Jepson Lab, including past and present members, who have been a continuous source of inspiration
- Dr. Ko-Fan Chen, who has always been honest, supportive, and engaged
- Dr. Alan Pittman for being a superb bioinformatics teacher
- Prof. Dimitri Kullmann for introducing me to the world of clinical neurology
- Dr. James Jepson, an extraordinary teacher and mentor who has provided constant encouragement and always prioritised well-being over productivity

I would also like to thank the following organisations, which have trusted me both personally and academically via financial investments, without which I would not have been able to reach this stage in my career:

- The Anglo-German Club e.V.
- The Hans Rudolf Foundation
- The Konrad Adenauer Foundation
- The German Academic Scholarship Foundation
- The Wellcome Trust

8 References

Adelman, J.P., Shen, K.-Z., Kavanaugh, M.P., Warren, R.A., Wu, Y.-N., Lagrutta, A., Bond, C.T., and Alan North, R. (1992). Calcium-Activated Potassium Channels Expressed from Cloned Complementary DNAs. Neuron *9*, 209–216.

Atasu, B., Hanagasi, H., Bilgic, B., Pak, M., Erginel-Unaltuna, N., Hauser, A.-K., Guven, G., Simón-Sánchez, J., Heutink, P., Gasser, T., et al. (2018). *HPCA* Confirmed as a Genetic Cause of DYT2-Like Dystonia Phenotype. Mov. Disord. *33*, 1354–1358.

Atkinson, N.S., Robertson, G.A., and Ganetzky, B. (1991). A Component of Calcium-Activated Potassium Channels Encoded by the *Drosophila slo* Locus. Science (80-.). *253*, 551–555.

Atkinson, N.S., Brenner, R., Chang, W., Wilbur, J., Larimer, J.L., and Yu, J. (2000). Molecular Separation of Two Behavioral Phenotypes by a Mutation Affecting the Promoters of a Ca-Activated K Channel. J. Neurosci. *20*, 2988–2993.

Bailey, C.S., Moldenhauer, H.J., Park, S.M., Keros, S., and Meredith, A.L. (2019). *KCNMA1*-linked channelopathy. J. Gen. Physiol. jgp.201912457.

Baines, R.A., Uhler, J.P., Thompson, A., Sweeney, S.T., and Bate, M. (2001). Altered Electrical Properties in *Drosophila* Neurons Developing without Synaptic Transmission. J. Neurosci. *21*, 1523–1531.

Balderas, E., Zhang, J., Stefani, E., and Toro, L. (2015). Mitochondrial BK$_{Ca}$ channel. Front. Physiol. *6*, 104.

Batla, A., Sánchez, M.C., Erro, R., Ganos, C., Stamelou, M., Balint, B., Brugger, F., Antelmi, E., and Bhatia, K.P. (2015). The role of cerebellum in patients with late onset cervical/segmental dystonia?-Evidence from the clinic. Park. Relat. Disord. *21*, 1317–1322.

Bean, B.P. (2007). The action potential in mammalian central neurons. Nat. Rev. Neurosci. *8*, 451–465.

Becker, M.N., Brenner, R., and Atkinson, N.S. (1995). Tissue-Specific Expression of a *Drosophila* Calcium-Activated Potassium Channel. J. Neurosci. *15*, 6250–6259.

Becker, T., Loch, G., Beyer, M., Zinke, I., Aschenbrenner, A.C., Carrera, P., Inhester, T., Schultze, J.L., and Hoch, M. (2010). FOXO-dependent regulation of innate immune homeostasis. Nature *463*, 369–373.

Bellen, H.J., Levis, R.W., He, Y., Carlson, J.W., Evans-Holm, M., Bae, E., Kim, J., Metaxakis, A., Savakis, C., Schulze, K.L., et al. (2011). The *Drosophila* Gene Disruption Project: Progress Using Transposons With Distinctive Site Specificities. Genetics *188*, 731–743.

Bennett, B.D., Callaway, J.C., and Wilson, C.J. (2000). Intrinsic Membrane Properties Underlying Spontaneous Tonic Firing in Neostriatal Cholinergic Interneurons. J. Neurosci. *20*, 8493–8503.

Berkefeld, H., Sailer, C.A., Bildl, W., Rohde, V., Thumfart, J.-O., Eble, S., Klugbauer, N., Reisinger, E., Bischofberger, J., Oliver, D., et al. (2006). BK$_{Ca}$-Cav Channel Complexes Mediate Rapid and Localized Ca^{2+}-Activated K$^+$ Signaling. Science (80-.). *314*, 615–620.

Bhatia, K.P. (2011). Paroxysmal Dyskinesias. Mov. Disord. *26*, 1157–1165.

Bhattacharya, S., Stewart, B.A., Niemeyer, B.A., Burgess, R.W., McCabe, B.D., Lin, P., Boulianne, G., O'Kane, C.J., and Schwarz, T.L. (2002). Members of the synaptobrevin/vesicle-associated membrane protein (VAMP) family in *Drosophila* are functionally interchangeable *in vivo* for neurotransmitter release and cell viability. Proc. Natl. Acad. Sci. *99*, 13867–13872.

Bier, E., Harrison, M.M., O'Connor-Giles, K.M., and Wildonger, J. (2018). Advances in Engineering the Fly Genome with the CRISPR-Cas System. Genetics *208*, 1–18.

Blakeley, J., and Jankovic, J. (2002). Secondary Paroxysmal Dyskinesias. Mov. Disord. *17*, 726–734.

Boison, D. (2016). Adenosinergic signaling in epilepsy. Neuropharmacology *104*, 131–139.

Brand, A.H., and Perrimon, N. (1993). Targeted gene expression as a means of altering cell fates and generating dominant phenotypes. Development *118*, 401–415.

Brenner, R., Chen, Q.H., Vilaythong, A., Toney, G.M., Noebels, J.L., and Aldrich, R.W. (2005). BK channel β4 subunit reduces dentate gyrus excitability and protects against temporal lobe seizures. Nat. Neurosci. *8*, 1752–1759.

Brockmann, K. (2009). The expanding phenotype of GLUT1-deficiency syndrome. Brain Dev. *31*, 545–552.

Brogiolo, W., Stocker, H., Ikeya, T., Rintelen, F., Fernandez, R., and Hafen, E. (2001). An evolutionarily conserved function of the *Drosophila* insulin receptor and insulin-like peptides in growth control. Curr. Biol. *11*, 213–221.

Buckmaster, P.S. (2012). Mossy Fiber Sprouting in the Dentate Gyrus. In Jasper's Basic Mechanisms of the Epilepsies [Internet]. 4th Edition., pp. 1–29.

Cao, Q., Zhong, X.Z., Zou, Y., Zhang, Z., Toro, L., and Dong, X.P. (2015). BK Channels Alleviate Lysosomal Storage Diseases by Providing Positive Feedback Regulation of Lysosomal Ca^{2+} Release. Dev. Cell *33*, 427–441.

Ceriani, M.F., Hogenesch, J.B., Yanovsky, M., Panda, S., Straume, M., and Kay, S.A. (2002). Genome-Wide Expression Analysis in *Drosophila* Reveals Genes Controlling Circadian Behavior. J. Neurosci. *22*, 9305–9319.

Chakrabarti, S., Poidevin, M., and Lemaitre, B. (2014). The *Drosophila* MAPK p38c Regulates Oxidative Stress and Lipid Homeostasis in the Intestine. PLoS Genet. *10*, e1004659.

Charlesworth, G., Angelova, P.R., Bartolomé-Robledo, F., Ryten, M., Trabzuni, D., Stamelou, M., Abramov, A.Y., Bhatia, K.P., and Wood, N.W. (2015). Mutations in *HPCA* Cause Autosomal-Recessive Primary Isolated Dystonia. Am. J. Hum. Genet. *96*, 657–665.

Chelikani, P., Fita, I., and Loewen, P.C. (2004). Diversity of structures and properties among catalases. Cell. Mol. Life Sci. *61*, 192–208.

Chen, K.-F., Lowe, S., Lamaze, A., Krätschmer, P., and Jepson, J. (2019). Neurocalcin regulates nighttime sleep and arousal in *Drosophila*. Elife *8*, e38114.

Chen, T.-W., Wardill, T.J., Sun, Y., Pulver, S.R., Renninger, S.L., Baohan, A., Schreiter, E.R., Kerr, R.A., Orger, M.B., Jayaraman, V., et al. (2013). Ultrasensitive fluorescent proteins for

imaging neuronal activity. Nature *499*, 295–300.

Chen, W.-J., Lin, Y., Xiong, Z.-Q., Wei, W., Ni, W., Tan, G.-H., Guo, S.-L., He, J., Chen, Y.-F., Zhang, Q.-J., et al. (2011). Exome sequencing identifies truncating mutations in *PRRT2* that cause paroxysmal kinesigenic dyskinesia. Nat. Genet. *43*, 1252–1255.

Cheng, Y., Gu, X.Q., Bednarczyk, P., Wiedemann, F.R., Haddad, G.G., and Siemen, D. (2008). Hypoxia Increases Activity of the BK-Channel in the Inner Mitochondrial Membrane and Reduces Activity of the Permeability Transition Pore. Cell. Physiol. Biochem. *22*, 127–136.

Cheng, Y., Gulbins, E., and Siemen, D. (2011). Activation of the Permeability Transition Pore by Bax via Inhibition of the Mitochondrial BK Channel. Cell. Physiol. Biochem. *27*, 191–200.

Cochemé, H.M., and Murphy, M.P. (2008). Complex I Is the Major Site of Mitochondrial Superoxide Production by Paraquat. J. Biol. Chem. *283*, 1786–1798.

Coleman, J., Jouannot, O., Ramakrishnan, S.K., Zanetti, M.N., Wang, J., Salpietro, V., Houlden, H., Rothman, J.E., and Krishnakumar, S.S. (2018). PRRT2 Regulates Synaptic Fusion by Directly Modulating SNARE Complex Assembly. Cell Rep. *22,* 820–831.

Conesa, A., Madrigal, P., Tarazona, S., Gomez-Cabrero, D., Cervera, A., McPherson, A., Szcześniak, M.W., Gaffney, D.J., Elo, L.L., Zhang, X., et al. (2016). A survey of best practices for RNA-seq data analysis. Genome Biol. *17*, 13.

Cowmeadow, R.B., Krishnan, H.R., and Atkinson, N.S. (2005). The *slowpoke* Gene Is Necessary for Rapid Ethanol Tolerance in *Drosophila*. Alcohol. Clin. Exp. Res. *29*, 1777–1786.

Cowmeadow, R.B., Krishnan, H.R., Ghezzi, A., Al'Hasan, Y.M., Wang, Y.Z., and Atkinson, N.S. (2006). Ethanol Tolerance Caused by *slowpoke* Induction in *Drosophila*. Alcohol. Clin. Exp. Res. *30,* 745–753.

Cunliffe, V.T., Baines, R.A., Giachello, C.N.G., Lin, W.H., Morgan, A., Reuber, M., Russell, C., Walker, M.C., and Williams, R.S.B. (2015). Epilepsy research methods update: Understanding the causes of epileptic seizures and identifying new treatments using non-mammalian model organisms. Seizure *24*, 44–51.

Delhomme, N., Mähler, N., Schiffthaler, B., Sundell, D., Mannepperuma, C., Hvidsten, T.R., and Street, N.R. (2014). Guidelines for RNA-Seq data analysis. Epigenesys.

Deng, D., Xu, C., Sun, P., Wu, J., Yan, C., Hu, M., and Yan, N. (2014). Crystal structure of the human glucose transporter GLUT1. Nature *510*, 121–125.

Devinsky, O., Vezzania, A., O'Brien, T.J., Jette, N., Scheffer, I.E., de Curtis, M., and Perucca, P. (2018). Epilepsy. Nat. Rev. Dis. Prim. *4*, 18024.

Ding, Y., Berrocal, A., Morita, T., Longden, K.D., and Stern, D.L. (2016). Natural courtship song variation caused by an intronic retroelement in an ion channel gene. Nature *536,* 329–332.

Dobin, A. (2017). STAR manual 2.5.3a.

Dobin, A., and Gingeras, T.R. (2015). Mapping RNA-seq Reads with STAR. Curr. Protoc. Bioinforma. *51*, 11.14.1-11.14.19.

Dobin, A., Davis, C.A., Schlesinger, F., Drenkow, J., Zaleski, C., Jha, S., Batut, P., Chaisson, M., and Gingeras, T.R. (2013). STAR: ultrafast universal RNA-seq aligner. Bioinformatics *29*, 15–21.

Du, W., Bautista, J.F., Yang, H., Diez-Sampedro, A., You, S.-A., Wang, L., Kotagal, P., Lüders, H.O., Shi, J., Cui, J., et al. (2005). Calcium-sensitive potassium channelopathy in human epilepsy and paroxysmal movement disorder. Nat. Genet. *37*, 733–738.

Dudoit, S., Yang, Y.H., Callow, M.J., and Speed, T.P. (2002). Statistical Methods for Identifying Differentially Expressed Genes in Replicated cDNA Microarray Experiments. Stat. Sin. *12*, 111–139.

Düfer, M., Neye, Y., Hörth, K., Krippeit-Drews, P., Hennige, A., Widmer, H., McClafferty, H., Shipston, M.J., Häring, H.U., Ruth, P., et al. (2011). BK channels affect glucose homeostasis and cell viability of murine pancreatic beta cells. Diabetologia *54*, 423–432.

Eijkelenboom, A., and Burgering, B.M.T. (2013). FOXOs: signalling integrators for homeostasis maintenance. Nat. Rev. Mol. Cell Biol. *14*, 83–97.

Elkins, T., and Ganetzky, B. (1988). The Roles of Potassium Currents in *Drosophila* Flight Muscles. J. Neurosci. *8*, 428–434.

Elkins, T., Ganetzky, B., and Wu, C.F. (1986). A *Drosophila* mutation that eliminates a calcium-dependent potassium current. Proc. Natl. Acad. Sci. *83*, 8415–8419.

Erro, R., Sheerin, U.M., and Bhatia, K.P. (2014). Paroxysmal Dyskinesias Revisited: A Review of 500 Genetically Proven Cases and a New Classification. Mov. Disord. *29*, 1108–1116.

Erro, R., Bhatia, K.P., Espay, A.J., and Striano, P. (2017). The Epileptic and Nonepileptic Spectrum of Paroxysmal Dyskinesias: Channelopathies, Synaptopathies, and Transportopathies. Mov. Disord. *00*, 1–10.

Faville, R., Kottler, B., Goodhill, G.J., Shaw, P.J., and van Swinderen, B. (2015). How deeply does your mutant sleep? Probing arousal to better understand sleep defects in *Drosophila*. Sci. Rep. *5*, 8454.

Fernandez, R., Tabarini, D., Azpiazu, N., Frasch, M., and Schlessinger, J. (1995). The *Drosophila* insulin receptor homolog: a gene essential for embryonic development encodes two receptor isoforms with different signaling potential. EMBO J. *14*, 3373–3384.

Fernández, M. de la P., Chu, J., Villella, A., Atkinson, N., Kay, S.A., and Ceriani, M.F. (2007). Impaired clock output by altered connectivity in the circadian network. Proc. Natl. Acad. Sci. *104*, 5650–5655.

Figueroa-Clarevega, A., and Bilder, D. (2015). Malignant *Drosophila* Tumors Interrupt Insulin Signaling to Induce Cachexia-like Wasting. Dev. Cell *33*, 47–55.

Fogle, K.J., Hertzler, J.I., Shon, J.H., and Palladino, M.J. (2016). The ATP-sensitive K channel is seizure protective and required for effective dietary therapy in a model of mitochondrial encephalomyopathy. J. Neurogenet. *30*, 247–258.

Ford, K.J., and Davis, G.W. (2014). Archaerhodopsin Voltage Imaging: Synaptic Calcium and BK Channels Stabilize Action Potential Repolarization at the *Drosophila* Neuromuscular Junction. J. Neurosci. *34*, 14517–14525.

Fortini, M.E., Skupski, M.P., Boguski, M.S., and Hariharan, I.K. (2000). A Survey of Human Disease Gene Counterparts in the *Drosophila* Genome. J. Cell Biol. *150*, F23–F29.

Fremont, R., Tewari, A., Angueyra, C., and Khodakhah, K. (2017). A role for cerebellum in the hereditary dystonia DYT1. Elife *6*, e22775.

Fruscione, F., Valente, P., Sterlini, B., Romei, A., Baldassari, S., Fadda, M., Prestigio, C., Giansante, G., Sartorelli, J., Rossi, P., et al. (2018). PRRT2 controls neuronal excitability by negatively modulating Na+ channel 1.2/1.6 activity. Brain *141*, 1000–1016.

Fuss, B., Becker, T., Zinke, I., and Hoch, M. (2006). The cytohesin Steppke is essential for insulin signalling in *Drosophila*. Nature *444*, 945–948.

Gardella, E., Becker, F., Møller, R.S., Schubert, J., Lemke, J.R., Larsen, L.H.G., Eiberg, H., Nothnagel, M., Thiele, H., Altmüller, J., et al. (2016). Benign Infantile Seizures and Paroxysmal Dyskinesia Caused by an *SCN8A* Mutation. Ann. Neurol. *79*, 428–436.

Gardiner, A.R., Jaffer, F., Dale, R.C., Labrum, R., Erro, R., Meyer, E., Xiromerisiou, G., Stamelou, M., Walker, M., Kullmann, D., et al. (2015). The clinical and genetic heterogeneity of paroxysmal dyskinesias. Brain *138*, 3567–3580.

Garelli, A., Gontijo, A.M., Miguela, V., Caparros, E., and Dominguez, M. (2012). Imaginal Discs Secrete Insulin-Like Peptide 8 to Mediate Plasticity of Growth and Maturation. Science (80-.). *336*, 579–582.

Garofalo, R.S. (2002). Genetic analysis of insulin signaling in *Drosophila*. Trends Endocrinol. Metab. *13*, 156–162.

Gasteiger, E., Gattiker, A., Hoogland, C., Ivanyi, I., Appel, R.D., and Bairoch, A. (2003). ExPASy: the proteomics server for in-depth protein knowledge and analysis. Nucleic Acids Res. *31*, 3784–3788.

Gentleman, R., Carey, V., Bates, D., Bolstad, B., Dettling, M., Dudoit, S., Ellis, B., Gautier, L., Ge, Y., Gentry, J., et al. (2004). Bioconductor: open software development for computational biology and bioinformatics. Genome Biol. *5*, R80.

Ghezzi, A., Al-Hasan, Y.M., Larios, L.E., Bohm, R.A., and Atkinson, N.S. (2004). *slo* K+ channel gene regulation mediates rapid drug tolerance. Proc. Natl. Acad. Sci. *101*, 17276–17281.

Ghezzi, A., Pohl, J.B., Wang, Y., and Atkinson, N.S. (2010). BK channels play a counter-adaptive role in drug tolerance and dependence. Proc. Natl. Acad. Sci. *107*, 16360–16365.

De Giorgis, V., and Veggiotti, P. (2013). GLUT1 deficiency syndrome 2013: Current state of the art. Seizure *22*, 803–811.

Girouard, H., Bonev, A.D., Hannah, R.M., Meredith, A., Aldrich, R.W., and Nelson, M.T. (2010). Astrocytic endfoot Ca2+ and BK channels determine both arteriolar dilation and constriction. Proc. Natl. Acad. Sci. *107*, 3811–3816.

Gloor, G.B., Preston, C.R., Johnson-Schlitz, D.M., Nassif, N.A., Phillis, R.W., Benz, W.K., Robertson, H.M., and Engels, W.R. (1993). Type I Repressors of *P* Element Mobility. Genetics *135*, 81–95.

Goldberg, J.A., and Wilson, C.J. (2005). Control of Spontaneous Firing Patterns by the Selective Coupling of Calcium Currents to Calcium-Activated Potassium Currents in Striatal Cholinergic Interneurons. J. Neurosci. *25*, 10230–10238.

Goldberg, J.A., Teagarden, M.A., Foehring, R.C., and Wilson, C.J. (2009). Nonequilibrium Calcium Dynamics Regulate the Autonomous Firing Pattern of Rat Striatal Cholinergic Interneurons. J. Neurosci. *29*, 8396–8407.

Goto, S., Lee, L. V., Munoz, E.L., Tooyama, I., Tamiya, G., Makino, S., Ando, S., Dantes, M.B., Yamada, K., Matsumoto, S., et al. (2005). Functional Anatomy of the Basal Ganglia in X-Linked Recessive Dystonia-Parkinsonism. Ann. Neurol. *58*, 7–17.

Graybiel, A.M., Canales, J.J., and Capper-Loup, C. (2000). Levodopa-induced dyskinesias and dopamine-dependent stereotypies: a new hypothesis. Trends Neurosci. *23*, 71–77.

Griguoli, M., Sgritta, M., and Cherubini, E. (2016). Presynaptic BK channels control transmitter release: physiological relevance and potential therapeutic implications. J. Physiol. *594*, 3489–3500.

Grönke, S., Clarke, D.F., Broughton, S., Andrews, T.D., and Partridge, L. (2010). Molecular Evolution and Functional Characterization of *Drosophila* Insulin-Like Peptides. PLoS Genet. *6*, e1000857.

Grover, D., Ford, D., Brown, C., Hoe, N., Erdem, A., Tavaré, S., and Tower, J. (2009). Hydrogen Peroxide Stimulates Activity and Alters Behavior in *Drosophila melanogaster*. PLoS One *4*, e7580.

Guan, X., Middlebrooks, B.W., Alexander, S., and Wasserman, S.A. (2006). Mutation of TweedleD, a member of an unconventional cuticle protein family, alters body shape in *Drosophila*. Proc. Natl. Acad. Sci. *103*, 16794–16799.

Haeusler, R.A., McGraw, T.E., and Accili, D. (2018). Biochemical and cellular properties of insulin receptor signalling. Nat. Rev. Mol. Cell Biol. *19*, 31–44.

Hafner, M., Schmitz, A., Grüne, I., Srivatsan, S.G., Paul, B., Kolanus, W., Quast, T., Kremmer, E., Bauer, I., and Famulok, M. (2006). Inhibition of cytohesins by SecinH3 leads to hepatic insulin resistance. Nature *444*, 941–944.

Hamada, F.N., Rosenzweig, M., Kang, K., Pulver, S.R., Ghezzi, A., Jegla, T.J., and Garrity, P.A. (2008). An internal thermal sensor controlling temperature preference in *Drosophila*. Nature *454*, 217–220.

Hayyan, M., Hashim, M.A., and AlNashef, I.M. (2016). Superoxide Ion: Generation and Chemical Implications. Chem. Rev. *116*, 3029–3085.

Hedges, S.B., Dudley, J., and Kumar, S. (2006). TimeTree: a public knowledge-base of divergence times among organisms. Bioinformatics *22*, 2971–2972.

Heigwer, F., Port, F., and Boutros, M. (2018). RNA interference (RNAi) screening in *Drosophila*. Genetics *208*, 853–874.

Heron, S.E., Grinton, B.E., Kivity, S., Afawi, Z., Zuberi, S.M., Hughes, J.N., Pridmore, C., Hodgson, B.L., Iona, X., Sadleir, L.G., et al. (2012). *PRRT2* Mutations Cause Benign Familial Infantile Epilepsy and Infantile Convulsions with Choreoathetosis Syndrome. Am. J. Hum. Genet. *90,* 152–160.

Hewes, R.S., Park, D., Gauthier, S.A., Schaefer, A.M., and Taghert, P.H. (2003). The bHLH

protein Dimmed controls neuroendocrine cell differentiation in *Drosophila*. Development *130*, 1771–1781.

Hill, V.M., O'Connor, R.M., Sissoko, G.B., Irobunda, I.S., Leong, S., Canman, J.C., Stavropoulos, N., and Shirasu-Hiza, M. (2018). A bidirectional relationship between sleep and oxidative stress in *Drosophila*. PLoS Biol. *16*, e2005206.

Houamed, K.M., Sweet, I.R., and Satin, L.S. (2010). BK channels mediate a novel ionic mechanism that regulates glucose-dependent electrical activity and insulin secretion in mouse pancreatic β-cells. J. Physiol. *588*, 3511–3523.

Hrdlickova, R., Toloue, M., and Tian, B. (2017). RNA-Seq methods for transcriptome analysis. Wiley Interdiscip. Rev. RNA *8*, e1364.

Hu, H., Shao, L.R., Chavoshy, S., Gu, N., Trieb, M., Behrens, R., Laake, P., Pongs, O., Knaus, H.G., Ottersen, O.P., et al. (2001). Presynaptic Ca^{2+}-Activated K^+ Channels in Glutamatergic Hippocampal Terminals and Their Role in Spike Repolarization and Regulation of Transmitter Release. J. Neurosci. *21*, 9585–9597.

Huang, D.W., Sherman, B.T., and Lempicki, R.A. (2009). Systematic and integrative analysis of large gene lists using DAVID bioinformatics resources. Nat. Protoc. *4*, 44–57.

Huber, W., Carey, V.J., Gentleman, R., Anders, S., Carlson, M., Carvalho, B.S., Bravo, H.C., Davis, S., Gatto, L., Girke, T., et al. (2015). Orchestrating high-throughput genomic analysis with Bioconductor. Nat. Methods *12*, 115–121.

Imbeaud, S., Graudens, E., Boulanger, V., Barlet, X., Zaborski, P., Eveno, E., Mueller, O., Schroeder, A., and Auffray, C. (2005). Towards standardization of RNA quality assessment using user-independent classifiers of microcapillary electrophoresis traces. Nucleic Acids Res. *33*, e56.

Ishikawa, Y., Okamoto, N., Nakamura, M., Kim, H., and Kamikouchi, A. (2017). Anatomic and Physiologic Heterogeneity of Subgroup-A Auditory Sensory Neurons in Fruit Flies. Front. Neural Circuits *11*, 46.

Jankovic, J. (2006). Treatment of dystonia. Lancet Neurol. *5*, 864–872.

Janky, R., Verfaillie, A., Imrichová, H., van de Sande, B., Standaert, L., Christiaens, V., Hulselmans, G., Herten, K., Naval Sanchez, M., Potier, D., et al. (2014). iRegulon: From a Gene List to a Gene Regulatory Network Using Large Motif and Track Collections. PLoS Comput. Biol. *10*, e1003731.

Jepson, J.E.C., Shahidullah, M., Lamaze, A., Peterson, D., Pan, H., and Koh, K. (2012). *dyschronic*, a *Drosophila* Homolog of a Deaf-Blindness Gene, Regulates Circadian Output and Slowpoke Channels. PLoS Genet. *8*, e1002671.

Jepson, J.E.C., Shahidullah, M., Liu, D., le Marchand, S.J., Liu, S., Wu, M.N., Levitan, I.B., Dalva, M.B., and Koh, K. (2014). Regulation of synaptic development and function by the *Drosophila* PDZ protein Dyschronic. Development *141*, 4548–4557.

Jokhi, V., Ashley, J., Nunnari, J., Noma, A., Ito, N., Wakabayashi-Ito, N., Moore, M.J., and Budnik, V. (2013). Torsin Mediates Primary Envelopment of Large Ribonucleoprotein Granules at the Nuclear Envelope. Cell Rep. *3*, 988–995.

Kadas, D., Ryglewski, S., and Duch, C. (2015). Transient BK outward current enhances motoneurone firing rates during *Drosophila* larval locomotion. J. Physiol. *593*, 4871–4888.

Kaji, R., Bhatia, K., and Graybiel, A.M. (2018). Pathogenesis of dystonia: is it of cerebellar or basal ganglia origin? J. Neurol. Neurosurg. Psychiatry *89*, 488–492.

Kandel, E., Schwartz, J.H., Jessell, T.M., Siegelbaum, S.A., and Hudspeth, A.J. (2013). Principles of Neural Science, Fifth Edition (McGraw-Hill).

Kanehisa, M., Furumichi, M., Tanabe, M., Sato, Y., and Morishima, K. (2017). KEGG: new perspectives on genomes, pathways, diseases and drugs. Nucleic Acids Res. *45*, D353–D361.

Kent, W.J., Sugnet, C.W., Furey, T.S., Roskin, K.M., Pringle, T.H., Zahler, A.M., and Haussler, D. (2002). The Human Genome Browser at UCSC. Genome Res. *12*, 996–1006.

Kim, J.H., Kim, D.-W., Kim, J. Bin, Suh, S., and Koh, S.-B. (2015). Thalamic Involvement in Paroxysmal Kinesigenic Dyskinesia: A Combined Structural and Diffusion Tensor MRI Analysis. Hum. Brain Mapp. *36*, 1429–1441.

Kuebler, D., Zhang, H., Ren, X., and Tanouye, M.A. (2001). Genetic Suppression of Seizure Susceptibility in *Drosophila*. J. Neurophysiol. *86*, 1211–1225.

Kukurba, K.R., and Montgomery, S.B. (2015). RNA Sequencing and Analysis. Cold Spring Harb. Protoc. 951–969.

Kurt, S., Sausbier, M., Rüttiger, L., Brandt, N., Moeller, C.K., Kindler, J., Sausbier, U., Zimmermann, U., van Straaten, H., Neuhuber, W., et al. (2012). Critical role for cochlear hair cell BK channels for coding the temporal structure and dynamic range of auditory information for central auditory processing. FASEB J. *26*, 3834–3843.

Kwon, Y., Song, W., Droujinine, I.A., Hu, Y., Asara, J.M., and Perrimon, N. (2015). Systemic Organ Wasting Induced by Localized Expression of the Secreted Insulin/IGF Antagonist *ImpL2*. Dev. Cell *33*, 36–46.

De La Chapelle, A. (2009). Genetic predisposition to human disease: allele-specific expression and low-penetrance regulatory loci. Oncogene *28*, 3345–3348.

Lack, J.B., Lange, J.D., Tang, A.D., Corbett-Detig, R.B., and Pool, J.E. (2016). A Thousand Fly Genomes: An Expanded *Drosophila* Genome Nexus. Mol. Biol. Evol. *33*, 3308–3313.

Lagrutta, A., Shen, K.-Z., North, R.A., and Adelman, J.P. (1994). Functional Differences among Alternatively Spliced Variants of *Slowpoke*, a *Drosophila* Calcium-activated Potassium Channel. J. Biol. Chem. *269*, 20347–20351.

Langley, C.H., Stevens, K., Cardeno, C., Lee, Y.C.G., Schrider, D.R., Pool, J.E., Langley, S.A., Suarez, C., Corbett-Detig, R.B., Kolaczkowski, B., et al. (2012). Genomic Variation in Natural Populations of *Drosophila melanogaster*. Genetics *192*, 533–598.

Latorre, R., Castillo, K., Carrasquel-Ursulaez, W., Sepulveda, R. V., Gonzalez-Nilo, F., Gonzalez, C., and Alvarez, O. (2017). Molecular Determinants of BK Channel Functional Diversity and Functioning. Physiol. Rev. *97*, 39–87.

Lawrence, M., Huber, W., Pagès, H., Aboyoun, P., Carlson, M., Gentleman, R., Morgan, M.T., and Carey, V.J. (2013). Software for Computing and Annotating Genomic Ranges. PLoS Comput.

Biol. *9*, e1003118.

LeDoux, M.S., Lorden, J.F., and Ervin, J.M. (1993). Cerebellectomy Eliminates the Motor Syndrome of the Genetically Dystonic Rat. Exp. Neurol. *120*, 302–310.

Lee, J., and Wu, C.-F. (2010). Orchestration of Stepwise Synaptic Growth by K+ and Ca2+ Channels in *Drosophila*. J. Neurosci. *30*, 15821–15833.

Lee, T., and Luo, L. (1999). Mosaic Analysis with a Repressible Cell Marker for Studies of Gene Function in Neuronal Morphogenesis. Neuron *22*, 451–461.

Lee, U.S., and Cui, J. (2009). β subunit-specific modulations of BK channel function by a mutation associated with epilepsy and dyskinesia. J. Physiol. *587*, 1481–1498.

Lee, H.-Y., Huang, Y., Bruneau, N., Roll, P., Roberson, E.D.O., Hermann, M., Quinn, E., Maas, J., Edwards, R., Ashizawa, T., et al. (2012a). Mutations in the Gene *PRRT2* Cause Paroxysmal Kinesigenic Dyskinesia with Infantile Convulsions. Cell Rep. *1*, 2–12.

Lee, H.-Y., Nakayama, J., Xu, Y., Fan, X., Karouani, M., Shen, Y., Pothos, E.N., Hess, E.J., Fu, Y.-H., Edwards, R.H., et al. (2012b). Dopamine dysregulation in a mouse model of paroxysmal nonkinesigenic dyskinesia. J. Clin. Invest. *122*, 507–518.

Lee, J., Ueda, A., and Wu, C.F. (2008). Pre- and Post-Synaptic Mechanisms of Synaptic Strength Homeostasis Revealed by *slowpoke* and *Shaker* K+ Channel Mutations in *Drosophila*. Neuroscience *154*, 1283–1296.

Lee, J., Ueda, A., and Wu, C.-F. (2014). Distinct Roles of *Drosophila cacophony* and *Dmca1D* Ca2+ Channels in Synaptic Homeostasis: Genetic Interactions with *slowpoke* Ca2+-Activated BK Channels in Presynaptic Excitability and Postsynaptic Response. Dev. Neurobiol. *74*, 1–15.

Lehner, B. (2013). Genotype to phenotype: lessons from model organisms for human genetics. Nat. Rev. Genet. *14*, 168–178.

Li, B., and Gao, T.-M. (2016). Chapter Five - Functional Role of Mitochondrial and Nuclear BK Channels. In Big on Bk, (Academic Press), pp. 163–191.

Li, B., Jie, W., Huang, L., Wei, P., Li, S., Luo, Z., Friedman, A.K., Meredith, A.L., Han, M.-H., Zhu, X.-H., et al. (2014). Nuclear BK channels regulate gene expression via the control of nuclear calcium signaling. Nat. Neurosci. *17*, 1055–1063.

Li, H., Handsaker, B., Wysoker, A., Fennell, T., Ruan, J., Homer, N., Marth, G., Abecasis, G., Durbin, R., and 1000 Genome Project Data Processing Subgroup (2009). The Sequence Alignment/Map format and SAMtools. Bioinformatics *25*, 2078–2079.

Li, X., Poschmann, S., Chen, Q., Fazeli, W., Oundjian, N.J., Snoeijen-Schouwenaars, F.M., Fricke, O., Kamsteeg, E.-J., Willemsen, M., and Wang, Q.K. (2018). De novo BK channel variant causes epilepsy by affecting voltage gating but not Ca2+ sensitivity. Eur. J. Hum. Genet. *26*, 220–229.

Lin, W.-H., Wright, D.E., Muraro, N.I., and Baines, R.A. (2009). Alternative Splicing in the Voltage-Gated Sodium Channel DmNa$_v$ Regulates Activation, Inactivation, and Persistent Current. J. Neurophysiol. *102*, 1994–2006.

Lin, W.-H., Günay, C., Marley, R., Prinz, A.A., and Baines, R.A. (2012). Activity-Dependent

Alternative Splicing Increases Persistent Sodium Current and Promotes Seizure. J. Neurosci. *32*, 7267–7277.

Long, E.O., and Dawid, I.B. (1980). Alternative Pathways in the Processing of Ribosomal RNA Precursor in *Drosophila melanogaster*. J. Mol. Biol. *138*, 873–878.

Love, M.I., Huber, W., and Anders, S. (2014). Moderated estimation of fold change and dispersion for RNA-seq data with DESeq2. Genome Biol. *15*, 550.

Love, M.I., Anders, S., Kim, V., and Huber, W. (2016). RNA-Seq workflow: gene-level exploratory analysis and differential expression [version 2; peer review: 2 approved]. F1000Research *4*, 1070.

Luan, H., Lemon, W.C., Peabody, N.C., Pohl, J.B., Zelensky, P.K., Wang, D., Nitabach, M.N., Holmes, T.C., and White, B.H. (2006). Functional Dissection of a Neuronal Network Required for Cuticle Tanning and Wing Expansion in *Drosophila*. J. Neurosci. *26*, 573–584.

Mahr, A., and Aberle, H. (2006). The expression pattern of the *Drosophila* vesicular glutamate transporter: A marker protein for motoneurons and glutamatergic centers in the brain. Gene Expr. Patterns *6*, 299–309.

Maltese, M., Martella, G., Madeo, G., Fagiolo, I., Tassone, A., Ponterio, G., Sciamanna, G., Burbaud, P., Conn, P.J., Bonsi, P., et al. (2014). Anticholinergic Drugs Rescue Synaptic Plasticity in DYT1 Dystonia: Role of M_1 Muscarinic Receptors. Mov. Disord. *29*, 1655–1665.

Manière, G., Ziegler, A.B., Geillon, F., Featherstone, D.E., and Grosjean, Y. (2016). Direct Sensing of Nutrients via a LAT1-like Transporter in *Drosophila* Insulin-Producing Cells. Cell Rep. *17*, 137–148.

Marder, E., and Bucher, D. (2001). Central pattern generators and the control of rhythmic movements. Curr. Biol. *11*, R986–R996.

Marley, R., and Baines, R.A. (2011). Increased persistent Na^+ current contributes to seizure in the slamdance bang-sensitive *Drosophila* mutant. J. Neurophysiol. *106*, 18–29.

Martella, G., Maltese, M., Nisticò, R., Schirinzi, T., Madeo, G., Sciamanna, G., Ponterio, G., Tassone, A., Mandolesi, G., Vanni, V., et al. (2014). Regional specificity of synaptic plasticity deficits in a knock-in mouse model of DYT1 dystonia. Neurobiol. Dis. *65*, 124–132.

Mencacci, N.E., Rubio-Agusti, I., Zdebik, A., Asmus, F., Ludtmann, M.H.R., Ryten, M., Plagnol, V., Hauser, A.K., Bandres-Ciga, S., Bettencourt, C., et al. (2015). A Missense Mutation in *KCTD17* Causes Autosomal Dominant Myoclonus-Dystonia. Am. J. Hum. Genet. *96*, 938–947.

Metzker, M.L. (2010). Sequencing technologies - the next generation. Nat. Rev. Genet. *11*, 31–46.

Miller, C. (2000). An overview of the potassium channel family. Genome Biol. *1*, reviews0004.1.

Mueckler, M., Caruso, C., Baldwin, S.A., Panico, M., Blench, I., Morris, H.R., Allard, W.J., Lienhard, G.E., and Lodish, H.F. (1985). Sequence and structure of a human glucose transporter. Science (80-.). *229*, 941–945.

Muraro, N.I., and Moffat, K.G. (2006). Down-regulation of *torp4a*, Encoding the *Drosophila* Homologue of TorsinA, Results in Increased Neuronal Degeneration. J. Neurobiol. *66*, 1338–1353.

Naganos, S., Horiuchi, J., and Saitoe, M. (2012). Mutations in the *Drosophila* insulin receptor substrate, CHICO, impair olfactory associative learning. Neurosci. Res. *73*, 49–55.

Nässel, D.R., Liu, Y., and Luo, J. (2015). Insulin/IGF signaling and its regulation in *Drosophila*. Gen. Comp. Endocrinol. *221*, 255–266.

Needleman, S.B., and Wunsch, C.D. (1970). A General Method Applicable to the Search for Similarities in the Amino Acid Sequence of Two Proteins. J. Mol. Biol. *48*, 443–453.

Ng, M., Roorda, R.D., Lima, S.Q., Zemelman, B. V, Morcillo, P., and Miesenböck, G. (2002). Transmission of Olfactory Information between Three Populations of Neurons in the Antennal Lobe of the Fly. Neuron *36*, 463–474.

Nobile, C., and Striano, P. (2014). Chapter 8 - PRRT2: A major cause of infantile epilepsy and other paroxysmal disorders of childhood. In Genetics of Epilepsy, (Elsevier), pp. 141–158.

Nunnari, J., and Suomalainen, A. (2012). Mitochondria: In Sickness and in Health. Cell *148*, 1145–1159.

Obenchain, V. (2016). Counting reads with summarizeOverlaps. Bioconductor Vignette.

Otto, N., Marelja, Z., Schoofs, A., Kranenburg, H., Bittern, J., Yildirim, K., Berh, D., Bethke, M., Thomas, S., Rode, S., et al. (2018). The sulfite oxidase Shopper controls neuronal activity by regulating glutamate homeostasis in *Drosophila* ensheathing glia. Nat. Commun. *9*, 3514.

Ozelius, L.J., Hewett, J.W., Page, C.E., Bressman, S.B., Kramer, P.L., Shalish, C., de Leon, D., Brin, M.F., Raymond, D., Corey, D.P., et al. (1997). The early-onset torsion dystonia gene (*DYT1*) encodes an ATP-binding protein. Nat. Genet. *17*, 40–48.

Park, J.H., Schroeder, A.J., Helfrich-Förster, C., Jackson, F.R., and Ewer, J. (2003). Targeted ablation of CCAP neuropeptide-containing neurons of *Drosophila* causes specific defects in execution and circadian timing of ecdysis behavior. Development *130*, 2645–2656.

Park, S., Alfa, R.W., Topper, S.M., Kim, G.E.S., Kockel, L., and Kim, S.K. (2014). A Genetic Strategy to Measure Circulating *Drosophila* Insulin Reveals Genes Regulating Insulin Production and Secretion. PLoS Genet. *10*, e1004555.

Parker, L., Howlett, I.C., Rusan, Z.M., and Tanouye, M.A. (2011). Seizure and Epilepsy: Studies of Seizure Disorders in *Drosophila*. In Recent Advances in the Use of Drosophila in Neurobiology and Neurodegeneration, (Academic Press), pp. 1–21.

Pavlakis, G.N., Jordan, B.R., Wurst, R.M., and Vournakis, J.N. (1979). Sequence and secondary structure of *Drosophila melanogaster* 5.8S and 2S rRNAs and of the processing site between them. Nucleic Acids Res. *7*, 2213–2238.

Peixoto, A.A., and Hall, J.C. (1998). Analysis of Temperature-Sensitive Mutants Reveals New Genes Involved in the Courtship Song of *Drosophila*. Genetics *148*, 827–838.

Perrimon, N., Ni, J., and Perkins, L. (2010). In vivo RNAi: Today and Tomorrow. Cold Spring Harb. Perspect. Biol. *2,* a003640.

Peschel, N., and Helfrich-Förster, C. (2011). Setting the clock - by nature: Circadian rhythm in the fruitfly *Drosophila melanogaster*. FEBS Lett. *585*, 1435–1442.

Pfeiffenberger, C., and Allada, R. (2012). *Cul3* and the BTB Adaptor *Insomniac* Are Key

Regulators of Sleep Homeostasis and a Dopamine Arousal Pathway in *Drosophila*. PLoS Genet. *8*, e1003003.

Pfeiffenberger, C., Lear, B.C., Keegan, K.P., and Allada, R. (2010). Locomotor Activity Level Monitoring Using the *Drosophila* Activity Monitoring (DAM) System. Cold Spring Harb. Protoc. *5*, 1238–1242.

Piwonska, M., Wilczek, E., Szewczyk, A., and Wilczynski, G.M. (2008). Differential Distribution of Ca^{2+}-Activated Potassium Channel β4 Subunit in Rat Brain: Immunolocalization in Neuronal Mitochondria. Neuroscience *153*, 446–460.

Platt, F.M., D'Azzo, A., Davidson, B.L., Neufeld, E.F., and Tifft, C.J. (2018). Lysosomal storage diseases. Nat. Rev. Dis. Prim. *4*, 27.

Poewe, W., Seppi, K., Tanner, C.M., Halliday, G.M., Brundin, P., Volkmann, J., Schrag, A.-E., and Lang, A.E. (2017). Parkinson Disease. Nat. Rev. Dis. Prim. *3*, 17013.

Pool, J.E., Corbett-Detig, R.B., Sugino, R.P., Stevens, K.A., Cardeno, C.M., Crepeau, M.W., Duchen, P., Emerson, J.J., Saelao, P., Begun, D.J., et al. (2012). Population Genomics of Sub-Saharan *Drosophila melanogaster*: African Diversity and Non-African Admixture. PLoS Genet. *8*, e1003080.

Pulver, S.R., Pashkovski, S.L., Hornstein, N.J., Garrity, P.A., and Griffith, L.C. (2009). Temporal Dynamics of Neuronal Activation by Channelrhodopsin-2 and TRPA1 Determine Behavioral Output in *Drosophila* Larvae. J. Neurophysiol. *101*, 3075–3088.

Pulver, S.R., Bayley, T.G., Taylor, A.L., Berni, J., Bate, M., and Hedwig, B. (2015). Imaging fictive locomotor patterns in larval *Drosophila*. J. Neurophysiol. *114*, 2564–2577.

Ranganayakulu, G., Elliott, D.A., Harvey, R.P., and Olson, E.N. (1998). Divergent roles for *NK-2* class homeobox genes in cardiogenesis in flies and mice. Development *125*, 3037–3048.

Rao, S.R., Olechnowicz, S.W.Z., Krätschmer, P., James, E.C.J., Edwards, C.M., and Edwards, J.R. (2019). Small Animal Video Tracking for Activity and Path Analysis Using a Novel Open-Source Multi-Platform Application (AnimApp). Sci. Rep. *9*, 12343.

Raz, A., Feingold, A., Zelanskaya, V., Vaadia, E., and Bergman, H. (1996). Neuronal Synchronization of Tonically Active Neurons in the Striatum of Normal and Parkinsonian Primates. J. Neurophysiol. *76*, 2083–2088.

Reese, M.G., Moore, B., Batchelor, C., Salas, F., Cunningham, F., Marth, G., Stein, L., Flicek, P., Yandell, M., and Eilbeck, K. (2010). A standard variation file format for human genome sequences. Genome Biol. *11*, R88.

Rein, K., Zöckler, M., Mader, M.T., Grübel, C., and Heisenberg, M. (2002). The *Drosophila* Standard Brain. Curr. Biol. *12*, 227–231.

Robinson, J.T., Thorvaldsdóttir, H., Winckler, W., Guttman, M., Lander, E.S., Getz, G., and Mesirov, J.P. (2011). Integrative genomics viewer. Nat. Biotechnol. *29*, 24–26.

Rubin, G.M., and Lewis, E.B. (2000). A Brief History of *Drosophila*'s Contributions to Genome Research. Science (80-.). *287*, 2216–2218.

Ryan, M.B., Bair-Marshall, C., and Nelson, A.B. (2018). Aberrant Striatal Activity in Parkinsonism

and Levodopa-Induced Dyskinesia. Cell Rep. *23*, 3438–3446.

Saito, M., and Wu, C.-F. (1991). Expression of Ion Channels and Mutational Effects in Giant *Drosophila* Neurons Differentiated from Cell Division-arrested Embryonic Neuroblasts. J. Neurosci. *11*, 2135–2150.

Salih, D.A.M., and Brunet, A. (2008). FoxO transcription factors in the maintenance of cellular homeostasis during aging. Curr. Opin. Cell Biol. *20*, 126–136.

Salvaterra, P.M., and Kitamoto, T. (2001). *Drosophila* cholinergic neurons and processes visualized with Gal4/UAS-GFP. Gene Expr. Patterns *1*, 73–82.

Sanes, J.R., and Hildebrand, J.G. (1976). Acetylcholine and Its Metabolic Enzymes in Developing Antennae of the Moth, *Manduca Sexta*. Dev. Biol. *52*, 105–120.

dos Santos, G., Schroeder, A.J., Goodman, J.L., Strelets, V.B., Crosby, M.A., Thurmond, J., Emmert, D.B., Gelbart, W.M., and the FlyBase Consortium (2014). FlyBase: introduction of the *Drosophila* melanogaster Release 6 reference genome assembly and large-scale migration of genome annotations. Nucleic Acids Res. *43*, D690–D697.

Sausbier, M., Hu, H., Arntz, C., Feil, S., Kamm, S., Adelsberger, H., Sausbier, U., Sailer, C.A., Feil, R., Hofmann, F., et al. (2004). Cerebellar ataxia and Purkinje cell dysfunction caused by Ca^{2+}-activated K^+ channel deficiency. Proc. Natl. Acad. Sci. *101*, 9474–9478.

Scheffer, I.E., Berkovic, S., Capovilla, G., Connolly, M.B., French, J., Guilhoto, L., Hirsch, E., Jain, S., Mathern, G.W., Moshé, S.L., et al. (2017). ILAE classification of the epilepsies: Position paper of the ILAE Commission for Classification and Terminology. Epilepsia *58*, 512–521.

Schindelin, J., Arganda-Carreras, I., Frise, E., Kaynig, V., Longair, M., Pietzsch, T., Preibisch, S., Rueden, C., Saalfeld, S., Schmid, B., et al. (2012). Fiji: an open-source platform for biological-image analysis. Nat. Methods *9*, 676–682.

Schopperle, W.M., Holmqvist, M.H., Zhou, Y., Wang, J., Wang, Z., Griffith, L.C., Keselman, I., Kusinitz, F., Dagan, D., and Levitan, I.B. (1998). Slob, a Novel Protein that Interacts with the Slowpoke Calcium-Dependent Potassium Channel. Neuron *20*, 565–573.

Schutte, R.J., Schutte, S.S., Algara, J., Barragan, E. V, Gilligan, J., Staber, C., Savva, Y. a, Smith, M. a, Reenan, R., and O'Dowd, D.K. (2014). Knock-in model of Dravet syndrome reveals a constitutive and conditional reduction in sodium current. J. Neurophysiol. *112*, 903–912.

Sheldon, A.L., Zhang, J., Fei, H., and Levitan, I.B. (2011). SLOB, a SLOWPOKE Channel Binding Protein, Regulates Insulin Pathway Signaling and Metabolism in *Drosophila*. PLoS One *6*, e23343.

Shen, Y., Lee, H.-Y., Rawson, J., Ojha, S., Babbitt, P., Fu, Y.-H., and Ptácek, L.J. (2011). Mutations in PNKD causing paroxysmal dyskinesia alters protein cleavage and stability. Hum. Mol. Genet. *20*, 2322–2332.

Shen, Y., Ge, W.-P., Li, Y., Hirano, A., Lee, H.-Y., Rohlmann, A., Missler, M., Tsien, R.W., Jan, L.Y., Fu, Y.-H., et al. (2015). Protein mutated in paroxysmal dyskinesia interacts with the active zone protein RIM and suppresses synaptic vesicle exocytosis. Proc. Natl. Acad. Sci. *112*, 2935–2941.

Sievers, F., Wilm, A., Dineen, D., Gibson, T.J., Karplus, K., Li, W., Lopez, R., McWilliam, H., Remmert, M., Söding, J., et al. (2011). Fast, scalable generation of high-quality protein multiple sequence alignments using Clustal Omega. Mol. Syst. Biol. *7*, 539.

Singh, S., and Wu, C.-F. (1990). Properties of Potassium Currents and their Role in Membrane Excitability in *Drosophila* Larval Muscle Fibers. J. Exp. Biol. *152*, 59–76.

Singh, H., Lu, R., Bopassa, J.C., Meredith, A.L., Stefani, E., and Toro, L. (2013). mitoBK$_{Ca}$ is encoded by the *Kcnma1* gene, and a splicing sequence defines its mitochondrial location. Proc. Natl. Acad. Sci. *110*, 10836–10841.

Slack, C., Giannakou, M.E., Foley, A., Goss, M., and Partridge, L. (2011). dFOXO-independent effects of reduced insulin-like signaling in *Drosophila*. Aging Cell *10*, 735–748.

Snead III, O.C. (1995). Basic Mechanisms of Generalized Absence Seizures. Ann. Neurol. *37*, 146–157.

Soltysinska, E., Bentzen, B.H., Barthmes, M., Hattel, H., Thrush, A.B., Harper, M.E., Qvortrup, K., Larsen, F.J., Schiffer, T.A., Losa-Reyna, J., et al. (2014). KCNMA1 Encoded Cardiac BK Channels Afford Protection against Ischemia-Reperfusion Injury. PLoS One *9*, e103402.

Speese, S.D., Ashley, J., Jokhi, V., Nunnari, J., Barria, R., Li, Y., Ataman, B., Koon, A., Chang, Y.-T., Li, Q., et al. (2012). Nuclear Envelope Budding Enables Large Ribonucleoprotein Particle Export during Synaptic Wnt Signaling. Cell *149*, 832–846.

St Johnston, D. (2002). The Art and Design of Genetic Screens: *Drosophila melanogaster*. Nat. Rev. Genet. *3*, 176–188.

Staber, C., Gell, S., Jepson, J.E.C., and Reenan, R.A. (2011). Perturbing A-to-I RNA Editing Using Genetics and Homologous Recombination. In Ruslan Aphasizhev (Ed.), RNA and DNA Editing: Methods and Protocols, Methods in Molecular Biology, (Humana Press), pp. 41–73.

Staley, K.J., White, A., and Dudek, F.E. (2011). Interictal spikes: harbingers or causes of epilepsy? Neurosci. Lett. *497*, 247–250.

Stavropoulos, N., and Young, M.W. (2011). *insomniac* and *Cullin-3* Regulate Sleep and Wakefulness in *Drosophila*. Neuron *72*, 964–976.

Strausfeld, N.J., and Hirth, F. (2013). Deep Homology of Arthropod Central Complex and Vertebrate Basal Ganglia. Science (80-.). *340*, 157–161.

Strauss, R. (2002). The central complex and the genetic dissection of locomotor behaviour. Curr. Opin. Neurobiol. *12*, 633–638.

Streit, A.K., Fan, Y.N., Masullo, L., and Baines, R.A. (2016). Calcium Imaging of Neuronal Activity in *Drosophila* Can Identify Anticonvulsive Compounds. PLoS One *11*, e0148461.

Südhof, T.C. (2012). Calcium Control of Neurotransmitter Release. Cold Spring Harb. Perspect. Biol. *4*, a011353.

Suls, A., Dedeken, P., Goffin, K., Van Esch, H., Dupont, P., Cassiman, D., Kempfle, J., Wuttke, T. V., Weber, Y., Lerche, H., et al. (2008). Paroxysmal exercise-induced dyskinesia and epilepsy is due to mutations in *SLC2A1*, encoding the glucose transporter GLUT1. Brain *131*, 1831–1844.

Sun, L., Gilligan, J., Staber, C., Schutte, R.J., Nguyen, V., O'Dowd, D.K., and Reenan, R. (2012).

A Knock-In Model of Human Epilepsy in *Drosophila* Reveals a Novel Cellular Mechanism Associated with Heat-Induced Seizure. J. Neurosci. *32*, 14145–14155.

Szepetowski, P., Rochette, J., Berquin, P., Piussan, C., Lathrop, G.M., and Monaco, A.P. (1997). Familial Infantile Convulsions and Paroxysmal Choreoathetosis: A New Neurological Syndrome Linked to the Pericentromeric Region of Human Chromosome 16. Am. J. Hum. Genet. *61*, 889–898.

Tabarki, B., AlMajhad, N., AlHashem, A., Shaheen, R., and Alkuraya, F.S. (2016). Homozygous *KCNMA1* mutation as a cause of cerebellar atrophy, developmental delay and seizures. Hum. Genet. *135*, 1295–1298.

Tabuchi, M., Monaco, J.D., Duan, G., Bell, B., Liu, S., Liu, Q., Zhang, K., and Wu, M.N. (2018). Clock-Generated Temporal Codes Determine Synaptic Plasticity to Control Sleep. Cell *175*, 1213–1227.

Tan, G.-H., Liu, Y.-Y., Wang, L., Li, K., Zhang, Z.-Q., Li, H.-F., Yang, Z.-F., Li, Y., Li, D., Wu, M.-Y., et al. (2018). PRRT2 deficiency induces paroxysmal kinesigenic dyskinesia by regulating synaptic transmission in cerebellum. Cell Res. *28*, 90–110.

Tan, G., Opitz, L., Schlapbach, R., and Rehrauer, H. (2019). Long fragments achieve lower base quality in Illumina paired-end sequencing. Sci. Rep. *9*, 2856.

Tennessen, J.M., Barry, W.E., Cox, J., and Thummel, C.S. (2014). Methods for studying metabolism in *Drosophila*. Methods *68*, 105–115.

The Gene Ontology Consortium (2007). The Gene Ontology project in 2008. Nucleic Acids Res. *36*, D440–D444.

Turrens, J.F. (2003). Mitochondrial formation of reactive oxygen species. J. Physiol. *552*, 335–344.

Ugrankar, R., Theodoropoulos, P., Akdemir, F., Henne, W.M., and Graff, J.M. (2018). Circulating glucose levels inversely correlate with *Drosophila* larval feeding through insulin signaling and SLC5A11. Commun. Biol. *1*, 110.

Ungar, D., and Hughson, F.M. (2003). SNARE Protein Structure and Function. Annu. Rev. Cell Dev. Biol. *19*, 493–517.

Untergasser, A., Cutcutache, I., Koressaar, T., Ye, J., Faircloth, B.C., Remm, M., and Rozen, S.G. (2012). Primer3—new capabilities and interfaces. Nucleic Acids Res. *40*, e115.

Valente, P., Castroflorio, E., Rossi, P., Fadda, M., Sterlini, B., Cervigni, R.I., Prestigio, C., Giovedì, S., Onofri, F., Mura, E., et al. (2016). PRRT2 Is a Key Component of the Ca^{2+}-Dependent Neurotransmitter Release Machinery. Cell Rep. *15*, 117–131.

Venken, K.J.T., Simpson, J.H., and Bellen, H.J. (2011). Genetic Manipulation of Genes and Cells in the Nervous System of the Fruit Fly. Neuron *72*, 202–230.

Vincze, T., Posfai, J., and Roberts, R.J. (2003). NEBcutter: a program to cleave DNA with restriction enzymes. Nucleic Acids Res. *31*, 3688–3691.

Wakabayashi-Ito, N., Doherty, O.M., Moriyama, H., Breakefield, X.O., Gusella, J.F., O'Donnell, J.M., and Ito, N. (2011). *dtorsin*, the *Drosophila* Ortholog of the Early-Onset Dystonia *TOR1A*

(*DYT1*), Plays a Novel Role in Dopamine Metabolism. PLoS One *6*, e26183.

Wakabayashi-Ito, N., Ajjuri, R.R., Henderson, B.W., Doherty, O.M., Breakefield, X.O., O'Donnell, J.M., and Ito, N. (2015). Mutant human torsinA, responsible for early-onset dystonia, dominantly suppresses GTPCH expression, dopamine levels and locomotion in *Drosophila melanogaster*. Biol. Open *4*, 585–595.

Wang, Y., and Südhof, T.C. (2003). Genomic definition of RIM proteins: evolutionary amplification of a family of synaptic regulatory proteins. Genomics *81*, 126–137.

Wang, D., Kranz-Eble, P., and De Vivo, D.C. (2000). Mutational Analysis of GLUT1 (SLC2A1) in Glut-1 Deficiency Syndrome. Hum. Mutat. *16*, 224–231.

Wang, J., Yu, S., Zhang, Q., Chen, Y., Bao, X., and Wu, X. (2017a). *KCNMA1* mutation in children with paroxysmal dyskinesia and epilepsy: Case report and literature review. Transl. Sci. Rare Dis. *2*, 165–173.

Wang, W., Zhang, X., Gao, Q., Lawas, M., Yu, L., Cheng, X., Gu, M., Sahoo, N., Li, X., Li, P., et al. (2017b). A voltage-dependent K$^+$ channel in the lysosome is required for refilling lysosomal Ca^{2+} stores. J. Cell Biol. *216*, 1715–1730.

Wang, Z., Gerstein, M., and Snyder, M. (2009). RNA-Seq: a revolutionary tool for transcriptomics. Nat. Rev. Genet. *10*, 57–63.

Wangler, M.F., Yamamoto, S., and Bellen, H.J. (2015). Fruit Flies in Biomedical Research. Genetics *199*, 639–653.

Wangler, M.F., Yamamoto, S., Chao, H.-T., Posey, J.E., Westerfield, M., Postlethwait, J., Members of the Undiagnosed Disease Network (UDN), Hieter, P., Boycott, K.M., Campeau, P.M., et al. (2017). Model Organisms Facilitate Rare Disease Diagnosis and Therapeutic Research. Genetics *207*, 9–27.

Warbington, L.C., Hillman, T., Adams, C., and Stern, M. (1996). Reduced transmitter release conferred by mutations in the *slowpoke*-encoded Ca^{2+}-activated K$^+$ channel gene of *Drosophila*. Invertebr. Neurosci. *2*, 51–60.

Wei, A., Solaro, C., Lingle, C., and Salkoff, L. (1994). Calcium Sensitivity of BK-type K$_{Ca}$ Channels Determined by a Separable Domain. Neuron *13*, 671–681.

Wesolowska, N., and Rong, Y.S. (2010). The past, present and future of gene targeting in *Drosophila*. Fly (Austin). *4*, 53–59.

Wichmann, T., and Dostrovsky, J.O. (2011). Pathological Basal Ganglia Activity in Movement Disorders. Neuroscience *198*, 232–244.

Winnebeck, E.C., Millar, C.D., and Warman, G.R. (2010). Why does insect RNA look degraded? J. Insect Sci. *10*, 159.

Wodarz, A., Hinz, U., Engelbert, M., and Knust, E. (1995). Expression of Crumbs Confers Apical Character on Plasma Membrane Domains of Ectodermal Epithelia of *Drosophila*. Cell *82*, 67–76.

Wu, M.N., and Lloyd, T.E. (2015). *Drosophila* models of neurologic disease. Exp. Neurol. *274*, 1–3.

Wu, Y., Yang, Y., Ye, S., and Jiang, Y. (2010). Structure of the gating ring from the human large-

conductance Ca^{2+}-gated K$^+$ channel. Nature *466*, 393–397.

Xu, W., Liu, Y., Wang, S., McDonald, T., Van Eyk, J.E., Sidor, A., and O'Rourke, B. (2002). Cytoprotective Role of Ca^{2+}-Activated K$^+$ Channels in the Cardiac Inner Mitochondrial Membrane. Science (80-.). *298*, 1029–1033.

Yang, H., Zhang, G., and Cui, J. (2015). BK channels: multiple sensors, one activation gate. Front. Physiol. *6*, 29.

Yang, J., Krishnamoorthy, G., Saxena, A., Zhang, G., Shi, J., Yang, H., Delaloye, K., Sept, D., and Cui, J. (2010). An Epilepsy/Dyskinesia-Associated Mutation Enhances BK Channel Activation by Potentiating Ca^{2+} Sensing. Neuron *66*, 871–883.

Yasuyama, K., and Salvaterra, P.M. (1999). Localization of Choline Acetyltransferase-Expressing Neurons in *Drosophila* Nervous System. Microsc. Res. Tech. *45*, 65–79.

Yuan, P., Leonetti, M.D., Pico, A.R., Hsiung, Y., and MacKinnon, R. (2010). Structure of the Human BK Channel Ca^{2+}-Activation Apparatus at 3.0 Å Resolution. Science (80-.). *329*, 182–186.

Yuan, P., Leonetti, M.D., Hsiung, Y., and MacKinnon, R. (2012). Open structure of the Ca^{2+} gating ring in the high-conductance Ca^{2+}-activated K$^+$ channel. Nature *481*, 94–98.

Zarin, A.A., Mark, B., Cardona, A., Litwin-Kumar, A., and Doe, C.Q. (2019). A *Drosophila* larval premotor/motor neuron connectome generating two behaviors via distinct spatio-temporal muscle activity. BioRxiv 617977.

Zeng, H., Weiger, T.M., Fei, H., Jaramillo, A.M., and Levitan, I.B. (2005). The Amino Terminus of Slob, Slowpoke Channel Binding Protein, Critically Influences Its Modulation of the Channel. J. Gen. Physiol. *125*, 631–640.

Zerbino, D.R., Achuthan, P., Akanni, W., Amode, M.R., Barrell, D., Bhai, J., Billis, K., Cummins, C., Gall, A., Girón, C.G., et al. (2018). Ensembl 2018. Nucleic Acids Res. *46*, D754–D761.

Zhang, B., and Stewart, B. (2010). Electrophysiological Recording from *Drosophila* Larval Body-Wall Muscles. Cold Spring Harb. Protoc. 1–10.

Zhang, Z.-B., Tian, M.-Q., Gao, K., Jiang, Y.-W., and Wu, Y. (2015). De Novo *KCNMA1* Mutations in Children With Early-Onset Paroxysmal Dyskinesia and Developmental Delay. Mov. Disord. *30*, 1290–1292.

Zhou, Y., Schopperle, W.M., Murrey, H., Jaramillo, A., Dagan, D., Griffith, L.C., and Levitan, I.B. (1999). A Dynamically Regulated 14–3–3, Slob, and Slowpoke Potassium Channel Complex in *Drosophila* Presynaptic Nerve Terminals. Neuron *22*, 809–818.

Zhu, M.X. (2017). A well-known potassium channel plays a critical role in lysosomes. J. Cell Biol. *216*, 1513–1515.

Zijlmans, M., Jiruska, P., Zelmann, R., Leijten, F.S.S., Jefferys, J.G.R., and Gotman, J. (2012). High-Frequency Oscillations as a New Biomarker in Epilepsy. Ann. Neurol. *71*, 169–178.

9 Appendix
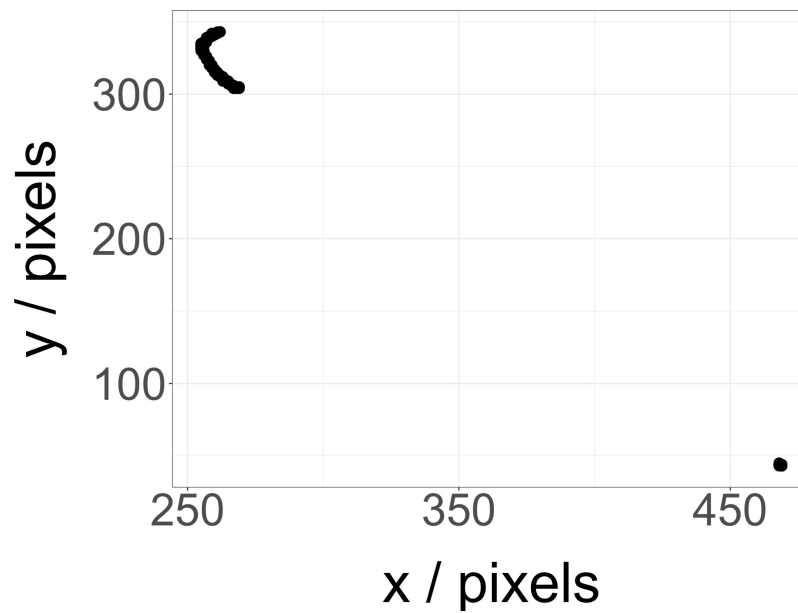
Figure 9.1 Example of Aberrant Larval Tracking

This larva, of genotype *72.1.1/+*, is the only larva, out of a total of 164, AnimApp failed to track properly. Improper tracking is identified visually by acknowledging that it would be impossible for a larva to jump ~200 pixels, which converts to ~5.5 cm. All other larval paths were possible. This larva was excluded from further analysis.

A

[Header]										
IEMFileVersion	4									
Investigator Name	Debbie Hughes									
Experiment Name	Agilent Exomes									
Date	23/09/2016									
Workflow	GenerateFASTQ									
Application	HiSeq FASTQ Only									
Assay	Agilent Enrichment									
Description	Agilent exomes run 1									
Chemistry	Amplicon									
[Reads]										
76										
76										
[Settings]										
Adapter	CTGTCTCTTATACACATCT									
ReverseComplement	0									
[Data]										
Lane	Sample_ID	Sample_Name	Sample_Plate	Sample_Well	I7_Index_ID	index	I5_Index_ID	index2	Sample_Project	Description
5	17_GEPD1		KAPA	A01		ATCACG				
5	17_GEPD2		KAPA	A02		TTAGGC				
5	17_GEPD5		KAPA	A03		TAGCTT				
5	18_GEPD1		KAPA	A04		CGATGT				
5	18_GEPD2		KAPA	A05		TGACCA				
5	18_GEPD3		KAPA	A06		ACAGTG				
5	18_GEPD4		KAPA	A07		GCCAAT				
5	18_GEPD5		KAPA	A08		CAGATC				
5	18_GEPD6		KAPA	A09		CTTGTA				

B

[Header]										
IEMFileVersion	4									
Investigator Name	Debbie Hughes									
Experiment Name	Agilent Exomes									
Date	23/09/2016									
Workflow	GenerateFASTQ									
Application	HiSeq FASTQ Only									
Assay	Agilent Enrichment									
Description	Agilent exomes run 1									
Chemistry	Amplicon									
[Reads]										
76										
76										
[Settings]										
Adapter	CTGTCTCTTATACACATCT									
ReverseComplement	0									
[Data]										
Lane	Sample_ID	Sample_Name	Sample_Plate	Sample_Well	I7_Index_ID	index	I5_Index_ID	index2	Sample_Project	Description
5	17_loxp1		KAPA	A01		GTGGCCTT				
5	17_loxp3		KAPA	A02		CGTACGTA				
5	17_loxp6		KAPA	A03		ATTCCTTT				
5	18_loxp1		KAPA	A04		AGTCAACA				
5	18_loxp2		KAPA	A05		AGTTCCGT				
5	18_loxp3		KAPA	A06		ATGTCAGA				
5	18_loxp4		KAPA	A07		CCGTCCCG				
5	18_loxp5		KAPA	A08		GTCCGCAC				
5	18_loxp6		KAPA	A09		GTGAAACG				

Figure 9.2 Sample Sheets Used for De-multiplexing of RNA-seq Data

During the conversion from BCL- to FASTQ file format, RNA-seq data were de-multiplexed based on index sequences (column 7 at the bottom of **A** and **B**). De-multiplexing runs were performed separately for 6-bp indices (**A**) and 8-bp indices (**B**). These sample sheets are based on templates provided by Deborah Hughes. Dr. Alan Pittman performed de-multiplexing.

Table 69 lists the 1036 significantly DEGs (FDR < 0.05), as identified by the DGE analysis described in Paragraph 5.4.6. (FB-ID = FlyBase-identifier; Mean = mean gene expression in normalised counts; log2FC = log$_2$(fold-change); FDR = false discovery rate; Gene = gene name). Fold-changes are presented relative to *slo^{loxP}/+*, with positive values indicating genes up-regulated in *slo^{E366G}/+*, and negative values indicating genes down-regulated in *slo^{E366G}/+*. This table is sorted by significance, with smaller FDRs at the top.

Table 69 Differentially Expressed Gene List

FB-ID	Mean	log2FC	FDR	Gene
FBgn0030773	3549.73262	-1.7098074	6.52E-59	CG9676
FBgn0039703	834.790327	-1.5213454	1.63E-50	CG7829
FBgn0052523	265.798827	-3.0244496	1.89E-41	CG32523
FBgn0033067	1016.04847	-1.4611967	1.71E-32	CG11211
FBgn0031306	6579.55166	-0.3923524	1.27E-29	CG4577
FBgn0039298	284.402164	-1.2342204	2.39E-27	to
FBgn0039430	3367.24617	-0.3440621	1.58E-26	CG5455
FBgn0028374	674.008251	-0.5250827	1.58E-26	Hug
FBgn0259226	583.377642	-0.5195097	5.45E-26	CG42326
FBgn0014019	6884.15053	-0.4345284	3.35E-22	Rh5
FBgn0243514	761.943326	0.81082722	5.29E-21	eater
FBgn0040502	8326.21149	-1.1155059	1.55E-20	CG8343
FBgn0036022	8350.66925	-0.9420731	1.60E-20	CG8329
FBgn0035207	5490.7641	0.25043493	3.37E-20	Herc4
FBgn0035766	1883.40999	0.57480876	4.63E-20	eco
FBgn0036015	7152.30965	-0.7160127	1.89E-19	CG3088
FBgn0035550	20.4356082	-5.1152893	1.89E-19	CG11349
FBgn0035189	716.522065	-0.8640943	1.71E-18	CG9119
FBgn0039543	568.250595	-0.6206445	6.66E-18	CROT
FBgn0001234	2357.95846	-0.328993	1.75E-17	lncRNA:Hsromega
FBgn0040601	18.1465684	-2.9615533	2.33E-17	CG13643
FBgn0023178	878.06907	-0.2951113	4.87E-17	Pdf
FBgn0036620	1561.48682	-0.3683267	2.09E-16	CG4842
FBgn0013813	463.851835	0.73758584	2.48E-16	Dhc98D
FBgn0010041	55.0248686	1.92997995	4.56E-16	GstD5
FBgn0039537	1404.9545	-0.3345209	6.33E-16	CG5590
FBgn0003250	12542.8011	-0.2802346	1.44E-15	Rh4
FBgn0039474	16.2178153	-4.4358386	1.44E-15	CG6283
FBgn0035160	81.8891073	-1.0373095	1.53E-15	hng3
FBgn0035382	235.372915	0.61271849	5.17E-15	Or63a
FBgn0043783	763.621593	-0.8296132	1.94E-14	CG32444
FBgn0003249	16964.971	-0.2431108	6.60E-14	Rh3
FBgn0262728	5006.91458	-0.1959504	1.42E-13	Pal2

FBgn0035438	1985.27679	-0.2448651	1.48E-13	PHGPx
FBgn0029093	10779.1054	-0.1728207	1.74E-13	cathD
FBgn0037298	2465.13497	-0.3267261	1.93E-13	Sccpdh1
FBgn0013812	93.2133252	1.25762369	3.37E-13	Dhc93AB
FBgn0035205	2184.93779	0.25730498	3.45E-13	Ctr9
FBgn0035726	2581.64488	-0.3877591	3.59E-13	CG9953
FBgn0032139	478.376304	0.35521273	1.62E-12	CG13116
FBgn0032652	2436.96034	-0.2568111	1.74E-12	CG6870
FBgn0267792	596.155285	0.48728041	4.09E-12	rgr
FBgn0003074	9090.72192	-0.1862617	5.13E-12	Pgi
FBgn0039770	670.383526	-0.2706541	6.45E-12	CG15537
FBgn0045038	653.845997	-0.3415125	1.99E-11	Proc
FBgn0016031	2305.36631	0.17310874	3.98E-11	lama
FBgn0005614	72970.1863	-0.3673527	3.98E-11	trpl
FBgn0032505	254.248704	8.24133101	1.07E-10	CG16826
FBgn0283437	2692.44751	-0.913452	1.07E-10	PPO1
FBgn0035206	738.100858	0.2840037	1.31E-10	CG9186
FBgn0035578	197.822588	-0.4890503	1.54E-10	CG13707
FBgn0036921	3931.07106	-0.1692141	2.20E-10	RhoGDI
FBgn0032538	365.786725	-0.4349093	2.32E-10	Vajk2
FBgn0036106	13555.4619	0.43317641	3.13E-10	CG6409
FBgn0266918	5245.29319	-0.1379594	3.68E-10	CG32486
FBgn0031902	419.342953	-0.3037581	6.24E-10	Wnt6
FBgn0032322	825.472567	0.45281265	9.99E-10	CG16743
FBgn0035676	788.7051	-0.2550177	9.99E-10	ssp6
FBgn0052392	157.250893	-0.569043	1.06E-09	CG32392
FBgn0027348	2406.28924	0.48479939	1.09E-09	bgm
FBgn0051207	691.191968	-0.2875409	1.86E-09	CG31207
FBgn0085334	13.8468092	-2.1833449	1.91E-09	CG34305
FBgn0027655	2131.15284	-0.2424644	1.92E-09	htt
FBgn0035523	834.070888	0.21437435	2.07E-09	Ctl1
FBgn0038257	466.253556	-0.5583844	2.19E-09	smp-30
FBgn0259209	1360.61134	0.30614825	2.26E-09	Mlp60A
FBgn0011672	1093.51126	0.22296609	2.69E-09	Mvl
FBgn0039609	511.367058	-0.3037757	2.85E-09	Nepl17
FBgn0036381	2011.50251	0.22134122	8.26E-09	CG8745
FBgn0014859	350.414292	-0.7234224	9.89E-09	Hr38
FBgn0039226	402.793142	-0.3222772	1.18E-08	Ude
FBgn0261859	4433.01555	0.22339925	1.25E-08	CG42788
FBgn0029896	5012.27233	0.17757862	1.25E-08	CG3168
FBgn0265182	4618.51687	-0.2472873	1.25E-08	CG44247
FBgn0035583	184.741383	-0.9471523	1.36E-08	CG13704

FBgn0015245	6423.13089	-0.1166087	1.39E-08	Hsp60A
FBgn0052282	599.157579	-0.5059436	1.40E-08	Drsl4
FBgn0036750	117.228731	-0.8069401	1.40E-08	CG6034
FBgn0011204	1273.26323	0.29988118	2.13E-08	cue
FBgn0044452	2276.67319	0.17864869	2.13E-08	Atg2
FBgn0041712	671.129032	-0.5913632	2.13E-08	yellow-d
FBgn0032436	43.1825053	-1.0433179	2.13E-08	CG5418
FBgn0010548	4467.93755	-0.1808586	2.82E-08	Aldh-III
FBgn0000241	990.88908	-0.2730976	3.18E-08	bw
FBgn0032726	696.030671	-0.5575626	4.24E-08	CG10621
FBgn0023526	1265.15013	0.17576429	5.21E-08	CG2865
FBgn0051075	1169.53478	-0.471006	5.77E-08	CG31075
FBgn0034660	585.431514	-0.3641283	7.10E-08	Loxl2
FBgn0038395	93.9465446	-0.7985562	7.52E-08	CG10407
FBgn0000044	9644.6385	0.342689	7.73E-08	Act57B
FBgn0023479	15231.4054	0.18935897	8.09E-08	teq
FBgn0035791	121.480021	-0.7344486	9.97E-08	CG8539
FBgn0054054	92.5938026	0.91372203	1.15E-07	CG34054
FBgn0039886	112.402953	0.50293112	1.23E-07	CG2003
FBgn0031775	352.253709	-0.6334201	1.35E-07	CG9150
FBgn0039052	230.434457	-0.8878484	1.53E-07	CG6733
FBgn0265103	41.383688	3.151232	1.87E-07	asRNA:CR44205
FBgn0267729	40.3028043	-0.8364978	1.87E-07	lncRNA:CR46060
FBgn0042201	6384.26918	-0.4048671	1.89E-07	Nplp3
FBgn0035246	6506.62092	-0.1158102	1.96E-07	CG13928
FBgn0040629	33.1722707	-2.7273906	2.36E-07	CAH5
FBgn0040532	3215.80722	0.18029243	2.98E-07	CG8369
FBgn0040309	5108.7154	-0.1591459	3.28E-07	Jafrac1
FBgn0266719	671.812413	0.22772303	4.03E-07	stac
FBgn0024943	6054.22287	-0.1725936	4.31E-07	PIP82
FBgn0033367	2704.70191	-0.7863852	4.39E-07	PPO2
FBgn0035985	1302.84855	0.20297448	4.49E-07	Cpr67B
FBgn0032336	1103.88862	-0.2558298	4.78E-07	AstC
FBgn0036992	3033.29752	0.56628873	4.94E-07	Hpd
FBgn0028648	189.528937	-0.3952394	5.13E-07	mRpL50
FBgn0051038	3440.75844	0.2111167	5.15E-07	CG31038
FBgn0087013	9005.2081	0.11047353	5.42E-07	Karybeta3
FBgn0016013	701.047012	0.2949784	5.64E-07	Faa
FBgn0013305	5053.23714	-0.1509428	5.80E-07	Nmda1
FBgn0014863	3235.98523	0.2881248	6.42E-07	Mlp84B
FBgn0035168	37.3827291	-0.8565345	6.96E-07	cep290
FBgn0038983	991.223599	-0.2617212	7.34E-07	CG5326

FBgn0030519	1551.41106	-0.1406713	7.87E-07	CG11151
FBgn0283471	2909.60076	0.25852771	8.02E-07	wupA
FBgn0038286	2418.30265	0.18279011	8.89E-07	CG6966
FBgn0040305	681.43332	0.2093576	8.93E-07	MTF-1
FBgn0035770	7053.18381	0.1733876	1.10E-06	pst
FBgn0038877	4346.97912	-0.1430508	1.10E-06	CG3308
FBgn0250839	1336.48395	-0.1692449	1.15E-06	CG2016
FBgn0026077	853.100043	-0.2602173	1.39E-06	Gasp
FBgn0036875	677.752753	0.31021059	1.44E-06	CG9449
FBgn0027932	4997.6632	0.1687865	1.45E-06	Akap200
FBgn0032685	726.892767	-0.255102	2.02E-06	CG10211
FBgn0031426	34.1305157	-0.9162223	2.06E-06	CG18641
FBgn0035398	104.487266	-0.5602471	2.19E-06	Cht7
FBgn0035348	5425.46153	-0.3602005	2.35E-06	CG16758
FBgn0031176	102.395416	8.27695356	2.51E-06	whe
FBgn0035627	33.7362351	0.78259294	2.51E-06	Sse
FBgn0030968	990.11815	-0.2990909	2.57E-06	CG7322
FBgn0035969	91.013109	-0.7510056	2.63E-06	CG4476
FBgn0053116	651.98678	-0.3041043	2.84E-06	CG33116
FBgn0040211	698.969973	0.38385542	2.87E-06	hgo
FBgn0020493	1145.362	0.18110681	2.99E-06	Dad
FBgn0023477	3704.40951	-0.2618205	2.99E-06	Taldo
FBgn0039051	55.7701352	-0.9434001	3.34E-06	CG17109
FBgn0052687	2126.63434	0.17332096	3.85E-06	CG32687
FBgn0040349	1140.92374	-0.3311703	3.85E-06	CG3699
FBgn0032721	1146.26634	-0.1554405	4.09E-06	CG10602
FBgn0035574	950.854843	-0.1689246	4.09E-06	RhoGEF64C
FBgn0264077	100.066766	0.60176938	4.17E-06	Cnx14D
FBgn0261560	2836.10222	0.2321486	4.21E-06	Thor
FBgn0267011	13.1145031	-1.3510189	4.65E-06	lncRNA:CR45455
FBgn0035346	794.886353	0.19469531	4.80E-06	CG1146
FBgn0033697	64.3794115	0.5921017	4.86E-06	Cyp6t3
FBgn0031850	3821.43008	-0.1460565	4.86E-06	Tsp
FBgn0004047	766.734763	-0.2555778	5.04E-06	Yp3
FBgn0032785	706.890539	-0.2771319	5.60E-06	CG10026
FBgn0039299	7.13856057	-2.0033061	5.60E-06	CG11854
FBgn0086677	4228.34923	-0.2304855	5.75E-06	jeb
FBgn0261113	10841.2282	-0.3016296	5.75E-06	Xrp1
FBgn0262838	144.784371	0.86774494	5.76E-06	CG43202
FBgn0035331	288.918475	0.28685696	6.45E-06	MsR1
FBgn0032945	132.08147	0.78855361	6.51E-06	CG8665
FBgn0027579	2638.29939	-0.2858127	6.51E-06	mino

FBgn0033603	154.685416	-0.4281812	6.85E-06	Cpr47Ef
FBgn0035076	1307.8928	-0.3597823	7.37E-06	Ance-5
FBgn0032382	3179.29499	0.23489647	7.55E-06	Mal-B2
FBgn0028497	3118.14931	-0.1324382	7.55E-06	CG3530
FBgn0033926	21032.3182	-0.7398553	7.55E-06	Arc1
FBgn0038946	2227.7875	-0.1908688	8.39E-06	rdhB
FBgn0039099	553.169621	0.26060965	8.40E-06	GILT2
FBgn0032879	1462.40196	-0.5167511	9.15E-06	CarT
FBgn0035186	345.173759	0.26082097	9.68E-06	CG13912
FBgn0002719	13855.2255	0.17380849	9.77E-06	Men
FBgn0003053	941.257544	-0.2138574	9.77E-06	peb
FBgn0035113	153.767464	-0.3751704	9.77E-06	pyx
FBgn0038129	692.875817	0.26489468	9.86E-06	TBC1D5
FBgn0031245	1290.62071	-0.147197	1.32E-05	CG3625
FBgn0000163	1745.87129	0.14323398	1.50E-05	baz
FBgn0011722	2249.42614	0.18735441	1.59E-05	Tig
FBgn0037835	1097.24594	-0.3214506	1.61E-05	CG14687
FBgn0036589	156.915736	-0.4858328	1.61E-05	CG13067
FBgn0033927	6644.26561	-0.7263265	1.61E-05	CR10102
FBgn0003390	646.708092	0.30469506	1.64E-05	shf
FBgn0037896	731.457181	-0.2294193	1.64E-05	ninaG
FBgn0036428	5559.42249	0.27366242	1.69E-05	Gbs-70E
FBgn0036364	470.711491	0.2612109	1.69E-05	CG14109
FBgn0001257	1662.79035	-0.3697802	1.69E-05	ImpL2
FBgn0261004	76.9471894	-0.5701596	1.73E-05	asl
FBgn0035873	82.434637	-0.5453211	1.74E-05	CG13670
FBgn0086708	2878.5322	-0.1431236	1.75E-05	stv
FBgn0035158	449.243735	0.29366344	1.77E-05	CG13895
FBgn0003248	4210.17343	0.14046437	1.98E-05	Rh2
FBgn0023212	2132.55116	0.13783543	1.98E-05	EloB
FBgn0001229	113.05832	-0.5041567	2.04E-05	Hsp67Bc
FBgn0039102	4082.0025	0.26228355	2.05E-05	SPE
FBgn0263973	487.137325	-0.21149	2.05E-05	jv
FBgn0036745	480.872454	-0.2219792	2.05E-05	CG7484
FBgn0030208	1075.0472	-0.140202	2.17E-05	PPP4R2r
FBgn0029820	1257.31591	0.15131886	2.24E-05	CG16721
FBgn0041224	6.71129698	-2.1072693	2.27E-05	Gr97a
FBgn0264894	3644.86441	0.14953195	2.28E-05	CG44085
FBgn0029720	884.899698	-0.1691173	2.28E-05	CG3009
FBgn0019830	1294.36372	-0.1934531	2.28E-05	colt
FBgn0025641	3386.81564	-0.1198783	2.31E-05	DAAM
FBgn0025676	455.464512	0.24742221	2.34E-05	CkIIalpha-i3

FBgn0053109	20.5447344	5.29440256	2.41E-05	CG33109
FBgn0003676	857.58202	-0.1948688	2.41E-05	CCT1
FBgn0037976	555.643084	-0.2163614	2.62E-05	Tk
FBgn0040752	4954.77701	0.16870292	2.78E-05	Prosap
FBgn0036318	2836.75853	-0.1128017	2.81E-05	Wbp2
FBgn0030505	4825.25046	0.15481926	2.87E-05	NFAT
FBgn0025454	7445.6001	0.25487006	2.91E-05	Cyp6g1
FBgn0038862	4017.03836	-0.2522548	3.00E-05	Usp8
FBgn0004167	7669.77223	0.20131787	3.05E-05	kst
FBgn0001092	11591.4547	-0.0945227	3.05E-05	Gapdh2
FBgn0015569	761.159908	-0.2140974	3.18E-05	alpha-Est10
FBgn0031418	1373.314	-0.3368909	3.18E-05	CG3609
FBgn0035383	658.645721	-0.1916683	3.45E-05	CPT2
FBgn0037090	1013.55543	-0.382008	3.46E-05	Est-Q
FBgn0032753	680.93839	-0.2839633	3.50E-05	CG17572
FBgn0032840	1512.76293	-0.1350859	3.63E-05	sNPF
FBgn0038172	2022.20828	0.17963158	3.90E-05	Adgf-D
FBgn0034140	2318.02324	0.29861622	4.11E-05	Lst
FBgn0261575	2872.33332	-0.4991951	4.35E-05	tobi
FBgn0030309	1011.0939	0.18864566	4.48E-05	CG1572
FBgn0036208	287.54309	-0.3235733	4.51E-05	CG10361
FBgn0052311	7504.06203	0.19257829	4.55E-05	zormin
FBgn0001992	42.9260085	-0.6307725	4.65E-05	Cyp303a1
FBgn0040382	11844.0979	-0.1121324	4.93E-05	CG5273
FBgn0033544	7925.88458	-0.1336325	4.93E-05	CG7220
FBgn0033158	41.9602448	-0.6021362	4.98E-05	CG12164
FBgn0264753	1421.50727	-0.2140286	5.18E-05	Rgk1
FBgn0026418	3108.86249	-0.1225876	5.22E-05	Hsc70Cb
FBgn0015218	3663.2914	-0.083991	5.60E-05	eIF4E1
FBgn0264272	1029.10441	-0.1814485	5.61E-05	mwh
FBgn0036046	963.251295	-0.1969827	5.70E-05	Ilp2
FBgn0020307	416.819136	-0.242734	6.37E-05	dve
FBgn0033970	664.673669	0.19267216	6.52E-05	CG10205
FBgn0039656	884.739383	0.20471223	6.60E-05	CG11951
FBgn0032836	3405.69531	0.22139773	7.58E-05	CG10680
FBgn0034538	176.33772	0.39164285	7.67E-05	CG16799
FBgn0034405	3528.16388	-0.1210624	8.08E-05	Jheh2
FBgn0034328	868.389311	1.59723558	8.20E-05	IM23
FBgn0036770	719.512711	0.19378904	8.20E-05	Prestin
FBgn0050052	1495.88576	0.19440633	9.03E-05	Obp49a
FBgn0032402	1442.52803	0.13204417	9.03E-05	CG14945
FBgn0033919	3093.80279	0.09969291	9.03E-05	CG8547

FBgn0032803	242.893327	-0.3268132	9.03E-05	CG13082
FBgn0025687	702.407518	0.39051519	9.06E-05	NA
FBgn0265935	1541.57857	0.15184899	9.09E-05	coro
FBgn0031692	2385.91732	0.20348162	9.10E-05	TpnC25D
FBgn0004169	5134.73991	0.24105662	9.20E-05	up
FBgn0052250	424.769082	-0.2182115	9.66E-05	PMP34
FBgn0023023	2624.80055	-0.1521235	0.00010611	CRMP
FBgn0038035	420.135454	-0.248873	0.00010611	NA
FBgn0036417	187.936316	-0.4300682	0.00010654	CG7906
FBgn0030377	20.704249	0.92909731	0.00010949	CG1924
FBgn0037448	806.779994	-0.1648459	0.00012263	CG15186
FBgn0011581	1642.24439	-0.1278907	0.00012348	Ms
FBgn0243586	8.0759438	-1.6192818	0.00012433	Tb
FBgn0040299	298.315739	0.26701866	0.00013776	Myo28B1
FBgn0001112	350.10395	-0.3125493	0.00013776	Gld
FBgn0004652	1817.02134	0.14550699	0.00013906	fru
FBgn0035388	1289.12663	0.13503848	0.0001398	CG2162
FBgn0037936	827.126894	-0.2585961	0.00014047	CG6908
FBgn0263039	344.098897	0.24482361	0.00014864	NA
FBgn0014163	6781.86938	0.11899322	0.00015247	fax
FBgn0003068	3170.38151	-0.2096108	0.00015337	per
FBgn0041188	6292.72353	-0.0838667	0.00015492	Atx2
FBgn0039028	43.5851912	-0.6579179	0.00015492	CG13840
FBgn0000308	6413.33587	-0.1115386	0.00015697	chic
FBgn0051414	465.854184	0.25089258	0.00016017	Gba1b
FBgn0038341	577.146946	0.27503271	0.00016667	NA
FBgn0021765	2124.95264	-0.1782669	0.00017093	scu
FBgn0039611	870.199608	-0.296841	0.00017718	Nepl18
FBgn0030041	1945.26353	0.30255252	0.00018485	CG12116
FBgn0051103	1015.09679	0.20949888	0.00018868	CG31103
FBgn0014018	2484.31823	0.26945935	0.00018907	Rel
FBgn0030981	14.3494618	1.1030354	0.00019009	CG14191
FBgn0032156	4889.52477	0.0870307	0.00019238	CG13124
FBgn0053993	115.351137	-0.3371101	0.00022601	CG33993
FBgn0264489	9059.89476	0.14831764	0.00026574	CG43897
FBgn0039485	347.641083	-0.2536169	0.00026755	CG17189
FBgn0285991	5169.57125	-0.0894187	0.00026808	hpRNA:CR18854
FBgn0250746	1058.23973	-0.1219602	0.00027775	Prosbeta7
FBgn0036666	1447.47467	-0.1141273	0.0003015	TSG101
FBgn0012344	1228.4059	-0.1398629	0.00030378	Dh44
FBgn0032609	90.5297019	-0.4809437	0.00030393	CG13280
FBgn0033928	122.133552	-0.639232	0.00032402	Arc2

279

FBgn0037387	4421.38595	0.22627908	0.00032412	CG1213
FBgn0000064	24809.0154	-0.0876895	0.00034848	Ald1
FBgn0039324	471.432213	-0.2372411	0.00034848	CG10553
FBgn0050411	24.1523177	-0.8811168	0.00034848	CG30411
FBgn0027610	2046.38706	0.09593824	0.00039074	Dic1
FBgn0019661	45497.3921	0.16445363	0.00040215	lncRNA:roX1
FBgn0039232	421.689921	0.21758504	0.00041445	sosie
FBgn0035360	61.6222633	0.45321505	0.00041938	CG1246
FBgn0285913	1542.62943	-0.1137773	0.00043306	red
FBgn0053143	1331.19412	-0.1978654	0.00045422	CG33143
FBgn0283680	1056.84936	-0.1733917	0.00048853	IP3K2
FBgn0003499	416.479119	-0.2297273	0.0005037	sr
FBgn0030151	1390.12222	0.11799993	0.00051721	CG1354
FBgn0034866	4.08017187	2.19059728	0.00052105	Or59c
FBgn0039234	754.794425	-0.1315817	0.000524	Nct
FBgn0035471	929.571414	-0.1595855	0.00053308	Sc2
FBgn0250871	1443.32078	0.15808833	0.00054095	pot
FBgn0283461	1382.18002	1.89608984	0.00055265	Drs
FBgn0034512	15082.0154	0.71695058	0.00055265	CG18067
FBgn0034638	6530.10564	0.12254287	0.00055275	CG10433
FBgn0085209	107.839978	-0.4121645	0.00056689	CG34180
FBgn0034966	115.100569	-0.3339116	0.00059561	CG13563
FBgn0025186	865.716323	-0.1243454	0.00061562	ari-2
FBgn0034602	329.773345	0.22317134	0.00061629	Lapsyn
FBgn0028544	93.6103859	-0.3607026	0.00065096	Vajk3
FBgn0030763	209.354431	-0.2550298	0.00065192	CG9782
FBgn0033268	11058.3474	-0.1721123	0.00066567	Obp44a
FBgn0035711	56.913432	0.49630372	0.00066654	CG8519
FBgn0040070	2474.16332	-0.0942122	0.00067879	Trx-2
FBgn0027574	298.128673	-0.2010784	0.00067879	CG5815
FBgn0002789	2009.39607	0.17292711	0.00068675	Mp20
FBgn0036334	915.888801	-0.1342784	0.00068885	CG11267
FBgn0036661	1034.17766	-0.1612524	0.00074563	CG9705
FBgn0001189	624.11511	0.1386838	0.00076078	hfw
FBgn0063923	569.496564	-0.1883808	0.00076078	Kaz1-ORFB
FBgn0019929	1725.59296	0.15549547	0.0007717	Ser7
FBgn0260747	3588.95951	-0.111516	0.00079235	Chchd2
FBgn0033913	2108.73695	0.17880697	0.00080893	CG8468
FBgn0004102	1215.63691	0.16835804	0.00083839	oc
FBgn0039500	31.128534	-0.5872326	0.00084665	CG5984
FBgn0003861	59537.9326	-0.1243734	0.000887	trp
FBgn0264541	11.3426023	2.1546723	0.00091558	CG43920

FBgn0036659	633.024783	0.41361779	0.0009229	CG9701
FBgn0025833	919.094786	-0.16121	0.0009229	CG8910
FBgn0004117	3445.32538	0.17241309	0.00095641	Tm2
FBgn0029843	1336.14235	-0.1119735	0.00097185	Nep1
FBgn0039628	1682.59214	-0.1493132	0.00097617	CG11841
FBgn0040736	8199.84319	0.48951486	0.00098659	IM3
FBgn0028583	221.959884	2.23693273	0.0009967	lcs
FBgn0284243	8884.08667	-0.1559131	0.0009967	betaTub56D
FBgn0085370	2615.3086	0.10122614	0.00099797	Pde11
FBgn0013772	656.771232	-0.3293364	0.00099835	Cyp6a8
FBgn0034329	3989.62291	0.77877719	0.00100629	IM1
FBgn0035173	2118.58058	-0.1293202	0.00102427	CG13907
FBgn0036125	66.1803888	0.47040198	0.00103741	lyd
FBgn0037126	591.75975	0.27821154	0.00103763	CG14567
FBgn0063491	1816.66068	-0.1777856	0.00104022	GstE9
FBgn0028988	1440.36666	0.27819003	0.00106934	Spn42Dd
FBgn0017545	15222.9652	0.0947948	0.00106934	RpS3A
FBgn0026438	8589.97093	-0.1185413	0.00106934	Eaat2
FBgn0036769	838.915057	-0.1371836	0.00106934	Tsp74F
FBgn0052407	662.32851	-0.1561505	0.00106934	CG32407
FBgn0033079	396.382667	0.22171541	0.00107268	Fmo-2
FBgn0011828	3253.37562	0.12565377	0.00107951	Pxn
FBgn0029504	2128.3101	0.14135289	0.00108229	CHES-1-like
FBgn0035255	95.0682623	-0.324779	0.00110926	RabX5
FBgn0260756	174.650151	0.24993613	0.00113847	CG42554
FBgn0030230	648.925404	-0.1449162	0.00116731	Rph
FBgn0025352	2732.1185	-0.1544614	0.00119543	Thiolase
FBgn0259979	1086.01011	-0.202121	0.00119637	CG17337
FBgn0033235	785.996834	-0.134916	0.00120303	CG8728
FBgn0037230	3094.18332	0.1973707	0.0012325	Nepl11
FBgn0261547	3136.45088	0.18173412	0.00123377	Exn
FBgn0037719	370.018669	-0.2232901	0.00124304	bocks
FBgn0036790	772.404691	0.18465652	0.00132733	AstC-R1
FBgn0035187	263.389264	-0.2385809	0.00133659	Trh
FBgn0266455	11.8874963	0.00388321	0.00134755	CG45080
FBgn0025583	8596.43262	0.5005696	0.00137907	IM2
FBgn0010611	1206.3615	0.14542	0.00144112	Hmgs
FBgn0026602	1242.07082	-0.1276671	0.00145913	Ady43A
FBgn0035434	1466.31262	-0.3926543	0.0014642	Drsl5
FBgn0016715	420.536131	-0.2197039	0.00151066	Reg-2
FBgn0039642	70.4351656	-0.4019676	0.00154368	CG11882
FBgn0028692	2049.17743	-0.0982883	0.00166778	Rpn2

FBgn0035553	472.168251	0.26586972	0.00168034	CG13722
FBgn0032694	952.398799	0.13739066	0.00170842	MESR3
FBgn0035488	787.983228	-0.1384073	0.00177403	CG11593
FBgn0031646	42.004923	-0.5354003	0.00177403	snsl
FBgn0031703	1134.03771	0.16764645	0.00179065	CG12512
FBgn0002778	870.218475	0.15647005	0.00179065	mnd
FBgn0032048	712.376436	-0.1411391	0.00180948	Dh31
FBgn0028400	5433.73281	-0.1111665	0.00182653	Syt4
FBgn0010278	502.8043	-0.180857	0.00182653	Ssrp
FBgn0034511	1349.96975	0.76756443	0.00183447	GNBP-like3
FBgn0037879	24.2667227	-0.6974051	0.00185428	scpr-C
FBgn0021979	5519.87877	-0.0930803	0.00187999	l(2)k09913
FBgn0040099	1622.20117	0.21126297	0.00188863	lectin-28C
FBgn0032451	780.627422	-0.1293584	0.00188863	spict
FBgn0051380	25.5801638	0.75675113	0.00194062	CG31380
FBgn0034139	251.795401	0.27063334	0.00194249	CG4927
FBgn0037324	67.8106805	0.5289718	0.00197139	Orco
FBgn0052191	683.291027	0.17215943	0.00197957	CG32191
FBgn0026562	4751.16472	0.12345833	0.00198173	SPARC
FBgn0264324	2255.822	0.12235842	0.00198173	spg
FBgn0039114	5595.39455	0.18464313	0.00198975	Lsd-1
FBgn0015801	1360.04947	0.12376123	0.00199607	Reg-5
FBgn0000406	13501.0359	0.11755605	0.0020068	Cyt-b5-r
FBgn0030246	842.516214	-0.1407368	0.0020068	CG1582
FBgn0263986	240.649399	-0.2505435	0.0020068	cd
FBgn0050371	7.60757797	2.74893711	0.00202239	CG30371
FBgn0030310	249.583099	0.30945801	0.00203855	PGRP-SA
FBgn0027594	2579.48773	0.0910552	0.00205881	drpr
FBgn0025621	1058.49147	0.12563383	0.00207747	CG16989
FBgn0036880	280.490821	-0.3195672	0.00207747	Cpr76Bc
FBgn0267013	229.037687	-0.7042758	0.00208489	lncRNA:CR45457
FBgn0030993	343.780009	0.2197588	0.00211121	Mec2
FBgn0283427	56630.9016	0.20714136	0.00212972	FASN1
FBgn0052365	131.473052	-0.2722848	0.00215177	CG32365
FBgn0038211	1259.93135	0.14859324	0.00216198	CG9649
FBgn0031689	6598.63138	-0.1957172	0.00216198	Cyp28d1
FBgn0033696	49.338527	0.75506037	0.00216521	Cyp6g2
FBgn0035982	562.870225	-0.2282009	0.00216521	CG4461
FBgn0003475	5324.63863	-0.0633333	0.00222158	spir
FBgn0003884	18236.7875	-0.1174695	0.00222158	alphaTub84B
FBgn0002567	5963.98735	-0.1224123	0.00222865	Rab32
FBgn0004240	378.23705	2.16312673	0.00224903	DptA

FBgn0014141	2641.05186	0.11939393	0.00224903	cher
FBgn0029117	147.489415	-0.252814	0.00224903	Surf1
FBgn0265575	718.905719	0.14864127	0.00226881	yin
FBgn0263762	6.46597086	0.00470497	0.00227841	CG43679
FBgn0037007	3140.45026	0.11968483	0.00228222	CG5059
FBgn0035557	11.0456908	-0.0530444	0.00236731	CG11353
FBgn0029839	336.601185	-0.1979353	0.00239155	CG4660
FBgn0019982	1107.45968	-0.1055584	0.00240918	Gs1l
FBgn0035817	1006.68024	-0.268992	0.00240918	CG7409
FBgn0036016	40.3050464	-0.477251	0.00243752	CG3306
FBgn0044047	1060.97536	0.17897759	0.00243822	Ilp6
FBgn0038595	11.1715621	0.94304035	0.00244709	CG7142
FBgn0020503	6574.31316	0.08414576	0.00244709	CLIP-190
FBgn0003285	306.503617	-0.1876836	0.00244709	rst
FBgn0026189	2412.99257	0.0997172	0.00246141	prominin-like
FBgn0050203	429.975227	-0.2714768	0.00246381	CG30203
FBgn0267506	328.77139	0.32969095	0.00249115	pre-rRNA:CR45846
FBgn0050026	438.921649	0.48989297	0.00252966	CG30026
FBgn0283462	18441.7753	0.60962325	0.00256923	IMPPP
FBgn0037537	3011.40718	-0.0811863	0.00256952	CG2767
FBgn0033122	334.34498	-0.1692502	0.00256971	CG17002
FBgn0053470	37015.6492	0.60372039	0.00258008	CG33470
FBgn0036199	606.709413	-0.1552722	0.00258008	Bmcp
FBgn0067905	3444.75954	0.44833135	0.00259241	IM14
FBgn0000121	153485.987	-0.1341436	0.00261522	Arr2
FBgn0035181	603.634964	-0.156959	0.00261522	CG9205
FBgn0050431	454.603957	-0.218501	0.00266742	CG30431
FBgn0003162	3864.04855	0.15413563	0.00272698	Pu
FBgn0037788	1860.87585	0.12701389	0.00273633	CAH7
FBgn0028833	2426.54567	-0.0916852	0.00276477	Dak1
FBgn0086450	1065.66341	0.13705714	0.00278406	su(r)
FBgn0037607	9236.89514	-0.1814599	0.00279749	CG8036
FBgn0013718	3276.43734	0.14010085	0.00282901	nuf
FBgn0002773	10999.2214	0.15541242	0.00288159	Mlc2
FBgn0086370	1088.32146	-0.1021017	0.00291107	sra
FBgn0001565	1688.1352	0.15042363	0.00294807	Hlc
FBgn0037697	877.558375	0.16494888	0.00296546	GstZ2
FBgn0038874	175.7926	-0.2520989	0.00302333	ETHR
FBgn0015010	49.2125278	1.89826782	0.00302549	Ag5r
FBgn0265577	17.9151708	2.39491097	0.00303783	lncRNA:CR44404
FBgn0010385	142.782068	1.26333202	0.00307501	Def
FBgn0033782	571.93473	0.29880298	0.00309695	sug

FBgn0025777	1890.42334	0.15469991	0.00309695	homer
FBgn0004133	624.439056	-0.1385348	0.00309925	blow
FBgn0086673	89.902552	-0.4353908	0.00310177	CG13272
FBgn0266405	46.107931	1.95655636	0.00312747	lncRNA:CR45045
FBgn0039722	879.812395	-0.2882323	0.00312747	Capa
FBgn0028399	4666.65911	-0.076673	0.00315836	TMS1
FBgn0000046	1737.6999	0.16942969	0.00319024	Act87E
FBgn0003391	1744.07476	0.12201601	0.00322234	shg
FBgn0267507	331.780221	0.32219598	0.00324997	pre-rRNA:CR45847
FBgn0028426	263.015541	0.56955563	0.00328477	RNaseZ
FBgn0029134	1219.64864	-0.1036548	0.00328477	Prosbeta5
FBgn0031858	1614.78081	-0.1193926	0.00336663	CG17378
FBgn0034501	10568.0812	0.11103279	0.00337022	CG13868
FBgn0000547	2860.56469	0.09766377	0.00337022	ed
FBgn0014020	5425.0324	0.08181695	0.00337022	Rho1
FBgn0027572	2044.54781	-0.0969023	0.00337022	CG5009
FBgn0035092	1571.564	-0.1230299	0.00337022	Nplp1
FBgn0039518	23.4173338	0.63868546	0.00342607	CG13978
FBgn0027525	4045.34341	0.09985956	0.00346707	LTV1
FBgn0038098	201.078483	-0.2145621	0.00350486	CG7381
FBgn0267508	226.446248	0.4610267	0.00352566	28SrRNA-Psi:CR45848
FBgn0036935	2986.45121	-0.1485584	0.0035648	CG14186
FBgn0012042	166.449159	1.71670218	0.00356535	AttA
FBgn0035802	1725.19766	0.11038247	0.00358117	Pura
FBgn0002780	1223.46376	0.13387802	0.00361455	mod
FBgn0020930	1078.32837	-0.1062135	0.00361455	Dgkepsilon
FBgn0032684	985.266199	-0.1628584	0.00361455	Ugt301D1
FBgn0030357	162.899069	0.26427039	0.00364542	Sclp
FBgn0015282	1241.60919	-0.1164788	0.00365217	Rpt2
FBgn0263077	15042.3972	0.14887453	0.00366849	CG43340
FBgn0031392	522.934049	-0.1480936	0.00371272	AIF
FBgn0014388	1488.63159	-0.1319121	0.00375401	sty
FBgn0030012	129.691219	0.29282127	0.0037682	CG18262
FBgn0265512	3901.6894	0.09946392	0.00377936	mlt
FBgn0036857	1039.39786	-0.1347675	0.00381405	Aldh7A1
FBgn0283499	1855.44672	0.24303631	0.0038349	InR
FBgn0036619	5785.00074	-0.221735	0.00389518	Cpr72Ec
FBgn0260474	722.577111	0.30694085	0.00395745	CG30002
FBgn0038038	1484.75491	-0.102339	0.00395745	Sccpdh2
FBgn0024179	1335.98963	-0.0935645	0.00397692	wit
FBgn0262614	7089.78628	0.13775911	0.00397905	pyd
FBgn0086906	18496.0761	0.2067055	0.0040755	sls

FBgn0051064	1503.39311	-0.1001745	0.00411203	CG31064
FBgn0261563	468.76584	-0.2077059	0.00411203	wb
FBgn0032798	1856.29864	-0.1245779	0.00413365	CG10132
FBgn0032109	1221.59519	-0.7009939	0.00428923	CG17005
FBgn0004889	2946.81533	-0.1155698	0.00434149	tws
FBgn0261243	1579.34166	-0.0944495	0.00436401	Psa
FBgn0035806	775.375966	0.43495423	0.00455525	PGRP-SD
FBgn0001297	4092.56282	-0.0903216	0.00455525	kay
FBgn0029002	107.161432	-0.2602918	0.00459461	miple2
FBgn0038850	16.0943204	0.92195814	0.00460223	CG17279
FBgn0032484	658.588056	0.15626152	0.0046185	kek4
FBgn0028479	3674.89041	-0.134336	0.00470048	Mtpalpha
FBgn0001296	1579.4284	-0.1045391	0.00476098	kar
FBgn0000024	9467.78898	0.14919821	0.00476568	Ace
FBgn0261985	2442.77848	-0.0919677	0.00485483	Ptpmeg
FBgn0035756	1744.43768	0.20561256	0.00485864	unc-13-4A
FBgn0040206	1247.55257	0.15307555	0.00485864	krz
FBgn0020660	4532.9007	0.09199919	0.00485864	eIF4B
FBgn0051522	3341.77041	-0.0913503	0.00485864	CG31522
FBgn0011768	1539.35092	-0.1369486	0.00485864	Fdh
FBgn0046114	1825.83471	0.13264218	0.00486146	Gclm
FBgn0028484	1586.03776	0.09839749	0.00495382	Ack
FBgn0036927	6708.29925	0.08366492	0.00498588	Gabat
FBgn0026570	165.777598	0.2340841	0.00501019	CG5704
FBgn0035477	939.965796	0.1021707	0.00501282	CG14982
FBgn0035816	1044.8659	0.13597835	0.00509769	CG13685
FBgn0038247	42.986074	-0.4106527	0.00511231	Cad88C
FBgn0037539	451.397312	-0.1716676	0.00517674	CG10435
FBgn0039523	33.808489	0.50426989	0.00523569	CG12885
FBgn0261628	108.345528	0.33967776	0.00524509	CG42711
FBgn0052695	250.975967	0.23652515	0.00524509	CG32695
FBgn0038465	3318.30388	0.19542159	0.00524509	Irc
FBgn0262531	24.3406358	-0.8235071	0.00524509	CG43085
FBgn0085771	3118.7028	0.52001632	0.00530344	28SrRNA-Psi:CR40741
FBgn0033483	725.516754	0.1098802	0.00530344	egr
FBgn0037842	226.720951	-0.1861967	0.00532895	CG6567
FBgn0260660	2060.23392	0.09184117	0.00536431	Mp
FBgn0035334	664.321123	-0.1525093	0.00536431	CG8993
FBgn0033358	489.476318	-0.1633364	0.00536431	spab
FBgn0003886	14.7047475	-0.8897445	0.00536431	alphaTub85E
FBgn0033875	2589.13049	0.14293656	0.00540296	CG6357
FBgn0086365	258.372778	-0.1871287	0.00560237	Orct2

FBgn0035159	50.2781033	-0.4386894	0.00562067	CG13896
FBgn0013272	13793.8243	0.05950509	0.00565992	Gp150
FBgn0026439	8227.71564	-0.074132	0.00565992	Eaat1
FBgn0052820	113.010697	-0.4299081	0.00565992	CG32820
FBgn0066365	5.92318149	-1.1818904	0.00565992	dyl
FBgn0004513	1496.6641	-0.0920997	0.00567603	Mdr65
FBgn0000008	545.382936	-0.1384046	0.00573437	a
FBgn0267798	11.9122192	-0.8988276	0.00574822	lncRNA:CR46123
FBgn0003462	5686.70201	-0.0943599	0.00575405	Sod1
FBgn0035166	151.874927	-0.2189017	0.0057817	JMJD5
FBgn0030508	1200.98632	0.11416662	0.00579135	CG15760
FBgn0029891	3346.51375	0.06969497	0.0059988	Pink1
FBgn0037063	1664.66771	-0.1099337	0.00600622	CG9391
FBgn0033215	85.3380799	-0.4101569	0.00631512	Dgat2
FBgn0267966	16.8931397	-0.7956163	0.00637537	asRNA:CR46246
FBgn0030731	2209.86031	-0.096848	0.00638675	Mfe2
FBgn0035709	8.96373368	1.07863859	0.00645518	eIF4E4
FBgn0285955	2537.26108	0.09304622	0.00656064	cv-c
FBgn0030103	56.8148886	-0.3565101	0.00656064	Obp8a
FBgn0087005	6703.75953	-0.1784508	0.00658979	rtp
FBgn0036597	218.382825	-0.227178	0.00659099	CG4962
FBgn0040028	163.856323	-0.4150033	0.00659321	CG17450
FBgn0031213	1315.33966	0.0969785	0.00667335	galectin
FBgn0270926	1167.07122	-0.1514588	0.00667335	AsnS
FBgn0267505	165.274253	0.30458088	0.00668051	pre-rRNA:CR45845
FBgn0039040	1673.88333	0.15825875	0.00669372	CG13833
FBgn0029769	617.661594	0.13487782	0.00670215	frma
FBgn0040734	1253.26403	0.54205324	0.0067551	CG15065
FBgn0036713	862.24274	-0.1276124	0.00676132	Mip
FBgn0040609	144.99013	-0.640654	0.00685038	CG3348
FBgn0023179	4683.96739	-0.0981798	0.00685396	amon
FBgn0265052	522.10271	-0.1271075	0.0068981	St3
FBgn0052698	902.121418	0.18727968	0.00696607	CARPB
FBgn0031700	87.6969458	0.31351206	0.0071388	CG14022
FBgn0036781	8.76665583	-0.0332606	0.00714367	CG13699
FBgn0036975	1870.12447	-0.1201002	0.00714803	CG5618
FBgn0031417	1048.46252	-0.2372167	0.00715053	CG3597
FBgn0004359	483.814518	0.13781533	0.00733044	T48
FBgn0041581	548.15466	1.36999067	0.00739381	AttB
FBgn0038237	2877.98776	0.0990146	0.00739381	Pde6
FBgn0259224	1374.92649	-0.1270241	0.00758976	CG42324
FBgn0263608	40.2779471	-0.4017681	0.00759442	l(3)72Dr

FBgn0033153	436.047857	-0.2658287	0.0077856	Gadd45
FBgn0036516	754.046623	-0.1143968	0.00790207	CG7656
FBgn0031987	486.071017	-0.1334904	0.00792391	CG12375
FBgn0033574	1188.33295	0.10759842	0.00794878	Spn47C
FBgn0038143	15810.2649	-0.0698781	0.00794878	CG9813
FBgn0035906	1155.61936	-0.1193213	0.0080029	GstO2
FBgn0039807	373.120629	0.16935241	0.00804056	CG15546
FBgn0051999	1362.72662	0.13672107	0.00810908	CG31999
FBgn0034761	1198.59114	0.24017168	0.008265	CG4250
FBgn0039254	491.214892	-0.1747625	0.00827122	Nmnat
FBgn0033739	2412.70677	0.08691783	0.00848222	Dyb
FBgn0035538	6612.47073	-0.1389827	0.00848222	DopEcR
FBgn0038738	2026.08418	-0.1187322	0.00848992	CG4572
FBgn0265598	1129.79302	0.09684473	0.00850939	Bx
FBgn0263106	2272.24921	-0.0938094	0.00850939	DnaJ-1
FBgn0031069	3579.22829	-0.1070453	0.00850939	Pmp70
FBgn0030610	452.377164	-0.1273369	0.008558	CG9065
FBgn0051326	3199.12907	0.16117309	0.00857252	CG31326
FBgn0035151	48.5333586	0.35286508	0.00867821	CG17129
FBgn0004401	4934.00743	-0.067149	0.00867821	Pep
FBgn0031432	223.462231	-0.424338	0.00869808	Cyp309a1
FBgn0033304	601.781516	0.1567815	0.00880661	Cyp6a13
FBgn0010053	2170.18643	-0.130539	0.00882909	Jheh1
FBgn0283531	228.630779	0.19177251	0.00895357	Duox
FBgn0037796	1101.82847	0.11056032	0.00901282	CG12814
FBgn0034259	426.085212	-0.1277889	0.00902731	P32
FBgn0052553	67.1502949	0.37534964	0.00903026	lncRNA:CR32553
FBgn0003721	4602.9292	0.1207903	0.00903485	Tm1
FBgn0030090	773.964164	0.12097607	0.00912525	fend
FBgn0263220	9016.07934	0.09285295	0.00912525	Hk
FBgn0029870	5115.3436	0.05816287	0.00912525	Marf
FBgn0029996	2955.15325	0.12535809	0.00920558	UbcE2H
FBgn0035830	662.025995	-0.1145436	0.0092105	CG8209
FBgn0034500	598.904376	-0.1647172	0.0092105	CG11200
FBgn0004436	2784.31853	0.09666732	0.00927379	Ubc6
FBgn0266756	5046.07134	0.12671521	0.00937273	btsz
FBgn0035718	7.9249539	0.96429108	0.00946397	CG14820
FBgn0028855	51.6517182	0.70545281	0.00946397	CG15282
FBgn0039495	346.962791	0.22181858	0.00946397	CG5909
FBgn0003149	3715.86662	0.1767919	0.00946397	Prm
FBgn0035344	1014.21152	-0.1268087	0.00946397	Cyp4d20
FBgn0031092	559.52991	-0.140162	0.00946397	CG9577

FBgn0086254	2537.51743	-0.1092729	0.00948274	CG6084
FBgn0039970	2861.44501	0.11670369	0.00960996	CG17508
FBgn0024957	2443.62233	0.15486089	0.00962983	Irp-1B
FBgn0037721	474.102792	-0.1645808	0.0096691	CG9427
FBgn0032882	540.803521	-0.121901	0.00972398	Ns4
FBgn0003716	1263.98937	0.10272245	0.00973721	tkv
FBgn0034717	814.378981	0.15873605	0.00978143	CG5819
FBgn0010621	994.709396	-0.1494817	0.0097884	CCT5
FBgn0051248	768.841926	0.11680955	0.00980137	CG31248
FBgn0002891	369.015951	-0.190096	0.00980137	mus205
FBgn0015576	3096.15371	-0.1347218	0.01007102	alpha-Est8
FBgn0085819	2947.097	0.46502322	0.01007251	28SrRNA-Psi:CR41609
FBgn0052056	1212.92755	-0.0831742	0.01017463	scramb1
FBgn0026576	3662.09736	-0.1648846	0.0101854	Pisd
FBgn0003189	831.059011	-0.1434096	0.01018578	r
FBgn0037327	1336.82841	-0.1151016	0.01024913	PEK
FBgn0033988	1541.1759	0.07852436	0.01031619	pcs
FBgn0262579	13959.4982	0.06543939	0.01038457	Ect4
FBgn0040064	2638.11894	-0.1236424	0.01042796	yip2
FBgn0026315	243.777747	-0.1658457	0.01061296	Ugt35A1
FBgn0036152	626.489802	0.11497207	0.01065319	CG6175
FBgn0266019	7103.00636	0.08122257	0.01065319	rudhira
FBgn0053296	291.821488	0.20392012	0.01078279	CG33296
FBgn0267913	345.218712	0.18048601	0.01080824	lncRNA:CR46194
FBgn0036351	8.0444923	-0.0314173	0.01080824	CG14107
FBgn0011283	70.1493014	0.9471584	0.01107807	Obp28a
FBgn0033936	106.452767	0.69777179	0.01107807	Achl
FBgn0031801	883.610987	0.23975376	0.01107807	CG9498
FBgn0030432	812.849828	0.09500201	0.01107807	CG4404
FBgn0038397	70.4344932	0.92146676	0.01114174	CG10185
FBgn0265413	986.668348	0.12037497	0.01116717	CG44325
FBgn0031111	142.135965	-0.2482759	0.0112011	Obp19c
FBgn0037819	472.605435	-0.1854202	0.01128096	CG14688
FBgn0037636	21858.0696	0.11132786	0.01129943	NA
FBgn0027835	7497.71452	0.10676767	0.01129943	Dp1
FBgn0027086	1431.22888	0.20026552	0.01142898	IleRS
FBgn0040582	1804.80368	0.5097036	0.0115076	CG5791
FBgn0037433	945.455364	-0.0920854	0.0115405	CG17919
FBgn0041713	475.466599	0.14040797	0.01156751	yellow-c
FBgn0064225	20913.6063	0.07225433	0.01164745	RpL5
FBgn0013307	449.005557	0.14553316	0.01168123	Odc1
FBgn0085453	563.959446	0.1968718	0.01177068	Mthfs

FBgn0013725	622.936756	-0.1173689	0.01183287	phyl
FBgn0003943	45844.115	-0.0920263	0.01185499	Ubi-p63E
FBgn0035888	927.987793	0.09619016	0.01185639	CG7120
FBgn0037443	2241.1588	-0.0691441	0.011936	Dmtn
FBgn0037889	9.05329791	-0.0360417	0.01197125	scpr-A
FBgn0033649	584.873204	0.1573734	0.01222055	pyr
FBgn0030160	7681.40104	0.0960189	0.01223104	CG9691
FBgn0062928	12.7669314	-0.0463412	0.01235067	hpRNA:CR33940
FBgn0051028	81.2539843	0.29290217	0.0123562	CG31028
FBgn0032835	5056.84568	0.39640134	0.01238578	CG16772
FBgn0050151	442.133868	0.16026194	0.01242143	CG30151
FBgn0010620	1120.10448	0.10831455	0.01242143	CG10939
FBgn0262782	8057.75658	-0.0910348	0.01249231	Mdh1
FBgn0036627	221.253224	0.18757423	0.01268846	Gagr
FBgn0035710	1822.71557	0.11620381	0.01271691	SP1173
FBgn0027592	422.681652	-0.1308338	0.01277336	MED15
FBgn0038830	212.263801	0.18554636	0.01292027	CG17272
FBgn0011766	2277.57875	-0.0854958	0.01294759	E2f1
FBgn0034480	48.5191225	-0.6129578	0.01297262	CG16898
FBgn0266599	42551.8453	-0.0721274	0.01302186	Hsc70-4
FBgn0039054	12781.696	-0.0843261	0.01305945	Cow
FBgn0025615	511.657781	-0.1160915	0.01305945	Torsin
FBgn0020653	3725.52388	-0.0895225	0.01308163	Trxr-1
FBgn0039429	8.84690357	-0.0371356	0.0130992	CG14238
FBgn0026593	1044.51115	-0.1309493	0.0130992	CG5707
FBgn0004837	315.546506	-0.1420263	0.0130992	Su(H)
FBgn0041210	2571.82243	0.0844941	0.0131987	HDAC4
FBgn0029666	759.64829	0.12827378	0.0132514	CG10803
FBgn0038017	114.07023	-0.312641	0.01340861	CG4115
FBgn0053784	21.3696034	-0.5069528	0.01347495	CG33784
FBgn0038074	1820.74165	0.48124211	0.01350141	Gnmt
FBgn0267012	444.208341	-0.6224272	0.01351439	lncRNA:CR45456
FBgn0026179	2902.46569	-0.0772816	0.01361436	siz
FBgn0011763	1514.277	0.07512603	0.01365936	Dp
FBgn0034628	597.305728	-0.1131483	0.01365936	Acox57D-p
FBgn0033820	13170.5289	0.12391253	0.01369619	CG4716
FBgn0033038	461.330798	-0.1174961	0.01381905	CG7791
FBgn0030257	69.0715203	0.29459946	0.01382429	SmydA-4
FBgn0031457	372.161366	-0.1307998	0.01382429	CG3077
FBgn0034076	41.6213209	1.7676726	0.014087	Jhedup
FBgn0034406	526.152253	-0.1597448	0.01419042	Jheh3
FBgn0039684	78.405266	0.41604045	0.01433234	Obp99d

FBgn0033250	11256.1542	0.10184643	0.01433234	CG14762
FBgn0017418	2452.40994	0.08072307	0.01434947	ari-1
FBgn0038809	4326.08101	0.06706107	0.01434947	CG16953
FBgn0261394	949.266427	-0.1062995	0.01434947	Prosalpha3
FBgn0038407	1940.71481	-0.1370976	0.01437953	CG6126
FBgn0264695	32789.3387	0.14599798	0.01441977	Mhc
FBgn0039316	76.2571062	0.30079481	0.01455411	CG11893
FBgn0259150	3096.63127	0.11787593	0.0145595	OtopLc
FBgn0036728	1851.81893	-0.1413971	0.01462279	UQCR-Q
FBgn0014033	1041.48911	0.15449747	0.01462546	Sr-CI
FBgn0034935	589.669639	-0.1680733	0.01468383	Orcokinin
FBgn0053147	2734.8396	0.11558219	0.01490273	Hs3st-A
FBgn0039348	1690.53798	-0.1610875	0.01491347	Npl4
FBgn0002526	1879.19161	0.14101291	0.01499011	LanA
FBgn0050423	1075.65518	-0.1015694	0.01499507	CG30423
FBgn0029959	686.845249	0.10880518	0.01511408	Rab39
FBgn0030850	1066.69084	0.08579535	0.01517242	stas
FBgn0086680	1893.28574	-0.1083097	0.01517242	vvl
FBgn0250843	686.085263	-0.1336833	0.01517242	Prosalpha6
FBgn0000535	3078.20599	0.13603287	0.01532302	eag
FBgn0034331	8903.33869	0.2387592	0.01536261	CG15067
FBgn0052121	103.910355	0.25302964	0.01559579	CG32121
FBgn0037487	55.3473707	0.3159657	0.01559839	thw
FBgn0063667	19.9189241	-0.5433321	0.01568428	CG32335
FBgn0041627	163.08788	-0.3750393	0.01571881	Ku80
FBgn0039490	5.63344376	-1.0691794	0.01594196	CG5882
FBgn0038681	2367.48578	0.09440278	0.0162507	Cyp12a4
FBgn0051729	5345.78882	0.07291063	0.01640507	CG31729
FBgn0085428	26.1032315	0.43211206	0.01641635	Nox
FBgn0261929	472.547403	0.1278575	0.01641635	5-HT2B
FBgn0016123	1184.39034	-0.1052008	0.01645591	Alp4
FBgn0050033	221.976063	0.17310471	0.0164698	CG30033
FBgn0027843	3194.63198	-0.0889063	0.0164698	CAH2
FBgn0035811	374.02762	-0.1482836	0.0164698	Mcad
FBgn0034136	421.590429	0.13805737	0.01659543	DAT
FBgn0034474	2554.69781	0.13290806	0.01670683	Obp56g
FBgn0062961	115.856118	0.26032444	0.01681238	lncRNA:CR33942
FBgn0037683	290.407032	0.21614242	0.01681238	CG18473
FBgn0000318	969.757274	-0.0932741	0.01685731	cl
FBgn0029937	428.204598	-0.1244063	0.01685731	CG8300
FBgn0035679	328.761292	-0.1781863	0.01685731	CG10467
FBgn0036622	250.769673	0.22744087	0.01709206	Agpat4

FBgn0031327	1480.36494	0.1267088	0.01721697	CG5397
FBgn0010414	418.870844	-0.1154828	0.01728325	SerT
FBgn0040001	58.1811929	0.28999361	0.01730255	FASN3
FBgn0036028	286.127936	-0.1390414	0.01731718	CG16717
FBgn0029174	1255.70297	-0.0809426	0.0174483	Fkbp59
FBgn0038914	209.717107	0.50082825	0.01781839	fit
FBgn0052819	53.8091366	-0.383941	0.01787418	CG32819
FBgn0027532	1061.78695	0.10030138	0.01812946	CG7139
FBgn0033465	1875.13668	-0.1058391	0.01813902	NA
FBgn0267435	42359.2472	-0.0843093	0.0182382	chp
FBgn0260941	3500.54421	0.11374686	0.01840823	app
FBgn0031816	449.633876	-0.117275	0.01854383	Rchy1
FBgn0037265	410.685798	-0.122694	0.01854383	spartin
FBgn0031999	158.375388	0.35568515	0.01868662	CG8419
FBgn0043535	786.277351	0.13323616	0.01868662	Obp57a
FBgn0035371	1720.52197	-0.0795573	0.01868662	AhcyL1
FBgn0004876	1935.21101	0.10656567	0.01869818	cdi
FBgn0259714	940.631817	0.11644276	0.01871014	DIP-epsilon
FBgn0033365	58.0978634	-0.2933763	0.01871014	CG8170
FBgn0015766	34032.4485	-0.0710662	0.01871297	Msr-110
FBgn0034994	7.27834679	0.86344488	0.01882574	Ir60a
FBgn0261618	8211.15373	0.09546729	0.01887308	larp
FBgn0036462	212.52003	-0.1677923	0.019035	mRpL39
FBgn0025633	1092.09946	0.09849904	0.01907235	CG13366
FBgn0265998	6905.57021	0.11680908	0.01907765	Doa
FBgn0032233	759.905106	0.09464918	0.01923176	dpr19
FBgn0053531	456.240853	0.12060816	0.01927447	Ddr
FBgn0011274	2791.8201	0.11320456	0.01927447	Dif
FBgn0085813	12827.1529	0.30367727	0.01928829	18SrRNA-Psi:CR41602
FBgn0003091	4524.67353	0.08612474	0.01928829	Pkc53E
FBgn0265253	10.518348	0.67633756	0.01930762	asRNA:CR44267
FBgn0063449	70.1120007	0.26843115	0.0195059	Uhg2
FBgn0011693	10169.5086	-0.1101916	0.0195076	Pdh
FBgn0028841	21.2149748	0.76834053	0.01962376	jhamt
FBgn0052082	3638.809	-0.0592509	0.01977484	IRSp53
FBgn0011770	1520.97844	-0.1144749	0.01980936	Gip
FBgn0039759	132.127358	0.63423546	0.02018282	CG9733
FBgn0036773	587.001122	0.10814226	0.0202703	CG13698
FBgn0010288	596.884616	-0.1043275	0.02033664	Uch
FBgn0022359	153.001092	0.19084555	0.02054414	Sodh-2
FBgn0028694	774.372828	-0.0970062	0.02089699	Rpn11
FBgn0011591	1116.48453	0.09933479	0.02099718	fng

FBgn0267511	14929.5843	0.38532046	0.02108947	28SrRNA-Psi:CR45851
FBgn0050154	41.6888545	0.36449442	0.02108947	CG30154
FBgn0052767	2984.91487	0.11844517	0.02108947	CG32767
FBgn0028327	3140.73673	0.09566531	0.02108947	l(1)G0320
FBgn0035402	654.312735	-0.1152136	0.02108947	Usp5
FBgn0029723	733.19572	0.09728919	0.02118846	Proc-R
FBgn0001250	2284.18809	0.07357082	0.02126623	if
FBgn0083977	132.113377	-0.1920898	0.02127425	CG34141
FBgn0034709	2911.36969	0.13060034	0.02129071	Swim
FBgn0036382	93.9390566	0.27039843	0.02129909	CG13737
FBgn0263144	1915.17604	0.06481714	0.02139894	bin3
FBgn0266580	1048.53775	0.14850802	0.02181443	Gp210
FBgn0004197	61.9332781	0.2708833	0.02184222	Ser
FBgn0000723	1856.29975	0.12705004	0.02184222	FER
FBgn0005278	5424.70721	0.0864766	0.02191708	Sam-S
FBgn0266774	4.59403367	1.07217051	0.02201095	lncRNA:CR45239
FBgn0028408	1696.06927	0.09169017	0.02201095	Drep2
FBgn0028695	1961.29794	-0.0778203	0.02201095	Rpn1
FBgn0038065	2085.59688	-0.0813252	0.02202971	Snx3
FBgn0037533	4635.73453	0.10348013	0.02212214	CD98hc
FBgn0042129	69.1953633	0.75450198	0.02224981	OS9
FBgn0043799	53.2363901	-0.3106648	0.0223034	CG31381
FBgn0029506	3154.59175	0.09003102	0.02240608	Tsp42Ee
FBgn0261552	27617.4876	0.09745134	0.0224609	ps
FBgn0262721	13.5077505	0.56616621	0.02260193	CG43165
FBgn0032297	2660.92987	0.13061828	0.02260193	CG17124
FBgn0035534	152.464565	-0.1723448	0.02260193	mRpS6
FBgn0037016	500.06263	0.10984646	0.02276324	CG13252
FBgn0260962	986.821491	-0.1001702	0.02284391	pic
FBgn0030234	724.343396	-0.1253828	0.02299074	CG15211
FBgn0030336	2640.87538	0.07291459	0.02317533	CG1578
FBgn0036213	9238.60017	0.07139902	0.02322889	RpL10Ab
FBgn0016075	7272.18258	0.10136591	0.02325921	vkg
FBgn0029892	104.350207	0.2069006	0.02364983	CG3184
FBgn0038683	826.740066	-0.1032509	0.02365408	CG11779
FBgn0037845	260.574224	-0.1569706	0.02381429	CG14694
FBgn0262532	55.8592515	0.34809208	0.02386796	CR43086
FBgn0034398	6470.68127	0.06853836	0.02414679	CG15098
FBgn0085195	2309.65489	-0.2730398	0.02414679	CG34166
FBgn0032181	13.4430314	1.25322496	0.02417069	CG13133
FBgn0001233	16376.7475	-0.1173075	0.02417604	Hsp83
FBgn0053556	2998.34753	-0.0869425	0.02449705	form3

FBgn0039897	1692.46275	0.11223961	0.02470668	CG1674
FBgn0263102	4733.21415	0.10776925	0.02470668	psq
FBgn0014189	1209.44839	-0.0827557	0.02470668	Hel25E
FBgn0028983	152.786326	-0.191911	0.02470668	Spn55B
FBgn0040735	1824.02466	0.21561697	0.02482485	CG16836
FBgn0040260	816.746289	-0.0954548	0.02489339	Ugt37D1
FBgn0038142	17.2339041	-0.6284777	0.02519489	CheA87a
FBgn0038115	654.304606	-0.1095249	0.02528364	CG7966
FBgn0015791	2144.68507	-0.0869258	0.02562214	Rab14
FBgn0031220	2044.38742	0.14342705	0.02574363	CG4822
FBgn0041579	1480.76424	1.34646159	0.02585847	AttC
FBgn0032216	697.035557	-0.0908389	0.02586265	Usp14
FBgn0034802	7418.39247	-0.0825748	0.02590328	CNBP
FBgn0033886	1209.56113	-0.0869892	0.02635971	Rpn13
FBgn0032834	85.3042037	0.24359447	0.02640001	CG13965
FBgn0032397	484.007732	-0.1146466	0.02640001	Tom70
FBgn0039858	21214.3103	0.08812608	0.02641033	CycG
FBgn0031998	425.951819	-0.1528597	0.0265706	SLC5A11
FBgn0030159	693.922951	0.10554774	0.02663928	CG9689
FBgn0010388	470.208547	1.33825163	0.02664657	Dro
FBgn0014396	17948.0563	-0.088912	0.02690168	tim
FBgn0000250	2858.13619	0.06988259	0.02709726	cact
FBgn0033129	117.638945	0.19899499	0.02758809	Tsp42Eh
FBgn0037249	4078.26058	0.06906382	0.02758809	eIF3a
FBgn0040793	2384.16152	-0.0982343	0.02758809	CG7630
FBgn0039155	472.651584	-0.1059008	0.02767219	Kal1
FBgn0259745	1772.00697	0.10389001	0.02778574	wech
FBgn0260753	1443.47667	-0.0732989	0.02778574	Pdfr
FBgn0002592	25.1086346	-0.3875823	0.02778574	E(spl)m2-BFM
FBgn0034253	155.660299	0.19478786	0.02794698	CG10936
FBgn0085408	906.389302	0.0992902	0.02806291	Shrm
FBgn0000116	28175.9065	-0.0887397	0.02828372	Argk
FBgn0031497	735.851833	-0.1068991	0.02860221	SerRS
FBgn0028699	1945.06333	0.08186319	0.02869567	Rh50
FBgn0028360	682.486924	-0.1232835	0.02891566	Cdc7
FBgn0037107	928.717812	0.10775965	0.02901871	CG7166
FBgn0264000	1239.16766	0.08534449	0.02908068	GluRIB
FBgn0039544	402.006635	-0.1217866	0.02916829	CG12877
FBgn0067102	690.109625	-0.1163721	0.02917666	GlcT
FBgn0039844	2539.18936	0.08967754	0.0295677	CG1607
FBgn0087012	1784.82686	-0.0791035	0.02957122	5-HT2A
FBgn0029851	41.8710845	0.58414042	0.0295782	CG14445

FBgn0043791	471.272965	0.43329516	0.0295782	phu
FBgn0265274	1825.62372	0.08000335	0.0295782	Inx3
FBgn0001291	658.548799	-0.1162855	0.0295782	Jra
FBgn0028542	347.879261	0.15839573	0.02972152	NimB4
FBgn0029834	2233.94007	-0.09613	0.02972152	CG5937
FBgn0000278	4.99251503	1.05785868	0.02999679	CecB
FBgn0283472	2802.41319	0.06793799	0.03057621	S6k
FBgn0038194	6302.44752	-0.1142487	0.03061498	Cyp6d5
FBgn0023174	1088.30617	-0.0826959	0.03100196	Prosbeta2
FBgn0025625	1947.52195	-0.0725713	0.03120766	Sik2
FBgn0037672	67.5043279	-0.2579977	0.03128405	sage
FBgn0011296	591.908398	0.14298827	0.03131774	l(2)efl
FBgn0051935	588.433598	0.10261362	0.03156682	CG31935
FBgn0032393	1431.06639	-0.079928	0.03188531	Nfs1
FBgn0035781	14.6123091	0.53345982	0.03193751	CG8560
FBgn0038742	699.128866	-0.1175121	0.03210228	Arc42
FBgn0004880	8755.67373	0.09090714	0.03231872	scrt
FBgn0035688	2954.15529	0.08656902	0.03231872	fmt
FBgn0042179	15.8087996	0.47176706	0.03263639	Ugt305A1
FBgn0034142	1774.42139	-0.0845083	0.03270595	CG8306
FBgn0034069	205.68174	-0.1645478	0.03303703	CG8401
FBgn0030893	204.077229	-0.1455016	0.03306348	RhoGAP16F
FBgn0034246	1309.20477	0.07995961	0.03308049	Dcr-2
FBgn0032482	3774.79949	-0.0723457	0.03308372	Pect
FBgn0039993	1488.71561	0.09263602	0.03323207	CG17691
FBgn0039089	961.32279	0.08864364	0.03327571	beat-IV
FBgn0259878	327.750037	0.1260997	0.03355968	Fs
FBgn0086358	1321.07941	-0.0865379	0.03355968	Tab2
FBgn0034436	590.601228	-0.1023797	0.03355968	CG11961
FBgn0037726	40.3813141	0.99557559	0.03358045	CG9492
FBgn0003328	623.461897	0.10081244	0.03358045	NA
FBgn0040653	20607.7554	0.24654971	0.03360745	IM4
FBgn0000667	2744.60875	0.09284039	0.03377871	Actn
FBgn0037712	221.832165	-0.1586092	0.03389422	CG16789
FBgn0032821	1920.52652	-0.1104043	0.03400324	CdGAPr
FBgn0039510	41.8358673	0.38665267	0.03446279	CG3339
FBgn0032222	924.706081	-0.0859569	0.03490056	CG5037
FBgn0031145	910.985567	-0.0849091	0.03498873	Ntf-2
FBgn0038214	65.0232694	0.35731117	0.03507195	CG9616
FBgn0029639	620.370805	0.22079174	0.03507195	CG14419
FBgn0030976	3259.77832	-0.0638948	0.03507195	CG7378
FBgn0024248	1113.7981	0.08161886	0.03532117	chico

FBgn0250869	1413.67836	-0.0868312	0.03543407	CG42240
FBgn0037163	1924.83947	-0.1010044	0.0354709	laza
FBgn0037836	77.7495968	0.24172238	0.03549526	CG14692
FBgn0001078	1485.03794	0.09679864	0.03549526	ftz-f1
FBgn0037410	782.216883	-0.1934195	0.03590579	Osi2
FBgn0036479	121.565744	0.18451969	0.03613903	CG13458
FBgn0051777	236.087577	-0.1479683	0.03613903	CG31777
FBgn0261553	2857.31934	0.08645198	0.03614072	CG42671
FBgn0004687	1988.39454	-0.0846292	0.03672578	Mlc-c
FBgn0037447	503.375135	0.12078435	0.03683072	Neurochondrin
FBgn0034396	381.685067	-0.1270564	0.03710373	CG15097
FBgn0038056	207.588429	-0.1496099	0.03729883	CG5961
FBgn0040493	686.115657	-0.0929254	0.03736399	grsm
FBgn0039205	151.901541	-0.160207	0.03740825	CG13623
FBgn0035410	503.902261	0.10073832	0.03765369	CG14964
FBgn0016672	3753.04965	-0.0669803	0.03765369	lpp
FBgn0034407	568.979961	1.21637008	0.03801415	DptB
FBgn0087011	456.792575	0.15260015	0.03803323	CG41520
FBgn0028494	60.356586	0.46691052	0.03810882	CG6424
FBgn0030332	479.849355	-0.122002	0.0381841	CG9360
FBgn0015039	3751.49009	-0.0908939	0.03837925	Cyp9b2
FBgn0036882	1717.30229	-0.0945994	0.0386366	CG9279
FBgn0085790	66.9540992	0.27949799	0.03889469	CR41507
FBgn0033602	526.161989	0.11860247	0.03889469	Cpr47Ee
FBgn0259175	1574.38445	0.09502417	0.03889469	ome
FBgn0264989	1189.74577	0.15466091	0.03904484	CG44140
FBgn0265487	5858.81205	0.13509356	0.03904484	mbl
FBgn0035372	533.6342	0.10850061	0.03917895	CG12093
FBgn0029824	616.851532	0.09558084	0.03917895	CG3726
FBgn0037935	1230.13062	0.07546365	0.03917895	CG6834
FBgn0035266	980.434632	0.13064944	0.03934208	Gk2
FBgn0004859	873.25728	0.12292023	0.03945961	ci
FBgn0035484	2263.95935	-0.1591677	0.03956241	CG11594
FBgn0035831	48.2301667	-0.2467884	0.03956241	CG8038
FBgn0035625	3133.61867	0.07949441	0.03968204	Blimp-1
FBgn0031753	113.680244	-0.1982474	0.03974953	CG13999
FBgn0000299	9035.94968	0.12098132	0.03991358	Col4a1
FBgn0013771	1233.84051	0.07540667	0.03991358	Cyp6a9
FBgn0027101	2205.84201	0.13337164	0.03995574	Dyrk3
FBgn0040397	1005.78858	0.09786782	0.04012791	CG3655
FBgn0051451	24793.2265	-0.107685	0.04022627	lncRNA:CR31451
FBgn0031250	131.585735	0.1646922	0.04045144	Ent1

FBgn0267431	37.0855009	0.29387276	0.04058194	Myo81F
FBgn0259111	3767.6794	0.0768486	0.04058194	Ndae1
FBgn0023495	12.1944957	-0.0308474	0.04058194	Lip3
FBgn0261999	1417.3329	-0.1267152	0.04059687	Ca-Ma2d
FBgn0052602	136.943914	-0.2371816	0.04086913	Muc12Ea
FBgn0034401	673.760009	0.12846649	0.04113495	MetRS
FBgn0264990	1207.4876	0.15362374	0.04119801	CG44141
FBgn0000370	5755.01402	0.09445849	0.04119801	crc
FBgn0002121	1637.63631	0.11300565	0.0413323	l(2)gl
FBgn0259711	90.1114187	-0.1919259	0.04161332	CG42365
FBgn0032796	1600.65435	0.07277495	0.04177242	CG10188
FBgn0034184	2358.70944	-0.0909982	0.04179038	CG9646
FBgn0026268	725.95017	0.38249718	0.04189287	antdh
FBgn0037363	2722.10666	0.0859213	0.04189287	Atg17
FBgn0033836	500.923129	-0.113741	0.04189287	CG18278
FBgn0050109	91.2116912	-0.2061461	0.04189287	CG30109
FBgn0262881	56.6519523	0.64834608	0.04194363	CG43236
FBgn0038299	495.797188	0.44349605	0.04224386	Spn88Eb
FBgn0262533	57.2616808	0.33460753	0.04233755	CR43087
FBgn0039685	888.447313	-0.3319913	0.04239294	Obp99b
FBgn0027786	1277.46383	-0.0686267	0.04257791	Mtch
FBgn0035370	941.457265	-0.0860492	0.04257791	Non2
FBgn0034618	3460.61595	0.08755506	0.04259851	CG9485
FBgn0036879	6.25779052	-0.0241771	0.04288245	Cpr76Bb
FBgn0029710	86.7835342	0.19265395	0.0431289	CG3568
FBgn0020414	2562.43633	0.07386403	0.04317375	Idgf3
FBgn0039806	26.2603715	0.34802357	0.04331843	CG15545
FBgn0085274	21.8687719	-0.3947129	0.04357046	CG34245
FBgn0000715	232.388607	0.17097907	0.04359749	FMRFa
FBgn0029944	209.465414	0.13600255	0.04389525	Dok
FBgn0037755	510.150906	0.10106462	0.04389525	CG12945
FBgn0039277	1314.47161	0.07767964	0.04389525	Nepl16
FBgn0032889	2346.00697	-0.1162638	0.04390893	CG9331
FBgn0051053	19.2482136	-0.4239496	0.04403068	CG31053
FBgn0263911	1625.15884	-0.0912233	0.04446195	COX8
FBgn0033093	544.960174	-0.1194266	0.04454543	CG3270
FBgn0259233	559.139428	-0.1455996	0.0447053	CG42331
FBgn0029898	1438.78125	0.13195484	0.04483505	CG14439
FBgn0036534	3993.58719	0.10726336	0.04483505	DCP2
FBgn0032129	3461.6124	0.09643087	0.04483505	jp
FBgn0039332	2100.63512	0.0907303	0.04483505	alrm
FBgn0000636	1365.85388	0.0648489	0.04483505	Fas3

FBgn0004397	4417.75832	-0.0845725	0.04496902	Vinc
FBgn0267253	1420.18448	-0.0751109	0.04510441	CG32700
FBgn0261584	59.3941789	0.25490729	0.04530199	CG42694
FBgn0036668	1239.5751	0.08316962	0.04581719	Zcchc7
FBgn0039417	133.905247	0.17029349	0.0459216	CG6073
FBgn0035111	941.622025	-0.0780258	0.0459216	Dis3l2
FBgn0034266	6.08320845	0.61017166	0.0460156	CG4975
FBgn0058470	1126.20826	0.23699443	0.04639193	CG40470
FBgn0010314	92.4792886	-0.521823	0.04639193	Cks30A
FBgn0034877	3395.53759	-0.0732639	0.04641756	levy
FBgn0028953	2320.97663	0.05471366	0.0466987	CG14478
FBgn0050410	608.355458	-0.1100617	0.04680255	Rpi
FBgn0027836	748.170679	0.1001625	0.04697348	Dgp-1
FBgn0263198	3225.45993	-0.0527889	0.04697348	Acn
FBgn0029997	1542.19047	0.09480998	0.04722753	CG2258
FBgn0085442	3565.38217	-0.0676837	0.04722753	NKAIN
FBgn0031995	2434.82733	0.06449445	0.04738084	CG8475
FBgn0028523	833.038573	0.09100745	0.04738452	CG5888
FBgn0032026	943.512584	0.07663155	0.04740052	CG7627
FBgn0033728	1722.10566	-0.1684897	0.04740052	Cpr49Ae
FBgn0010551	1459.6636	-0.0776012	0.04807929	Phb2
FBgn0063496	15.3632416	0.00730511	0.04812387	GstE4
FBgn0025800	3576.63405	0.081165	0.04825416	Smox
FBgn0264563	5.23641348	0.6674684	0.04827074	CG43935
FBgn0041236	7.99043158	0.53526915	0.04861848	Gr59d
FBgn0033170	1037.87519	0.11206661	0.04866174	sPLA2
FBgn0028990	1432.1538	0.10196862	0.04884803	Spn27A
FBgn0010213	1425.90246	-0.0913916	0.04884803	Sod2
FBgn0034075	994.347844	0.09258136	0.04889612	Asph
FBgn0082954	16.7546011	0.37642328	0.04895675	snoRNA:Psi28S-3571
FBgn0032453	1341.95935	-0.0866824	0.04895675	CG6180
FBgn0033692	350.542478	-0.1135579	0.04895675	wash
FBgn0259229	82.4023501	0.2777851	0.04902508	CG42329
FBgn0011361	1641.2997	-0.0904964	0.04915766	ND-ACP
FBgn0037818	180.094536	-0.1594712	0.0494081	CG6465
FBgn0029912	838.536002	-0.0759508	0.04955078	CG4557
FBgn0046258	31.5345717	-0.2869443	0.04971545	CG12880